Titre: Title:	Reduced-order modeling of mistuned bladed disks with geometric and contact nonlinearities
Auteur: Author:	Elise Delhez
Date:	2022
Type:	Mémoire ou thèse / Dissertation or Thesis
Référence: Citation:	Delhez, E. (2022). Reduced-order modeling of mistuned bladed disks with geometric and contact nonlinearities [Ph.D. thesis, Polytechnique Montréal]. PolyPublie. https://publications.polymtl.ca/10683/

POLYTECHNIQUE MONTRÉAL
affiliée à l'Université de Montréal

ET

UNIVERSITÉ DE LIÈGE

Reduced-order modeling of mistuned bladed disks with geometric and contact nonlinearities

ELISE DELHEZ
Département de génie mécanique

Thèse présentée en vue de l'obtention du diplôme de *Philosophiæ Doctor*
Génie mécanique

Septembre 2022

POLYTECHNIQUE MONTRÉAL
affiliée à l'Université de Montréal

ET

UNIVERSITÉ DE LIÈGE

Cette thèse intitulée :

Reduced-order modeling of mistuned bladed disks with geometric and contact nonlinearities

présentée par **Elise DELHEZ**
en vue de l'obtention du diplôme de *Philosophiæ Doctor*
a été dûment acceptée par le jury d'examen constitué de :

Frédérick GOSSELIN, président
Alain BATAILLY, membre et directeur de recherche
Jean-Claude GOLINVAL, membre et codirecteur de recherche
Florence NYSSEN, membre et codirectrice de recherche
Olivier BRÜLS, membre
Jean DE CAZENOVE, membre
Evangéline CAPIEZ-LERNOUT, membre externe

ACKNOWLEDGEMENTS

First of all, I would like to express my deep gratitude to Professors Jean-Claude Golinval and Alain Batailly. As supervisors, they have really helped me with their useful critiques and their support throughout this work. I also thank Dr. Florence Nyssen for her availability and her precious advice.

I acknowledge the members of my thesis committee, Professors Jean-Philippe Ponthot and Olivier Brüls, for their relevant remarks.

Words cannot express my gratitude to Louis for his valuable advice and for the multi-threaded implementation of tensor products without which the numerical simulations would still be running.

I am also grateful to the Belgian National Fund for Scientific Research (F.R.S.-FNRS) for its financial support through the Aspirant FNRS and mobility grants. The Zonta International foundation, the Wallonia-Brussels Federation and the Canada Research Chairs Program are also thanked for the provided funding.

At last, I wish to extend my special thanks to my colleagues from the University of Liège and Polytechnique Montréal, my friends and my family for their support.

RÉSUMÉ

Les travaux de recherche présentés dans cette thèse ont permis de développer une méthodologie pour étudier de manière numériquement efficace les interactions en contact de disques aubagés désaccordés présentant un comportement géométriquement non linéaire. Cette méthodologie basée sur des techniques de réduction de modèles permet de contourner la difficulté liée au coût numérique exorbitant des simulations numériques non linéaires pour décrire précisément la dynamique des structures industrielles.

Dans un premier temps, une méthodologie est développée pour étudier les interactions en contact d'une aube unique en rotation avec non-linéarités géométriques. La procédure de réduction est basée sur le concept de dérivées modales qui est ici adapté pour permettre de conserver des degrés de liberté physiques dans l'espace réduit pour l'implémentation du contact. Un critère de sélection des dérivées modales est proposé pour limiter la taille du modèle réduit. La projection dans l'espace réduit des forces non linéaires dues aux grands déplacements est évaluée avec la *stiffness evaluation procedure*. Le contact est traité numériquement avec multiplicateurs de Lagrange. La méthodologie est ensuite généralisée au cas des roues aubagées complètes en utilisant des méthodes de synthèse modale avec interfaces fixes. La méthodologie finale est compatible avec l'introduction de désaccordage dans le modèle réduit.

Dans ce travail, la méthodologie est appliquée au cas du rotor 37 de la NASA. Il s'agit d'un modèle ouvert d'un étage de compresseur permettant la reproductibilité des résultats et leur comparaison. Les résultats obtenus et, lorsque c'est possible, leur comparaison avec les résultats obtenus avec le modèle éléments finis non réduit, donnent confiance dans la méthodologie. Des analyses plus poussées relatives à la consommation du jeu et à l'utilisation d'un algorithme de continuation séquentielle pour déterminer les courbes de réponses en fréquence permettent de comprendre et caractériser l'influence des non-linéarités géométriques sur la dynamique en contact de la structure.

En plus de fournir une description précise de la dynamique de la structure dans le temps, la méthodologie développée permet aussi d'extraire des quantités d'intérêt utiles aux chercheurs et motoristes comme les cartes d'interactions au contact, les cartes d'usure, les vitesses de rotation critiques et les champs de contraintes dans la structure. La stratégie développée est dite non intrusive et peut donc être combinée à n'importe quel logiciel éléments finis commercial.

ABSTRACT

This thesis introduces a new methodology to study the dynamics of mistuned bladed disks with geometric and contact nonlinearities in a numerically efficient way. The methodology is based on a reduction procedure. This allows to overcome the difficulties related to the high computational costs of nonlinear dynamic simulations performed on industrial finite element models.

First, a methodology is developed to study the contact interactions of a single rotating blade with geometric nonlinearities. The reduction method is based on the modal derivative approach, which is adapted to retain physical degrees-of-freedom in the reduced space for the implementation of contact. In order to limit the size of the reduced system, a modal derivative selection criterion is proposed. The nonlinear internal forces due to large displacements are evaluated in the reduced space using the stiffness evaluation procedure. Contact is numerically handled using Lagrange multipliers. The methodology is then generalized to full bladed disk structures using component mode synthesis techniques with fixed interfaces. Mistuning can also be included in the reduced space.

Through this work, the numerical strategy is applied to an open industrial compressor bladed disk model based on the NASA rotor 37 in order to promote the reproducibility of results. The obtained results and, when applicable, their comparison with full-order model results give confidence in the methodology. In-depth analyses, including clearance consumption computations and frequency analyses with a continuation procedure, allow to understand and characterize the combined influence of contact and geometric nonlinearities on the structure's dynamics.

Besides providing an accurate description of the time dynamics of the structure, the new methodology also allows to extract quantities of interest that are relevant for both researchers and industrial designers such as contact interaction maps, contact wear maps, critical angular speeds or stress fields in the structure. This non-intrusive strategy can be used in combination with any commercial finite element software.

TABLE OF CONTENTS

LIST OF TABLES

LIST OF FIGURES

LIST OF ACRONYMS AND SYMBOLS

Acronyms

1B, 2B	First bending mode, second bending mode
1T	First torsion mode
AFT	Alternating frequency/time
CB	Craig-Bampton
CFD	Computational fluid dynamics
CMS	Component mode synthesis
CPU	Central processing unit
DEIM	Discrete empirical interpolation method
DOF	Degree-of-freedom
DRAM	Dynamic random access memory
EO	Engine order
FE	Finite element
FOM	Full-order model
FRC	Frequency response curve
HBM	Harmonic balance method
HCF	High-cycle fatigue
IM	Internal mode
LE	Leading edge
LNM	Linear normal mode
MC	Mid-chord
MD	Modal derivative
MEMS	Microelectromechanical systems
MI	Modal interaction
MMI	Maximum modal interaction
ND	Nodal diameter
NEMS	Nanoelectromechanical systems
NFRC	Nonlinear frequency response curve
NIFO	Nonlinear identification through feedback of the outputs
NNM	Nonlinear normal mode
POD	Proper orthogonal decomposition
POM	Proper orthogonal mode

POV	Proper orthogonal value
RAM	Random access memory
RL-HBM	Regularized-Lanczos harmonic balance method
ROM	Reduced-order model
SAFE	Singh's advanced frequency evaluation
SM	Static mode
SMVW	Symmetric modal virtual work
SOD	Smooth orthogonal decomposition
SOM	Smooth orthogonal mode
SOV	Smooth orthogonal value
SPM	Smooth projection mode
STEP	Stiffness evaluation procedure
SVD	Singular value decomposition
TE	Trailing edge

Symbols

α, β	Parameters of Rayleigh structural damping model
γ	Smoothing parameter in the regularized penalty contact law
Γ	Boundary of the structure
Γ_c	Contact surface
δ	Level of deformation
$\Delta_\delta^{\mathrm{X}}$	Clearance consumption in mode X at the level of deformation δ
ζ_j	Lanczos factor of harmonic j
θ	In-plane rotation
κ	Penalty coefficient in the regularized penalty contact law
λ_j	j^{th} smooth orthogonal value
μ	Dynamic friction coefficient
μ_s	Static friction coefficient
ν	Poisson's ratio
ξ_j	Modal damping coefficient for mode j
ρ	Density
ω	Pulsation of a harmonic excitation
ω_j	j^{th} blade's eigenpulsation
Ω	Angular speed
Ω_N	Nominal angular speed

a	Length of square cross section side
A	Amplitude of a harmonic excitation
c	Clearance in deformed configuration
c_0	Clearance between the blade-tip nodes and the casing
e_j	j^{th} criterion in performance indicator
$e_{\text{o}j}$	Engine order j
E	Young's modulus
$\bar{E}$	Energy
E_j	j^{th} excitation case
E_n	Nominal value of the Young's modulus
f	Frequency of a harmonic excitation
f_j	j^{th} blade's eigenfrequency
g	Gap function
h	Time step of integration
H	Number of harmonics in the HBM
I	Performance indicator
L	Length of the beam
LF	Localization factor
m	Number of displacement snapshots in the POD
N	Number of nodes on which the excitation is distributed
N_b	Number of impacting nodes
N_c	Number of criteria in performance indicator
N_d	Number of nodal diameters
N_{DOF}	Number of degrees-of-freedom of the structure
N_h	Number of time steps in AFT
N_s	Number of sectors
N_{static}	Number of nonlinear forces static evaluations in the STEP
p_0	Penetration of the casing with respect to the trajectory of a tip node
r	Reduced-order model size
r_b	Number of constraint modes in the reduction basis
r_c	Number of fixed interface linear normal modes in the reduction basis
r_{cyclic}	Number of linear normal modes for the reduction of the cyclic boundary
r_f	Number of POD modes for the nonlinear forces filtering
r_{MD}	Number of modal derivatives in the reduction basis
r_{POD}	Number of POD modes in the reduction basis
R_g	Fixed reference frame

R_m	Rotating frame
t	Time
$t_{c,\mathrm{N}}$	Contact pressure in the normal direction
T	Period of a harmonic excitation
$\mathcal{T}$	Kinetic energy
u	Axial displacement
v	Transverse displacement
V	Volume of the structure
$\mathcal{V}$	Strain energy
$W_{jk}^{(\alpha)}$	Weight associated to MD $\boldsymbol{\zeta}_{jk}$ according to selection criterion α
$\mathcal{W}$	Work of external forces
$\boldsymbol{\eta}$	Generalized coordinates related to linear normal modes
$\bar{\boldsymbol{\eta}}$	Generalized coordinates related to Craig-Bampton modes
$\boldsymbol{\eta}_c$	Generalized coordinates related to fixed interface linear normal modes
$\boldsymbol{\eta}_{\mathrm{cyclic}}$	Generalized coordinates related to the reduction of the cyclic boundary
$\boldsymbol{\eta}_{\mathrm{MD}}$	Generalized coordinates related to modal derivatives
$\boldsymbol{\eta}^n$	Generalized coordinates related to sector n
$\boldsymbol{\eta}_{\mathrm{POD}}$	Generalized coordinates related to POD modes
$\boldsymbol{\lambda}$	Lagrange multipliers
$\boldsymbol{\omega}$	Angular speed vector describing the rotation of R_m with respect to R_g
$\mathbf{a}_k, \mathbf{b}_k$	Fourier coefficients of the displacement
$\mathbf{a}_k^c, \mathbf{b}_k^c$	Fourier coefficients of the contact forces
$\mathbf{b}$	Displacement vector describing the translation of R_m with respect to R_g
$\mathbf{d}$	Distance between the impacting nodes and the obstacle
$\mathbf{d}^p$	Distance predicted between the impacting nodes and the obstacle
$\mathbf{f}$	Vector of external body forces in R_m
$\mathbf{f}_c$	Vector of nonlinear forces due to contact interactions
$\hat{\mathbf{f}}_c$	Vector of Fourier coefficients related to $\mathbf{f}_c$
$\mathbf{f}_e$	Vector of external forces
$\hat{\mathbf{f}}_e$	Vector of Fourier coefficients related to $\mathbf{f}_e$
$\mathbf{f}_{ei}$	Centrifugal force vector
$\mathbf{g}_{\mathrm{nl}}$	Nonlinear internal forces due to large displacements
$\hat{\mathbf{g}}_{\mathrm{nl}}$	Vector of Fourier coefficients related to $\mathbf{g}_{\mathrm{nl}}$
$\mathbf{g}_{\mathrm{nl}}^f$	POD-filtered nonlinear internal forces due to large displacements
$\mathbf{g}_{\mathrm{nl}}^n$	Nonlinear internal forces due to large displacements at DOFs $\bar{\mathbf{u}}^n$
$\mathbf{q}$	Vector of generalized coordinates in reduced space

$\mathbf{r}$	Residue
$\mathbf{s}$	Displacement vector in R_m
$\mathbf{t}$	Vector of surface tractions in R_m
$\mathbf{t}_c$	Vector of contact forces in R_m
$\mathbf{t}_{c,\mathrm{T}}$	Vector of tangential contact forces in R_m
$\mathbf{u}$	Relative displacement vector around prestressed equilibrium
$\breve{\mathbf{u}}$	Relative displacement vector in cyclic coordinates
$\hat{\mathbf{u}}$	Vector of Fourier coefficients related to $\mathbf{u}$
$\mathbf{u}^\star$	Displacement snapshot
$\mathbf{u}^c$	Corrected displacement field (accounting for contact constraints)
$\breve{\mathbf{u}}_j$	Harmonic j of the relative displacement vector in cyclic coordinates
$\mathbf{u}^n$	Relative displacement vector of sector n around prestressed equilibrium
$\bar{\mathbf{u}}^n$	Relative displacement vector of sector n without cyclic boundary DOFs
$\mathbf{u}^p$	Predicted displacement field (without contact constraints)
$\mathbf{u}_r$	Radial displacement amplitude for each blade
$\mathbf{u}_s$	Prestressed equilibrium state
$\mathbf{v}_\mathrm{T}$	Relative tangential velocity in R_m
$\mathbf{w}_j$	Fourier vector j
$\mathbf{x}$	Position vector in R_m
$\mathbf{y}$	Position vector in R_g
$\boldsymbol{\Gamma}$	Mapping of the reduction procedure
$\boldsymbol{\epsilon}$	Strain tensor
$\mathbf{Z}$, $\boldsymbol{\zeta}_{jk}$	Fixed interface MD of CB modes, MD of mode j with respect to mode k
$\bar{\mathbf{Z}}$, $\bar{\boldsymbol{\zeta}}_{jk}$	Modal derivatives of CB modes, MD of mode j with respect to mode k
$\boldsymbol{\Theta}$, $\boldsymbol{\theta}_j$	Fixed interface linear normal modes, j^{th} mode of the basis
$\boldsymbol{\Lambda}$, $\boldsymbol{\lambda}_j$	Smooth projection modes, j^{th} mode of the basis
$\boldsymbol{\Xi}$, $\boldsymbol{\xi}_{jk}$	Modal derivatives of LNM, MD of mode j with respect to mode k
$\boldsymbol{\Pi}$	Linear normal modes of cyclic boundary substructures
$\boldsymbol{\sigma}$	Stress tensor
$\boldsymbol{\Sigma}$	Autocovariance matrix
$\boldsymbol{\Upsilon}$	Orthogonalization basis in Petrov-Galerkin method
$\boldsymbol{\Phi}$, $\boldsymbol{\phi}_j$	Reduction basis, j^{th} mode of the basis
$\hat{\boldsymbol{\Phi}}$, $\hat{\boldsymbol{\phi}}_j$	Linear normal modes, j^{th} mode of the basis
$\tilde{\boldsymbol{\Phi}}$, $\tilde{\boldsymbol{\phi}}_j$	Linear normal modes in deformed configuration, j^{th} mode of the basis
$\breve{\boldsymbol{\Phi}}$, $\breve{\boldsymbol{\phi}}_j$	CB modes in deformed configuration, j^{th} mode of the basis
$\boldsymbol{\Phi}_f$	Basis for the POD filtering of nonlinear internal forces

$\boldsymbol{\Phi}_{\mathrm{I}}$, $\boldsymbol{\Phi}_{\mathrm{II}}$	Reduction bases for the first and second projections
$\bar{\boldsymbol{\Phi}}^n$	Reduction basis of internal and blade-tip DOFs of sector n
$\boldsymbol{\Phi}^{\mathrm{POD}}$, $\boldsymbol{\phi}_j^{\mathrm{POD}}$	POD modes, j^{th} mode of the basis
$\boldsymbol{\Phi}^{\mathrm{SOD}}$, $\boldsymbol{\phi}_j^{\mathrm{SOD}}$	SOD modes, j^{th} mode of the basis
$\boldsymbol{\Psi}$, $\boldsymbol{\psi}_j$	Constraint modes, j^{th} mode of the basis
$\boldsymbol{\Omega}$	Angular velocity matrix
$\mathbf{A}$	Third-order tensor of quadratic stiffness coefficients
$\mathbf{A}^n$	Third-order tensor of quadratic stiffness coefficients for sector n
$\boldsymbol{\mathcal{A}}$	Functional form for the quadratic stiffness term
$\mathbf{B}$	Fourth-order tensor of cubic stiffness coefficients
$\mathbf{B}^n$	Fourth-order tensor of cubic stiffness coefficients for sector n
$\boldsymbol{\mathcal{B}}$	Functional form for the cubic stiffness term
$\mathbf{C}$	Equivalent damping matrix
$\mathbf{C}_{\mathrm{N}}$	Contact constraint matrix in the normal direction
$\mathbf{C}_{\mathrm{NT}}$	Contact constraint matrix in the normal and tangential directions
$\mathbf{C}_{\mathrm{T}}$	Contact constraint matrix in the tangential direction
$\mathbf{D}$	Viscous damping matrix
$\mathbf{E}$	Green-Lagrange strain tensor
$\mathbf{F}$	Deformation gradient
$\mathbf{F}_c$	Matrix of contact forces
$\hat{\mathbf{F}}_c$	Matrix of Fourier coefficients related to $\mathbf{F}_c$
$\mathbf{F}_e$	Matrix of external forces
$\hat{\mathbf{F}}_e$	Matrix of Fourier coefficients related to $\mathbf{F}_e$
$\mathbf{F}_{a,b}^{\mathrm{NL}}$	Nonlinear forces extracted from FE model in the STEP
$\mathbf{F}_{\mathbb{C}}$	Fourier matrix in complex form
$\mathbf{F}_{\mathbb{R}}$	Fourier matrix in real form
$\mathbf{G}$	Gyroscopic coupling matrix
$\mathbf{G}_{\mathrm{nl}}$	Matrix of nonlinear internal forces
$\hat{\mathbf{G}}_{\mathrm{nl}}$	Matrix of Fourier coefficients related to $\mathbf{G}_{\mathrm{nl}}$
$\mathbf{G}_{\mathrm{nl}}^{\star}$	Matrix of nonlinear internal forces snapshots
$\mathbf{H}$	Fourth-order elasticity tensor
$\mathbf{I}$	Identity matrix
$\mathbf{K}$	Stiffness matrix
$\hat{\mathbf{K}}$	Projection of the stiffness matrix onto $\boldsymbol{\Phi}_{\mathrm{I}}$
$\mathbf{K}^{(c)}$	Centrifugal stiffness matrix
$\mathbf{K}^{(e)}$	Elastic stiffness matrix

$\mathbf{K}^{(g)}$	Geometric prestressed stiffness matrix
$\mathbf{K}_T$	Tangent stiffness matrix
$\mathbf{M}$	Mass matrix
$\hat{\mathbf{M}}$	Projection of the mass matrix onto $\mathbf{\Phi}_{\mathrm{I}}$
$\mathbf{N}$	Matrix of shape functions of the finite element formalism
$\mathbf{Q}$	Generalized forces in Lagrange formalism
$\mathbf{R}$	Rotation matrix
$\bar{\mathbf{R}}$	Reaction forces
$\mathbf{S}$	Second Piola-Kirchhoff stress tensor
$\mathbf{T}$	Basis of harmonic functions
$\mathbf{U}$	Matrix of relative displacements around prestressed equilibrium
$\hat{\mathbf{U}}$	Matrix of Fourier coefficients related to $\mathbf{U}$
$\mathbf{U}^\star$	Matrix of displacement snapshots
$\bar{\mathbf{U}}$, $\bar{\mathbf{S}}$, $\bar{\mathbf{V}}$	Matrices of singular value decomposition
$\mathbf{U}^p$	Matrix of predicted displacements fields (without contact constraints)
$\mathbf{V}^\star$	Matrix of velocity snapshots
$\mathbf{Z}$	Global dynamic stiffness matrix
$\dot{\square}$	Time derivative
$\ddot{\square}$	Second order time derivative
$\tilde{\square}$	Projection onto the reduced space
$\square_b$	Components related to boundary (blade-tip) degrees-of-freedom
$\square_{\mathrm{cyclic}}$	Components related to the degrees-of-freedom of the cyclic boundary
$\square_e$	Characteristics of the external excitation
$\square^{\mathrm{FOM}}$	Computed with the full-order model
$\square_i$	Components related to internal degrees-of-freedom
$\square^{(j)}$	Related to angular speed Ω_j
$\square_{\mathrm{left}}$	Components related to the DOFs of the left cyclic boundary
$\square_n$	Approximation at time t_n
$\square^n$	Related to sector n
$\square_{\mathrm{right}}$	Components related to the DOFs of the right cyclic boundary
$\square^{\mathrm{ROM}}$	Computed with the reduced-order model
$\square_t$	Characteristics of the training excitation

CHAPTER 1 INTRODUCTION

General context

In the general movement towards greener aviation and in the framework of the new environmental regulations, engine manufacturers aim at drastically reducing their environmental footprint [4,88]. New engine architectures are therefore being considered to improve the performance of turbojet engines and cut their fuel consumption. Economic reasons also motivate these new developments. The design of the rotating bladed disks considered in this thesis is expected to greatly contribute to these general objectives.

Energy efficiency can be improved by controlling the clearance between the blade-tips and the stationary surrounding casing in order to reduce aerodynamic leaks. This strategy inherently leads to more frequent occurrences of direct contacts between the rotating blades and the casing, even in nominal operating conditions, that may induce nonlinear vibrations [165,180, 189]. Blades are also designed increasingly lighter and more flexible to be in line with the tight weight constraints [79, 178, 223]. Large displacements and large deformations, leading to a geometrically nonlinear behavior of the structure, can therefore no longer be neglected [244].

Because of the high costs associated to full-scale experimental setups, it is particularly important that accurate predictive numerical strategies are available to engine manufacturers [7]. However, as the use of thinner blades with reduced clearance with respect to the surrounding casing leads to large amplitude vibrations and contact events, classical linear models may yield inaccurate results. While geometric nonlinearities have been the subject of research works focusing on fan stages, contact induced vibrations have been mostly investigated within low- and high-pressure compressor stages. The combined effects of these two kinds of nonlinearities are therefore not well characterized. New numerical tools allowing to account for these nonlinear structural considerations from the beginning of the design process are thus needed.

Besides these nonlinear considerations, it should be noted that in practice, real bladed disks differ from their nominal cyclically periodic designs [45]. Manufacturing or wear can cause small random blade-to-blade variations. The representation of this so-called mistuning in numerical models also requires the development of dedicated methods.

Turbomachines bladed structures are generally modeled by 3D finite element models with very accurate geometric details and material distribution. Current industrial numerical models of bladed structures are therefore characterized by a huge number of degrees-of-freedom

and their direct use in dynamic analysis requires high computational capabilities. This is particularly true in a nonlinear context and for mistuned structures. This is the reason why many recent works are devoted to the construction of nonlinear reduced-order models that can be used to reduce the computational burden in a design process, but also as fast executing replacements of the full-order model or to extract relevant information hidden in the full-order model. Different categories of reduction methods can be identified, from goal-oriented reduction approaches [37], where the entire finite element model is directly reduced to a cost-function that does not contain any information about the physical properties of the model, to physical reduction methods. Among the existing physical reduction methods, the projection on a reduced space is widely used in the literature because of its ease of implementation, but also because it preserves the general expression of the equation of motion so that the same time integration algorithms as those used for the full-order model can be used.

In a linear context, the dynamics of cyclically symmetric structures is generally studied in the harmonic space where the dynamic problem can be written as a set of sub-problems for each harmonic using Fourier formalism [30, 166, 222]. This cyclic symmetry formulation can be used in classical linear reduced-order modeling techniques (such as Craig-Bampton or Craig-Martinez reduction methods [53,55,192]) to efficiently compute the reduction basis [15].

The linear reduced-order modeling techniques that allow to keep physical degrees-of-freedom in the reduced space can be combined with penalty methods [201] or Lagrange multiplier approaches [42] to efficiently account for contact nonlinearities. These reduction methods have proven to provide accurate prediction of contact dynamics, and in particular of rubbing events between blades and casings [21].

These linear reduction techniques may however be ill-suited in the case of severe localized nonlinearities or in the case of distributed nonlinearities (as geometric nonlinearities). Indeed, even if some high-frequency linear modes could capture the nonlinear behavior of the structure, these modes are truncated in the reduction procedure. Including these modes in the reduction basis would lead to reduction bases of large size and the benefit of the reduction procedure would be lost [149, 229].

In the case of strong contact nonlinearities, the nonlinear nature of the system may be included in the reduction basis, for instance by the use of nonlinear complex modes [103,104].

The model order reduction of mechanical systems undergoing large displacements started to gain the attention of researchers in the last few years. The different projective reduction methods differ by the choice of the reduction basis and by the way the nonlinear internal forces are evaluated in the reduced space. Different projection bases have been investigated in a nonlinear context: linear bases [13, 66], bases obtained from Proper Orthogonal Decom-

position (POD) [115, 178], linear bases augmented with modal derivatives [109, 235, 242] or with dual modes [149, 171], bases composed of Ritz vectors [108] and Krylov bases [12] for instance. The reduced nonlinear forces can be identified with intrusive and non-intrusive methods. In intrusive methods, reduced nonlinear forces are obtained by direct projection of the full-order nonlinear forces [40, 46, 220]. These methods are based on the relationship between the finite element tensors and their modal counterparts. However, the expression of the full-order nonlinear forces cannot always be extracted from commercial finite element software packages. Non-intrusive methods compatible with standard finite element software packages have therefore been derived. In such methods, the reduced nonlinear forces are expressed as a polynomial form of the reduced coordinates whose coefficients are identified with nonlinear static evaluations with imposed displacements (enforced displacement method or STiffness Evaluation Procedure (STEP) [155]) or imposed forces (applied force method [146]). There is a need to assess the applicability of these methods to the analysis of the combined effect of geometric and contact nonlinearities on industrial structures.

Objectives

In this context, the objective of this research work is to develop a methodology to study in a numerically efficient way the contact interactions of bladed disks with the surrounding casing accounting for their geometrically nonlinear behavior. The methodology is based on reduction techniques to allow the efficient analysis of industrial structures. For more realism, the methodology needs to be compatible with the introduction of mistuning in the reduced space. In this work, computations are carried out in the time domain in order to capture transient phenomena, which are key for the rise of some critical interactions [152]. We show that the methodology can be easily extended to the frequency domain.

From the industrial point of view, the objective of this work is also to develop practical and easy to use tools for the design of turbomachines. Nowadays, the preliminary design of turbomachines in industry is mainly driven by aerodynamic considerations and the absence of contact occurrence is only checked at the end of the process. The new tools in development will allow to provide guidelines to engineers to account for nonlinear structural aspects in an accurate way from the beginning of the design. This will allow to accelerate the design phase, to design safer engines, but also to avoid oversizing of aircraft engines.

Outline

In chapter 2, the relevant background about the dynamics of tuned and mistuned bladed disks is summarized. The sources of nonlinearities are also detailed, together with the modeling of the subsequent nonlinear behavior in structural dynamics, and in particular in rotor dynamics.

Chapter 3 is dedicated to the numerical simulation of multi-nonlinear dynamic systems. It highlights the existence of two paradigms for solving the equation of motion: time domain methods and frequency domain methods.

In chapter 4, various existing reduced-order modeling techniques developed for the efficient analysis of structures with geometric nonlinearities are presented. Some personal adjustments of these methods to better fit the dynamics of bladed disks are also detailed.

In chapter 5, three different reduction methods are selected as interesting candidates. They are applied to an industrial test case subjected to an equivalent aerodynamic loading without contact interactions. The performance and robustness of each method are assessed. These studies allow to highlight the strengths and weaknesses of the different methods. Parametric reduced-order models are also built to account for the effect of rotation in a numerically efficient way.

In chapter 6, the selected reduction methods are used to study contact interactions of a rotating blade. The most suitable reduction method is selected and used to perform detailed time and frequency analyses, focusing on rubbing interactions. Two contact scenarios are investigated, one with direct contact between the blade and the casing, and one with an abradable coating deposited on the casing.

In chapter 7, the methodology is generalized to study the dynamics of full bladed disks. The methodology is first validated without contact nonlinearities and then applied to an industrial bladed disk model with both geometric and contact nonlinearities. The chapter ends with a discussion regarding the introduction of mistuning in the reduced-order model.

CHAPTER 2 DYNAMICS OF BLADED DISKS

This first part of the presented research work summarizes the theoretical background about the dynamics of bladed disks required to understand the studies described in the following parts. The industrial context of the research is first introduced with some generalities on turbomachines and on the design of bladed disks, at the heart of the present work. The second section focuses on the modeling of bladed disks. The subsequent two sections highlight that the actual behavior of bladed disks departs from the theoretical, linear and symmetrical one. The fourth section introduces the concept of mistuning, breaking the symmetry of bladed disks and the fifth section describes the different kinds of nonlinearities arising in turbomachines and their influence on the dynamics. The chapter ends with a summary of the main assumptions made in this work.

2.1 Industrial context

2.1.1 Generalities on turbomachines

The term turbomachine refers to any device that extracts energy from or imparts energy to a moving stream of fluid [183]. More precisely, a turbomachine is a power- or heat-generating machine that employs the dynamic action of a rotating element called the rotor in order to change the energy content of the fluid continuously flowing through the machine. Applications can be found in various fields of engineering such as power generation or transport.

Turbomachines are used for the generation of power in different ways [36]. Wind turbines have the ability to efficiently use the wind to generate electricity. Hydroelectric turbomachines use the potential energy stored in water to turn a generator and produce electricity. In steam turbines, high pressure steam is forced over blades attached to a shaft which turns a generator. Gas turbines work like steam turbines.; air is forced in through a series of blades that turn a shaft. Fuel is then mixed with the air and the power is increased by a combustion reaction. Steam and gas turbines are also present in marine applications [111].

Most aeronautical engines (as turbojet, turboprop, or turboshaft engines) are also turbomachines [181]. These turbomachines are composed of one or several compressor and turbine stages that allow for the compression and expansion of the gas flux passing through the engine (Fig. 2.1). Fuel is injected between the last compression stage and the first turbine stage. Each compressor and turbine stage is made up of a fixed part linked to the casing and a rotating part linked to the shaft. These parts carry blades, whose aerodynamic profile is

defined in the design phase of the engine in order to optimize the compression and expansion of the gas. These turbomachine components comprising both rotor disk and blades are called bladed disks.

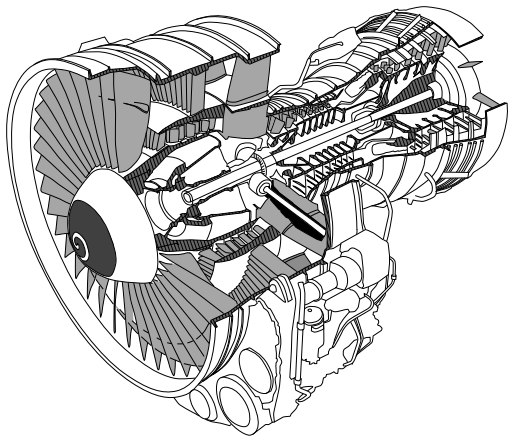

FIGURE 2.1 – Cut view of an aircraft engine [20].

2.1.2 Bladed disks design

Traditionally, bladed disks are manufactured as bladed-disk assemblies [203]. The blades are individually attached to a bare disk. Weight-intensive blade root constructions are therefore necessary such as screws, bolts or dovetail attachments. These attachments are prone to crack initiation and subsequent propagation.

A blade integrated disk (blisk) consists of a single part, instead of an assembly of a disk and individual, removable blades [27]. Blisks may be additively manufactured, 3D-printed, integrally cast, machined from a solid piece of material or made by friction welding of the individual blades to the rotor disk. Blisk technology is therefore a lightweight solution. Because of the lack of friction between blades' roots and the disk, blisks are characterized by small mechanical damping compared to bladed disk assemblies. A stress-optimized design is achieved which allows to reach higher rotation speeds and thus higher compression ratios compared to conventional disks with separate blades. This leads to more powerful engines [208, 209, 233]. However, any damage to the blades requires the full removal of the engine. The maintenance of such elements cannot be done on the flight line and must often be performed at a specialized facility. Such maintenance is often more costly than for traditional bladed disks.

While in service, bladed disks are subjected to various static and dynamic loads that can be detrimental for the engine integrity and cause accelerated fatigue and wear if they are not controlled.

On the one hand, bladed disks are subjected to excitations from mechanical sources that cause vibrations of the structure. In the case of uneven distribution of the mass around the axis of rotation, the rotating bladed disks can be excited by imbalance forces whose pulsation corresponds to the rotation speed. In accidental configurations, such as a blade-loss event, bladed disks can also be subjected to shock excitations. Moreover, bladed disks can undergo contact events, as described in section 2.4.3.

On the other hand, bladed disks are also subjected to aeroelastic excitations. Fixed and rotating turbomachines stages are subjected to the pressure fluctuations caused by the upstream and downstream stages. These excitations take the form of engine order excitations, whose frequencies are integer multiples of the angular speed, directly related to the number of obstacles in the flow. Moreover, the acceleration of the fluid from subsonic to transonic regimes can result in sonic shocks that induce unsteady loadings on the blades. Due to the high Reynolds numbers involved, complex aerodynamic computations are required to accurately capture turbulent effects. Vibration energy of a particular blade can also be transferred to other blades by means of pressure waves in the surrounding flow field. This phenomenon is typically referred to as aerodynamic coupling [26, 85, 107, 118, 162].

From a structural point of view, the mechanical behavior of blades is of the utmost interest for designers. Blade damage, or worse, blade loss, is very detrimental for the engine. It does not only lead to a decrease in the efficiency of the engine, but also to an unbalance of the rotating system that may cause significant stresses transmitted to the shaft bearings. High-cycle fatigue (HCF) failures of blades is one of the major causes of blade loss. The vibratory behavior of blades is therefore a major concern when dealing with turbomachines design. HCF is a major cost, safety and reliability issue for gas-turbine engines [43, 45, 94]. Because of the high costs associated to full-scale experimental setups, it is particularly important for manufacturers to rely on accurate numerical models. Comprehensive modeling, analysis and understanding of bladed disks vibration are critical to reduce the occurrence of HCF and improve the performance and reliability of turbine engines.

The lifespan of industrial bladed disks can be very sensitive to mistuning effects (more details in section 2.3) combined to the presence of nonlinearities (more details in section 2.4). For a long time, numerical simulations of bladed-disk assemblies or blisks have been carried out with very simple numerical models. Security factors were added to take into account the unknown impact of mistuning and nonlinearities. This led to oversized engines and required costly experimental certification [32]. Nowadays, the objective is to introduce all these complex phenomena in a systematic and accurate way in numerical models.

2.2 Modeling of bladed disks

2.2.1 Finite element modeling

Industrial turbomachines bladed disks are generally described by 3D finite element models that typically comprise several thousands of elements, such as tetrahedral volume elements [24, 177] or hexahedral quadratic elements [13]. Such 3D models are required to have an accurate description of the structure dynamics but require high computational capabilities [72]. These models are also called full-order models (FOMs) in contrast to the reduced-order models (ROMs) introduced in chapter 4 that allow to lower the computation time by reducing the number of parameters used to describe the dynamics.

The equation of motion of a rotating structure spatially discretized according to its finite element model is mathematically established in Appendix A. The discretized equation of motion governing the relative displacement $\mathbf{u}$ around an initial prestressed static equilibrium state $\mathbf{u}_s$ induced by the rotation of the structure (and function of the constant rotation speed Ω) writes

$$\mathbf{M}\ddot{\mathbf{u}}+[\mathbf{D}+\mathbf{G}(\Omega)]\,\dot{\mathbf{u}}+\left[\mathbf{K}^{(e)}+\mathbf{K}^{(c)}(\Omega)+\mathbf{K}^{(g)}(\mathbf{u}_s)\right]\mathbf{u}+\mathbf{g}_{\text{nl}}(\mathbf{u},\mathbf{u}_s)=\mathbf{f}_e(t)+\mathbf{f}_c(\mathbf{u}+\mathbf{u}_s,\dot{\mathbf{u}}). \quad (2.1)$$

This equation balances the inertial term ($\mathbf{M}$ is the mass matrix with symmetry and positive definiteness properties.), the linear damping term ($\mathbf{D}$ is the viscous damping matrix with symmetry and positive semi-definiteness properties.), the gyroscopic coupling term ($\mathbf{G}(\Omega)$ is the gyroscopic coupling matrix with antisymmetry property.), the elastic stiffness term ($\mathbf{K}^{(e)}$ is the elastic stiffness matrix with symmetry and positive definiteness properties.), the centrifugal stiffness term ($\mathbf{K}^{(c)}(\Omega)$ is the centrifugal stiffness matrix with symmetry and negative definiteness properties.), the geometric stiffness term ($\mathbf{K}^{(g)}(\mathbf{u}_s)$ is the geometric prestressed stiffness matrix with symmetry and positive definiteness properties.), the nonlinear internal forces $\mathbf{g}_{\text{nl}}(\mathbf{u},\mathbf{u}_s)$, the external force vector $\mathbf{f}_e(t)$ and the nonlinear forces due to contact $\mathbf{f}_c(\mathbf{u}+\mathbf{u}_s,\dot{\mathbf{u}})$.

The viscous damping matrix $\mathbf{D}$ accounts for viscous damping effects. It is generally built based on a damping model, such as the Rayleigh structural damping model [73]. In such a model, the damping matrix is built as a linear combination of the mass and linear elastic stiffness matrices

$$\mathbf{D}=\alpha\mathbf{M}+\beta\mathbf{K}^{(e)}, \quad (2.2)$$

where the parameters α and β are parameters that need to be identified, for instance based on experimental modal analysis [2].

The gyroscopic coupling and the centrifugal stiffness terms allow to account for the rotation of the structure.

The geometric stiffness term is based on the constraints acting on the structure. Commercial finite element software can be used to compute the prestressed state of the blades and disk at a given rotation speed through a linear static analysis [177] or a nonlinear static analysis [104] in order to build the geometric stiffness matrix $\mathbf{K}^{(g)}(\mathbf{u}_s)$.

For the sake of conciseness, the equation of motion (2.1) can be rewritten as

$$\mathbf{M}\ddot{\mathbf{u}} + \mathbf{C}(\Omega)\dot{\mathbf{u}} + \mathbf{K}(\Omega, \mathbf{u}_s)\mathbf{u} + \mathbf{g}_{\text{nl}}(\mathbf{u}, \mathbf{u_s}) = \mathbf{f}_e(t) + \mathbf{f}_c(\mathbf{u} + \mathbf{u}_s, \dot{\mathbf{u}}), \tag{2.3}$$

where the equivalent damping and stiffness matrices are respectively defined as

$$\mathbf{C}(\Omega) = \mathbf{D} + \mathbf{G}(\Omega) \qquad \text{and} \qquad \mathbf{K}(\Omega, \mathbf{u}_s) = \mathbf{K}^{(e)} + \mathbf{K}^{(c)}(\Omega) + \mathbf{K}^{(g)}(\mathbf{u}_s). \tag{2.4}$$

The classical approach to study the dynamics of rotating structures considers that the vibrations $\mathbf{u}$ around the prestressed equilibrium state $\mathbf{u}_s$ remain small and that the geometric nonlinearities are only induced by the effect of rotation [87]. This is equivalent to neglecting the nonlinear term $\mathbf{g}_{\text{nl}}(\mathbf{u}, \mathbf{u}_s)$ in (2.1) and (2.3). The nonlinear forces due to contact are also generally not considered in a first step. The effects of these nonlinearities will be discussed in section 2.4.

2.2.2 Cyclic symmetry formulation

In the absence of mistuning, turbomachine bladed disks are cyclically periodic structures, *i.e.* structures composed of a finite number of identical sectors coupled together. A tuned N_s-blade bladed disk is composed of N_s identical sectors defined as the combination of one blade and the corresponding disk segment (see Fig. 2.2). Such structures are characterized by specific properties that can be exploited to facilitate and accelerate their dynamic analysis. They should not be confused with rotationally symmetric structures, such as circular plates or space antennas.

In a linear context, mode shapes of cyclically periodic structures consist of identical displacements in each sector (same motion amplitude) except for a fixed sector-to-sector phase difference. The vibratory energy is uniformly distributed over the structure and the mode shapes are sinusoidal in the circumferential direction. The mode shapes of bladed disks are therefore characterized by zero displacement lines across the disk called nodal diameters. Because the number of sectors is a discrete quantity, the maximum number of nodal diameters

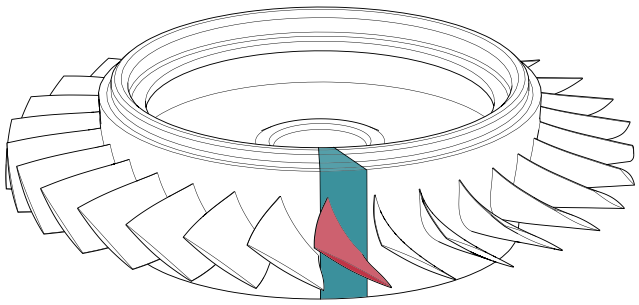

FIGURE 2.2 – Schematic view of a turbomachine bladed disk with one disk sector (■) and the corresponding blade (■) highlighted.

of a N_s-bladed disk is $\lfloor N_s/2 \rfloor$ according to the Nyquist-Shannon sampling theory [195]. Most natural frequencies ω_k of tuned bladed disks appear in pairs due to the perfect symmetry of the problem. For a bladed disk with N_s blades,

$$\omega_k = \omega_{N_s-k}, \quad k = 1, \ldots, \lfloor N_s/2 \rfloor. \tag{2.5}$$

Such solutions are called degenerate solutions. The associated mode shapes are characterized by the same number of nodal diameters but are shifted by a quarter of a period. The solutions related to ω_0 (vibration in phase of all sectors) and to $\omega_{N_s/2}$ if N_s is even (vibration in phase opposition of the sectors) do not appear in pairs and are called nondegenerate solutions [213].

The cyclic symmetry formulation can be used to study the linear dynamics of a cyclically symmetric structure [215]. As the mode shapes of the structure have identical motion amplitudes in each sector and a fixed sector-to-sector phase difference, the modeling of a single reference sector allows to reconstruct the dynamics of the complete structure [34, 35, 98, 226]. The displacement vector of the structure $\mathbf{u}$ can be written as

$$\mathbf{u} = \begin{bmatrix} \mathbf{u}^1 \\ \mathbf{u}^2 \\ \vdots \\ \mathbf{u}^{N_s} \end{bmatrix}, \tag{2.6}$$

where $\mathbf{u}^k$ stands for the displacement of the k-th sector. Using the discrete Fourier transform, the displacement vector $\mathbf{u}^k$ can be related to the cyclic components $\check{\mathbf{u}}_j$ ($j = 1, ..., N_s$) as

$$\mathbf{u}^k = \frac{1}{N_s} \sum_{j=1}^{N_s} \check{\mathbf{u}}_j e^{i\frac{2\pi(j-1)(k-1)}{N_s}} \quad \text{and, conversely,} \quad \check{\mathbf{u}}_j = \sum_{k=1}^{N_s} \mathbf{u}^k e^{-i\frac{2\pi(j-1)(k-1)}{N_s}}. \tag{2.7}$$

These equations can be written as the outer products

$$\mathbf{u} = \frac{1}{N_s}(\mathbf{F}_{\mathbb{C}}^{\star} \otimes \mathbf{I})\check{\mathbf{u}} \quad \text{and} \quad \check{\mathbf{u}} = (\mathbf{F}_{\mathbb{C}} \otimes \mathbf{I})\mathbf{u}, \tag{2.8}$$

where $\check{\mathbf{u}}$ is the vector of cyclic components and the Fourier matrix $\mathbf{F}_{\mathbb{C}}$ is built from the Fourier vector

$$\mathbf{w}_j = \begin{bmatrix} 1 & e^{-i\frac{2\pi(j-1)}{N_s}} & \cdots & e^{-i\frac{2\pi(j-1)(N_s-1)}{N_s}} \end{bmatrix} \tag{2.9}$$

as

$$\mathbf{F}_{\mathbb{C}} = \begin{bmatrix} \mathbf{w}_1^{\mathrm{T}} & \mathbf{w}_2^{\mathrm{T}} & \cdots & \mathbf{w}_{N_s}^{\mathrm{T}} \end{bmatrix}^{\mathrm{T}}. \tag{2.10}$$

The use of the discrete Fourier transform allows to express the equation of motion written in the physical space (2.3) in the cyclic basis as a set of uncoupled subproblems (one equation for each harmonic) [105]. The quantities (displacements, forces) in physical coordinates for the N_s disk sectors are expressed as a linear combination of the corresponding quantities in cyclic coordinates for the fundamental disk sector [32]. Due to the discrete character of the problem, this description is fully equivalent.

Anticipating on section 2.4, it should be stressed that this cyclic symmetry formulation is only applicable for linear structures. Nonlinearities induce a coupling between the harmonic components so that the subproblems are no longer decoupled in this case.

2.3 Mistuned bladed disks

In practical applications, bladed disks differ from their nominal cyclically periodic designs. They show small random blade-to-blade variations breaking the symmetry of the structure so that the cyclic symmetry formulation introduced in section 2.2.2 can no longer be used. Such variations are referred to as mistuning when the phenomenon is not intentional and to detuning when it is intentional. These variations are usually small (leading to differences on the blade natural frequencies on the order of a few percent of the nominal values). Symmetrical physical systems tend however to be extremely sensitive to perturbations of their symmetry, as observed in atomic physics by Cohen-Tannoudji [51], in solid physics by Anderson [10] and also in several studies dedicated to the dynamics of periodic and cyclic structures [91–93,179]. Hodges showed that mistuning is a kind of Anderson localization, characterized by increasing mode localization levels in case of increased disorder of substructures [91]. It is therefore important to be able to account for mistuning in the numerical simulations.

2.3.1 Causes

Various parameters whose spatial variations have a significant impact on the behavior of the tuned structure have been identified from lumped parameter models as well as more realistic bladed disk models. Random blade-to-blade geometry variations can be the direct consequence of the manufacturing process and the associated tolerances [39]. They can also appear due to a nonuniform operational wear or an accidental scenario such as a foreign object impact [70, 136]. The presence of irregularities in the material properties is another cause of mistuning. The strain gage instrumentation of the structure also affects its symmetry [25, 119]. These parameters variations directly affect the mass, the damping and the stiffness of the structure [44, 106, 150, 175, 246].

2.3.2 Consequences

Several surveys on mistuning can be found in the literature [45, 203, 207]. The experimental, numerical and analytical study of mistuned bladed disks allows to highlight the main consequences of mistuning on the dynamics of the structure.

Frequency splitting The degenerate natural frequencies of the tuned structure separate in distinct natural frequencies for the mistuned structure. Zenneck showed both analytically and experimentally that the degenerate mode pairs split into two distinct modes [248]. Ewins demonstrated that these two modes can be observed separately if the frequency separation is greater than the modal damping factor [70]. Mistuning therefore leads to an increase of the bandwidth of eigenfrequencies so that the bandwidth of possible resonance enlarges, which has to be taken into account during the design to avoid critical resonances in operation.

Maximum forced response amplitude increase Mistuning causes an increase of the amplitude of the maximum forced response. This dynamic amplification has been highlighted with simple numerical models [68, 238], advanced industrial models [45, 119] and experimentally [69, 70]. The amplification factor is usually defined as the ratio between the largest amplitude response of the mistuned bladed disk and the largest amplitude response in the tuned case [161, 238]. Since mistuning is a random phenomenon, the amplification factor distribution and its maximal value may be estimated using statistical approaches. Increase of blade amplitudes ranging between 20% and 400% compared to the tuned case have been observed in the literature [27, 69, 172, 238].

Mode localization The mode shapes of a mistuned structure present a localization of the energy on a subset of blades rather than being uniformly distributed throughout the system. This leads to an amplification of the vibration levels and stresses of these blades compared to their tuned nominal counterpart and increases the risk of HCF failures [106,114]. Certain blades may exhibit a much shorter lifespan than would be predicted by a fatigue life assessment based on the nominal assembly.

Aerodynamic stability Mistuning can have beneficial effects in case of aeroelastic instabilities, such as aerodynamic flutter. Mistuning is therefore often intentionally introduced to stabilize the vibrations in the case of blade flutter [29, 112, 196].

2.3.3 Modeling

Due to the random nature of mistuning, stochastic analyses are required to quantify its effect on the bladed disk dynamics. Different approaches can be used such as Monte Carlo simulations [167], polynomial chaos expansions [67, 200] or asymptotic expansions to derive analytic solutions [41, 148, 199, 236].

2.4 Nonlinear dynamics

Linearization is an idealization, an exception to the rule: nonlinearity is a frequent occurrence in real-life applications [116]. In structural dynamics, different mechanisms are responsible for nonlinear behavior.

While a linear material model relies on the assumption that stresses are proportional to strains, this is not the case in general. Material nonlinearities thus refer to material laws such that stresses are not proportional to strains (nonlinear elastic law) or such that there exist permanent irreversible deformations (elasto-plasticity or elasto-viscoplasticity). Then, geometric nonlinear behavior occurs when the system experiences large displacements or deformations. Material and geometric nonlinearities are two kinds of distributed nonlinearities. Nonlinearity may also result from nonlinear boundary conditions or nonlinear external body forces. In particular, contact nonlinearities occur at the interface between components. This is a kind of localized nonlinearity. Fluid/structure interaction is also an essentially nonlinear phenomenon.

These different kinds of nonlinearities exist in turbomachines and the analysis of nonlinear phenomena in aeronautical turbomachines is a research field in expansion, especially in the current environmental context. This research project mainly focuses on geometric nonlinear-

ities and contact nonlinearities that are described in more details in the next paragraphs.

The dynamics of nonlinear periodic structures can significantly differ from the dynamics of linear periodic structures. For instance, nonlinear mode localization may occur in perfectly cyclic nonlinear systems (tuned bladed disk) if the ratio between the coupling of the substructures and the nonlinearity is small [223]. These nonlinear vibrations can have an effect on the life duration of the structure, or even be detrimental for the structural integrity of the engine. It is therefore very important to be able to model and predict with accuracy the nonlinear behavior of mechanical structures, with the final objective of accounting for these nonlinear considerations in the design.

2.4.1 Nonlinear modal analysis

In linear systems, the modal parameters (mode shapes, natural frequencies, damping ratios) are computed by solving an eigenvalue problem. In nonlinear systems, the definition and computation of the modal parameters of the structures differ from the linear context. In particular, the concept of nonlinear modes has been extensively studied during the last decades.

Nonlinear modes were first introduced by Rosenberg in the 1960s [185]. He defined a normal mode as a vibration in unison of the system, *i.e.* a synchronous motion, and presented a geometric method to compute these nonlinear modes. The definition was then extended to a (not necessarily synchronous) periodic motion of the conservative system. This definition of nonlinear normal modes (NNMs) allows to account for the modal interactions (internal resonances) which lead to nonsynchronous periodic motions of the structure. Different numerical algorithms for the computation of NNMs of conservative systems have been developed [80, 101, 116, 158, 170]. Laxalde and Thouverez then introduced the concept of complex nonlinear modes as an extension of NNMs to nonconservative systems [129]. Complex nonlinear modes of motion are defined as oscillations of the autonomous damped system with potentially a phase difference between its degrees-of-freedom.

The properties of nonlinear modes differ in several points from the properties of linear normal modes [116, 224, 225]. First, nonlinear modes have a fundamental limitation compared with their linear counterpart. Because of the lack of orthogonality relations between nonlinear modes, the general motion of a nonlinear system cannot be expressed as a superposition of individual nonlinear modes. This complicates their exploitation as bases for order reduction of the nonlinear dynamics. It should be noted that nonlinear modal superposition has however been investigated by several authors based on the single nonlinear mode method [49, 75, 193, 214]. Contrary to linear modes, nonlinear modes can therefore be coupled: they may

interact through an exchange of energy. These internally resonant nonlinear modes are generated through bifurcations. Then, nonlinear mode shapes are dependent on the energy of the system and vary with the amplitude of vibration. Lastly, while linear modes are always neutrally stable, nonlinear modes can be stable or unstable [157]. Unstable nonlinear modes are however not physically realizable as small perturbations of the initial conditions that generate the motion lead to the elimination of the mode oscillation. The stability of periodic solutions can be determined by the Floquet theory.

2.4.2 Geometric nonlinearities

Geometric nonlinearities are encountered when the structure undergoes large displacements or large deformations. Such behavior is known as geometrically nonlinear because the geometry of the structure changes significantly. It is particularly pronounced for thin and slender structures. Note that this geometrically nonlinear behavior can also be exploited for a desired function. For instance, in the MEMS and NEMS domains, mechanical frequency dividers are achieved by chaining components working in the nonlinear regime [130, 212].

Geometric nonlinearities in turbomachines In the past, the level of vibration of the blades in nominal conditions remained most of the time sufficiently small to study the deformation and displacement of the structure accurately with linear tools. In classical approximations, geometric nonlinearities are therefore only considered when computing the prestressed state induced by rotation and the linear vibrations around this nonlinear prestressed equilibrium state are studied. Large displacements were only observed in exceptional operating regimes of bladed disks. For instance, in the case of flutter, very low damping levels and nearly unstable situations can occur for which the linear theory does not provide accurate results.

The current environmental concerns lead engine manufacturers to drastically reduce their impact on the environment [88]. To achieve this, new engine architectures are being considered to improve the performance of turbojet engines and reduce their fuel consumption. This is also motivated by economic factors. For turbofan engines, one of the avenues considered to improve the performance is to increase the dilution ratio of the engine, *i.e.* the ratio between the flow of cold air and the flow of hot air through the combustion chamber. In order to compensate for the increase in size of the propeller, lightweight materials such as carbon fiber are used to manufacture the blades. The use of lighter and more slender and flexible blades can lead to large strain/displacements which require to consider nonlinear dynamic equations involving geometric nonlinearities.

Modeling It is important to get a good understanding of these phenomena in order to improve the design of the structures in terms of weight, materials and dimensions. Different authors studied the effects of geometric nonlinearities on thin structures such as thin rectangular plates [28], circular shells [219] and beams [135].

The dynamics of structures with geometric nonlinearities can be described with second order nonlinear differential equations. If a finite element model of the structure is built, the semi-discretized equation of motion corresponding to the spatial discretization takes the general form (2.3), where $\mathbf{g}_{\text{nl}}(\mathbf{u}, \mathbf{u}_s)$ accounts for the geometrically nonlinear behavior. Going back to the mathematical establishment of the equation of motion in appendix A, this term is directly linked to the strain energy

$$\mathcal{V} = \frac{1}{2} \int_V \boldsymbol{\sigma} : \boldsymbol{\epsilon} \; dV, \tag{2.11}$$

where $\boldsymbol{\sigma}$ and $\boldsymbol{\epsilon}$ respectively stand for the stress and strain tensors. Different measures of stress and strain, which are equivalent in a linear context, can be defined. In the case of 3D elements, it can be shown that when defining the stress tensor as the second Piola-Kirchhoff stress tensor, measuring the strain with the Green-Lagrange tensor (see appendix A) and considering a hyperelastic material model such as Saint Venant-Kirchhoff model, *i.e.* a linear relation between the strain and the stress tensors, the nonlinear stiffness term $\mathbf{g}_{\text{nl}}(\mathbf{u}, \mathbf{u}_s)$ is composed of a quadratic and a cubic parts [76, 149, 220] and writes

$$\mathbf{g}_{\text{nl}}(\mathbf{u}, \mathbf{u}_s) = \boldsymbol{\mathcal{A}}(\mathbf{u}, \mathbf{u}) + \boldsymbol{\mathcal{B}}(\mathbf{u}, \mathbf{u}, \mathbf{u}), \tag{2.12}$$

using the functional notation $\boldsymbol{\mathcal{A}}(\cdot, \cdot)$ and $\boldsymbol{\mathcal{B}}(\cdot, \cdot, \cdot)$ for the quadratic and cubic terms with coefficients gathered in the third-order tensor[1] $\mathbf{A}(\mathbf{u}_s)$ and the fourth-order tensor $\mathbf{B}(\mathbf{u}_s)$ [230]. In the following, the elements of the tensors will be denoted by

$$A^m_{ij} = \mathbf{A}[i, j, m] \qquad \text{and} \qquad B^m_{ijk} = \mathbf{B}[i, j, k, m]. \tag{2.13}$$

The explicit indicial expression of the nonlinear internal forces writes

$$g^m_{\text{nl}}(\mathbf{u}) = \sum_{i=1}^{N_{\text{DOF}}} \sum_{j=i}^{N_{\text{DOF}}} A^m_{ij} \; u_i u_j + \sum_{i=1}^{N_{\text{DOF}}} \sum_{j=i}^{N_{\text{DOF}}} \sum_{k=j}^{N_{\text{DOF}}} B^m_{ijk} \; u_i u_j u_k, \tag{2.14}$$

with $m = 1, 2, \ldots, N_{\text{DOF}}$. The limited ranges of the indices can be exploited to reduce computational and storage requirements. The third- and fourth-order tensors $\mathbf{A}(\mathbf{u}_s)$ and

[1] The term 'tensor' used here simply refers to a multidimensional array with more than two dimensions.

$\mathbf{B}(\mathbf{u}_s)$ can generally not be extracted from standard finite element software used in industry. Specific methods can be used to interpolate the nonlinear stiffness term between known values [14, 46].

In practice, commercial finite element software is often based on updated Lagrangian formulations so that the linearity between the Green-Lagrange strain tensor and the second Piola-Kirchhoff stress tensor is not guaranteed [232]. Because of this inconsistency between the general elasticity formulation and the finite element formulation, the expression of the nonlinear internal forces (2.12) is not exact in this case.

Example 2.1 – Clamped-clamped von Kàrmàn beam

The influence of geometric nonlinearities can be illustrated on a simple academic structure: a clamped-clamped beam, as shown in Fig. 2.3. This test case is largely used in a geometrically nonlinear context [78, 109, 142]. The beam has a uniform square cross section. The geometric and material properties of the beam are summarized in Table 2.1. The strains are measured with the Green-Lagrange tensor with the von Kàrmàn approximation, which consists in neglecting the nonlinear terms except the quadratic term in the transverse displacement for the axial deformation [159]. Under the assumption of an Euler-Bernoulli beam, the shear is also neglected.

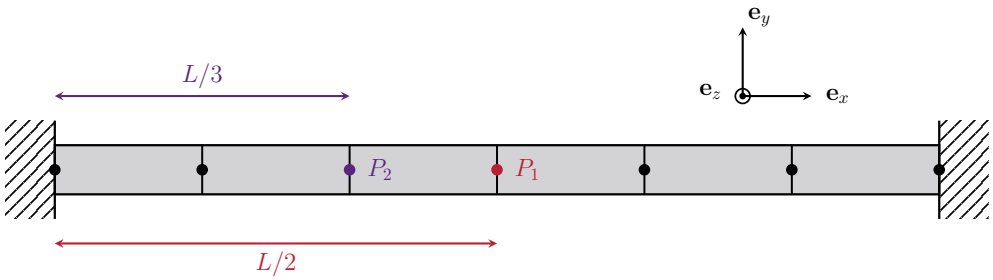

FIGURE 2.3 – Finite element model of the clamped-clamped beam.

Based on these assumptions, a finite element model of the beam is built using beam elements with three degrees-of-freedom per node (axial displacement u, transverse displacement v and in-plane rotation θ) [78]. The transverse and axial displacements are interpolated using Hermite polynomials. Rayleigh damping is assumed, with $\mathbf{C} = 3\mathbf{M}$. The beam is divided into 30 elements. The frequency of the first bending mode of the beam, which is purely transverse, equals 160 Hz.

Parameter	*Symbol*	*Value*	*Units*
Density	ρ	7,800	kg/m^3
Young's modulus	E	210	GPa
Poisson's ratio	ν	0.3	[-]
Length	L	1	m
Side of the section	a	3	cm

TABLE 2.1 – Material and geometric properties of the beam.

The beam is excited by a harmonic excitation of amplitude $A_e = 200$ N at its center (node P_1) in the transverse direction $\mathbf{e}_y$ to mainly excite its first bending mode. The frequency response curve (FRC) is obtained by increasing/decreasing progressively the frequency of the excitation and extracting the amplitude of the response of the beam. More details regarding the nonlinear simulations are provided in chapter 3. The FRC corresponding to the transverse displacement at P_1 and the axial displacement at P_2 (see Fig. 2.3) are shown in Fig. 2.4. The results accounting for the geometric nonlinearities are compared with the results obtained by neglecting them.

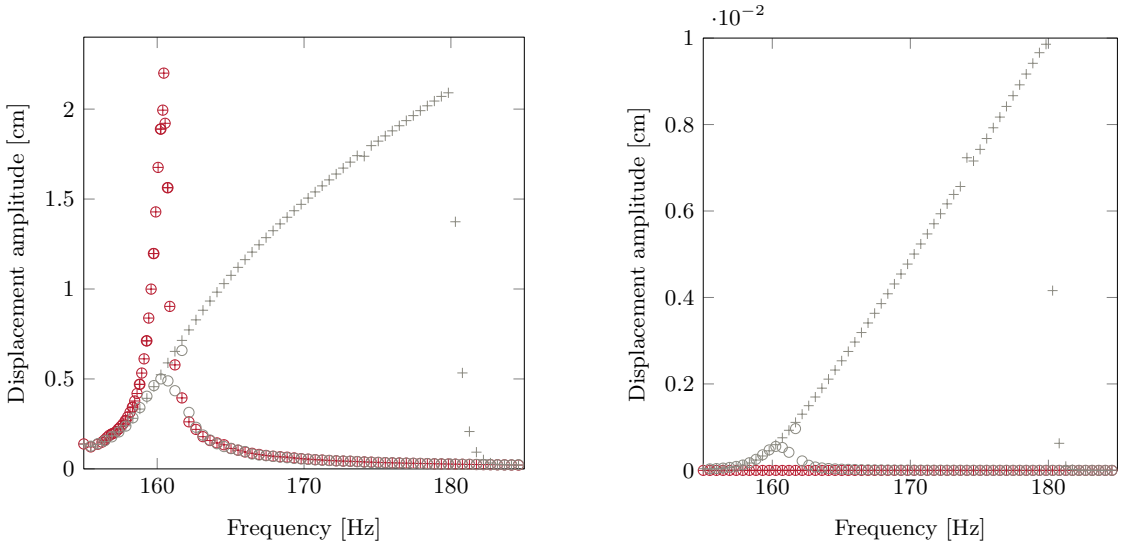

(a) Transverse displacement at P_1.

(b) Axial displacement at P_2.

FIGURE 2.4 – Frequency response curves (upward (+) and downward (○) frequency sweeps), without (+/○) and with (+/○) geometric nonlinearities.

The analysis of the FRC related to the transverse displacement in Fig. 2.4a demonstrates the influence of geometric nonlinearities. In the linear case, resonance, where the maximal amplitude is reached, occurs at the first natural frequency (160 Hz). In the nonlinear case, the FRC is inclined to the right and resonance occurs at 180 Hz. Also, the analysis highlights the existence of several solutions for a given frequency.

In the linear case, the displacement is purely transverse: the axial displacement is equal to zero on the whole frequency range (see Fig. 2.4b). In the nonlinear case, non-zero axial displacements are observed. In this case, geometric nonlinearities are therefore responsible for a coupling between pure transverse bending modes and axial (or membrane) modes. The transverse and axial components of the displacement along the beam at the linear and nonlinear resonances are shown in Fig. 2.5.

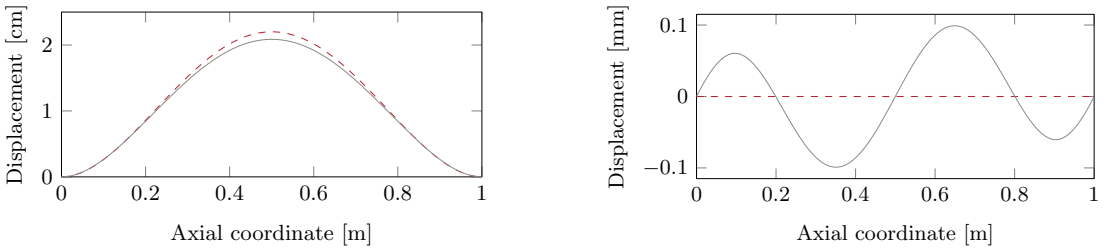

(a) Transverse displacement.

(b) Axial displacement.

FIGURE 2.5 – Beam displacement at linear resonance (----) and nonlinear resonance (——).

2.4.3 Contact nonlinearities

Contact nonlinearities are the second kind of nonlinearities studied in this work.

Contact nonlinearities in turbomachines In turbomachinery design, energy efficiency can be improved by controlling the clearance between the blade-tips and the stationary surrounding casing in order to reduce aerodynamic leaks. In practice, decreasing the clearance by 25% allows to increase the engine efficiency by 1%, saving 200,000 liters of fuel per year for a middle-range aircraft [128]. As a consequence, structural contacts between rotating and stationary components, *i.e.* between blade-tips and the casing, can occur in nominal operating conditions and can no longer be neglected [8, 189]. Because some blades are now made of lighter composite materials featuring lower admissible stress than titanium alloys, these contact interactions can damage the structure [165]. In order to mitigate damaging

vibratory phenomena, an abradable coating is usually added along the casing contact surface. This coating acts as a sacrificial material that is worn out in the case of blade/casing contacts [180, 247]. The abradable coating should be resilient enough in order not to be damaged by the gas flow, but should also have good abrasive properties when impacted by the blades [182]. In practice, these coatings are often laid by plasma praying of composite powders comprising a metal base (providing good cohesion) and a polymer filler generating porosities (providing good abrasion).

Apart from blade/casing contacts, other kinds of contact nonlinearities exist in turbomachines (see the contact interfaces in Fig. 2.6). In bladed disk assemblies, nonlinearities are for instance present at the friction interfaces at the joint between the different blades and the disk where energy dissipation is important [191]. Contact may also occur between two neighboring blade's shrouds [6] or between shaft and bearings [48].

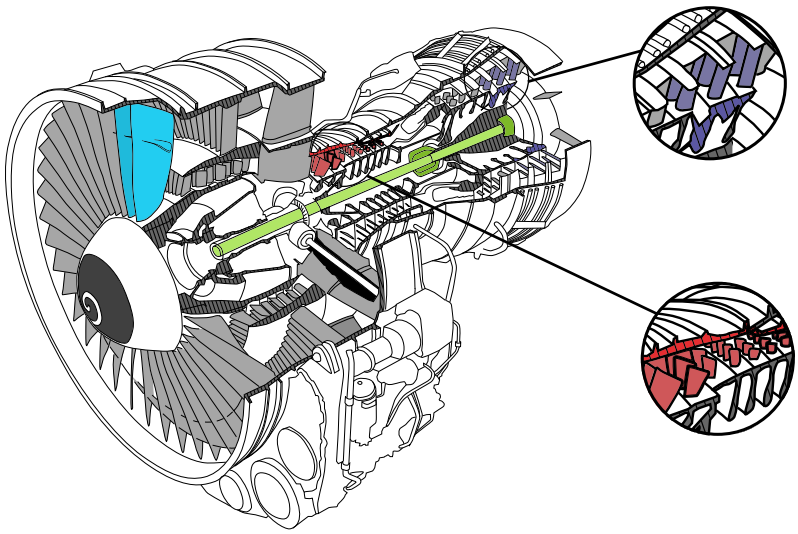

FIGURE 2.6 – Main contact interfaces in aircraft engines: blade/blade (■), blade/casing (■), shaft/bearing (■) and blade/disk (■).

Modeling Because full-scale experiments are extremely costly, test benches usually focus on the characterization of specific phenomena such as the wear mechanisms of the abradable layer [144,249] or the blade dynamics [58,163]. From a numerical standpoint, the understanding of the blade-tip/casing contact interactions has therefore motivated many research works initiated by different manufacturers [151, 174, 216, 240]. Different numerical strategies have been developed to model and predict contact interactions [151,174] as penalty methods [201], Lagrange multipliers [42] or the augmented Lagrangian approach [139].

In the field of turbomachinery, each contact interface is characterized by its own specificities, which require dedicated modeling tools. In particular, blade-tip/casing contacts may yield several types of interactions, namely rubbing interactions [16], modal interactions [134] and whirl motions [190], each of them requiring a specific numerical framework. For instance, rubbing interactions involve large amplitude vibrations of a single blade, without significant vibration of the disk and the casing. In this case, the casing is usually supposed to be rigid but a very precise modeling of the blade/casing interface is required [132, 180, 240]. In modal interactions, the modes of the full bladed disk and of its surrounding casing are characterized by the same number of nodal diameters so that both structures may exchange energy through repeated contacts. The flexibility of the casing has therefore to be considered in the simulations [17]. Lastly, whirl motions correspond to orbital motions of the shaft that can arise in accidental configurations, for instance following bearing failures. The study of whirl motions requires the modeling of the full bladed disk, the shaft and the casing and a precise modeling of inertial effects [169, 190]. Note that these three types of interactions can also be combined. Different numerical strategies for the modeling of the removal of an abradable coating on the casing have also been developed [8, 165, 180].

Blade-tip/casing contact can be described as a unilateral contact between a flexible body (the blade) and a rigid obstacle (the casing). Let's denote by Γ_c the contact surface of the flexible body and introduce the gap function $g(\mathbf{x})$, defining the distance between each point M of Γ_c with vector position $\mathbf{x}$ and its closest counterpart on the rigid obstacle. The contact conditions take the form of Kuhn-Tucker optimality conditions

$$\forall \mathbf{x} \in \Gamma_c, \quad t_{c,\mathrm{N}}(\mathbf{x}) \geqslant 0, \quad g(\mathbf{x}) \geqslant 0 \quad \text{and} \quad t_{c,\mathrm{N}}(\mathbf{x}) g(\mathbf{x}) = 0, \tag{2.15}$$

where $t_{c,\mathrm{N}}(\mathbf{x})$ stands for the contact pressure, normal to Γ_c at $\mathbf{x}$. Friction is usually managed with the Coulomb law. The relative tangential (or sliding) velocity $\mathbf{v}_\mathrm{T}$ is null while

$$\|\mathbf{t}_{c,\mathrm{T}}\| \leqslant \mu_s t_{c,\mathrm{N}}, \tag{2.16}$$

where $\mathbf{t}_{c,\mathrm{T}}$ is the vector of tangential contact forces and μ_s is the static friction coefficient. This corresponds to a sticking phase. When motion is initiated,

$$\mathbf{t}_{c,\mathrm{T}} = -\mu t_{c,\mathrm{N}} \frac{\mathbf{v}_\mathrm{T}}{\|\mathbf{v}_\mathrm{T}\|}, \tag{2.17}$$

where μ is the dynamic friction coefficient. This is the sliding phase.

2.5 Partial conclusions

The dynamics of bladed disks is generally studied with finite element models that can be derived from the weak form of the dynamic problem. This chapter highlights the complex nature of the dynamics of bladed structures in turbomachines. First, bladed disks differ from their nominal cyclically periodic designs and present blade-to-blade variations known as mistuning. Second, the dynamics of bladed disks is fundamentally nonlinear.

In the following, different assumptions are made regarding the modeling of bladed disks:

- the material is homogeneous, isotropic, non-dissipative and elastic;
- the angular speed is supposed to remain constant in module and in direction;
- in nonlinear studies, both the prestressed state $\mathbf{u}_s$ and the displacement $\mathbf{u}$ with respect to the prestressed state are considered as geometrically nonlinear.

CHAPTER 3 MULTI-NONLINEAR DYNAMIC SIMULATION

In general, the equations of motion of mechanical structures take the form of coupled second order differential equations. In the specific case of rotating structures, such as bladed disks, the equations of motion are given by (2.3). Two paradigms are available to solve these nonlinear equations, namely time integration based methods and frequency methods. In this chapter, these two families of methods are presented, together with the associated implementation challenges. The content of this chapter is very general, and not restricted to turbomachines dynamics.

3.1 Time methods

The time response can be computed using time integration schemes [73]. In such methods, the time interval of interest is discretized in a finite number of instants t_n and the solution at each instant is computed using the solutions at previous instants. Some integration schemes, such as the Euler explicit and implicit methods and the family of Runge-Kutta methods [194] require to rewrite the second order differential problems (2.3) into first order ordinary differential equations. Other integration schemes directly work with the second order ordinary differential equations, such as the explicit central difference time integration scheme, where the first and second derivatives are approximated by central finite differences. The linear and nonlinear Newmark-β algorithms [160] are also often implemented in commercial finite element software as in the nonlinear module Mecano of SAMCEF used in this work [197]. The family of generalized-α methods [89], that allows to combine an integration scheme of second order accuracy with a numerical damping in the high frequency range [50], is also widely used.

3.1.1 Accounting for contact

The numerical strategy adopted here is based on the work of Carpenter and relies on the explicit central difference time integration scheme with the handling of contact using Lagrange multipliers [42]. Friction is described by a Coulomb law, under the assumption of sliding friction. In the specific case of rotating bladed disks, the assumption is well justified as the tangential speed due to rotation is significantly larger than the vibration speed of the structure.

By noting $\mathbf{u}_n$, the numerical approximation of the exact value of the displacement field $\mathbf{u}(t_n)$, the equation of motion (2.3) at time step t_n is written as

$$\mathbf{M}\ddot{\mathbf{u}}_n + \mathbf{C}\dot{\mathbf{u}}_n + \mathbf{K}\mathbf{u}_n + \mathbf{g}_{\text{nl}}(\mathbf{u}_n) = \mathbf{f}_e(t_n) + \mathbf{C}_{\text{NT}}^{\text{T}}\boldsymbol{\lambda}, \tag{3.1}$$

where $\boldsymbol{\lambda}$ is the vector of Lagrange multipliers, corresponding to the contact forces in the normal direction, and the matrix $\mathbf{C}_{\text{NT}}$ is the sum of the contact constraint matrices in the normal direction $\mathbf{C}_{\text{N}}$ and in the tangential direction $\mathbf{C}_{\text{T}}$ (obtained from the Coulomb law). This equation must be solved with the non-penetration constraint

$$\mathbf{d}_n = \mathbf{d}_0 - \mathbf{C}_{\text{N}}\mathbf{u}_n \geqslant \mathbf{0}, \tag{3.2}$$

where $\mathbf{d}_n$ stands for the distances between the blade-tip nodes and the casing at time step t_n and $\mathbf{d}_0$ for the initial distances between the structures[1].

The classical explicit central finite difference scheme used in this work yields

$$\ddot{\mathbf{u}}_n = \frac{\mathbf{u}_{n+1} - 2\mathbf{u}_n + \mathbf{u}_{n-1}}{h^2} \quad \text{and} \quad \dot{\mathbf{u}}_n = \frac{\mathbf{u}_{n+1} - \mathbf{u}_{n-1}}{2h}, \tag{3.3}$$

where h is the time step of integration.

The algorithm is based on a prediction/correction scheme. The displacement $\mathbf{u}_{n+1}$ is given by

$$\mathbf{u}_{n+1} = \mathbf{u}_{n+1}^p + \mathbf{u}_{n+1}^c, \tag{3.4}$$

i.e. the sum of the predicted displacement $\mathbf{u}_{n+1}^p$ computed without contact constraints and of the corrected displacement $\mathbf{u}_{n+1}^c$ accounting for the contact constraints.

At each time step $t_{n+1} = t_n + h$, the displacement field is first predicted without accounting for possible contact interaction as

$$\mathbf{u}_{n+1}^p = (2\mathbf{M} + h\mathbf{C})^{-1}\left[2h^2\left[\mathbf{f}_e(t_n) - \mathbf{g}_{\text{nl}}(\mathbf{u}_n)\right] + \left(4\mathbf{M} - 2h^2\mathbf{K}\right)\mathbf{u}_n + (h\mathbf{C} - 2\mathbf{M})\,\mathbf{u}_{n-1}\right]. \tag{3.5}$$

The correction part of the displacement is given by

$$\mathbf{u}_{n+1}^c = 2h^2\,(2\mathbf{M} + h\mathbf{C})^{-1}\,\mathbf{C}_{\text{NT}}^{\text{T}}\boldsymbol{\lambda}, \tag{3.6}$$

where $\boldsymbol{\lambda}$ is still unknown at this step of the procedure.

The predicted displacement field $\mathbf{u}_{n+1}^p$ is then used to evaluate the gap $\mathbf{d}_{n+1}^p$ between the N_b

[1] This vectors inequality should be interpreted component-wise.

impacting nodes (on the blade) and the contact surface (the rigid casing) as

$$\mathbf{d}_{n+1}^{p} = \mathbf{d}_0 - \mathbf{C}_{\mathrm{N}}\mathbf{u}_{n+1}^{p}. \tag{3.7}$$

Given (3.4) and (3.7), the non-penetration constraint (3.2) is rewritten in an equivalent form

$$\mathbf{d}_{n+1}^{p,-} - \mathbf{C}_{\mathrm{N}}\mathbf{u}_{n+1}^{c} = \mathbf{0}, \tag{3.8}$$

where $\mathbf{d}_{n+1}^{p,-}$ is the projection on $\mathbb{R}_{-}^{N_b}$ of $\mathbf{d}_{n+1}^{p}$.

Comparing (3.6) and (3.8), the Lagrange multipliers are given by

$$\boldsymbol{\lambda} = \left[2h^2\mathbf{C}_{\mathrm{N}}\left(2\mathbf{M} + h\mathbf{C}\right)^{-1}\mathbf{C}_{\mathrm{NT}}^{\mathrm{T}}\right]^{-1}\mathbf{d}_{n+1}^{p,-}. \tag{3.9}$$

If penetration is detected between the blade and the rigid casing, contact forces are therefore introduced in the normal and tangential directions through the Lagrange multipliers to cancel the penetration at the impacting nodes. These contact forces are then used to correct the displacement at all nodes with (3.6).

3.1.2 High performance implementation

When the number of degrees-of-freedom increases, the evaluation of the nonlinear internal forces with (2.12) can become computationally expensive as the size of the tensor $\mathbf{B}$ increases with the fourth power of N_{DOF}.

The contact algorithm described in section 3.1.1 takes the form of a time loop with a succession of matrix/vector products. At each time step, the nonlinear internal forces due to large displacements are evaluated in the prediction step given by (3.5). The prediction step of the contact algorithm can be rewritten as

$$\mathbf{u}_{n+1}^{p} = \mathbf{X}_0\mathbf{f}_e(t_n) + \mathbf{X}_1\mathbf{u}_n + \mathbf{X}_2\mathbf{u}_{n-1} + \boldsymbol{\mathcal{X}}_3\left(\mathbf{u}_n, \mathbf{u}_n\right) + \boldsymbol{\mathcal{X}}_4\left(\mathbf{u}_n, \mathbf{u}_n, \mathbf{u}_n\right), \tag{3.10}$$

where $\mathbf{u}_{n+1}^{p}$ is the prediction of the displacement at time t_{n+1}, $\mathbf{f}_e$ is the vector of external forces, $\mathbf{u}_n$ and $\mathbf{u}_{n-1}$ are the displacements computed at time t_n and t_{n-1} and where

$$\mathbf{X}_0 = 2h^2\left(2\mathbf{M} + h\mathbf{C}\right)^{-1}, \tag{3.11}$$

$$\mathbf{X}_1 = \left(2\mathbf{M} + h\mathbf{C}\right)^{-1}\left(4\mathbf{M} - 2h^2\mathbf{K}\right), \tag{3.12}$$

$$\mathbf{X}_2 = \left(2\mathbf{M} + h\mathbf{C}\right)^{-1}\left(h\mathbf{C} - 2\mathbf{M}\right), \tag{3.13}$$

$$\boldsymbol{\mathcal{X}}_3(\cdot,\cdot) = -2h^2\left(2\mathbf{M}+h\mathbf{C}\right)^{-1}\boldsymbol{\mathcal{A}}(\cdot,\cdot), \tag{3.14}$$

and

$$\boldsymbol{\mathcal{X}}_4(\cdot,\cdot,\cdot) = -2h^2\left(2\mathbf{M}+h\mathbf{C}\right)^{-1}\boldsymbol{\mathcal{B}}(\cdot,\cdot,\cdot). \tag{3.15}$$

Coefficients of functional forms $\boldsymbol{\mathcal{X}}_3(\cdot,\cdot)$ and $\boldsymbol{\mathcal{X}}_4(\cdot,\cdot,\cdot)$ are gathered in the third-order tensor $\mathbf{X}_3$ and the fourth-order tensor $\mathbf{X}_4$. Matrices and tensors $\mathbf{X}_i$ $(i=0,\ldots,4)$ are constant and can be computed once at the beginning of the simulation. Preliminary simulations using this algorithm based on Lagrange multipliers show that a small time step of integration of the order of 10^{-7} second has to be considered, so that a huge number of evaluations of the nonlinear internal forces are required to reach the steady-state regime. The implementation described in the next paragraph allows to reduce the computational burden.

At each time step, the matrices and tensors $\mathbf{X}_i$ $(i=0,\ldots,4)$ are transferred from the memory to the processor, they are respectively multiplied by $\mathbf{f}_e(t_n)$, $\mathbf{u}_n$, $\mathbf{u}_{n-1}$ and used in the nonlinear functions (that can be seen as 'tensors products'), and the resulting quantities are summed up. These two steps (transfer from RAM and mathematical operations) have to be considered when optimizing the code to reduce computation times. In practice, on powerful computation servers, computations are often limited by the DRAM bandwidth, more than by the number of operations that can be done per second. In the matrix/vector products in (3.10), each element of the matrices is used only once in the multiplications, which is not very efficient. In practice, different simulations are required to capture the dynamics of the system at different angular speeds, or for different contact conditions. Instead of running these simulations sequentially, independently from each other, we suggest to run them in parallel, advancing in time the different solutions all together, which allows a repeated and hence more efficient use of the data in memory. Provided the matrices and tensors $\mathbf{X}_i$ $(i=0,\ldots,4)$ are the same for each simulation, the prediction step of the contact algorithm given by (3.10) can be rewritten as

$$\mathbf{U}_{n+1}^p = \mathbf{X}_0\mathbf{F}_e(t_n) + \mathbf{X}_1\mathbf{U}_n + \mathbf{X}_2\mathbf{U}_{n-1} + \boldsymbol{\mathcal{X}}_3\left(\mathbf{U}_n,\mathbf{U}_n\right) + \boldsymbol{\mathcal{X}}_4\left(\mathbf{U}_n,\mathbf{U}_n,\mathbf{U}_n\right), \tag{3.16}$$

where the matrices $\mathbf{U}_{n+1}^p$, $\mathbf{F}_e$, $\mathbf{U}_n$ and $\mathbf{U}_{n-1}$ are respectively the concatenations of the vectors $\mathbf{u}_{n+1}^p$, $\mathbf{f}_e$, $\mathbf{u}_n$ and $\mathbf{u}_{n-1}$ related to each simulation and where

$$\left\{\boldsymbol{\mathcal{X}}_3\left(\mathbf{U}_n,\mathbf{U}_n\right)\right\}[m,p] = \sum_{i=1}^{N_{\mathrm{DOF}}}\sum_{j=i}^{N_{\mathrm{DOF}}}\mathbf{X}_3[m,i,j]\,\mathbf{U}_n[i,p]\,\mathbf{U}_n[j,p] \tag{3.17}$$

and

$$\{\boldsymbol{\mathcal{X}}_4(\mathbf{U}_n,\mathbf{U}_n,\mathbf{U}_n)\}[m,p]=\sum_{i=1}^{N_{\mathrm{DOF}}}\sum_{j=i}^{N_{\mathrm{DOF}}}\sum_{k=j}^{N_{\mathrm{DOF}}}\mathbf{X}_4[m,i,j,k]\,\mathbf{U}_n[i,p]\,\mathbf{U}_n[j,p]\,\mathbf{U}_n[k,p]\,. \quad (3.18)$$

In this way, the matrix/vector products are replaced by matrix/matrix products where the elements of the matrices loaded from the memory are used several times, which is more efficient and can theoretically accelerate the computation. As the $\mathbf{X}_i$ $(i=0,\ldots,4)$ only depend on the time step of integration and on the structural matrices, the different simulations performed together can be characterized by different contact conditions, such as different friction coefficients or clearance values for instance, or different angular speeds. As shown in chapter 6, this can be particularly beneficial to build interaction maps as it requires to perform contact simulations on a wide range of angular speeds.

Linear terms The products $\mathbf{X}_0\mathbf{F}_e(t_n)$, $\mathbf{X}_1\mathbf{U}_n$ and $\mathbf{X}_2\mathbf{U}_{n-1}$ in (3.16) involve 2D matrices and can be computed easily. The gain in computation time can though be illustrated with this simple products. For instance, consider the product $\mathbf{X}_1\mathbf{u}_n$, to be computed for 1,000 samples of vector $\mathbf{u}_n$, corresponding to different simulations at different angular speeds, for a constant matrix $\mathbf{X}_1$ of order N_{DOF}. The products can be computed in two different ways:

(i) As 1,000 independent matrix/vector products;

(ii) As 1 matrix/matrix product, *i.e.* by computing $\mathbf{X}_1\mathbf{U}_n$ where $\mathbf{U}_n$ is the concatenations of the 1,000 samples of $\mathbf{u}_n$.

The products are carried out in Python, on NumPy arrays, for 50 different values of N_{DOF} between 4^2 and 4^5. The products are also computed using the compiler Numba. The corresponding computation times are shown in Fig. 3.1a. The results correspond to mean values over 200 realizations and are obtained on 10 cores. Note that the maximal value $N_{\mathrm{DOF}}=4^5$ considered here is small compared to the number of degrees-of-freedom of typical industrial structures. However, the numerical strategy will be applied here on reduced-order models whose size does not exceed this value.

The results confirm that even for simple 2D products, performing a matrix/matrix product instead of a succession of matrix/vector products allows to decrease the computation time between one and two orders of magnitude. The use of the compiler Numba allows to considerably accelerate the computation.

The same results are presented in Fig. 3.1b in terms of the number of operations per second. The horizontal asymptote in the matrix/vector product curve confirms that in this case, the

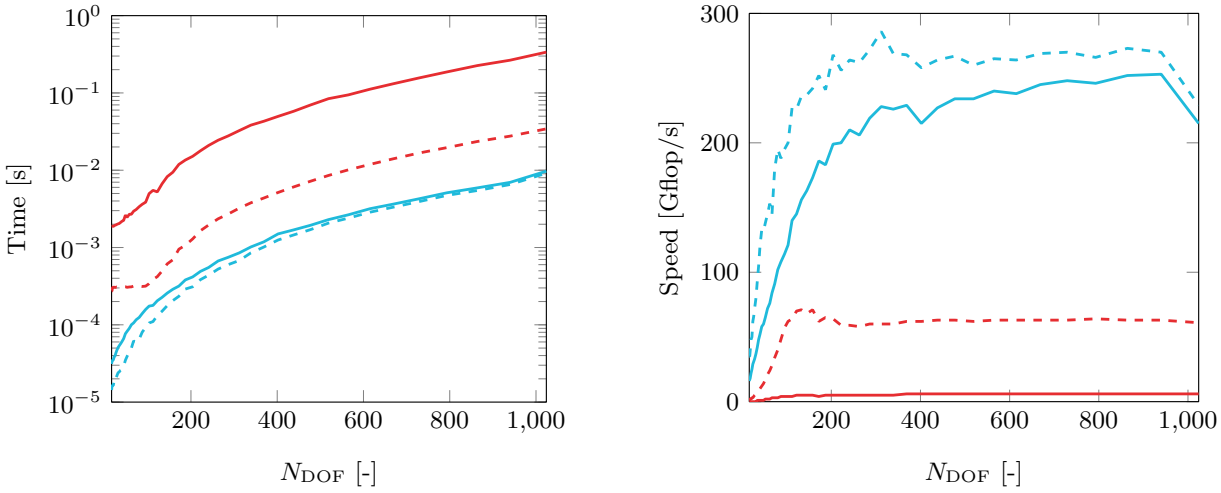

(a) Computation time.

(b) Speed of computation.

FIGURE 3.1 – Performance for the computation of $\mathbf{X}_1\mathbf{u}_n$ for 1,000 samples of $\mathbf{u}_n$: matrix/vector products (——) and matrix/matrix product (——); without Numba (——) and with Numba (- - - -).

computation speed is restricted by the speed of the memory. The use of a matrix/matrix product allows to considerably increase the number of operations per second as the elements of the matrix $\mathbf{X}_1$ are used several times in the multiplication.

Nonlinear terms The functional forms $\boldsymbol{\mathcal{X}}_3(\mathbf{U}_n, \mathbf{U}_n)$ and $\boldsymbol{\mathcal{X}}_4(\mathbf{U}_n, \mathbf{U}_n, \mathbf{U}_n)$ are kinds of products of 3D tensors and 4D tensors whose computation has to be optimized to avoid losing the benefit of the numerical strategy. In order to remove useless monomials redundancy in the products, the tensors $\mathbf{X}_3$ and $\mathbf{X}_4$ are first transformed to 'upper triangular' or 'upper pyramidal' tensors, *i.e.* $\mathbf{X}_3[m,i,j] = 0$ except for $i \leqslant j$ and $\mathbf{X}_4[m,i,j,k] = 0$ except for $i \leqslant j \leqslant k$. An adapted tensor multiplication function, accounting for the particular sparse structure of tensors $\mathbf{X}_3$ and $\mathbf{X}_4$, has been implemented on top of the BLIS framework to perform efficiently the products [227]. The multi-threaded implementation is inspired from the BLIS implementation of the product of triangular matrices [204].

In order to illustrate the efficiency of the procedure, consider that the nonlinear part of (3.10), $\boldsymbol{\mathcal{X}}_3(\mathbf{u}_n, \mathbf{u}_n) + \boldsymbol{\mathcal{X}}_4(\mathbf{u}_n, \mathbf{u}_n, \mathbf{u}_n)$, has to be evaluated for 1,000 values of $\mathbf{u}_n$, for constant functional forms $\boldsymbol{\mathcal{X}}_3(\cdot,\cdot)$ and $\boldsymbol{\mathcal{X}}_4(\cdot,\cdot,\cdot)$. These nonlinear term is computed in two ways:

(i) As 1,000 independent evaluations of $\boldsymbol{\mathcal{X}}_3(\mathbf{u}_n, \mathbf{u}_n) + \boldsymbol{\mathcal{X}}_4(\mathbf{u}_n, \mathbf{u}_n, \mathbf{u}_n)$, with the functional forms evaluated as in (2.14), and using the compiler Numba;

(ii) As 1 evaluation of $\boldsymbol{\mathcal{X}}_3(\mathbf{U}_n, \mathbf{U}_n) + \boldsymbol{\mathcal{X}}_4(\mathbf{U}_n, \mathbf{U}_n, \mathbf{U}_n)$ where $\mathbf{U}_n$ is the concatenations of the 1,000 samples of $\mathbf{u}_n$, with the adapted tensor multiplication function implemented.

The corresponding computation times are given in Fig. 3.2 for N_{DOF} between 4^2 and 4^4. Again, the results correspond to mean values over 200 realizations and are obtained on 10 cores. They show that the strategy is very efficient to compute the nonlinear forces, as a reduction of computation time larger than two orders of magnitudes is achieved.

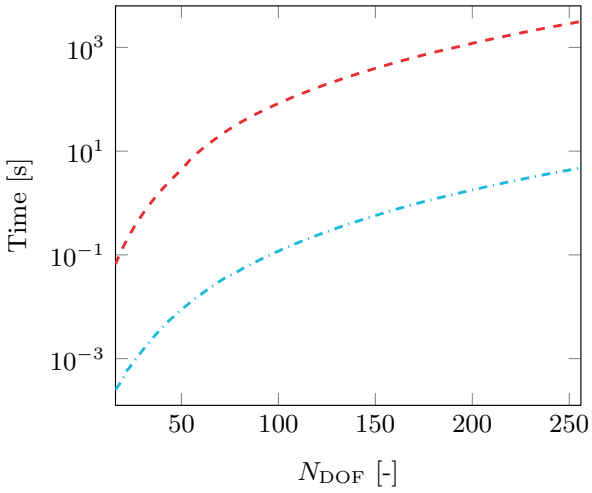

FIGURE 3.2 – Computation time of $\boldsymbol{\mathcal{X}}_3(\mathbf{u}_n, \mathbf{u}_n) + \boldsymbol{\mathcal{X}}_4(\mathbf{u}_n, \mathbf{u}_n, \mathbf{u}_n)$ for 1,000 samples of $\mathbf{u}_n$: independent evaluations (- - - -) and tensor products (-·-·-).

The results presented here are only related to the gain in computation time for the evaluation of matrix products, and do not consider all the steps of the contact algorithm presented in section 3.1.1. When applied to the full contact algorithm, the numerical strategy with memory sharing presented in this section allows to considerably reduce computation times (by a factor between 5 and 15, depending on the processor). More details regarding the actual acceleration of the simulations will be provided further when presenting the results on industrial structures (see section 6.5.4).

3.2 Frequency methods

When only the permanent regime is studied, the time integration methods presented in section 3.1 are not well suited as they first have to go through the transient regime before reaching the steady-state response. In contrast, frequency methods, as the Harmonic Balance Method (HBM), are very efficient for the computation of the steady-state response of nonlinear systems [33, 125, 129].

3.2.1 Harmonic balance method

The HBM consists in writing the solution $\mathbf{u}(t)$ of the equation of motion (2.3) as a Fourier series truncated at harmonic H as

$$\mathbf{u}(t) = \frac{\mathbf{a}_0}{2} + \sum_{k=1}^{H} \left[\mathbf{a}_k \cos(k\omega t) + \mathbf{b}_k \sin(k\omega t)\right], \tag{3.19}$$

where ω is the fundamental pulsation and the coefficients $\mathbf{a}_k$ $(k = 0, \ldots, H)$ and $\mathbf{b}_k$ $(k = 1, \ldots, H)$ are the Fourier coefficients of the displacement $\mathbf{u}$. This equation can be written in the form of a Galerkin projection as

$$\mathbf{u}(t) = \mathbf{T}(t)\hat{\mathbf{u}}, \tag{3.20}$$

where

$$\mathbf{T}(t) = \left[\frac{1}{2} \quad \cos(\omega t) \quad \sin(\omega t) \quad \cdots \quad \cos(H\omega t) \quad \sin(H\omega t)\right] \otimes \mathbf{I}_{N_{\mathrm{DOF}}} \tag{3.21}$$

and

$$\hat{\mathbf{u}} = \left[\mathbf{a}_0^{\mathrm{T}} \quad \mathbf{a}_1^{\mathrm{T}} \quad \mathbf{b}_1^{\mathrm{T}} \quad \cdots \quad \mathbf{a}_H^{\mathrm{T}} \quad \mathbf{b}_H^{\mathrm{T}}\right]^{\mathrm{T}}. \tag{3.22}$$

The velocity and acceleration can therefore be computed as

$$\dot{\mathbf{u}}(t) = \mathbf{T}(t)\boldsymbol{\nabla}\hat{\mathbf{u}} \qquad \text{and} \qquad \ddot{\mathbf{u}}(t) = \mathbf{T}(t)\boldsymbol{\nabla}^2\hat{\mathbf{u}}, \tag{3.23}$$

where

$$\boldsymbol{\nabla} = \mathrm{diagblock}\left(0, \boldsymbol{\nabla}_1, \ldots, \boldsymbol{\nabla}_H\right) \quad \text{and} \quad \boldsymbol{\nabla}^2 = \boldsymbol{\nabla}\boldsymbol{\nabla}, \quad \text{with} \quad \boldsymbol{\nabla}_k = \begin{bmatrix} 0 & k\omega \\ -k\omega & 0 \end{bmatrix} \otimes \mathbf{I}_{N_{\mathrm{DOF}}}. \tag{3.24}$$

Injecting the approximations (3.20) and (3.23) in (2.3) provides the residue

$$\mathbf{r} = \mathbf{M}\mathbf{T}\boldsymbol{\nabla}^2\hat{\mathbf{u}} + \mathbf{C}\mathbf{T}\boldsymbol{\nabla}\hat{\mathbf{u}} + \mathbf{K}\mathbf{T}\hat{\mathbf{u}} + \mathbf{g}_{\mathrm{nl}} - \mathbf{f}_e - \mathbf{f}_c. \tag{3.25}$$

The HBM then consists in orthonormalizing the residue with respect to the harmonic functions in $\mathbf{T}(t)$, using the scalar product

$$\langle f | g \rangle = \frac{2}{T}\int_0^T f(t)g(t)dt. \tag{3.26}$$

The projections of the residue on the test functions write

$$\langle \mathbf{r}|1/2\rangle = \mathbf{K}\mathbf{a}_0 + \langle \mathbf{g}_{\text{nl}}|1/2\rangle - \langle \mathbf{f}_e|1/2\rangle - \langle \mathbf{f}_c|1/2\rangle \tag{3.27}$$
$$\langle \mathbf{r}|\cos(k\omega t)\rangle = \left[\mathbf{K} - (k\omega)^2\mathbf{M}\right]\mathbf{a}_k + k\omega\mathbf{C}\mathbf{b}_k + \langle \mathbf{g}_{\text{nl}}|\cos(k\omega t)\rangle - \langle \mathbf{f}_e|\cos(k\omega t)\rangle - \langle \mathbf{f}_c|\cos(k\omega t)\rangle$$
$$\langle \mathbf{r}|\sin(k\omega t)\rangle = \left[\mathbf{K} - (k\omega)^2\mathbf{M}\right]\mathbf{b}_k - k\omega\mathbf{C}\mathbf{a}_k + \langle \mathbf{g}_{\text{nl}}|\sin(k\omega t)\rangle - \langle \mathbf{f}_e|\sin(k\omega t)\rangle - \langle \mathbf{f}_c|\sin(k\omega t)\rangle$$

Cancelling these projections gives the HBM equation in the frequency domain

$$\mathbf{Z}(\omega)\hat{\mathbf{u}} + \hat{\mathbf{g}}_{\text{nl}}(\hat{\mathbf{u}},\omega) = \hat{\mathbf{f}}_e(\omega) + \hat{\mathbf{f}}_c(\hat{\mathbf{u}},\omega), \tag{3.28}$$

where the new unknowns are the $N_{\text{DOF}}(2H+1)$ Fourier coefficients $\hat{\mathbf{u}}$, where

$$\mathbf{Z}(\omega) = \text{diagblock}\left(\mathbf{K}, \mathbf{Z}_1, \ldots, \mathbf{Z}_H\right) \quad \text{with} \quad \mathbf{Z}_k = \begin{bmatrix} \mathbf{K} - (k\omega)^2\mathbf{M} & k\omega\mathbf{C} \\ -k\omega\mathbf{C} & \mathbf{K} - (k\omega)^2\mathbf{M} \end{bmatrix}, \tag{3.29}$$

and where $\hat{\mathbf{g}}_{\text{nl}}$, $\hat{\mathbf{f}}_c$ and $\hat{\mathbf{f}}_e$ are respectively the vectors of Fourier coefficients related to the forces $\mathbf{g}_{\text{nl}}$, $\mathbf{f}_c$ and $\mathbf{f}_e$.

When the pulsation ω is fixed, the nonlinear algebraic system of equations (3.28) can be solved using iterative methods such as Newton-Raphson method [245], quasi-Newton method or Newton-Krylov method [120]. When the parameter ω varies, continuation algorithms can be used to follow the solutions branches, for instance to build frequency response curves.

3.2.2 Treatment of nonlinear forces

The analytical determination of the harmonic coefficients related to the nonlinear forces, $\hat{\mathbf{g}}_{\text{nl}}$ and $\hat{\mathbf{f}}_c$, is only possible in very simple cases, such as polynomial nonlinearities, and leads to long expressions. It is however possible to use the Alternating Frequency/Time (AFT) numerical method to evaluate the nonlinear forces in the frequency domain, based on their knowledge in the time domain [38].

3.2.2.1 Alternating Frequency/Time method

At each iteration of the iterative method used to solve (3.28), the displacement and velocity fields are computed in the time domain on one or several periods using the inverse discrete Fourier transform matrix $\mathbf{F}_{\mathbb{R}}^{-1}$ as

$$\mathbf{u} = \mathbf{F}_{\mathbb{R}}^{-1}\hat{\mathbf{u}} \quad \text{and} \quad \dot{\mathbf{u}} = \mathbf{F}_{\mathbb{R}}^{-1}\boldsymbol{\nabla}\hat{\mathbf{u}}, \tag{3.30}$$

where

$$\mathbf{F}_{\mathbb{R}}^{-1} = \begin{bmatrix} 1/2 & \cos(\omega t_1) & \sin(\omega t_1) & \cdots & \cos(H\omega t_1) & \sin(H\omega t_1) \\ \vdots & \vdots & \vdots & \ddots & \vdots & \vdots \\ 1/2 & \cos(\omega t_{N_h}) & \sin(\omega t_{N_h}) & \cdots & \cos(H\omega t_{N_h}) & \sin(H\omega t_{N_h}) \end{bmatrix} \otimes \mathbf{I}_{N_{\mathrm{DOF}}}, \tag{3.31}$$

where N_h is the number of time steps in the temporal signal. Based on the knowledge of the displacement and velocity fields, the nonlinear forces $\mathbf{g}_{\mathrm{nl}}(\mathbf{u})$ and $\mathbf{f}_c(\mathbf{u}, \dot{\mathbf{u}})$ are then computed in the time domain. The nonlinear forces can then be computed in the frequency domain using the direct discrete Fourier transform matrix $\mathbf{F}_{\mathbb{R}}$ as

$$\hat{\mathbf{x}} = \mathbf{F}_{\mathbb{R}}\mathbf{x}, \tag{3.32}$$

where $\mathbf{x}$ stands for $\mathbf{g}_{\mathrm{nl}}$ or $\mathbf{f}_c$ and

$$\mathbf{F}_{\mathbb{R}} = \frac{2}{N_h} \begin{bmatrix} 1 & \dots & 1 \\ \cos(\omega t_1) & \dots & \cos(\omega t_{N_h}) \\ \sin(\omega t_1) & \dots & \sin(\omega t_{N_h}) \\ \vdots & \ddots & \vdots \\ \cos(H\omega t_1) & \dots & \cos(H\omega t_{N_h}) \\ \sin(H\omega t_1) & \dots & \sin(H\omega t_{N_h}) \end{bmatrix} \otimes \mathbf{I}_{N_{\mathrm{DOF}}}. \tag{3.33}$$

3.2.2.2 Accounting for contact

Penalty approaches, where contact forces are defined proportionally to the computed interpenetrations of the structures, are particularly well suited when using an AFT scheme. However, when dealing with structural contacts, it has been shown that the HBM is prone to the Gibbs phenomenon, which is related to the non-uniform convergence of Fourier series for the approximation of nonsmooth functions [147]. This translates into spurious oscillations appearing in the vicinity of discontinuities. Without adjustment, this method performs poorly.

A methodology has been recently proposed to smoothen contact management [52]. First, the penalty contact law is regularized in order to mitigate the Gibbs phenomenon [241]. The normal components of the contact forces are evaluated as

$$t_{c,N}(t) = \kappa \frac{g(t)}{2} + \sqrt{\left[\kappa \frac{g(t)}{2}\right]^2 + \gamma^2}, \tag{3.34}$$

where $g(t)$ is the distance between the contact node and the casing, $\kappa \in \mathbb{R}_+$ is the penalty coefficient and $\gamma \in \mathbb{R}_+$ is a smoothing parameter. This regularization of the contact law greatly increases the numerical robustness of the HBM but does not prevent spurious oscillations on the displacements, velocities and contact forces. To further mitigate the effects of the Gibbs phenomenon, filtering techniques may be employed with the aim of altering the Fourier coefficients to make them decay faster. In particular, the Lanczos filtering technique in the frequency domain is found to provide the best compromise between spurious oscillations mitigation and an accurate approximation of the original waveform in the vicinity of discontinuous areas [100]. With this filtering technique, the contact forces write

$$\mathbf{f}_c(\mathbf{u}, \dot{\mathbf{u}}) = \frac{\mathbf{a}_0^c}{2} + \sum_{k=1}^{H} \zeta_k \left[\mathbf{a}_k^c \cos(k\omega t) + \mathbf{b}_k^c \sin(k\omega t)\right], \tag{3.35}$$

where ζ_k are the Lanczos factors and the coefficients $\mathbf{a}_k^c$ and $\mathbf{b}_k^c$ are the Fourier coefficients of the contact forces. This methodology is known as the Regularized-Lanczos HBM (RL-HBM).

3.2.3 High performance implementation

In this frequency methodology, nonlinear internal forces due to large displacements and their first derivatives have to be evaluated at each iteration of the iterative method used to solve (3.28). As explained in section 3.1.2, this can become computationally expensive when the number of degrees-of-freedom increases. Similarly to what is done in section 3.1.2, the methodology can be used to solve (3.28) for different contact configurations at the same time, *i.e.* to solve

$$\mathbf{Z}(\omega)\hat{\mathbf{U}} + \hat{\mathbf{G}}_{\mathrm{nl}}(\hat{\mathbf{U}}, \omega) = \hat{\mathbf{F}}_e(\omega) + \hat{\mathbf{F}}_c(\hat{\mathbf{U}}, \omega), \tag{3.36}$$

where the matrices $\hat{\mathbf{U}}$, $\hat{\mathbf{G}}_{\mathrm{nl}}$, $\hat{\mathbf{F}}_e$ and $\hat{\mathbf{F}}_c$ are respectively the concatenations of the vectors $\hat{\mathbf{u}}$, $\hat{\mathbf{g}}_{\mathrm{nl}}$, $\hat{\mathbf{f}}_e$ and $\hat{\mathbf{f}}_c$ related to each simulation. In this way, the nonlinear internal forces and their derivatives are evaluated by matrix/matrix products, which is more profitable and can accelerate the computation.

3.3 Partial conclusions

In practice, both time and frequency strategies are required. On the one hand, time methods allow to compute any type of response of the system: diverging solutions, chaos, as well as transient phenomena. They are also more easily compatible with multiphysics algorithms. However, time integration does not provide the required qualitative understanding of the system. On the other hand, frequency methods provide this qualitative view of the system

and easily allow to assess the stability of a solution but are currently not compatible with large numerical models and do not capture transient phenomena.

In this work, computations are made in the time domain in order to capture transient phenomena due to the occurrence of contact events, which are key for the rise of some critical interactions [152]. Nonetheless, as shown further, most developments are compatible with frequency methods.

CHAPTER 4 REDUCED-ORDER MODELING

Nowadays, it is relatively fast and easy to build finite element models of 3D structures that are very accurate in geometric details and material distribution. These finite element models are generally characterized by a high number of degrees-of-freedom. In the absence of symmetry (for mistuned bladed disks in particular), the cyclic symmetry formulation introduced in section 2.2.2 cannot be used and the whole finite element model must be considered. This is also true for nonlinear systems as mode shapes are not pure nodal diameter modes. The time integration of the corresponding equations therefore requires high computational capabilities. Many efforts are nowadays dedicated to the construction of reduced-order models (ROMs) using modal analysis and substructuration techniques.

The final objective of the reduction techniques is to decrease the number of parameters describing the system while ensuring that the reduced-order model is able to represent with a good accuracy the dynamics of the full-order model. Complex phenomena such as mistuning or nonlinearities must therefore be taken into account in the reduced-order models of bladed structures.

Reduced-order models can be beneficial for various reasons. They are used to reduce the computational burden in a design process, but also as fast executing substitutes of the full-order model or to extract pertinent information hidden in the full-order model. Recent studies also show that reduced-order models can be advantageously used to create digital twins of real structures [83]. Such digital twins can be updated based on measurements on the physical structure and used for predictive maintenance to detect abnormal behavior or estimate the remaining lifetime of the structure [5].

There are already tendencies to anticipate a further surge in computational power and a corresponding decline of the need for reduced-order models [86]. However, for the near future, it seems that the demand for more accurate simulations is still growing much faster than the available computational capacity.

This chapter starts with some generalities on model order reduction and, in particular, introduces the concept of reduced-order modeling by subspace projection. This introduction is followed by a review of the most popular reduced-order modeling techniques developed for nonlinear systems. The reduction methods presented are very general and not restricted to turbomachines dynamics.

4.1 Generalities on model order reduction

Model order reduction consists in reducing the physical degrees-of-freedom $\mathbf{u}$ into a smaller set of generalized coordinates $\mathbf{q}$ through a linear or nonlinear mapping $\mathbf{\Gamma}$. In projection methods, the equation of motion is then projected onto a reduced space. In the case of a nonlinear mapping, the projection is often executed on the tangent space around an equilibrium position, as in the quadratic manifold approach [99]. Conversely, invariant manifold methods avoid this projection by assuming the reduced dynamics form to be known *a priori* [82, 218]. In such methods, the shape of the mapping has to be guessed so that such methods are generally applied to known polynomial nonlinearities. In this work devoted to geometric and contact nonlinearities, only projection methods are considered.

Different approaches exist to define the mapping, *i.e.* the change of coordinates between full space and reduced space. On the one hand, the mapping can be defined based on the physics of the problem through the computation of intrinsic characteristics of the system (linear or nonlinear normal modes for instance) [219]. On the other hand, data-driven methods can be used. Such methods require samples of system trajectories obtained from numerical simulations or experiments to train the system [71]. Machine learning techniques, as neural networks, are more and more used in this context [59].

4.1.1 Model order reduction by Galerkin projection

Let's define $\mathbf{u} \in \mathbb{R}^{N_{\text{DOF}}}$ as the exact solution of the equation of motion (2.3). The Galerkin approach consists in finding an approximate solution $\mathbf{u}^{\text{ROM}}$ lying in a subspace of $\mathbb{R}^{N_{\text{DOF}}}$ spanned by a basis $\mathbf{\Phi}$. The reduction writes

$$\mathbf{u}(t) \approx \mathbf{u}^{\text{ROM}}(t) = \mathbf{\Phi}\mathbf{q}(t) = \sum_{j=1}^{r} \boldsymbol{\phi}_j q_j(t), \tag{4.1}$$

where $\mathbf{q} \in \mathbb{R}^r$ are the new unknowns of the problem, known as the generalized coordinates, with $r \leqslant N_{\text{DOF}}$ (in practice $r \ll N_{\text{DOF}}$). Because of the approximation, injecting (4.1) in (2.3) leads to the definition of the residue

$$\mathbf{r} = \mathbf{M}\mathbf{\Phi}\ddot{\mathbf{q}} + \mathbf{C}(\Omega)\mathbf{\Phi}\dot{\mathbf{q}} + \mathbf{K}(\Omega, \mathbf{u}_s)\mathbf{\Phi}\mathbf{q} + \mathbf{g}_{\text{nl}}(\mathbf{\Phi}\mathbf{q}, \mathbf{u_s}) - \mathbf{f}_e(t) - \mathbf{f}_c(\mathbf{\Phi}\mathbf{q} + \mathbf{u}_s, \mathbf{\Phi}\dot{\mathbf{q}}). \tag{4.2}$$

The procedure consists in finding the solution $\mathbf{q}$ such that the residue is orthogonal to a subspace of $\mathbb{R}^{N_{\text{DOF}}}$ spanned by a basis $\mathbf{\Upsilon}$, *i.e.*

$$\mathbf{\Upsilon}^{\text{T}}\mathbf{r} = \mathbf{0}. \tag{4.3}$$

The procedure is known as the Petrov-Galerkin method when $\boldsymbol{\Phi} \neq \boldsymbol{\Upsilon}$ and the Galerkin method when $\boldsymbol{\Phi} = \boldsymbol{\Upsilon}$. For the Galerkin method, that will be used through this work, Eq. (4.3) writes

$$\tilde{\mathbf{M}}\ddot{\mathbf{q}} + \tilde{\mathbf{C}}(\Omega)\dot{\mathbf{q}} + \tilde{\mathbf{K}}(\Omega, \mathbf{u}_s)\mathbf{q} + \tilde{\mathbf{g}}_{\text{nl}}(\mathbf{q}, \mathbf{u}_s) = \tilde{\mathbf{f}}_e(t) + \tilde{\mathbf{f}}_c(\mathbf{q}, \dot{\mathbf{q}}), \tag{4.4}$$

where the projected matrices take the expressions

$$\tilde{\mathbf{M}} = \boldsymbol{\Phi}^{\mathrm{T}}\mathbf{M}\boldsymbol{\Phi}, \qquad \tilde{\mathbf{C}} = \boldsymbol{\Phi}^{\mathrm{T}}\mathbf{C}\boldsymbol{\Phi}, \qquad \tilde{\mathbf{K}} = \boldsymbol{\Phi}^{\mathrm{T}}\mathbf{K}\boldsymbol{\Phi} \tag{4.5}$$

and the projected vectors are defined as

$$\tilde{\mathbf{g}}_{\text{nl}}(\mathbf{q}, \mathbf{u}_s) = \boldsymbol{\Phi}^{\mathrm{T}}\mathbf{g}_{\text{nl}}(\boldsymbol{\Phi}\mathbf{q}, \mathbf{u}_s), \qquad \tilde{\mathbf{f}}_e = \boldsymbol{\Phi}^{\mathrm{T}}\mathbf{f}_e, \qquad \tilde{\mathbf{f}}_c = \boldsymbol{\Phi}^{\mathrm{T}}\mathbf{f}_c. \tag{4.6}$$

The initial conditions on the generalized coordinates related to the reduced model are obtained from the initial conditions on the degrees-of-freedom of the full-order model by a least-squares approximation, *i.e.*

$$\mathbf{q}(0) = \left(\boldsymbol{\Phi}^{\mathrm{T}}\boldsymbol{\Phi}\right)^{-1}\boldsymbol{\Phi}^{\mathrm{T}}\mathbf{u}(0) \qquad \text{and} \qquad \dot{\mathbf{q}}(0) = \left(\boldsymbol{\Phi}^{\mathrm{T}}\boldsymbol{\Phi}\right)^{-1}\boldsymbol{\Phi}^{\mathrm{T}}\dot{\mathbf{u}}(0). \tag{4.7}$$

The different existing projection-based reduced-order modeling methods differ by the choice of the projection basis and by the way the nonlinear forces are evaluated in the reduced space. Various approaches to identify the nonlinear forces in the reduced space are described in section 4.2 and a review of the projection bases used in the literature is proposed in section 4.3.

4.1.2 Distinction between offline and online stages

Projection-based model order reduction methods discriminate between an expensive offline stage where the projection basis is computed and the reduced-order model is built and an efficient online stage where the problem is solved. Figure 4.1 schematically represents the distinction between offline and online stages. The offline stage takes the full-order finite element model as an input. In this stage, the reduction basis is built, the full-order matrices are projected onto the reduction basis and the expression of the nonlinear internal forces is identified with an appropriate method. Numerical simulations are performed in the online stage. In this stage, the initial conditions and the excitation are first projected onto the reduced space. The equation of motion in the reduced space is then numerically integrated in time before the solution may be re-projected onto the full-order space.

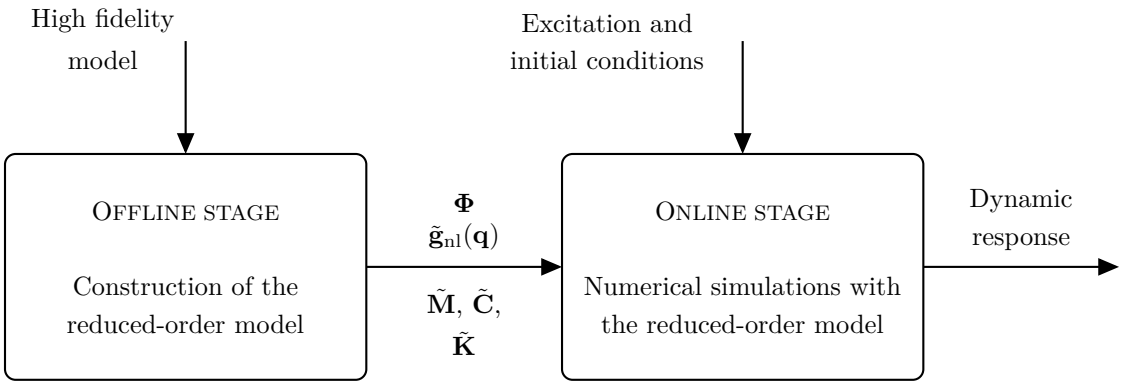

Figure 4.1 – Offline and online stages in model order reduction.

A large variety of reduced-order modeling techniques applicable to a broad range of engineering problems can be found in the literature. The trade-off between gain in computational effort and error committed defines the success of the application of the reduced-order model (ROM). The order r of the ROM defines its size and has to be chosen so that the ROM can retain the crucial properties of the finite element model. For some techniques, the computational cost of the transformation between the full-order model (FOM) and the ROM (*i.e.* the offline cost) can exceed the computational cost of a single FOM computation. However, one has to keep in mind that the offline stage is performed only once for a given reduction basis, while the reduced-order model can be used in the online stage to study different excitation conditions and therefore replace several FOM computations.

4.1.3 Contact interfaces in ROMs

As reduced-order models will be used in this work in combination with contact algorithms, it is interesting to focus on techniques that allow to keep the physical contact interface in the reduced space. Indeed, retaining the physical degrees-of-freedom corresponding to the contact interface in the reduced coordinates $\mathbf{q}$ allows to easily check the contact conditions without having to go back in the full-order space, which would be computationally inefficient. Existing reduction methods therefore have to be adapted (when required) in order to retain physical degrees-of-freedom in the reduced space.

The physical displacement vector $\mathbf{u}$ is therefore partitioned into its inner degrees-of-freedom and boundary interface degrees-of-freedom, $\mathbf{u}_i$ and $\mathbf{u}_b$,

$$\mathbf{u} = \begin{bmatrix} \mathbf{u}_i \\ \mathbf{u}_b \end{bmatrix}. \tag{4.8}$$

The boundary interface degrees-of-freedom should be included in the reduced basis. The structural matrices $\mathbf{M}$, $\mathbf{C}$ and $\mathbf{K}$ and the force vectors $\mathbf{g}_{\text{nl}}$, $\mathbf{f}_e$ and $\mathbf{f}_c$ are partitioned accordingly with respect to inner (subscript i) and boundary (subscript b) degrees-of-freedom

$$\mathbf{X} = \begin{bmatrix} \mathbf{X}_{ii} & \mathbf{X}_{ib} \\ \mathbf{X}_{bi} & \mathbf{X}_{bb} \end{bmatrix} \qquad \text{and} \qquad \mathbf{x} = \begin{bmatrix} \mathbf{x}_i \\ \mathbf{x}_b \end{bmatrix}, \tag{4.9}$$

where $\mathbf{X}$ stands for the mass, damping or stiffness matrix and $\mathbf{x}$ stands for the nonlinear, external or contact force vector. This partitioning and the associated notations will be used for the presentation of the reduction methods in the next sections.

4.1.4 Multi-nonlinear simulations

Model order reduction by projection preserves the general form of the equation of motion, *i.e.* (2.3) and (4.4) have the same structure. When the reduction methods are adapted to keep physical degrees-of-freedom among the generalized coordinates, as detailed in section 4.1.3, the usual algorithms defined for high fidelity finite element models introduced in chapter 3 can therefore be directly applied in the reduced space.

In practice, the time algorithm defined in section 3.1 and the frequency method based on the HBM described in section 3.2 can also be used to compute the solution $\mathbf{q}(t)$ of the reduced equation of motion (4.4) instead of $\mathbf{u}(t)$, by replacing matrices $\mathbf{M}$, $\mathbf{C}$ and $\mathbf{K}$ and vectors $\mathbf{g}_{\text{nl}}$, $\mathbf{f}_c$ and $\mathbf{f}_e$ by their projections $\tilde{\mathbf{M}}$, $\tilde{\mathbf{C}}$ and $\tilde{\mathbf{K}}$ and vectors $\tilde{\mathbf{g}}_{\text{nl}}$, $\tilde{\mathbf{f}}_c$ and $\tilde{\mathbf{f}}_e$ and considering the size of the reduced space r instead of the total number of degrees-of-freedom N_{DOF}.

Once a reduced-order model has been built, it can be used for computations in the time domain with classical time integration schemes or in the frequency domain with the HBM for instance. As mentioned in the introduction of this work, we will focus in the following on the comparison of the reduction methods in the time domain, keeping in mind that their use in frequency domain could be the subject of future works.

4.2 Reduced nonlinear internal forces

Different methods have been developed to evaluate $\tilde{\mathbf{g}}_{\text{nl}}(\mathbf{q}, \mathbf{u}_s)$, the nonlinear internal forces due to large displacements in the reduced space. These methods are classified as intrusive (or direct, explicit) and non-intrusive (or indirect, implicit) methods.

4.2.1 Intrusive methods

In intrusive methods, the projected nonlinear term is directly computed from the knowledge of the finite element tensors and the projection basis [40, 220]. These methods are based on the relationship between the finite element tensors and their modal counterparts. However, the finite element tensors of quadratic and cubic stiffness terms cannot always be extracted from commercial finite element software. Even when the full finite element model is available, these intrusive methods are computationally inefficient because the computational complexity of Galerkin projection of the nonlinear terms still depends on the total number of degrees-of-freedom.

The Discrete Empirical Interpolation Method (DEIM) has been proposed to reduce the computational effort [46]. In the DEIM, the Galerkin projection of the nonlinear internal forces is obtained by interpolation of the nonlinear forces computed with the high fidelity model at a given number of chosen interpolation points.

4.2.2 Non-intrusive methods

The methods used to evaluate $\tilde{\mathbf{g}}_{\text{nl}}(\mathbf{q}, \mathbf{u}_s)$ are classified as non-intrusive when they do not require the knowledge of the finite element formulation used in the software and to extract information from the source code. Such methods are compatible with standard finite element packages as the nonlinear internal forces are identified based on inputs/outputs from the software. Among them, the stiffness evaluation procedure and its variants are largely used in structural dynamics. Data-driven methods are also developed, based on experimental measurements or simulated signals.

4.2.2.1 Stiffness evaluation procedure

The stiffness evaluation procedure (STEP) was first introduced by Muravyov and Rizzi [155]. It consists in imposing static displacement fields and determining the corresponding nonlinear internal forces. In the STEP, the nonlinear reduced term is assumed to be a polynomial of degree 3 in terms of the generalized coordinates $\mathbf{q}$. Depending on the formulation of the geometric nonlinearities in the finite element discretization, this expansion can be exact or truncated [76]. The polynomial formulation reads

$$\tilde{\mathbf{g}}_{\text{nl}}(\mathbf{q}) = \widetilde{\boldsymbol{\mathcal{A}}}(\mathbf{q}, \mathbf{q}) + \widetilde{\boldsymbol{\mathcal{B}}}(\mathbf{q}, \mathbf{q}, \mathbf{q}), \tag{4.10}$$

using a functional notation for the quadratic and cubic terms with coefficients gathered in the third-order tensor $\tilde{\mathbf{A}}$ and the fourth-order tensor $\tilde{\mathbf{B}}$. In the following, the elements of the tensors will be denoted by

$$\tilde{A}^m_{ij} = \tilde{\mathbf{A}}[i,j,m] \qquad \text{and} \qquad \tilde{B}^m_{ijk} = \tilde{\mathbf{B}}[i,j,k,m]. \tag{4.11}$$

Single-dimension tensors extracted from the tensors $\tilde{\mathbf{A}}$ and $\tilde{\mathbf{B}}$ are denoted by

$$\tilde{\mathbf{A}}_{ij} = \tilde{\mathbf{A}}[i,j,:] \qquad \text{and} \qquad \tilde{\mathbf{B}}_{ijk} = \tilde{\mathbf{B}}[i,j,k,:]. \tag{4.12}$$

The explicit indicial expression of the nonlinear internal forces writes

$$\tilde{g}^m_{\mathrm{nl}}(\mathbf{q}) = \sum_{i=1}^{r}\sum_{j=i}^{r} \tilde{A}^m_{ij}\, q_i q_j + \sum_{i=1}^{r}\sum_{j=i}^{r}\sum_{k=j}^{r} \tilde{B}^m_{ijk}\, q_i q_j q_k, \tag{4.13}$$

with $m = 1, 2, \ldots, r$.

Coefficients $\tilde{A}^m_{ij}$ and $\tilde{B}^m_{ijk}$ from Eq. (4.13) are determined by nonlinear forces static evaluations performed on the full-order finite element model. First, the coefficients with equal indices $\tilde{A}^m_{ii}$ and $\tilde{B}^m_{iii}$ $(i = 1, \ldots, r)$ are determined by imposing displacements of the form

$$\mathbf{u} = +q_i\boldsymbol{\phi}_i \qquad \text{and} \qquad \mathbf{u} = -q_i\boldsymbol{\phi}_i \qquad (i = 1, \ldots, r), \tag{4.14}$$

where $\boldsymbol{\phi}_i$ is the i^{th} mode of the reduction basis $\boldsymbol{\Phi}$, and computing the associated nonlinear forces

$$\mathbf{F}^{\mathrm{NL}}_a = \mathbf{g}_{\mathrm{nl}}\left(\mathbf{u} = +q_i\boldsymbol{\phi}_i\right) \qquad \text{and} \qquad \mathbf{F}^{\mathrm{NL}}_b = \mathbf{g}_{\mathrm{nl}}\left(\mathbf{u} = -q_i\boldsymbol{\phi}_i\right). \tag{4.15}$$

The absolute values of the modal coordinates q_i imposed must be chosen sufficiently large to activate the nonlinear behavior of the structure but sufficiently small to remain in the convergence limit of the finite element software. The Galerkin projections of these forces provide the reduced nonlinear forces

$$\tilde{\mathbf{F}}^{\mathrm{NL}}_a = \boldsymbol{\Phi}^{\mathrm{T}}\mathbf{F}^{\mathrm{NL}}_a = \boldsymbol{\Phi}^{\mathrm{T}}\mathbf{g}_{\mathrm{nl}}\left(\mathbf{u} = +q_i\boldsymbol{\phi}_i\right) = \tilde{\mathbf{g}}_{\mathrm{nl}}\left(\mathbf{q} = [0 \cdots + q_i \cdots 0]^{\mathrm{T}}\right) \tag{4.16}$$

and

$$\tilde{\mathbf{F}}^{\mathrm{NL}}_b = \boldsymbol{\Phi}^{\mathrm{T}}\mathbf{F}^{\mathrm{NL}}_b = \boldsymbol{\Phi}^{\mathrm{T}}\mathbf{g}_{\mathrm{nl}}\left(\mathbf{u} = -q_i\boldsymbol{\phi}_i\right) = \tilde{\mathbf{g}}_{\mathrm{nl}}\left(\mathbf{q} = [0 \cdots - q_i \cdots 0]^{\mathrm{T}}\right). \tag{4.17}$$

Combining (4.13), (4.16) and (4.17) yields the system of equations

$$\begin{cases} \tilde{\mathbf{F}}_a^{\mathrm{NL}} = \tilde{\mathbf{A}}_{ii} q_i^2 + \tilde{\mathbf{B}}_{iii} q_i^3 \\ \tilde{\mathbf{F}}_b^{\mathrm{NL}} = \tilde{\mathbf{A}}_{ii} q_i^2 - \tilde{\mathbf{B}}_{iii} q_i^3 \end{cases} \tag{4.18}$$

where q_i, $\tilde{\mathbf{F}}_a^{\mathrm{NL}}$ and $\tilde{\mathbf{F}}_b^{\mathrm{NL}}$ are known. The vectors $\tilde{\mathbf{A}}_{ii}$ and $\tilde{\mathbf{B}}_{iii}$ can therefore be identified as

$$\begin{cases} \tilde{\mathbf{A}}_{ii} = \dfrac{\tilde{\mathbf{F}}_a^{\mathrm{NL}} + \tilde{\mathbf{F}}_b^{\mathrm{NL}}}{2q_i^2} \\ \\ \tilde{\mathbf{B}}_{iii} = \dfrac{\tilde{\mathbf{F}}_a^{\mathrm{NL}} - \tilde{\mathbf{F}}_b^{\mathrm{NL}}}{2q_i^3} \end{cases} \tag{4.19}$$

The coefficients with two unequal indices $\tilde{A}_{ij}^m$, $\tilde{B}_{iij}^m$ and $\tilde{B}_{ijj}^m$ $(i < j)$ can be identified in the same way by imposing displacements of the form

$$\begin{aligned} \mathbf{u} = +q_i\boldsymbol{\phi}_i + q_j\boldsymbol{\phi}_j, \quad \mathbf{u} = -q_i\boldsymbol{\phi}_i - q_j\boldsymbol{\phi}_j \\ \text{and} \quad \mathbf{u} = +q_i\boldsymbol{\phi}_i - q_j\boldsymbol{\phi}_j \quad (i,\, j = 1, \ldots, r \;\; ; \;\; i < j). \end{aligned} \tag{4.20}$$

The coefficients with three unequal indices $\tilde{B}_{ijk}^m$ $(i < j < k)$ can be identified by imposing displacements of the form

$$\mathbf{u} = +q_i\boldsymbol{\phi}_i + q_j\boldsymbol{\phi}_j + q_k\boldsymbol{\phi}_k \qquad (i,\, j,\, k = 1, \ldots, r \;\; ; \;\; i < j < k). \tag{4.21}$$

The total number N_{static} of required nonlinear forces static evaluations is given by

$$N_{\mathrm{static}} = \frac{r^3}{6} + r^2 + \frac{5r}{6}, \tag{4.22}$$

where r is the number of modes retained in the reduction basis. This number can be viewed as a measure of the fixed cost of the reduced-order analysis as the model reduction must be performed regardless of the simulated response time to be computed.

Theoretically, the identified coefficients are independent of the level at which the data are obtained. In practice, however, this may not be the case due to the inconsistency between the general elasticity formulation and the finite element formulation in the commercial software. Wang *et al.* proposed a multiple-level identification strategy to reduce this inconsistency [231]. The coefficients are identified at a series of displacement levels. For each stiffness coefficient, a local relative gradient metric is used to find the displacement level at which the

coefficient has the least variation. The value at this level is taken as the identified coefficient.

When the basis of the reduced-order model is large, this identification method requires a large number of simulations. A method using the tangent stiffness matrix

$$\mathbf{K}_T(\mathbf{u}) = \mathbf{K} + \frac{\partial \mathbf{g}_{\text{nl}}}{\partial \mathbf{u}} \tag{4.23}$$

instead of the force in the identification has been developed [171]. This method relies on the availability of the tangent stiffness matrix for each imposed displacement but allows a reduction of the computational effort to the order of r^2.

4.2.2.2 Data-driven methods

The nonlinear parameters of the reduced-order model can also be identified experimentally. For instance, Spottswood and Allemang proposed a method based upon the Nonlinear Identification through Feedback of the Outputs (NIFO) method that allows to simultaneously identify multiple nonlinear relationships between measurement locations [1, 206].

Recently, it has also been suggested that the reduced nonlinear operator could be identified using machine learning techniques, such as artificial neural networks [90].

4.3 Reduction basis

Structures with nonlinearities have been studied with the harmonic balance method by projecting the system on the nonlinear degrees-of-freedom in order to reduce the size of the model [156, 173]. This method is suitable for relatively small systems with localized nonlinearities (such as contact interfaces). For large systems, or in the case of distributed nonlinearities (such as geometric nonlinearities), the size of the resulting system is still too large to be studied. Specific nonlinear reduction methods, characterized by specific reduction bases, are therefore developed.

4.3.1 Linear reduction basis

Before presenting reduction methods specifically developed for the study of geometrically nonlinear systems, it is interesting to see the limitations of traditional reduction bases largely used in a linear context. Three different families of reduction methods are presented here. Their use in a nonlinear context is described at the end of the section.

4.3.1.1 Linear normal modes

The most intuitive model order reduction technique is the modal truncation. In this reduction method, the full-order finite element model is projected onto a subset of the linear normal modes (LNM) of the structure $\hat{\boldsymbol{\phi}}_j$, defined as

$$\left[\mathbf{K} - \omega_j^2 \mathbf{M}\right] \hat{\boldsymbol{\phi}}_j = \mathbf{0}, \qquad j = 1, 2, \cdots, N_{\text{DOF}}. \tag{4.24}$$

The choice of the modes included in the reduction basis can be based on frequency criteria. This method does not allow to keep physical degrees-of-freedom in the reduced space and is therefore not suitable for the implementation of contact.

4.3.1.2 CMS methods with fixed interface

The development of Component Mode Synthesis (CMS) techniques was initiated by the work of Hurty [96]. Three sets of modes were considered for the reduction: fixed interface normal modes, static constraint modes and rigid body modes. Then, Craig and Bampton formulated a simplified CMS technique [54] that does not consider the rigid body modes of Hurty. The physical degrees-of-freedom $\mathbf{u}$ of the structure are separated in inner degrees-of-freedom $\mathbf{u}_i$ and boundary interface degrees-of-freedom $\mathbf{u}_b$ according to (4.8) and the stiffness and mass matrices are partitioned accordingly.

In the Craig-Bampton reduction method, each substructure is reduced using a projection basis $\boldsymbol{\Phi}$ composed of r_b constraint modes $\boldsymbol{\Psi}$ and r_c fixed interface linear normal modes $\boldsymbol{\Theta}$ of the substructure. The displacement of the substructure in the full-order finite element model is approximated as

$$\mathbf{u} = \boldsymbol{\Phi}\mathbf{q} = \begin{bmatrix} \boldsymbol{\Psi} & \boldsymbol{\Theta} \end{bmatrix} \begin{bmatrix} \mathbf{u}_b \\ \boldsymbol{\eta}_c \end{bmatrix}, \tag{4.25}$$

where the generalized coordinates $\mathbf{q}$ are composed of the boundary interface degrees-of-freedom $\mathbf{u}_b$ and the modal coordinates $\boldsymbol{\eta}_c$. The number of vectors in the projection basis is $r = r_c + r_b$. The constraint modes, also called Guyan static modes, correspond to the static deformation of the structure to unitary displacement at the boundary degrees-of-freedom. They can be written as

$$\boldsymbol{\Psi} = \begin{bmatrix} \boldsymbol{\Psi}_i \\ \mathbf{I} \end{bmatrix}, \tag{4.26}$$

where $\mathbf{\Psi}_i$ is the solution of

$$\mathbf{K}\mathbf{\Psi} = \begin{bmatrix} \mathbf{K}_{ii} & \mathbf{K}_{ib} \\ \mathbf{K}_{bi} & \mathbf{K}_{bb} \end{bmatrix} \begin{bmatrix} \mathbf{\Psi}_i \\ \mathbf{I} \end{bmatrix} = \begin{bmatrix} \mathbf{0} \\ \bar{\mathbf{R}} \end{bmatrix}, \tag{4.27}$$

which gives

$$\mathbf{\Psi}_i = -\mathbf{K}_{ii}^{-1}\mathbf{K}_{ib}. \tag{4.28}$$

The fixed interface linear normal modes correspond to the modes of the structure clamped at the boundary interface degrees-of-freedom. They can be written as

$$\mathbf{\Theta} = \begin{bmatrix} \mathbf{\Theta}_{i,r_c} \\ \mathbf{0} \end{bmatrix}, \tag{4.29}$$

where $\mathbf{\Theta}_{i,r_c}$ is formed by truncating to the first r_c modes the solution $\mathbf{\Theta}_i$ of the eigenvalue problem

$$\mathbf{K}_{ii}\mathbf{\Theta}_i = \mathbf{M}_{ii}\mathbf{\Theta}_i\,\boldsymbol{\omega}^2, \tag{4.30}$$

where $\boldsymbol{\omega}^2$ is the diagonal matrix of the eigenfrequencies squared.

This reduction method has been widely used and applied to a wide range of engineering structures [18, 31, 124, 221]. An advantage of this method is that it captures with accuracy the motion at the boundary degrees-of-freedom because there is a one-to-one correspondence between the constraint modes and physical degrees-of-freedom in each interface between components. The principal drawback of the method is the use of fixed interface modes while experimental data are often obtained for free interface conditions. A convergence analysis is required to select the number of modes used in the reduction [73]. A criterion relevant to the problem must be chosen (such as a cutoff frequency or a limit effective modal mass).

4.3.1.3 CMS methods with free interface

Further developments of CMS techniques have been proposed in the literature. Goldman was the first to formulate a CMS technique with free interface normal modes [77]. MacNeal proposed a hybrid CMS technique with mixed interface representation [141]. He was also the first to account for the residual flexibility from the unused component modes to improve accuracy. Rubin included residual inertial and dissipative effects in addition to the residual flexibility [186]. Craig and Chang proposed an exceptionally compact residual flexibility CMS technique [55] where only the generalized coordinates pertaining to the free interface component normal modes appear in the assembled system of equations of motion. The Craig-Martinez reduction method considers a pseudo-static correction in order to keep physical

degrees-of-freedom in the reduced space [145]. Attachment modes, corresponding to the static deformation of the structure to unitary forces at the boundary degrees-of-freedom, can also be added to enrich the reduction basis [56].

4.3.1.4 Application in a nonlinear context

The reduction bases presented in the previous paragraphs have been widely used in structural dynamics and are well established in a linear context. It can be tempting to directly use these linear projection bases in combination with the methods presented in section 4.2 to project the nonlinear internal forces to reduce the full nonlinear finite element model. However, different studies have shown that, without correction, these linear reduction bases are not suitable for the modeling of geometric nonlinearities [13, 79]. They rely indeed on intrinsic properties such as eigenvalues or eigenmodes that, as explained in section 2.4, do not exist for nonlinear systems or are hard to compute. Even if some high-frequency linear modes could capture the geometrically nonlinear behavior of the structure, these modes are often truncated in the reduction procedure. Including these modes in the reduction basis would lead to reduction bases of large size and the benefit of the reduction procedure would be lost [149,229]. When the structure exhibits a nonlinear behavior due to large displacements or due to contact/friction effects, the reduced-order model should integrate these nonlinearities into its construction to get a better representativeness of the reduction basis, as shown in the next sections.

Example 4.1 – Craig-Bampton reduction

The Craig-Bampton reduction method is applied to the clamped-clamped beam introduced in example 2.1 in section 2.4.2. The reduced nonlinear internal forces are evaluated with the STEP. The degree-of-freedom corresponding to the transverse displacement at node P_1 is kept in the reduced space. As a first step, only the corresponding constraint mode and the first two fixed interface linear normal modes are added to the reduction basis. These modes, represented in Fig. 4.2 are purely transverse.

The nonlinear frequency response curve obtained with this reduced-order model is shown in Fig. 4.3 and compared with the reference solution obtained with the full-order model. This reduction basis does not allow to correctly capture the resonance. Adding more transverse constraint modes does not significantly improve the results. This is not surprising as geometric nonlinearities induce in this case a coupling between the transverse and axial displacements, as highlighted in section 2.4.2.

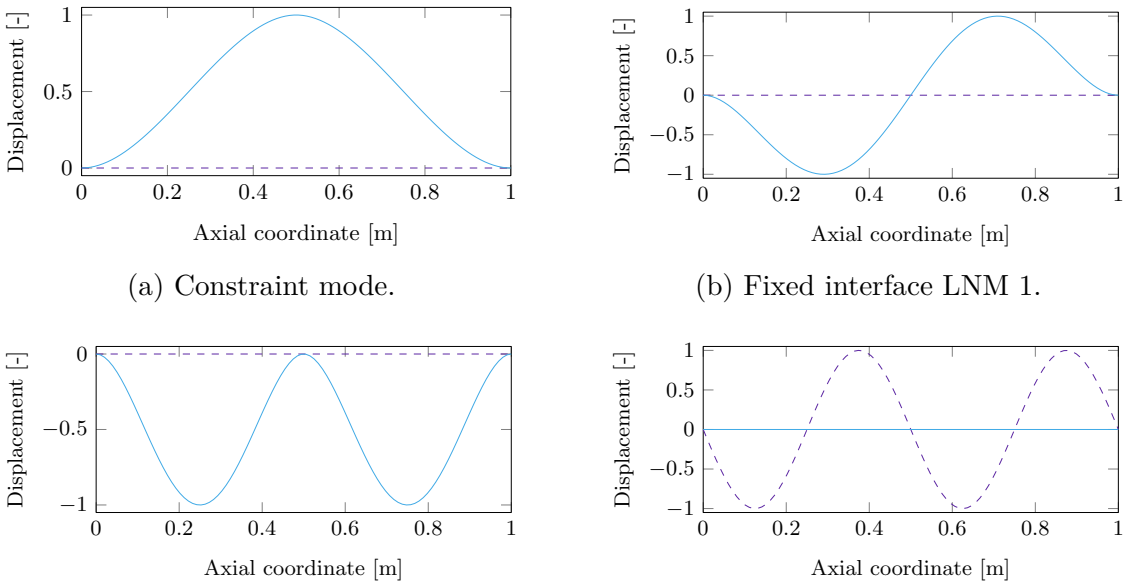

(a) Constraint mode.

(b) Fixed interface LNM 1.

(c) Fixed interface LNM 2.

(d) Fixed interface LNM 14.

FIGURE 4.2 – Craig-Bampton modes of the clamped-clamped beam: transverse displacement (——) and axial displacement (- - - -).

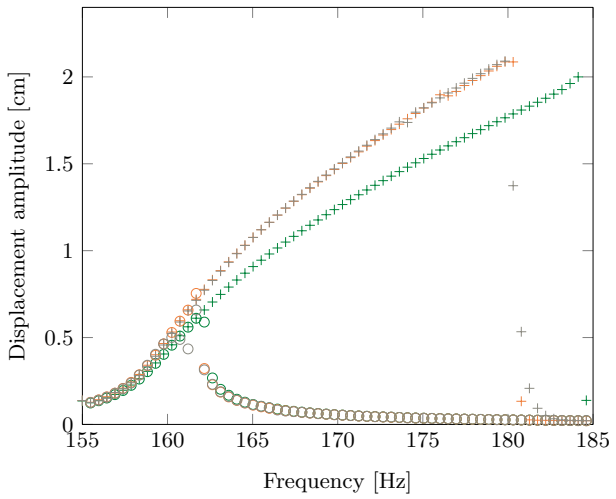

FIGURE 4.3 – Nonlinear frequency response curves (upward (+) and downward (○) frequency sweeps): reference solution (+/○) and solutions obtained with Craig-Bampton ROM with fixed interface LNM 1 and 2 (+/○) and with fixed interface LNM 1, 2, and 14 (+/○).

Based on the analysis performed in example 2.1, the fourth axial fixed interface LNM, corresponding to the fourteenth fixed interface LNM is added in the reduction basis. This mode is represented in Fig. 4.2 and is very similar to the actual deformation of the beam at resonance (see Fig. 2.5b). As shown in Fig. 4.3, much better results are obtained.

For this simple test case, it is relatively simple to select by hand the linear modes to include in the reduction basis. For more complex industrial structures, it is difficult to predict the coupling between the modes and select *a priori* the high-frequency modes to include in the reduction basis. Specific methods have therefore to be developed.

4.3.2 Proper and smooth orthogonal decomposition reduction methods

Proper and smooth orthogonal decomposition reduction methods are data-driven methods which identify the optimal reduction subspace from the results of a training simulation performed with the full-order finite element model.

4.3.2.1 Proper orthogonal decomposition

The Proper Orthogonal Decomposition (POD), also known as the Karhunen-Loève decomposition, was proposed independently by several authors in the 40's [110, 122, 137]. The model reduction by POD is a data-driven method which identifies the optimal subspace from a set of displacement snapshots obtained from simulations with the full-order model or from experimental measurements. If the m displacement snapshots are denoted by $\mathbf{u}^\star(t_i)$ $(i = 1, \ldots, m)$ and collected in a matrix

$$\mathbf{U}^\star = \begin{bmatrix} \mathbf{u}^\star(t_1) & \mathbf{u}^\star(t_2) & \cdots & \mathbf{u}^\star(t_m) \end{bmatrix}, \tag{4.31}$$

the principle of the POD reduction method consists in finding the subspace $\mathbf{\Phi}$ such that the projection of the data matrix $\mathbf{U}^\star$ onto $\mathbf{\Phi}$ has maximal spatial variance. One way of finding the solution of this optimization problem consists in solving the eigenvalue problem of the autocovariance matrix, defined for zero mean data as

$$\mathbf{\Sigma}_{uu} = {\mathbf{U}^\star}^{\mathrm{T}} \mathbf{U}^\star. \tag{4.32}$$

The eigenvalues of the autocovariance matrix are called the proper orthogonal values (POVs) and the eigenvectors are the proper orthogonal modes (POMs). The POMs may be used as a basis for the decomposition of the response. The POM associated to the greatest POV

is the optimal vector to characterize the ensemble of snapshots. The POM associated with the second greatest POV is the optimal vector to characterize the ensemble of snapshots but restricted to the space orthogonal to the first POM, and so forth. The reduction basis $\mathbf{\Phi}$ of the POD reduction method therefore consists in the first POMs corresponding to the largest POVs. It should be noted that there is no general physical interpretation of the modes extracted from the decomposition because of their signal-dependent nature.

The POD basis can also be obtained by solving the Singular Value Decomposition (SVD) of the data matrix $\mathbf{U}^\star$

$$\mathbf{U}^\star = \bar{\mathbf{U}}\bar{\mathbf{S}}\bar{\mathbf{V}}^{\mathrm{T}}. \tag{4.33}$$

The left singular vectors contained in the orthogonal matrix $\bar{\mathbf{U}}$ correspond to the POMs, eigenvectors of the autocovariance matrix and the singular values σ_i contained in the diagonal matrix $\bar{\mathbf{S}}$ correspond to the square roots of the POVs multiplied by the number of samples m. The energy of the vector sequence $\mathbf{u}^\star(t_i)$ collected in the matrix $\mathbf{U}^\star$ is given by

$$\bar{E}(\mathbf{U}^\star) = \sum_{i=1}^{p} \sigma_i^2, \tag{4.34}$$

where $p = \min(N_{\mathrm{DOF}}, m)$, N_{DOF} being the number of degrees-of-freedom of the structure [115]. This expression of the energy can be directly used to select the number of POD modes to include in the reduction basis. A common practice consists in choosing the r dominant modes that capture more than 99.9% of the energy of the training signal.

The POMs are orthogonal to each other while the mode shapes are orthogonal with respect to the mass and stiffness matrices. The POD minimizes the average squared distance between the original signal and its reduced linear representation, *i.e.* the projection basis $\mathbf{\Phi}$ is solution of the minimization problem

$$\min \sum_{i=1}^{m} ||\mathbf{u}^\star(t_i) - \mathbf{\Phi}\mathbf{q}(t_i)||^2. \tag{4.35}$$

The reduction by proper orthogonal decomposition offers an optimal flexibility since it only requires representative simulations of the high dimensional model. The reduced-order modeling by proper orthogonal decomposition has therefore been widely applied in structural dynamics, but also in fluid dynamics and aero-elasticity, electromechanical applications or elasto-plastic problems. A more detailed overview of the POD and its history can be found in the literature [115].

One of the main drawbacks of this method is the need for training simulations performed with the high fidelity model. In some applications, the simulation of the full finite element model required to build the matrix of snapshots is not feasible or requires high computational capabilities. Moreover, this method is very dependent on the initial simulation performed to build the snapshots matrix, since the states that are not triggered by the initial simulation are not included in the reduction basis and cannot be represented. In particular, the proper orthogonal decomposition method is very sensitive to the excitation used in the training simulation.

4.3.2.2 Smooth orthogonal decomposition

Keeping in mind the drawbacks of the POD, Chelidze and Zhou proposed a variant of the POD which allows to build a more robust, *i.e* less sensitive to the initial training simulation, reduced-order model called the Smooth Orthogonal Decomposition (SOD) [47]. The so-called smooth orthogonal method consists in finding the basis $\mathbf{\Lambda}$ such that the projection of the data matrix $\mathbf{U}^\star$ onto $\mathbf{\Lambda}$ has maximal spatial variance and minimal time roughness, *i.e.* solving the problem

$$\max \|\mathbf{U}^\star \mathbf{\Lambda}\|^2 \quad \text{subject to} \quad \min \|\mathbf{V}^\star \mathbf{\Lambda}\|^2, \tag{4.36}$$

where $\mathbf{V}^\star$ are the velocity snapshots from the training simulation.

The solution of the SOD problem can be obtained by solving the generalized eigenvalue problem

$$\mathbf{\Sigma}_{vv} \boldsymbol{\lambda}_k = \lambda_k \mathbf{\Sigma}_{uu} \boldsymbol{\lambda}_k, \tag{4.37}$$

where $\mathbf{\Sigma}_{vv}$ is the autocovariance matrix of the velocity matrix $\mathbf{V}^\star$. The λ_k are the smooth orthogonal values (SOVs) and the $\boldsymbol{\lambda}_k$ are the smooth projection modes (SPMs). Smooth orthogonal modes (SOMs) are defined as the columns of

$$\mathbf{\Phi} = \mathbf{\Lambda}^{-\mathrm{T}}, \tag{4.38}$$

where $\mathbf{\Lambda}$ contains the SPMs. The reduction basis of the SOD reduction method therefore consists in the first SOMs corresponding to the smallest SOVs.

4.3.2.3 ROM compatible with contact

In their general formulations, the POD and SOD methods do not allow to retain physical degrees-of-freedom in the reduced space and are therefore not suitable for the implementation of contact. In order to ease the implementation of contact interfaces, it is proposed in this

work to adapt these reduction methods by defining the projection basis $\boldsymbol{\Phi}$ as a combination of constraint modes and POMs/SOMs.

The constraint modes $\boldsymbol{\Psi}$ correspond to the linear static deformation of the structure to unitary displacement at the boundary degrees-of-freedom, as in the Craig-Bampton reduction method. They are defined by (4.26) and computed using (4.27). The POMs/SOMs are computed in the same way as described previously. According to the degrees-of-freedom partitioning, they write

$$\boldsymbol{\Phi}_s = \begin{bmatrix} \boldsymbol{\Phi}_{s,i} \\ \boldsymbol{\Phi}_{s,b} \end{bmatrix}. \tag{4.39}$$

The interface component of the POD/SOD basis is not zero since the interface is not fixed. Since the interface motion is already fully represented by the constraint modes, the POD/SOD vectors are turned into fixed interface modes by subtracting the component already present in the constraint modes

$$\begin{bmatrix} \boldsymbol{\Phi}^{\text{POD/SOD}} \\ \mathbf{0} \end{bmatrix} = \begin{bmatrix} \boldsymbol{\Phi}_{s,i} \\ \boldsymbol{\Phi}_{s,b} \end{bmatrix} - \begin{bmatrix} \boldsymbol{\Psi}_i \\ \mathbf{I} \end{bmatrix} \boldsymbol{\Phi}_{s,b}. \tag{4.40}$$

The reduction basis is therefore composed of r_b constraint modes and $r_{\text{POD/SOD}}$ POD/SOD modes and write

$$\boldsymbol{\Phi} = \begin{bmatrix} \boldsymbol{\Psi}_i & \boldsymbol{\Phi}^{\text{POD/SOD}} \\ \mathbf{I} & \mathbf{0} \end{bmatrix}. \tag{4.41}$$

Example 4.2 – Proper orthogonal decomposition

The reduction by proper orthogonal decomposition compatible with contact proposed in this work is combined with the STEP and applied to the clamped-clamped beam. The snapshots are obtained by computing the dynamic response of the beam to a harmonic excitation of amplitude $A_t = 200$ N and frequency $f_t = 160$ Hz applied at P_1 in the transverse direction. The two dominant POD modes shown in Fig. 4.4 are included in the reduction basis.

The nonlinear frequency response curve obtained with this reduced-order model is shown in Fig. 4.5. A good match with the reference solution is obtained. It is remarkable that the axial displacement of the first POD mode extracted with the singular value decomposition is very close to the actual axial displacement of the beam (see Fig. 2.5b).

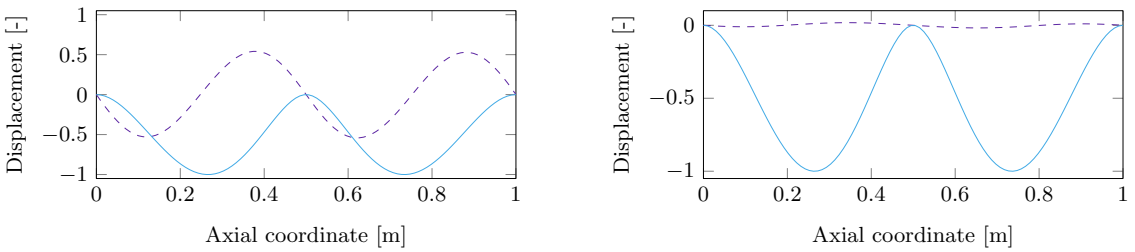

(a) POD mode 1.

(b) POD mode 2.

FIGURE 4.4 – POD modes of the clamped-clamped beam: transverse displacement (——) and axial displacement multiplied by 100 (- - - -).

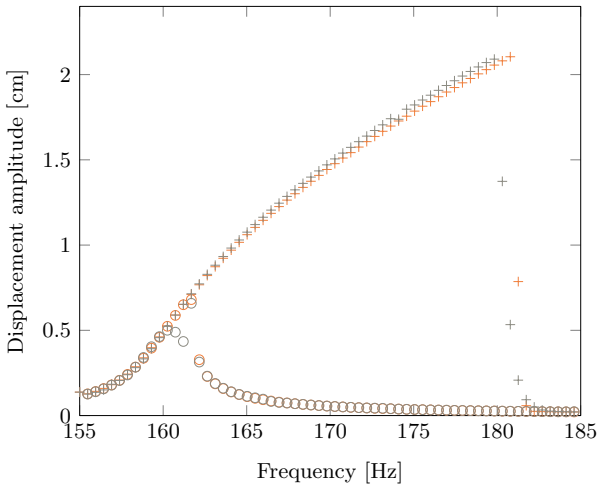

FIGURE 4.5 – Nonlinear frequency response curves (upward (+) and downward (○) frequency sweeps): reference solution (+/○) and solution obtained with POD ROM (+/○).

4.3.3 Linear reduction basis with POD correction

As explained in section 4.3.1 and illustrated on a simple test case, linear reduction bases composed of LNM or Craig-Bampton modes can prove ill-suited to the study of nonlinear systems when a large number of degrees-of-freedom are impacted by strong nonlinearities because of the lack of representativeness of the reduction basis.

It is possible to correct the evaluation of nonlinear internal forces based, for instance, on a POD filtering approach [13]. In practice, the nonlinear forces are collected from a given number of snapshots that represent a set of characteristic displacements in the response

$\mathbf{u}_1^\star$, ..., $\mathbf{u}_m^\star$,

$$\mathbf{G}_{\text{nl}}^\star = \left[\mathbf{g}_{\text{nl}}(\mathbf{u}_1^\star) \quad \mathbf{g}_{\text{nl}}(\mathbf{u}_2^\star) \quad \cdots \quad \mathbf{g}_{\text{nl}}(\mathbf{u}_m^\star)\right]. \tag{4.42}$$

The nonlinear basis $\mathbf{\Phi}_f$ used for the filtering is obtained by implementing the SVD of matrix $\mathbf{G}_{\text{nl}}^\star$. The nonlinear basis consists in the truncation to r_f modes in the resulting left singular vectors of the SVD basis. The nonlinear forces in the full-order model are then filtered with this basis $\mathbf{\Phi}_f$ as

$$\mathbf{g}_{\text{nl}}^f(\mathbf{u}) = \mathbf{\Phi}_f \mathbf{\Phi}_f^{\text{T}} \mathbf{g}_{\text{nl}}(\mathbf{u}) \tag{4.43}$$

and the resulting filtered forces $\mathbf{g}_{\text{nl}}^f(\mathbf{u})$ are used as an input to the STEP method instead of the exact nonlinear forces $\mathbf{g}_{\text{nl}}(\mathbf{u})$.

Example 4.3 – Craig-Bampton with POD correction

A Craig-Bampton reduction basis with one constraint mode and two fixed interface linear normal modes is built. As shown in section 4.3.1, this reduction basis does not allow to capture the nonlinear resonance. The NFRC obtained without and with POD correction are compared in Fig. 4.6. The reduction basis is the same in both cases and only composed of purely transverse modes: it does not allow to represent axial displacement. However, the POD correction allows to improve the results.

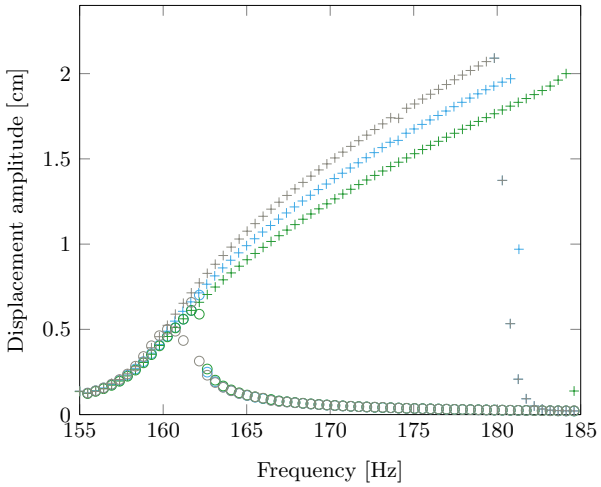

FIGURE 4.6 – Nonlinear frequency response curves (upward (+) and downward (○) frequency sweeps): reference solution (+/○) and solutions obtained with Craig-Bampton ROM with fixed interface LNM 1 and 2 without POD correction (+/○) and with POD correction (+/○).

4.3.4 Modal derivatives

The nonlinear reduction methods presented in sections 4.3.2 and 4.3.3 highly depend on the training simulations performed to define the singular value decomposition problems. The different drawbacks associated with simulation-dependent reduction methods, *i.e.* reduction methods that require the time integration of the full-order equation of motion, motivate the development of simulation-free reduction methods. The enhancement of linear bases with modal derivatives, which capture the nonlinear deflections by an asymptotic expansion of the displacement in the direction of the retained linear modes, was first identified by Idelsohn and Cardona as an efficient way of accounting for the nonlinear behavior of the structures in a reduced space [97]. The method was then studied by different authors, with the development of different strategies to compute these modal derivatives [57, 202, 217], and applied to various academic and industrial structures with geometric nonlinearities [109, 143]. This reduction approach was also extended to CMS techniques [235, 237, 242]. The reduction method with modal derivatives has also proven to be efficient to study structures in the frequency domain [234] and compute the nonlinear normal modes [205].

4.3.4.1 Linear normal modes and modal derivatives

As shown in section 4.3.1.1, the projection of the governing equations onto a reduction basis formed by a reduced set of vibration modes is a well-known technique in linear structural dynamics. The main limitation of the different approaches used to extend the vibration mode projection methods to nonlinear analyses resides in the fact that the vibration basis changes as the configuration of the system changes. When the displacements cannot be considered as small, the displacement $\mathbf{u}$ can be expressed as a linear combination of r_{LNM} instantaneous vibration modes of the structure by

$$\mathbf{u} = \sum_{j=1}^{r_{\text{LNM}}} \tilde{\boldsymbol{\phi}}_j(\mathbf{u})\eta_j, \tag{4.44}$$

where the coefficients η_j are the modal coordinates (combined in a vector $\boldsymbol{\eta}$) and the modes $\tilde{\boldsymbol{\phi}}_j$ are the solutions of

$$\left[\mathbf{K}_T(\mathbf{u}) - \omega_j^2\mathbf{M}\right]\tilde{\boldsymbol{\phi}}_j(\mathbf{u}) = \mathbf{0}, \qquad j = 1, 2, \cdots, r_{\text{LNM}}, \tag{4.45}$$

where the tangent matrix $\mathbf{K}_T$ is defined by (4.23). Expanding $\mathbf{u}(\boldsymbol{\eta})$ in Taylor series around the equilibrium position $\boldsymbol{\eta} = \mathbf{0}$ gives

$$\mathbf{u} = \sum_{j=1}^{r_{\mathrm{LNM}}} \left.\frac{\partial \mathbf{u}}{\partial \eta_j}\right|_{\boldsymbol{\eta}=\mathbf{0}} \eta_j + \frac{1}{2} \sum_{j=1}^{r_{\mathrm{LNM}}} \sum_{k=1}^{r_{\mathrm{LNM}}} \left.\frac{\partial^2 \mathbf{u}}{\partial \eta_j \partial \eta_k}\right|_{\boldsymbol{\eta}=\mathbf{0}} \eta_j \eta_k + \cdots . \tag{4.46}$$

The derivatives of the displacement vector with respect to the modal amplitudes η_j can be computed from (4.44) and are given by

$$\frac{\partial \mathbf{u}}{\partial \eta_j} = \tilde{\boldsymbol{\phi}}_j(\mathbf{u}) + \sum_{k=1}^{r_{\mathrm{LNM}}} \frac{\partial \tilde{\boldsymbol{\phi}}_k}{\partial \eta_j} \eta_k. \tag{4.47}$$

Evaluating this expression at the static equilibrium yields

$$\left.\frac{\partial \mathbf{u}}{\partial \eta_j}\right|_{\boldsymbol{\eta}=\mathbf{0}} = \tilde{\boldsymbol{\phi}}_j(\mathbf{0}) = \hat{\boldsymbol{\phi}}_j. \tag{4.48}$$

These derivatives correspond to the linear vibration modes $\hat{\boldsymbol{\phi}}_j$ defined by (4.24). The second order derivatives of the displacement vector with respect to the modal amplitudes are given by

$$\frac{\partial^2 \mathbf{u}}{\partial \eta_j \partial \eta_k} = \frac{\partial \tilde{\boldsymbol{\phi}}_j}{\partial \eta_k} + \frac{\partial \tilde{\boldsymbol{\phi}}_k}{\partial \eta_j} + \sum_{l=1}^{r_{\mathrm{LNM}}} \frac{\partial^2 \tilde{\boldsymbol{\phi}}_l}{\partial \eta_j \partial \eta_k} \eta_l. \tag{4.49}$$

Evaluating this expression at the static equilibrium yields

$$\left.\frac{\partial^2 \mathbf{u}}{\partial \eta_j \partial \eta_k}\right|_{\boldsymbol{\eta}=\mathbf{0}} = \left.\frac{\partial \tilde{\boldsymbol{\phi}}_j}{\partial \eta_k}\right|_{\boldsymbol{\eta}=\mathbf{0}} + \left.\frac{\partial \tilde{\boldsymbol{\phi}}_k}{\partial \eta_j}\right|_{\boldsymbol{\eta}=\mathbf{0}}. \tag{4.50}$$

Injecting (4.48) and (4.50) in (4.46) and neglecting the higher-order terms gives

$$\mathbf{u} = \sum_{j=1}^{r_{\mathrm{LNM}}} \hat{\boldsymbol{\phi}}_j \eta_j + \frac{1}{2} \sum_{j=1}^{r_{\mathrm{LNM}}} \sum_{k=1}^{r_{\mathrm{LNM}}} \left[\left.\frac{\partial \tilde{\boldsymbol{\phi}}_j}{\partial \eta_k}\right|_{\boldsymbol{\eta}=\mathbf{0}} + \left.\frac{\partial \tilde{\boldsymbol{\phi}}_k}{\partial \eta_j}\right|_{\boldsymbol{\eta}=\mathbf{0}} \right] \eta_j \eta_k. \tag{4.51}$$

The derivatives

$$\boldsymbol{\xi}_{jk} = \left.\frac{\partial \tilde{\boldsymbol{\phi}}_j}{\partial \eta_k}\right|_{\boldsymbol{\eta}=\mathbf{0}} \tag{4.52}$$

are called the modal derivatives. They represent how vibration modes change when the system is perturbed in the shape of a vibration mode. Slaats *et al.* presented three approaches to compute these modal derivatives [202]. The most commun way to compute the modal derivatives $\boldsymbol{\xi}_{jk}$ is to differentiate the eigenvalue problem (4.45) with respect to the modal

amplitudes η_k

$$\left[\mathbf{K}_T(\mathbf{u}) - \omega_j^2 \mathbf{M}\right] \frac{\partial \tilde{\boldsymbol{\phi}}_j}{\partial \eta_k} + \left[\frac{\partial \mathbf{K}_T}{\partial \eta_k} - \frac{\partial \omega_j^2}{\partial \eta_k}\mathbf{M}\right] \tilde{\boldsymbol{\phi}}_j(\mathbf{u}) = \mathbf{0}. \tag{4.53}$$

It has been shown that the terms associated to the mass can be neglected [97, 202]. By doing so, the problem becomes

$$\mathbf{K}_T(\mathbf{u}) \frac{\partial \tilde{\boldsymbol{\phi}}_j}{\partial \eta_k} = -\frac{\partial \mathbf{K}_T}{\partial \eta_k} \tilde{\boldsymbol{\phi}}_j(\mathbf{u}). \tag{4.54}$$

Evaluating this expression at the static equilibrium, the modal derivatives are therefore computed by solving the linear systems

$$\mathbf{K}\boldsymbol{\xi}_{jk} = -\left.\frac{\partial \mathbf{K}_T}{\partial \eta_k}\right|_{\boldsymbol{\eta}=\mathbf{0}} \hat{\boldsymbol{\phi}}_j. \tag{4.55}$$

In the case where the finite element package provides the tangent stiffness matrix, the derivative of the tangent stiffness matrix can be computed by finite differences as

$$\left.\frac{\partial \mathbf{K}_T}{\partial \eta_k}\right|_{\boldsymbol{\eta}=\mathbf{0}} = \frac{\mathbf{K}_T\left(\epsilon_k \hat{\boldsymbol{\phi}}_k\right) - \mathbf{K}}{\epsilon_k}, \tag{4.56}$$

where the coefficients ϵ_k should be carefully defined. These derivatives can also be evaluated using central finite differences as

$$\left.\frac{\partial \mathbf{K}_T}{\partial \eta_k}\right|_{\boldsymbol{\eta}=\mathbf{0}} = \frac{\mathbf{K}_T\left(\epsilon_k \hat{\boldsymbol{\phi}}_k\right) - \mathbf{K}_T\left(-\epsilon_k \hat{\boldsymbol{\phi}}_k\right)}{2\epsilon_k}. \tag{4.57}$$

This can modify the shape of the modal derivatives but does not seem to influence the results of the dynamic simulations performed with the reduced-order model [142]. However, this differentiation scheme requires twice more evaluations of the stiffness matrix. The right-hand side of Eq. (4.55) can also be written in terms of the second derivative of the nonlinear internal forces, which can be useful to evaluate the modal derivatives in the case where the finite element package only outputs the reaction forces due to nonlinear static displacements [109].

It can be shown that static modal derivatives, computed by neglecting the inertia terms as in (4.54), are symmetric [235], *i.e.*

$$\boldsymbol{\xi}_{jk} = \boldsymbol{\xi}_{kj}. \tag{4.58}$$

According to (4.51), the displacement field $\mathbf{u}$ is written as a combination of linear normal modes and modal derivatives. This expression of the displacement has led to studies on quadratic manifolds for the reduced-order modeling of nonlinear structures [99, 188]. Here,

the quadratic terms $\eta_i\eta_j$ are considered as linear generalized coordinates combined in vector $\boldsymbol{\eta}_{\text{MD}}$. The associate reduction writes

$$\mathbf{u} = \boldsymbol{\Phi}\mathbf{q} = \begin{bmatrix} \hat{\boldsymbol{\Phi}} & \boldsymbol{\Xi} \end{bmatrix} \begin{bmatrix} \boldsymbol{\eta} \\ \boldsymbol{\eta}_{\text{MD}} \end{bmatrix}, \tag{4.59}$$

where the reduction basis $\boldsymbol{\Phi}$ includes a selection of r_{LNM} vibration modes at equilibrium (defined by (4.24) and combined in $\hat{\boldsymbol{\Phi}}$) and the corresponding $r_{\text{LNM}}(r_{\text{LNM}}+1)/2$ modal derivatives (defined by (4.52) and combined in $\boldsymbol{\Xi}$).

4.3.4.2 Craig Bampton modes and modal derivatives

The reduction method based on linear vibration modes and their modal derivatives does not allow to keep physical degrees-of-freedom in the reduced space. One way to fix this issue is to use modal derivatives in combination with the Craig-Bampton reduction basis [243].

As in (4.44), the displacement $\mathbf{u}$ is written as

$$\mathbf{u} = \sum_{j=1}^{r_b+r_c} \breve{\boldsymbol{\phi}}_j(\mathbf{u})\bar{\eta}_j, \tag{4.60}$$

where the generalized coordinates $\bar{\eta}_j$ are composed of the boundary interface degrees-of-freedom $\mathbf{u}_b$ and the modal coordinates $\boldsymbol{\eta}_c$ (see section 4.3.1.2) and where $\breve{\boldsymbol{\phi}}_j$ stands for the j^{th} mode of the reduction basis $\breve{\boldsymbol{\Phi}}(\mathbf{u})$, denoting the $r_b + r_c$ Craig-Bampton modes computed at a certain level of deformation $\mathbf{u}$. In practice, the modes $\breve{\boldsymbol{\Phi}}(\mathbf{u})$ are computed in the same way as the modes $\boldsymbol{\Psi}$ and $\boldsymbol{\Theta}$ in (4.26) and (4.29) by using the tangent stiffness matrix $\mathbf{K}_T(\mathbf{u})$ instead of the stiffness matrix $\mathbf{K}$ in (4.27) and (4.30).

As in (4.46), the displacement $\mathbf{u}$ can be expanded in Taylor series around the equilibrium position $\bar{\boldsymbol{\eta}} = \mathbf{0}$ as

$$\mathbf{u} = \sum_{j=1}^{r_b+r_c} \left.\frac{\partial \mathbf{u}}{\partial \bar{\eta}_j}\right|_{\bar{\boldsymbol{\eta}}=\mathbf{0}} \bar{\eta}_j + \frac{1}{2}\sum_{j=1}^{r_b+r_c}\sum_{k=1}^{r_b+r_c} \left.\frac{\partial^2 \mathbf{u}}{\partial \bar{\eta}_j \partial \bar{\eta}_k}\right|_{\bar{\boldsymbol{\eta}}=\mathbf{0}} \bar{\eta}_j\bar{\eta}_k + \cdots . \tag{4.61}$$

The derivatives of the displacement vector with respect to the modal amplitudes $\bar{\eta}_j$ can be computed from (4.60) and are given by

$$\left.\frac{\partial \mathbf{u}}{\partial \bar{\eta}_j}\right|_{\bar{\boldsymbol{\eta}}=\mathbf{0}} = \breve{\boldsymbol{\phi}}_j(\mathbf{0}). \tag{4.62}$$

These derivatives correspond to the linear Craig-Bampton modes. The second order deriva-

tives of the displacement vector are defined as the modal derivatives

$$\bar{\boldsymbol{\zeta}}_{jk} = \left.\frac{\partial^2 \mathbf{u}}{\partial \bar{\eta}_j \partial \bar{\eta}_k}\right|_{\bar{\boldsymbol{\eta}}=\mathbf{0}} \qquad j,\, k = 1, \cdots, r_b + r_c. \tag{4.63}$$

The expression of the modal derivatives is here derived from the static problem [243]

$$\mathbf{K}\mathbf{u} + \mathbf{g}_{\mathrm{nl}}(\mathbf{u}) = \mathbf{f}_e, \tag{4.64}$$

where the imposed static load writes

$$\mathbf{f}_e = \mathbf{K} \sum_{j=1}^{r_b+r_c} \breve{\boldsymbol{\phi}}_j(\mathbf{0}) \bar{\eta}_j. \tag{4.65}$$

Differentiating two times Eq. (4.64) with respect to the generalized coordinates yields

$$\frac{\partial \mathbf{K}_T}{\partial \bar{\eta}_k} \frac{\partial \mathbf{u}}{\partial \bar{\eta}_j} + \mathbf{K}_T \frac{\partial^2 \mathbf{u}}{\partial \bar{\eta}_j \partial \bar{\eta}_k} = \mathbf{0}. \tag{4.66}$$

Evaluating this expression at the static equilibrium, the modal derivatives are therefore computed by solving the linear systems

$$\mathbf{K}\bar{\boldsymbol{\zeta}}_{jk} = -\left.\frac{\partial \mathbf{K}_T}{\partial \bar{\eta}_k}\right|_{\bar{\boldsymbol{\eta}}=\mathbf{0}} \breve{\boldsymbol{\phi}}_j(\mathbf{0}). \tag{4.67}$$

Considering the partitioning generally adopted for the Craig-Bampton method, the modal derivatives can be expressed as

$$\bar{\boldsymbol{\zeta}}_{jk} = \begin{bmatrix} \bar{\boldsymbol{\zeta}}_{jk,i} \\ \bar{\boldsymbol{\zeta}}_{jk,b} \end{bmatrix}. \tag{4.68}$$

The interface component of the modal derivatives $\bar{\boldsymbol{\zeta}}_{jk,b}$ is not zero since the interface is not fixed. Since the interface motion is already fully represented by the constraint modes, the modal derivatives are turned into fixed interface modes by subtracting the component already present in the constraint modes

$$\begin{bmatrix} \boldsymbol{\zeta}_{jk} \\ \mathbf{0} \end{bmatrix} = \begin{bmatrix} \bar{\boldsymbol{\zeta}}_{jk,i} \\ \bar{\boldsymbol{\zeta}}_{jk,b} \end{bmatrix} - \begin{bmatrix} \boldsymbol{\Psi}_i \\ \mathbf{I} \end{bmatrix} \bar{\boldsymbol{\zeta}}_{jk,b}. \tag{4.69}$$

It can be shown that modal derivatives are symmetric [235], *i.e.*

$$\boldsymbol{\zeta}_{jk} = \boldsymbol{\zeta}_{kj}. \tag{4.70}$$

The augmented Craig-Bampton reduction basis $\mathbf{\Phi}$ and the associated reduction technique write

$$\mathbf{u} = \mathbf{\Phi}\mathbf{q} = \begin{bmatrix} \mathbf{\Psi}_i & \mathbf{\Theta}_{i,r_c} & \mathbf{Z} \\ \mathbf{I} & \mathbf{0} & \mathbf{0} \end{bmatrix} \begin{bmatrix} \mathbf{u}_b \\ \boldsymbol{\eta}_c \\ \boldsymbol{\eta}_{\mathrm{MD}} \end{bmatrix}, \tag{4.71}$$

where the modal derivatives $\boldsymbol{\zeta}_{jk}$ are combined in $\mathbf{Z}$ and $\boldsymbol{\eta}_{\mathrm{MD}}$ are the associated new generalized coordinates. The reduction basis is therefore constructed with r_b constraint modes, r_c selected internal vibration modes and the corresponding $(r_b + r_c)(r_b + r_c + 1)/2$ modal derivatives.

Example 4.4 – Modal derivatives

The modal derivative approach is used to reduce the clamped-clamped beam. The Craig-Bampton reduction basis composed of one static mode and two transverse fixed interface LNM (see Fig. 4.2) is enriched with the modal derivative of the static mode with respect to itself shown in Fig. 4.7. The axial component of this modal derivative has the shape of a fourth membrane mode and is very close to the actual displacement predicted at the nonlinear resonance with the full-order model (see Fig. 2.5b).

The nonlinear frequency response curve obtained is shown in Fig. 4.8. This reduced-order model allows to accurately predict the nonlinear resonance.

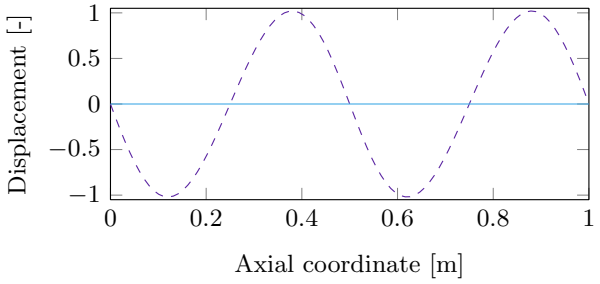

FIGURE 4.7 – Modal derivative of the constraint mode with respect to itself for the clamped-clamped beam: transverse displacement (——) and axial displacement (- - - -).

In this simple example, the Craig-Bampton basis is composed of 3 linear modes so that 6 modal derivatives can be computed. Based on our knowledge of the system, the modal derivative the closest to a fourth membrane mode has been selected. In practice, for more complex industrial structures, it is not possible to select *a priori*

the modal derivatives to include in the reduction basis by hand. Modal derivatives selection criteria are therefore required. This is the subject of the next section.

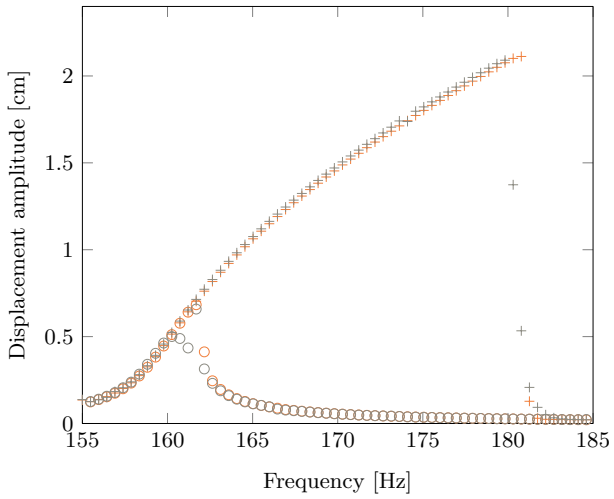

FIGURE 4.8 – Nonlinear frequency response curves (upward (+) and downward (○) frequency sweeps): reference solution (+/○) and solution obtained with the modal derivative ROM (+/○).

4.3.4.3 Selection of modal derivatives

The size of the reduction basis increases quadratically with the number of Craig-Bampton modes. It is however expected that only a few modal derivatives are necessary to capture the nonlinear behavior of the structure [217]. In order to limit the size of the reduction basis, it is necessary to define a selection criterion that allows to determine *a priori* which modal derivatives should be included in the reduction basis to achieve accurate results.

Different selection procedures are described in the literature but they are often limited to the selection of modal derivatives of linear normal modes, and not of Craig-Bampton modes. As orthogonality properties of linear normal modes do not hold for Craig-Bampton modes, these selection criteria have to be adapted. Three selection criteria are presented here. They all consist in associating a weight W_{jk} to each modal derivative $\boldsymbol{\zeta}_{jk}$ and selecting the best modal derivative subset based on the magnitude of these weights, the highest values of the weight corresponding to the most relevant modal derivatives. The selection methods are purely heuristic methods that differ by the definition of the weight. The choice of the number of modal derivatives to include in the reduction basis will be discussed further, when presenting the results on an industrial model (see section 5.4.3).

Maximum Modal Interaction (MMI) The first approach is adapted from the works of Tiso [217]. The linear response $\mathbf{u}(t)$ of the system to a given external loading is computed with the full-order finite element model by solving Eq. (2.3) where the nonlinear terms are neglected ($\mathbf{g}_{\text{nl}}(\mathbf{u}) = \mathbf{0}$ and $\mathbf{f}_c(\mathbf{u}, \dot{\mathbf{u}}) = \mathbf{0}$). The response is expressed in the Craig-Bampton reduced space through Eq. (4.1), where $\mathbf{\Phi}$ is the linear Craig-Bampton basis. Assuming that the contribution of the modal derivatives is of second order, their mutual relevance can be assessed by

$$W_{jk}^{(1)} = |\boldsymbol{\phi}_j| \max(|q_j(t)|) \cdot |\boldsymbol{\phi}_k| \max(|q_k(t)|). \tag{4.72}$$

The actual interaction between the modes is not quantified. It is only assumed that two Craig-Bampton modes that contribute significantly to the reduced solution are likely to interact a lot.

Modal Interaction (MI) Going one step further, Jain *et al.* proposed to consider the complete interaction between the linear modes in the simulation of duration T [99]. The weights are defined as

$$W_{jk}^{(2a)} = \int_0^T |q_j(t) q_k(t)| dt, \tag{4.73}$$

with mass-normalized modes. Alternatively, the weights can also be defined as

$$W_{jk}^{(2b)} = |\boldsymbol{\phi}_j^{\text{T}} \boldsymbol{\phi}_k| \int_0^T |q_j(t) q_k(t)| dt, \tag{4.74}$$

with no assumption on the modes normalization.

Symmetric Modal Virtual Work (SMVW) In this criterion, weights are assigned to modal derivatives according to the virtual work done by the nonlinear linear elastic forces arising from one linear mode upon another mode. This criterion has been introduced by Jain *et al.* [99] and later adapted for static modal derivatives, *i.e.* obtained by neglecting the inertial contribution as it is done here [187]. The criterion is used here with Craig-Bampton modes. As above, a linear simulation allows to compute the time varying amplitude of each linear generalized coordinate. For each pair of modes, the time $t_{jk}^{\max}$ is determined by

$$t_{jk}^{\max} = \arg\max \left[q_j(t) q_k(t) \right]^2. \tag{4.75}$$

The virtual work of mode pair $\boldsymbol{\phi}_j$ and $\boldsymbol{\phi}_k$ is defined in a symmetric way as

$$W_{jk}^{(3)} = \sqrt{\left[\boldsymbol{\phi}_k^{\text{T}} \mathbf{g}_{\text{nl}} \left(\boldsymbol{\phi}_j q_j(t_{jk}^{\max}) \right) \right]^2 + \left[\boldsymbol{\phi}_j^{\text{T}} \mathbf{g}_{\text{nl}} \left(\boldsymbol{\phi}_k q_k(t_{jk}^{\max}) \right) \right]^2}. \tag{4.76}$$

Example 4.5 – Selection of modal derivatives

As shown in example 4.4, for simple academic models, the modal derivatives can be selected based on our knowledge of the system. For the specific case of the clamped-clamped beam with a Craig-Bampton basis composed of one static mode (SM) and two fixed interface linear normal modes (or internal modes – IM), the modal derivative of the static mode with respect to itself was added in the reduction basis. It could be interesting to check that the selection criteria presented above lead to the same conclusion.

The weights computed with each criterion for each modal derivative are shown in Fig. 4.9. A logarithmic scale is used for the weights to better show the relative contributions of the modes. In the four cases, the modal derivative of the static mode with respect to itself is indeed characterized by the highest weight.

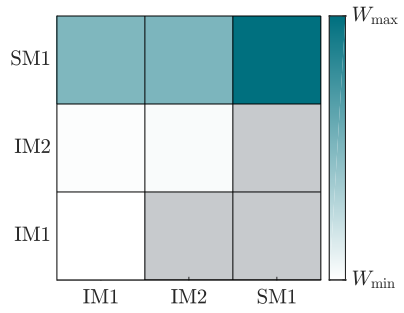

(a) Selection criterion 1.

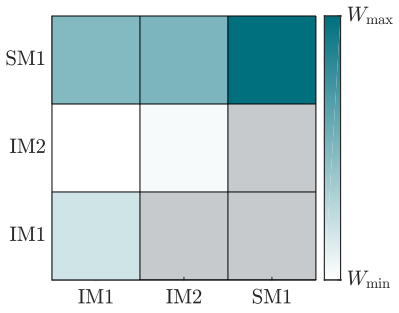

(b) Selection criterion 2a.

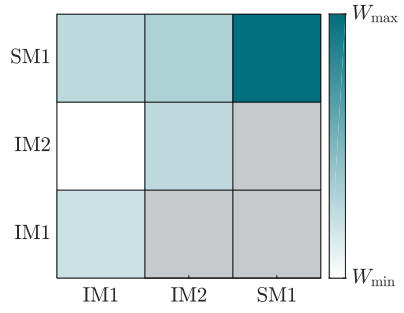

(c) Selection criterion 2b.

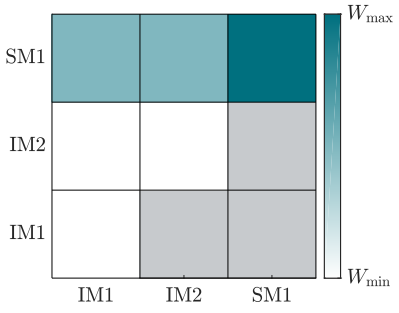

(d) Selection criterion 3.

FIGURE 4.9 – Weights associated to each modal derivative (logarithmic scale).

4.3.5 Nonlinear normal modes-based reduction methods

Nonlinear complex modes (defined in section 2.4) are interesting candidates in devising new effective and efficient approaches to reduce nonlinear models as they are able to reflect strong nonlinear behavior. The works of Laxalde and Thouverez [129] and Krack *et al.* [123] were the first ones to show that nonlinear modes can be efficient in reduced-order modeling. Since these works, different reduction methods have been developed by Joannin *et al.* [102–104]. These methods have only been applied to structures with friction contact nonlinearities but it is expected that the versatility of nonlinear complex modes would also allow to tackle other types of nonlinearities such as geometric nonlinearities.

4.4 Partial conclusions

This non-exhaustive literature review focuses on the reduced-order modeling techniques of nonlinear structures by Galerkin projection. It shows that the different reduction methods differ by the choice of the reduction basis and how the geometrically nonlinear term is evaluated in the reduced space. Two families of methods have been identified: data-driven methods, which require training data obtained from simulations performed with the full-order model or from experimental measurements, and methods relying on intrinsic modal characteristics of the system. Some methods have been adapted to keep physical degrees-of-freedom in the reduced space and allow the implementation of contact in an efficient way.

The application of the reduction methods to an academic test case, a clamped-clamped beam, shows that they are good candidates for the reduction of geometrically nonlinear structures and already allows to highlight some of their limitations. It is legitimate to ask how these reduction methods perform for real 3D structures. In the following, the different reduction methods are applied to an industrial blade structure (see chapter 5). Their use in contact simulations is assessed in chapter 6 and their extension to cyclically symmetric structures is studied in chapter 7.

CHAPTER 5 SINGLE BLADE WITH GEOMETRIC NONLINEARITIES

The objective of this chapter is to develop a reduction methodology to study the dynamics of single rotating blades with geometric nonlinearities. Three reduction methods are selected as interesting candidates for the subsequent studies. The considered reduction methods are applied to an industrial test case subjected to harmonic excitations and the accuracy and versatility of the methods are assessed with a scalar performance indicator. The influence of the rotation speed of the blade on its dynamics is also studied by the means of parametric reduced-order models.

The results of this chapter have been partially presented at the conference ASME Turbo Expo 2020 [60].

5.1 Blade of interest

5.1.1 Open blade model description

The methodology is applied on an industrial blade model based on the NASA rotor 37. NASA rotor 37 is a transonic axial flow compressor stage with 36 blades (see Fig. 5.1). It was initially designed and tested at NASA's Lewis Research Center in the late 70's as part of aerodynamic research [154, 184]. NASA rotor 37 notably served as a benchmark to validate numerical methods and assess the performance of numerical solvers in the fields of computational fluid dynamics throughout the 1990s [65]. More recently, NASA rotor 37 has been used as a benchmark in structural dynamics, and more specifically for contact simulations [52, 153, 180]. Its open geometry easily allows methods validation and results reproducibility and comparison.

Rotor 37 is made of 200-grade maraging steel, a nickel alloy [184], with Young's modulus $E = 180$ GPa, Poisson's ratio $\nu = 0.3$, density $\rho = 8,000$ kg/m^3 and yield stress $\sigma_Y = 1.38$ GPa. The blade is 7 cm in height. The blade geometry is described with a finite element model composed of quadratic pentahedral elements. The discretized mesh of the blade is represented in Fig. 5.2. It counts $20,657$ nodes, *i.e.* $61,971$ degrees-of-freedom. The blade is clamped at its root. The first three eigenfrequencies of the blades are $f_1 = 839$ Hz, $f_2 = 2,508$ Hz and $f_3 = 3,035$ Hz (corresponding pulsations: $\omega_1 = 5,272$ rad/s, $\omega_2 = 15,760$ rad/s and $\omega_3 = 19,071$ rad/s). The three associated mode shapes are represented in Fig. 5.3. They correspond respectively to the first bending (1B), first torsion (1T) and second bending (2B) modes. The damping matrix $\mathbf{C}$ is computed in the modal domain. Modal damping

coefficients $\xi_{1-3} = 5 \cdot 10^{-4}$ for the first three modes and $\xi_{4+} = 5 \cdot 10^{-3}$ for the higher frequency modes are considered in the whole study in agreement with previous studies performed on the same structure [52].

FIGURE 5.1 – Picture of NASA rotor 37 [95].

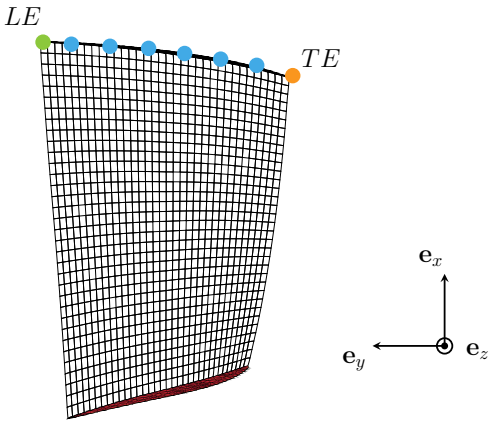

FIGURE 5.2 – Single blade of NASA rotor 37 with mesh used for the finite element simulations. The red surface (■) is clamped. The eight colored nodes are the blade-tip nodes retained for contact simulations. Among those nodes, the node TE is located at the trailing edge (●) and the node LE is located at the leading edge (●).

5.1.2 Geometric nonlinearities influence

Previous studies performed on the rotor 37 did not consider the influence of geometric nonlinearities [52, 153, 180]. In these studies, the dynamics of the structure is studied by solving

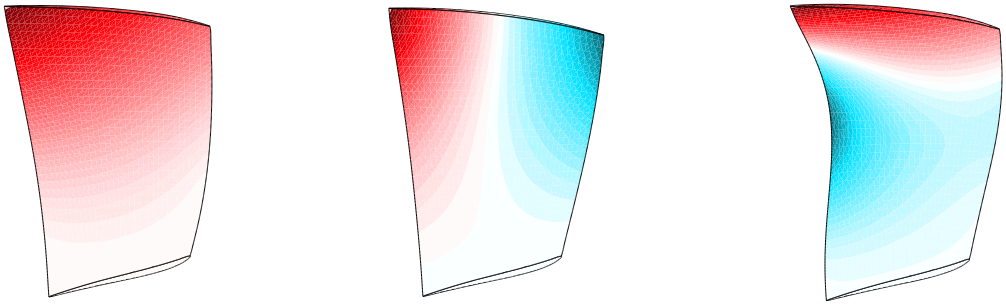

(a) Mode 1 (1B). (b) Mode 2 (1T). (c) Mode 3 (2B).

FIGURE 5.3 – First three free vibration modes of the NASA rotor 37 blade.

the equation of motion

$$\mathbf{M}\ddot{\mathbf{u}} + \mathbf{C}(\Omega)\dot{\mathbf{u}} + \mathbf{K}(\Omega, \mathbf{u}_s)\mathbf{u} = \mathbf{f}_e(t) + \mathbf{f}_c(\mathbf{u} + \mathbf{u}_s, \dot{\mathbf{u}}), \tag{5.1}$$

where the stiffness term is linearized, instead of Eq. (2.3).

However, numerical simulations performed on the finite element model of the rotor 37 blade show that geometric nonlinearities may affect significantly the response of the structure, even for small amplitudes of vibration. To illustrate this, the blade is excited at the leading edge (node LE in Fig. 5.2) in the $\mathbf{e}_y$ direction by a harmonic excitation of amplitude $A_e = 300$ N and pulsation $\omega_e = 2,000$ rad/s. The characteristics of this excitation are summarized in Table 5.1 (excitation E_1)[1]. Contact interactions are not considered, *i.e.* $\mathbf{f}_c(\mathbf{u}, \dot{\mathbf{u}}) = \mathbf{0}$ in (2.3).

	Amplitude [N]	*Pulsation [rad/s]*	*Number of excited nodes*	*Direction*
Excitation E_1	300	2,000	1	$\mathbf{e}_y$
Excitation E_2	300	4,000	1	$\mathbf{e}_y$
Excitation E_3	300	2,000	8	$\mathbf{e}_y$

TABLE 5.1 – Definition of the excitation cases.

The response of the blade to this excitation is computed in the previously studied linear context, *i.e.* by neglecting the geometric nonlinearities and solving Eq. (5.1), and in a nonlinear context, accounting for the geometric nonlinearities. As a first step, the effects of rotation are neglected, *i.e.* the structure is assumed to be at rest, with $\Omega = 0$. The time responses in the $\mathbf{e}_x$ direction at node LE are compared in Fig. 5.4 both in transient and

[1]The other excitation cases are used further.

steady-state regimes. Significant differences are observed between both signals. In particular, the nonlinear response has a much richer frequency content than the linear one. This is patent in Fig. 5.5 where the responses are compared in the frequency domain. For the transient linear solution, energy is only localized at the frequency of the excitation and at the frequencies of the excited mode shapes. For the transient nonlinear solution, harmonics and subharmonics of the excitation pulsation and eigenfrequencies are also excited. In steady-state regime, the linear response has only one harmonic component, as expected by linear theory, while some harmonics of the excitation pulsation are also excited in the nonlinear case.

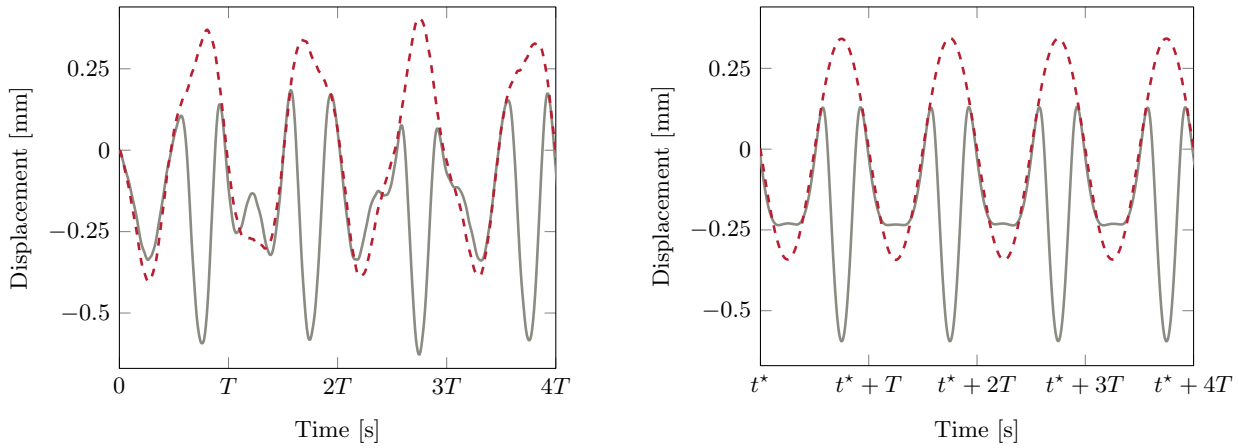

(a) Transient response.

(b) Steady-state response.

FIGURE 5.4 – Linear (- - - -) and nonlinear (——) responses of the blade at node LE in the $\mathbf{e}_x$ direction (time-domain) computed with the full-order finite element model (external excitation E_1).

This example shows that geometric nonlinearities may have a strong effect on the dynamics of the blade, even for displacement amplitudes smaller than 1 mm that could for instance be induced by contact interactions with the casing. It is therefore of considerable importance to be able to account for geometric nonlinearities in the reduced-order models used to predict contact interactions.

5.2 Reduction methods selection

As detailed in chapter 4, nonlinear projection-based reduced-order modeling techniques differ by the choice of the reduction basis and by the way the nonlinear forces are evaluated in the reduced space. Based on the state-of-the-art analysis in chapter 4, three model order

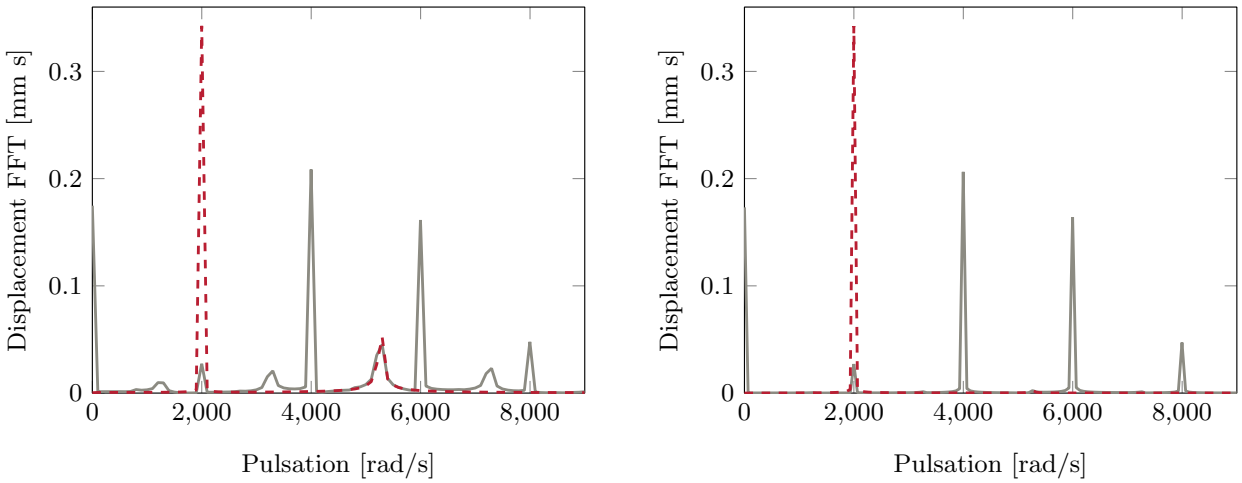

(a) Transient response.

(b) Steady-state response.

FIGURE 5.5 – Linear (- - - -) and nonlinear (——) responses of the blade at node LE in the $\mathbf{e}_x$ direction (frequency-domain) computed with the full-order finite element model (external excitation E_1).

reduction methods, characterized by different definitions of the reduction basis, are selected as interesting candidates.

The first reduction method is based on the POD (see section 4.3.2). The second reduction method is derived from the classical Craig-Bampton method with POD correction of the nonlinear forces (see section 4.3.3). The third reduction method uses the concept of modal derivatives (see section 4.3.4). These reduction methods are detailed in the next paragraphs. The reduction approaches based on nonlinear normal modes have not been retained in this work because the computation of these nonlinear modes is particularly costly for industrial structures with geometric nonlinearities. As shown in section 4.1.4, the three reduction methods are not restricted to simulations in the time domain but can be used in combination with frequency methods.

5.2.1 Proper orthogonal decomposition

The first reduction method is based on the POD introduced in section 4.3.2. More precisely, the modified version of the method, which allows to keep physical degrees-of-freedom in the reduced space, is used. The reduction basis $\mathbf{\Phi}$ is therefore defined by (4.41), combining r_{POD} fixed interface POD modes and r_b constraint modes. The nonlinear internal forces are evaluated in the reduced space with the STEP (see section 4.2).

5.2.2 Craig-Bampton with POD correction

In the second reduction method, the reduction basis is defined as the Craig-Bampton basis given by (4.25) and composed of r_c fixed interface linear normal modes and r_b constraint modes. The nonlinear internal forces are evaluated in the reduced space with the STEP with a filtering of the input nonlinear forces through a POD basis, as detailed in section 4.3.3.

5.2.3 Modal derivatives

In the third reduction method, the projection basis is defined as Craig-Bampton modes and a selection of their modal derivatives, as introduced in section 4.3.4. The reduction basis $\mathbf{\Phi}$ is given by (4.71) and composed of r_c fixed interface linear normal modes, r_b constraint modes and r_{MD} modal derivatives. The modal derivatives are selected with the selection criteria introduced in section 4.3.4, as shown below. The nonlinear internal forces are evaluated in the reduced space with the STEP.

5.3 Performance indicator definition

In order to assess the performance of the reduction methods and ease their comparison, a scalar performance indicator is defined. The indicator accounts for local and global comparison criteria. It can be computed for each reduction method and for each size of the reduced space.

The performance indicator I is defined is a weighted sum of N_c different criteria

$$I = \sum_{i=1}^{N_c} w_i e_i. \tag{5.2}$$

Each criterion e_i varies between 0 (worst case) and 1 (perfect agreement between the solutions obtained with the full- and reduced-order models). The sum of the weighting factors w_i equals 1. The relative magnitudes of the weighting factors reflect the relative influence of the different criteria in the performance indicator definition. The performance indicator therefore also ranges from 0 to 1, the higher the performance indicator, the better the reduction method.

Four criteria are selected in order to account for the global and local differences between the time solutions obtained with the full-order finite element model $\mathbf{u}^{\mathrm{FOM}}(t)$ and the reduced-order model $\mathbf{u}^{\mathrm{ROM}}(t) = \mathbf{\Phi}\,\mathbf{q}(t)$ [138].

- The first criterion is defined as the covariance criterion at maximal force amplitude

$$e_1 = \frac{\left[\mathbf{x}_1^{\mathrm{T}}\mathbf{x}_2\right]^2}{\left[\mathbf{x}_1^{\mathrm{T}}\mathbf{x}_1\right]\left[\mathbf{x}_2^{\mathrm{T}}\mathbf{x}_2\right]}, \tag{5.3}$$

where $\mathbf{x}_1 = \mathbf{u}^{\mathrm{FOM}}(t_{\max})$, $\mathbf{x}_2 = \mathbf{u}^{\mathrm{ROM}}(t_{\max})$ and $t_{\max}$ corresponds to the time when the excitation reaches its first maximal value.

- The second criterion is computed from the relative error on the energy (defined as the sum of the kinetic energy and the linear energy of deformation) and writes

$$e_2 = \max\left(0, 1 - \frac{\sqrt{\sum_t \left[\Delta\bar{E}(t)\right]^2}}{\sqrt{\sum_t \left[\bar{E}^{\mathrm{FOM}}(t)\right]^2}}\right), \tag{5.4}$$

where

$$\bar{E}(t) = \frac{1}{2}\dot{\mathbf{u}}(t)^{\mathrm{T}}\mathbf{M}\dot{\mathbf{u}}(t) + \frac{1}{2}\mathbf{u}(t)^{\mathrm{T}}\mathbf{K}\mathbf{u}(t) \tag{5.5}$$

and

$$\Delta\bar{E}(t) = \bar{E}^{\mathrm{FOM}}(t) - \bar{E}^{\mathrm{ROM}}(t). \tag{5.6}$$

- The third criterion is based on the relative oscillations deviation at blade-tip and is defined as

$$e_3 = \max\left(0, 1 - \sqrt{\frac{1}{3N_{\mathrm{tip}}}\sum_{i\in\mathrm{index}_{\mathrm{tip}}}\left(\frac{o_i^{\mathrm{FOM}} - o_i^{\mathrm{ROM}}}{o_i^{\mathrm{FOM}}}\right)^2}\right), \tag{5.7}$$

where N_{tip} is the number of nodes located at blade-tip, $\mathrm{index}_{\mathrm{tip}}$ stands for the indices corresponding to the degrees-of-freedom of these blade-tip nodes and

$$o_i = \max[\mathbf{u}_i(t)] - \min[\mathbf{u}_i(t)]. \tag{5.8}$$

- The fourth criterion evaluates the relative error on the displacement at the blade-tip nodes and is defined as

$$e_4 = \max\left(0, 1 - \frac{\sqrt{\sum_t \Delta\mathbf{u}_b(t)^{\mathrm{T}}\Delta\mathbf{u}_b(t)}}{\sqrt{\sum_t \mathbf{u}_b^{\mathrm{FOM}}(t)^{\mathrm{T}}\mathbf{u}_b^{\mathrm{FOM}}(t)}}\right), \tag{5.9}$$

where

$$\Delta\mathbf{u}_b(t) = \mathbf{u}_b^{\mathrm{FOM}}(t) - \mathbf{u}_b^{\mathrm{ROM}}(t). \tag{5.10}$$

Criteria e_1 and e_2 are global criteria: they allow to account for the differences in shape and in energy between the solutions obtained with the full-order and the reduced-order models over the entire blade. Criterion e_3 quantifies the error on the peak-to-peak amplitude of the oscillations at the blade-tip. Criterion e_4 quantifies the error on the amplitude of the displacement at the blade-tip nodes. Criteria e_3 and e_4 allow to account specifically for the local error at the tip. The local criteria are particularly important when considering contact simulations as contact will occur at blade-tip. The weighting factors are defined such that global factors (and therefore local factors) account for 50% ($w_1 = w_2 = w_3 = w_4 = 0.25$).

The computation time has voluntarily not been included in the performance indicator. As shown further, the quantity of interest, *i.e.* the online computation time required to integrate in time the equation of motion and re-project the response in the full-order space, is mainly related to the size r of the reduction basis and nearly independent of the reduction method. The computation time is the subject of a dedicated investigation in section 5.5.2.

5.4 Overview of reduction methods

The three reduction methods selected in section 5.2 are characterized by different parameters. Some parameters directly influence the size of the resulting reduced-order model while other parameters are internal to the methods. The influence of the latter is analyzed in this section, individually for each reduction method. In order to ease the analysis, the physical interface kept in the reduced space has only one node. The $r_b = 3$ degrees-of-freedom corresponding to the node LE at the blade-tip leading edge are kept in the reduced space. The different reduction methods are used to compute the nonlinear response of the structure to the harmonic excitation E_1 (see Table 5.1). The influence of the reduction basis size will be studied in section 5.5 when comparing the different reduction methods.

5.4.1 POD

The reduction method by POD is a data-driven method. The displacement snapshots used to build the basis are obtained by computing the nonlinear response of the blade to a training excitation with the full-order model during one period. As a first step, the training excitation is defined as the harmonic excitation E_1 in Table 5.1. A reduction basis composed of $r_b = 3$ static modes and $r_{\text{POD}} = 10$ POD modes is built. According to Eq. (4.34), these 10 POD modes capture 99.7% of the energy of the training data. The reduced-order model is used to compute the response to the external excitation E_1, *i.e.* the training excitation and the external excitation have the same characteristics. The results are shown in Fig. 5.6. An

excellent agreement between the solutions is observed, even after the first time period used in the training phase.

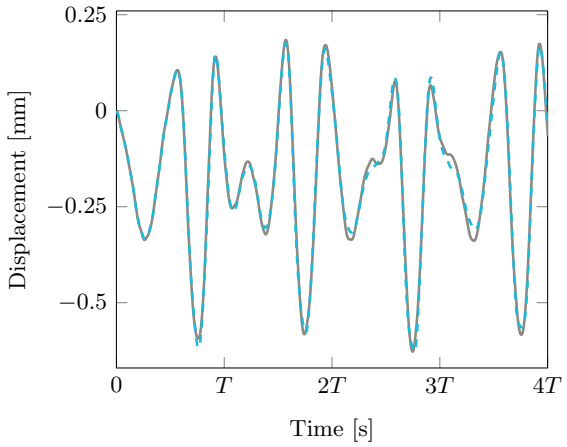

FIGURE 5.6 – Comparison of the reference solution (——) with the solution obtained with the POD method with training excitation E_1 (- - - -).

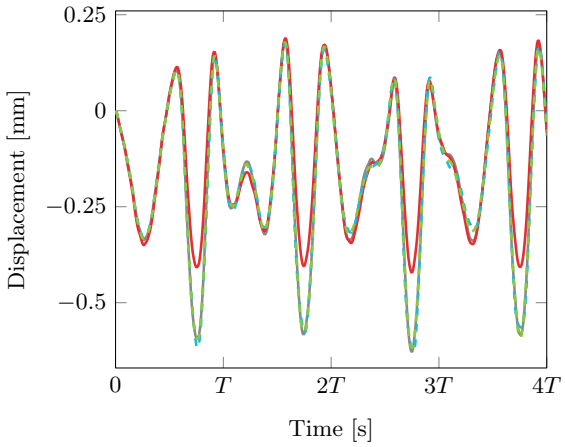

FIGURE 5.7 – Comparison of the reference solution (——) with the solutions obtained with the POD method: $A_t = 25$ N (——), $A_t = 300$ N (- - - -), $A_t = 500$ N (- - - -).

As mentioned above, one of the main drawbacks of the POD reduction method is the dependence of the reduced basis on the simulation training. Figures 5.7, 5.8 and 5.9 show the sensibility to changes in the simulation training, respectively to changes in amplitude of the training excitation, changes in pulsation of the training excitation and changes of excited degrees-of-freedom.

Figure 5.7 has been obtained by modifying the amplitude A_t of the training excitation, all other parameters keeping the same values as previously. It shows that changing the amplitude of the training excitation does not have a negative effect on the capacity of the reduced basis to represent the response of the structure, as long as the amplitude is sufficient to excite the nonlinearities of the structure. Figure 5.8 suggests that the pulsation of the training excitation ω_t has also little influence on the results as long as it mainly excites the first mode of the structure. Figure 5.9 has been obtained by modifying the number of nodes N_t on which the external excitation is applied in the training excitation. The excited nodes are located at the tip (colored nodes in Fig. 5.2, counted from the node LE). The figure shows that the spatial shape of the excitation has an influence on the results. The more the spatial shape of the training excitation differs from the external excitation applied, the worst the results become.

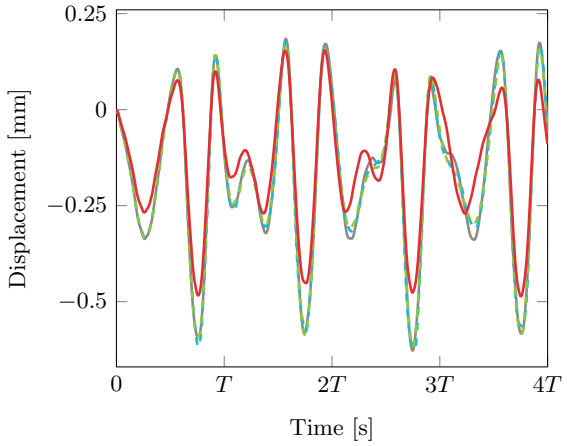

FIGURE 5.8 – Comparison of the reference solution (——) with the solutions obtained with the POD method: $\omega_t = 1,000$ rad/s (- - - -), $\omega_t = 2,000$ rad/s (- - - -), $\omega_t = 10^4$ rad/s (——).

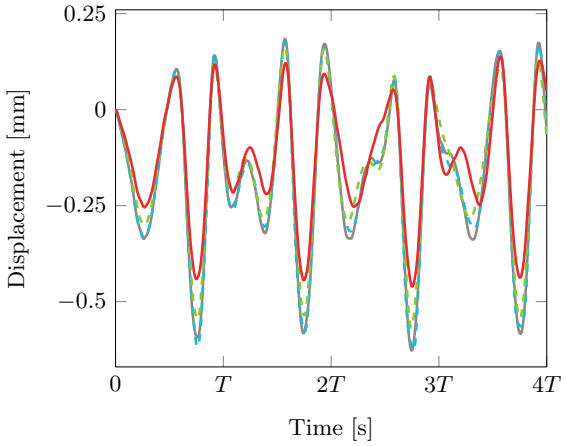

FIGURE 5.9 – Comparison of the reference solution (——) with the solutions obtained with the POD method: $N_t = 1$ (——), $N_t = 2$ (- - - -), $N_t = 8$ (——).

5.4.2 Linear basis with POD correction

A Craig-Bampton reduction basis with $r_b = 3$ constraint modes and $r_c = 10$ internal modes is considered. Without correction, this reduced model does not capture the nonlinear nature of the system. This is illustrated in Fig. 5.10, which compares the reference nonlinear solution of the structure with the solution obtained with the usual linear Craig-Bampton reduction method where the nonlinear internal forces are evaluated with the STEP. Very poor results are obtained, even worse than when geometric nonlinearities are simply neglected.

As explained in section 4.3.3, results can be enhanced by filtering the nonlinear internal forces through a POD correction before applying the STEP. The training excitation used for the POD filtering of the nonlinear internal forces is here defined as the excitation E_1 in Table 5.1, *i.e.* a harmonic excitation of amplitude $A_t = 300$ N and pulsation $\omega_t = 2,000$ rad/s applied at node LE in the $\mathbf{e}_y$ direction.

Figure 5.11 shows the influence of the number of POD vectors r_f retained for the forces filtering. When the number of POD vectors is too small, the nonlinear internal forces are over-filtered and therefore not well represented in the reduced basis. When r_f is too large, the solution tends toward the solution obtained without filtering. The optimal number of POD vectors is found to be $r_f = 8$ in this particular case.

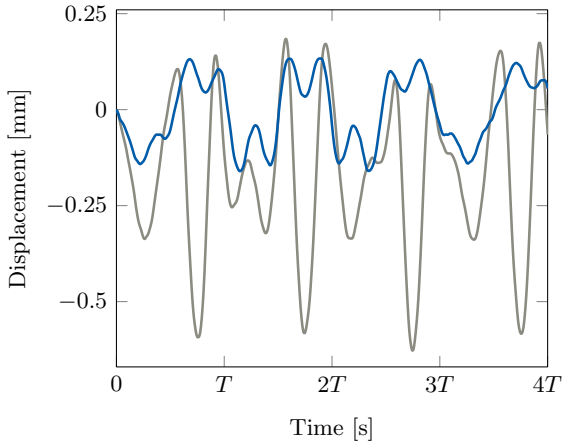

FIGURE 5.10 – Comparison of the nonlinear reference solution (——) with the solution obtained with the CB method without POD correction (——).

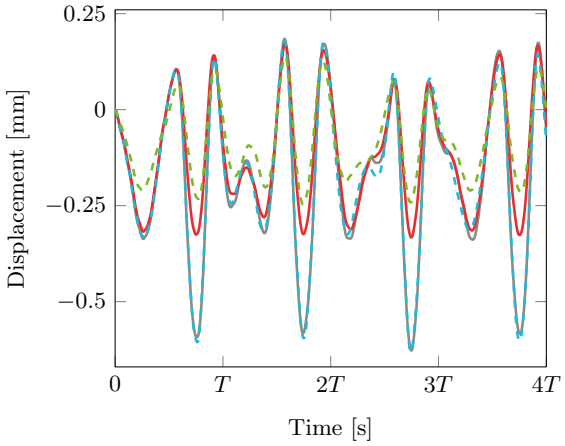

FIGURE 5.11 – Comparison of the reference solution (——) with the solutions obtained with the CB method with POD correction: $r_f = 4$ (——), $r_f = 8$ (- - - -) and $r_f = 12$ (- - - -).

Similarly to what has been observed in section 5.4.1, the amplitude and the pulsation of the training solution have little influence on the reduced solution. The influence of the spatial shape of the training excitation used for the POD filtering is more pronounced.

5.4.3 Modal derivatives

The blade is reduced through a basis composed of the Craig-Bampton modes and the associated modal derivatives. In a first step, the reduction basis is composed of $r_b = 3$ static modes, $r_c = 5$ internal modes and the $r_{\text{MD}} = 36$ corresponding modal derivatives. It should be noted that it is not guaranteed that the modal derivatives obtained with the methodology described in section 4.3.4 are orthogonal and linearly independent. In order to avoid having redundant information in the reduced basis, the modal derivatives are orthonormalized with a modified Gram-Schmidt procedure which also allows to remove from the basis the linearly dependent vectors. This transformation allows to get better results and to accelerate the convergence of the nonlinear integration scheme. In practice, a mode is removed from the basis when the ratio between the norm of the resulting orthogonolized mode and the norm of the initial mode is less than 10^{-3}. Here, the Gram-Schmidt procedure leads to remove two modal derivatives from the basis.

The reduction method does not depend on any training simulation but the resulting reduced model has a larger size than reduced models obtained with the other reduction methods as the number of modal derivatives increases quadratically with the number of linear modes. It is however expected that all modal derivatives are not necessary to capture the nonlinear behavior of the structure. A subset of modal derivatives needs to be selected *a priori* with an appropriate selection criterion. In the following, the different modal derivatives selection criteria defined in section 4.3.4 are applied to the blade model and compared.

Different reduced-order models are built with $r_b = 3$ degrees-of-freedom (corresponding to the node LE) kept in the reduced space. The reduction bases are composed of $r_c = 10$ internal modes and $r_{\text{MD}} = 10$ modal derivatives selected according to the different criteria. As a reminder, the criteria consist in associating a weight W_{jk} to each modal derivative and selecting the modal derivatives with the highest weights. The training excitation, used in the dynamic simulation required for the weights computation, is defined as the harmonic excitation E_1.

The reduced-order models are used to compute the response of the structure to the excitation E_1. The transient responses at node LE obtained with the different selection criteria are shown in Fig. 5.12a and Fig. 5.12b and compared with the reference nonlinear solution. The response obtained with a reduction basis composed of $r_{\text{MD}} = 10$ randomly chosen modal derivatives is also represented in Fig. 5.12a.

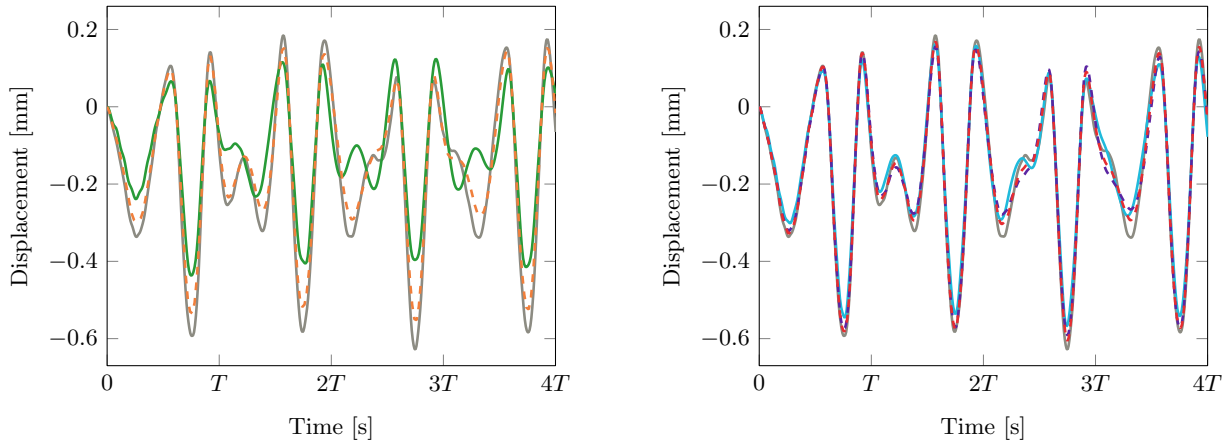

(a) With 10 randomly chosen MD (——), the 10 MD selected with criterion 1 (- - - -).

(b) With the 10 MD selected with criterion 2a (- - - -), criterion 2b (- - - -) and criterion 3 (——).

FIGURE 5.12 – Comparison of the reference transient response of the structure (——) with the responses obtained with the modal derivative approach.

Qualitatively, the results underline the importance of defining a good selection criterion for the modal derivatives. Whereas a relatively good match is observed between the curves corresponding to the selection criteria 1 to 3 and the reference nonlinear solution, the solution obtained with the randomly chosen modal derivatives is very inaccurate. These results also allow to quantitatively assess the relevance of each selection criterion. Among the studied criteria, criteria 2a and 2b yield the best results, followed by criterion 1 and criterion 3. All the criteria allow to capture the nonlinear features of the response. Quantitatively, the performance indicator is given by $I = 0.93$ for criterion 1, $I = 0.96$ for criterion 2a, $I = 0.97$ for criterion 2b, and $I = 0.91$ for criterion 3. Other studies, that are not detailed here for the sake of conciseness, have been performed with other external excitations and confirm the choice of the selection criterion 2b for the next analyses.

The weights associated to each modal derivative (according to selection criterion 2b) and the ranking of the 10 selected modal derivatives are shown in Fig. 5.13. The modal derivative with the highest weight is the derivative of the second static mode with respect to itself, the modal derivative with the second highest weight is the derivative of the second static mode with respect to the third static mode, and so on. More generally, the modal derivatives included in the reduction basis correspond to the derivatives of the static modes with respect to themselves and of the static modes with respect to the first internal modes.

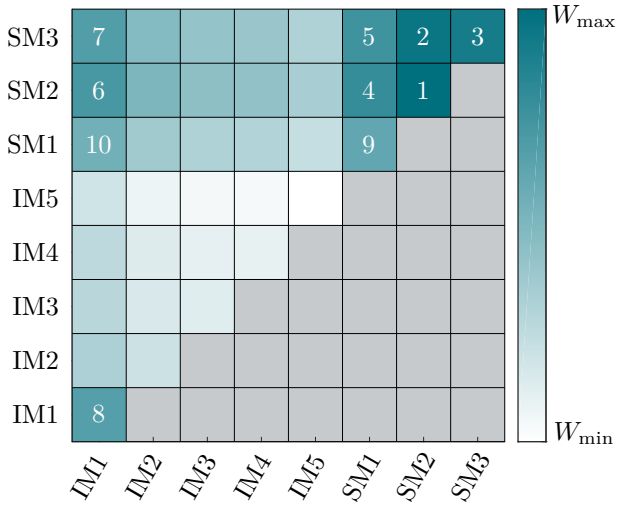

FIGURE 5.13 – Weights $W_{jk}^{(2b)}$ associated to each modal derivative and their ranking (logarithmic scale).

The transient response obtained with criterion 2b is compared in Fig. 5.14a with the response computed with a reduction basis where all $r_{\mathrm{MD}} = 36$ modal derivatives are included. The addition of the remaining 26 modal derivatives in the reduction basis does not significantly

enhance the performance of the reduction method. Indeed, the performance indicator is only slightly increased to $I = 0.98$ while the size r of the reduction basis is multiplied by more than 2. These results confirm that it is not necessary to include all modal derivatives in the reduction basis to have good performance. This selection criterion is therefore a powerful tool that allows to reduce the size of the reduction basis while ensuring an accurate prediction of the structure dynamic response.

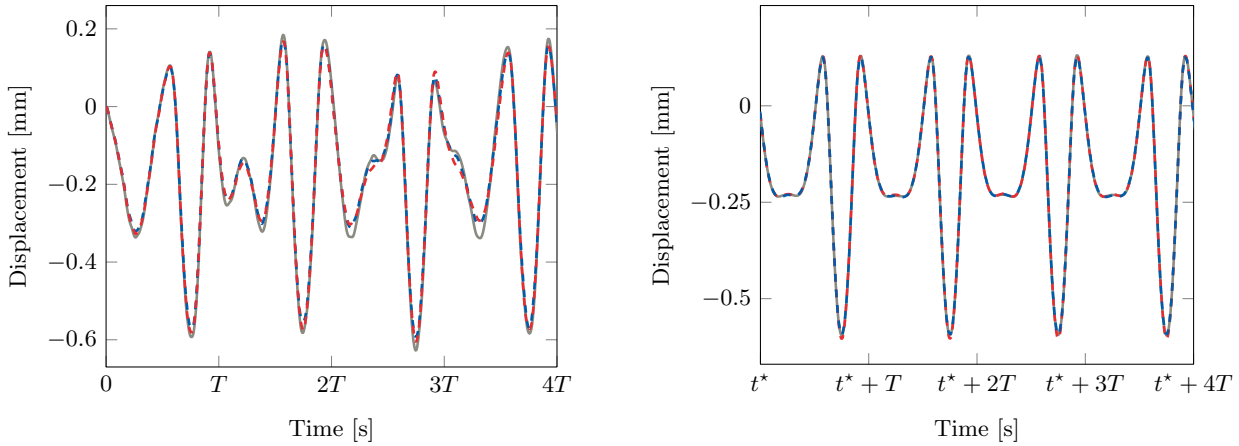

(a) Transient regime.

(b) Steady-state regime.

FIGURE 5.14 – Comparison of the reference transient response of the structure (——) with the responses obtained with the modal derivative approach with all $r_{\mathrm{MD}} = 36$ modal derivatives (- - - -) and with the best 10 modal derivatives according to selection criterion 2b (- - - -).

The steady-state responses computed with the same reduction bases are shown in Fig. 5.14b and compared with the reference nonlinear solution. The different reduced models provide very accurate predictions and the initial errors do not build up during the simulation, which underlines the relevance of the proposed selection criterion.

5.4.4 Reduced nonlinear internal forces

In the three selected reduction methods, the nonlinear internal forces due to large displacements are evaluated in the reduced space with the STEP described in section 4.2. This identification method is based on static analyses with imposed displacements of the form (4.14), (4.20) and (4.21). According to the theoretical formulation of the ROM based on the general elasticity theory, the identified coefficients are independent of the level at which the data are obtained. In practice, however, this is not necessary the case due to the possible inconsistency between the general elasticity formulation and the finite element

formulation in the commercial software.The amplitude of the imposed displacement $u_{\max}$, *i.e.* the absolute values of the modal coordinates q_i, q_j and q_k, has to be sufficiently large to activate the nonlinear behavior of the structure, but sufficiently small to stay in the convergence limit of the finite element software.

The reduction basis is built based on the modal derivative approach, with $r_b = 3$ static modes, $r_c = 5$ internal modes and $r_{\text{MD}} = 10$ modal derivatives. The nonlinear stiffness elements of tensors $\tilde{\mathbf{A}}$ and $\tilde{\mathbf{B}}$ in (4.10) are identified with the STEP by prescribing displacements of amplitudes $u_{\max}$. The dominant coefficients are given in Fig. 5.15 for three values of $u_{\max}$ below the convergence limit of the finite element software. The identified values of the coefficients are extremely close for the three values of $u_{\max}$ considered. This confirms the consistency between the general elasticity formulation and the formulation of the geometric nonlinearities in the finite element software.

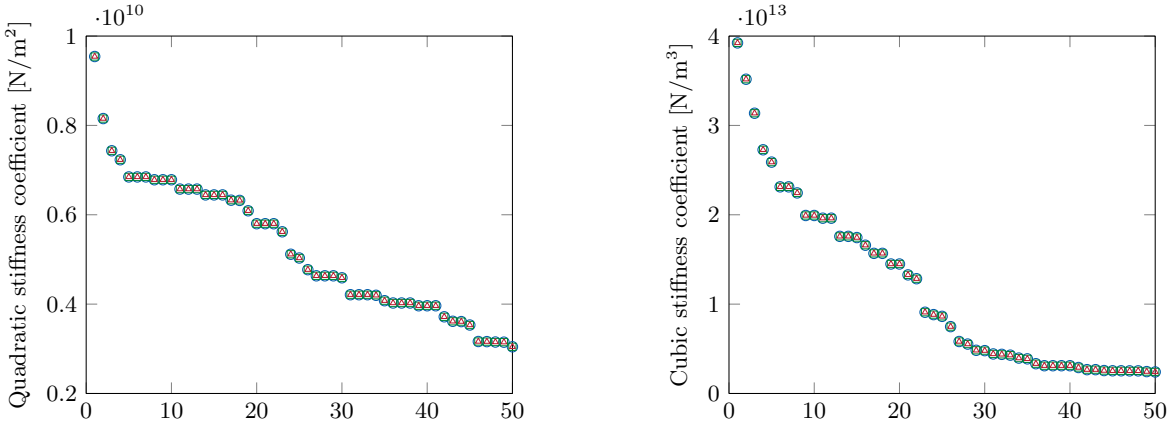

(a) Quadratic stiffness.

(b) Cubic stiffness.

FIGURE 5.15 – Dominant reduced nonlinear stiffness coefficients identified with the STEP: $u_{\max} = 0.1$ cm (△), $u_{\max} = 5$ cm (□) and $u_{\max} = 7$ cm (○).

5.5 Confrontation of reduction methods

Now that the three reduction methods selected have been presented and studied individually, the indicator of performance introduced in section 5.3 is used to compare the three reduction methods in terms of accuracy and versatility. The reduction methods are also compared in terms of computational cost.

The reduced-order models are built in the offline stage of the numerical procedure. In order to ease the comparison, the physical interface kept in the reduced space has only one node.

The $r_b = 3$ degrees-of-freedom corresponding to the node LE at the blade-tip leading edge are kept in the reduced space. For the three reduction methods, the nonlinear internal forces are evaluated with the STEP (see section 4.2). The training excitation used in the offline stage for the construction of the POD reduction basis, for the POD filtering of the nonlinear forces in the Craig-Bampton method and for the selection of the modal derivatives is defined as the harmonic excitation E_1.

The characteristics of the reduction bases are summarized in Table 5.2. In order to study how richer reduction bases can enhance the accuracy of the predictions, different sizes r of the reduction bases are considered for each method.

	r_b	r_c	r_{MD}	r_{POD}
POD	3	/	/	$r-3$
CB with POD correction	3	$r-3$	/	/
CB and MD	3	4	$r-7$	/

TABLE 5.2 – Characteristics of the reduction bases.

5.5.1 Accuracy

As mentioned in section 2.1.2, the flow between the blades is particularly complex due to the geometry of these elements, the relative movements between the rotor and the stator and the extreme conditions in terms of pressure and temperature. This induces complex unsteady loadings on the blades, which are coupled with the vibrations of the blades and require aeroelastic analysis to be accurately predicted. The study of unsteady aerodynamics is out of the scope of this thesis. The aerodynamic loading is here represented as a harmonic external excitation at the tip of the blade.

The accuracy of the reduction methods is first assessed in the specific case where the external excitation is defined in the same way as the training excitation. Although the training excitation is limited to a single period, the external excitation is here extended to ten periods in order to assess the capability of the reduced-order models to accurately predict nonlinear transient phenomena.

The response of the structure is computed for each reduction method, for different sizes of the reduction bases, and the performance indicator is evaluated for each case. The evolution of I for each reduction method with the number of vectors in the reduction basis r is shown in Fig. 5.16. The reduction bases built by POD clearly outperform the other reduction methods in this particular case. Very good results are obtained with a small reduction basis size; the

performance indicator takes values very close to 1 when r is larger than 10. According to Eq. (4.34), these 10 POD modes capture 99.7% of the energy of the training data.

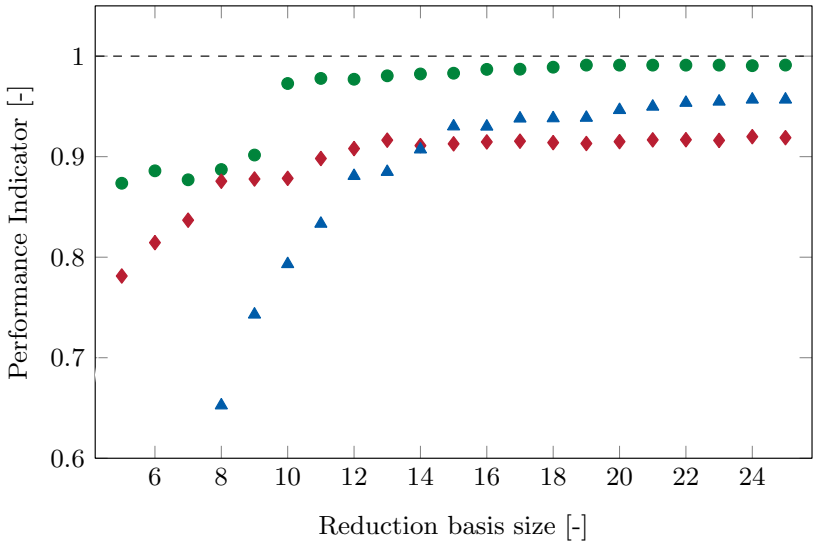

FIGURE 5.16 – Evolution of the performance indicator for the different reduction methods (POD (●), Craig-Bampton with POD filtering (♦), modal derivatives (▲)) as a function of the size of the reduction basis (external excitation E_1 and training excitation E_1).

The Craig-Bampton basis with POD filtering and the modal derivative approach give slightly less accurate results. Smaller reduction bases are required with the Craig-Bampton method to provide satisfactory results (performance index larger than 0.9) but it is remarkable that the modal derivative approach allows to reach higher performance indicators. For large sizes of the reduction basis, the difference in performance criteria is reflected in the global criteria: reduction bases with modal derivatives allow a better representation of the global behavior of the blade dynamics. This can be highlighted by comparing the von Mises stress fields obtained with the different approaches. Figure 5.17 shows the von Mises stress fields corresponding to the displacement fields predicted by the different reduction methods for a constant reduction basis size $r = 20$. The stress field is computed at the time $t_{\max}$ corresponding to the second peak of the excitation. This figure confirms that the solution obtained with the modal derivatives is more accurate at the scale of the entire blade than the solution obtained with the Craig-Bampton method.

The von Mises stress field is also represented for the POD reduction method and is very close from the reference stress field computed with the full-order finite element model. This confirms that the reduction method by POD gives excellent results both locally and globally, which is coherent with the close-to-one values of the performance indicator obtained.

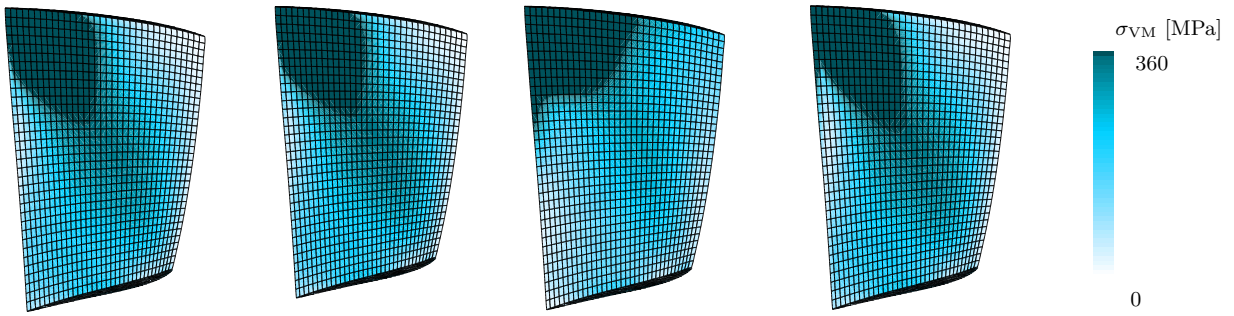

(a) Reference solution. (b) POD. (c) CB with POD filtering. (d) Modal derivatives.

FIGURE 5.17 – Comparison of the von Mises stress fields at $t_{\max}$ obtained with the full-order finite element model and with three reduced-order models ($r = 20$).

5.5.2 Computational cost

Keeping in mind that the main objective of the reduction methods is to accelerate the simulations while ensuring a high level of accuracy, this section is dedicated to the confrontation of the three employed reduction methods in terms of computation times. It is worth reminding that the idea of reduced-order modeling is to invest computational effort in the offline stage in order to reduce the computational cost of the online stage. In industrial applications, the primary objective is to minimize the computational time required by the online stage (online time) so that repeated time simulations can be performed with the same reduced model in the most efficient way. For the sake of completeness, a comparative study of the computational time required by the offline stage (offline time) is also presented in this section. This allows to have an idea of the overall reduction time, which is a measure of the total effort needed to compute the response of the structure using a reduction procedure.

The different computation times presented in the following correspond to single CPU sequential times on an Intel Xeon E5-2698 v4 processor (2.2 GHz). The core numerical tool is written in Python. The computation times are compared for the different reduction methods with the same reduction basis size $r = 20$ which leads to performance indicators larger than 0.9 for the three reduction methods studied.

The offline time consists in the sum of the time t_1 required to build the reduction basis, the time t_2 required to identify the nonlinear forces with the STEP and the time t_3 required to project the full-order matrices onto the reduced space. The time t_3 is completely negligible with respect to t_2. Similarly, t_1 is usually negligible with respect to t_2, except for the POD reduction method where a full nonlinear simulation has to be performed. When POD filtering

of the nonlinear forces is not considered, t_2 is proportional to r^3, where r is the number of vectors in the reduction basis. When POD filtering is considered, the time of the full-order nonlinear simulation has to be accounted for in t_2. Note that for the specific model studied, each static nonlinear simulation with imposed displacements takes 40 s.

Table 5.3 compares the offline costs of the three studied reduction methods, for a constant basis size $r = 20$. As expected, the two reduction methods based on a POD require slightly more computational resources. It should be pointed out that the elements of tensors $\tilde{\mathbf{A}}$ and $\tilde{\mathbf{B}}$ of the same category (*i.e.* coefficients with equal indices, coefficients with two unequal indices and coefficients with three unequal indices) can be identified independently. For instance, according to Eq. (4.19), the vectors $\tilde{\mathbf{A}}_{11}$ and $\tilde{\mathbf{B}}_{111}$ can be identified independently from the vectors $\tilde{\mathbf{A}}_{22}$ and $\tilde{\mathbf{B}}_{222}$. Parallel computing can therefore be used to reduce computation times. In practice, the nonlinear force static evaluations performed on the full-order finite element model can be done in parallel to build the tensors $\tilde{\mathbf{A}}$ and $\tilde{\mathbf{B}}$, allowing to divide the computation time by the number of CPU cores or the number of software licenses available if a commercial finite element software is used.

	Offline time [min]	*Online time [s]*
POD	1,350	5
CB with POD correction	1,360	5
CB and MD	1,320	5
Reference solution	/	12,000

TABLE 5.3 – Comparison of the offline and online computation times for the three reduction methods ($r = 20$) and the high fidelity model.

The online time is mainly dominated by the time corresponding to the numerical integration of the equation of motion. Table 5.3 compares the online time costs of the different reduction methods (with a reduction basis size $r = 20$) to each other and to the time taken by the nonlinear solver of SAMCEF to integrate numerically the full-order equation of motion. These computation times are measured in the framework of the simulations performed in section 5.5.1, *i.e.* simulations of 0.03 s with a time step of integration $h = 10^{-4}$ s. The online time is directly related to the size r of the reduction basis, and nearly independent from the reduction method used. The different reduction methods allow to reduce the computation time by a factor $2,400$ with respect to the nonlinear reference model. However, as shown in the previous section, reduction bases of the same size r do not provide the same performance for the different reduction methods. For instance, reduced models built by POD allow to

reach a performance indicator of 0.9 for $r = 10$. For such a reduction basis size, the online computation time drops down to 2 s. A compromise therefore has to be found between accuracy of the results and computation time.

5.5.3 Versatility

The performance indicator I is used here to assess the robustness of each reduction method with respect to a variation of the external excitation in terms of pulsation, amplitude or spatial shape, *i.e.* to assess the accuracy of the reduced-order models when used to predict the structure dynamics for an excitation different from the excitation used to build the ROM.

5.5.3.1 Pulsation and amplitude variation

The reduction bases used in Fig. 5.16 are reused to compute the response of the structure to the harmonic excitation E_2, which is characterized by the same amplitude, direction and spatial shape than E_1 but has a pulsation $\omega_e = 4,000$ rad/s. The performance indicator is computed for the different methods, for each reduction basis size. The results are presented in Fig. 5.18.

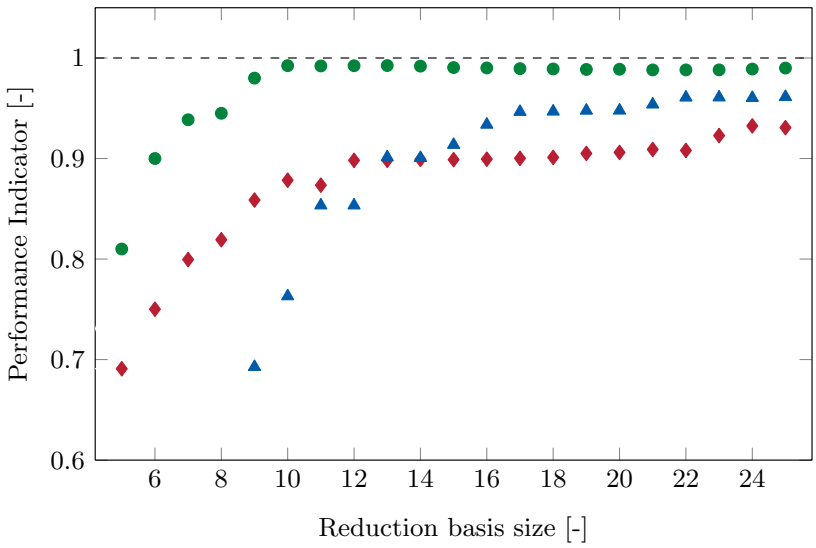

FIGURE 5.18 – Evolution of the performance indicator for the different reduction methods (POD (●), Craig-Bampton with POD filtering (♦), modal derivatives (▲)) as a function of the size of the reduction basis (external excitation E_2 and training excitation E_1).

The performances of the different reduction methods do not seem to be affected when another excitation pulsation is considered, provided the pulsation is sufficiently close to the

training pulsation so that the external excitation does not significantly excite other modes of the structure. The relative performances of the methods are also conserved: the POD method provides the best results. The modal derivative method provides better results than the Craig-Bampton method with POD filtering when large sizes of the reduction basis are considered. The study of the robustness of the methods to change in the amplitude of the external excitation leads to similar conclusions.

5.5.3.2 Spatial shape variation

The robustness of the methods with respect to variation of the spatial distribution of the external excitation is then assessed. The reduction bases used in Fig. 5.16 and in Fig. 5.18 are used to compute the response of the structure to the harmonic excitation E_3 which has the same amplitude, pulsation and direction than E_1 but is distributed on the $N_e = 8$ blade-tip nodes represented in Fig. 5.2. The results are presented in Fig. 5.19. The performance of the POD method clearly drops when a different spatial distribution of the excitation is considered. The performance of the Craig-Bampton method with POD filtering is also slightly decreased. The performance of the modal derivative method remains approximately the same. A wider numerical study, considering different excitations and different numbers of physical degrees-of-freedom in the reduced space, confirms these conclusions (not shown here for the sake of conciseness). The modal derivative approach appears therefore as the most versatile reduction method among those analyzed here.

POD reduction method The results plotted in Fig. 5.19 highlight the lack of versatility of the POD reduction method when the external excitation differs from the excitation used as a training to build the reduction basis. Based on this observation, a more systematic study of the influence of the shape of the training excitation has been performed. In practice, different POD bases have been built, based on different training simulations. The POD bases are composed of $r_b = 3$ static modes and $r_{\text{POD}} = 10$ POD modes obtained by SVD of the response of the structure to harmonic external excitations distributed on $N_t = 1, 2, \ldots, 8$ blade-tip nodes. The eight reduction bases have then been used to compute the response of the structure to different harmonic external excitations distributed on $N_e = 1, 2, \ldots, 8$ blade-tip nodes and the value of the performance indicator has been computed for each combination of POD basis and external excitation. Figure 5.20 represents how I evolves when the spatial distribution of the POD training excitation and the spatial distribution of the external excitation vary. As expected, the highest values of the performance indicator are obtained on the main diagonal of the figure, *i.e.* when the POD basis is used to compute the

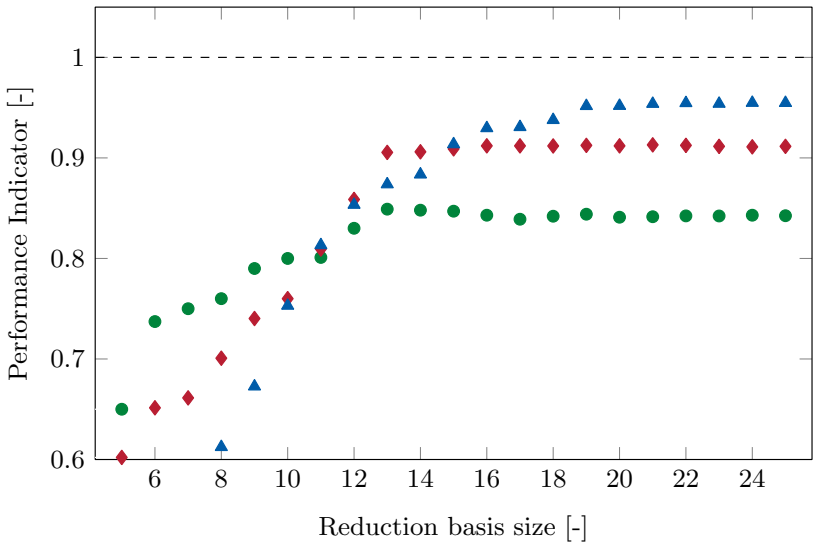

FIGURE 5.19 – Evolution of the performance indicator for the different reduction methods (POD (●), Craig-Bampton with POD filtering (♦), modal derivatives (▲)) as a function of the size of the reduction basis (external excitation E_3 and training excitation E_1).

response of the structure to an external excitation whose spatial shape corresponds to the spatial shape of the training excitation. When the spatial shape of the external excitation differs from the training excitation applied, the performance indicator decreases. This figure provides guidelines for the choice of the training excitation to get the most robust reduction method. As a general rule, the training excitation should be as close as possible to the external excitation for which the reduced model will be used. In this particular case, choosing $N_t = 4$ seems to be a good compromise as it leads to performance indicator values higher than 0.95 when N_e varies between 1 and 8. It is also interesting to notice that the method is more robust for $N_t = 8$ than for $N_t = 1$. In particular, using a reduction basis with $N_t = 8$ to compute the response of the structure to an external excitation with $N_e = 1$ provides better results than using a reduction basis with $N_t = 1$ to compute the response of the structure to an external excitation with $N_e = 8$.

In order to improve the performance of the POD reduction method, it is also possible to build the reduction basis by combining in the snapshots matrix (4.31) two sets of data corresponding to the time responses of the structure to two different external excitations. Here, the snapshots are extracted from the response of the structure to an excitation applied at the trailing edge extremity at blade-tip (node TE, see Fig. 5.2) and to an excitation applied at the leading edge extremity at blade-tip (node LE). A POD basis composed of $r_b = 3$ static modes, $r_{\text{POD}} = 10$ POD modes is built. The reduction basis is used to compute

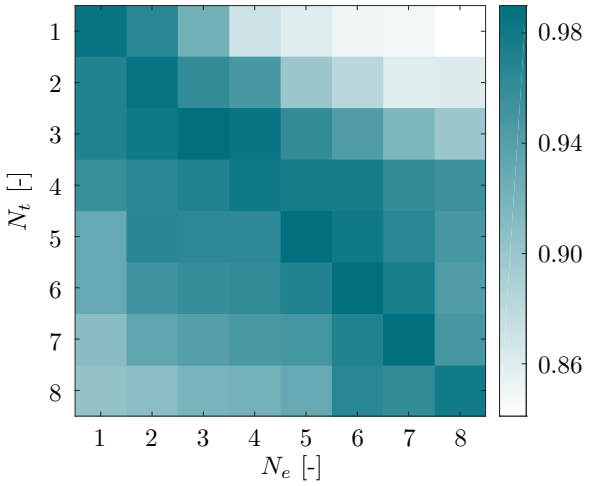

FIGURE 5.20 – Performance indicator I as a function of the number of nodes excited in the POD training (N_t) and by the external excitation (N_e) with $r_b = 3$ and $r_{\text{POD}} = 10$.

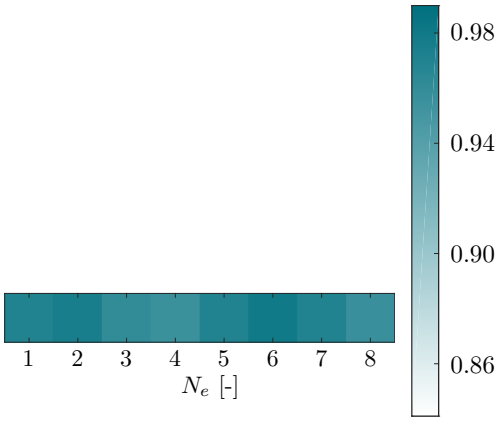

FIGURE 5.21 – Performance indicator I as a function of the number of nodes excited by the external excitation (N_e) with $r_b = 3$ and $r_{\text{POD}} = 10$ (training excitations at LE and TE).

the response of the structure to different external excitations and the performance indicator is computed in each case. As shown in Fig. 5.21, this procedure allows to keep a performance indicator close to one for a large range of excitations.

With the growing popularity of artificial intelligence, different authors have proposed machine learning techniques to compensate for the lack of versatility of data-driven methods such as the POD method. The main idea is to divide the parameter space into several local regions and to build a reduced-order model for each region individually. Deep learning techniques, such as clustering algorithms, can then be used to choose the best reduced-order model during a single numerical simulation and to update it [74, 81].

5.6 Angular speed influence

The results presented in sections 5.1 to 5.5 have been obtained by neglecting the rotation of the blade. In practice, the structure has a non-zero angular speed Ω. The nominal angular speed of the rotor 37 is $\Omega_N = 17,188.7$ RPM (approximately $1,800$ rad/s) [184]. As shown when deriving the equation of motion (2.3), the rotation speed has a direct influence on the stiffness matrix, the nonlinear internal forces and the gyroscopic matrix, and therefore influences the dynamics of the blade.

The Campbell diagram of the blade is shown in Fig. 5.22. It represents the evolution of the first three eigenfrequencies of the blade (first bending mode, first torsion mode and second bending mode) with the angular speed when the centrifugal effects are computed through linear or nonlinear static analyses, *i.e.* by neglecting or not the term $\mathbf{g}(\mathbf{u}_s)$ in (A.38). In SAMCEF, the linear and nonlinear static analyses are done respectively with the modules Asef and Mecano. The first engine order lines are also plotted in the Campbell diagram.

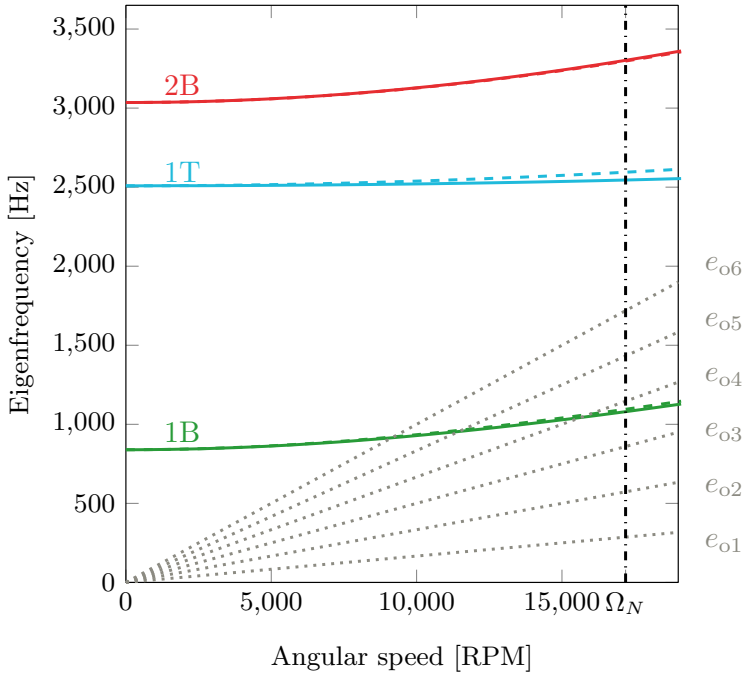

FIGURE 5.22 – Campbell diagram of the NASA rotor 37 blade with linear prestress (——) and nonlinear prestress (- - - -) and first engine order lines (·····).

The rotation speed has a strong effect on the frequencies of the bending modes. For instance, the frequency of the first bending mode increases by 35% over the rotation speed range $[0\ ;\ 20,000]$ RPM. It is important to account for these effects of the blade rotation in the reduced-order models.

5.6.1 Reduced-order model at non-zero angular speed

In the previous sections, reduced-order models built at $\Omega = 0$ have been used to study the dynamics of the structure at $\Omega = 0$. To predict the time response of the blade at a higher angular speed $\Omega = \Omega^\star$, it could be tempting to use the reduction basis built at zero angular speed in combination with the stiffness matrix extracted from the finite element software at

$\Omega^\star$. This way of proceeding does not, however, provide accurate results because the reduction basis built at zero rotation speed is not suitable to represent the response at high rotation speeds.

To illustrate this, the modal derivatives reduction basis built at zero angular speed (size $r = 18$) is used to compute the response to the harmonic excitation E_1 at different rotation speeds. The performance indicator is computed for each case and the results are presented in Fig. 5.23. The performance of the method clearly drops when the rotation speed departs from zero. The same exercise is performed with a reduced-order model built at $\Omega = 5,000$ RPM. Good performances are obtained around $5,000$ RPM but the performance drops when a wider angular speed range is considered. These results motivate the need to build reduced-order models valid in specific ranges of the angular speed.

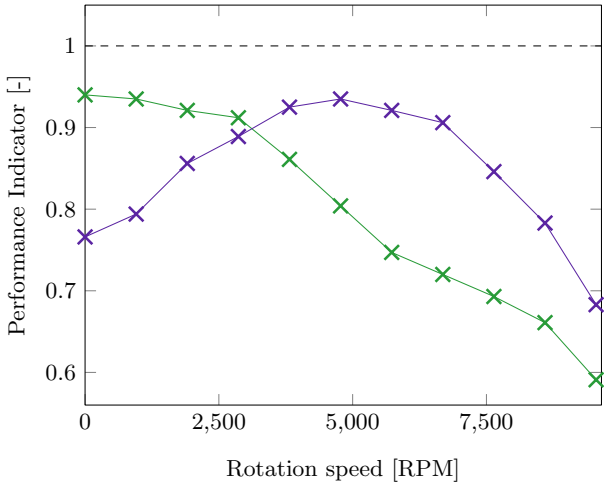

FIGURE 5.23 – Performance indicator as a function of the angular speed with MD reduced-order models built at $\Omega = 0$ RPM ($\times$) and at $\Omega = 5,000$ RPM ($\times$) (external excitation E_1).

5.6.2 Parametric reduced-order model

Research has been conducted on developing reduced-order models that can accommodate the variation of specific parameters in the reduced space [9,84,228]. These models are referred to as parametric reduced-order models. In the specific field of turbomachinery, these parametric models are particularly useful to account for the influence of the rotation speed on the dynamic properties of the structure. Indeed, such models allow to avoid building individual reduced-order models for each single rotation speed by repeating the computationally costly offline part of the numerical procedure.

The basic idea is to build a reduced-order model valid in a specific rotation speed range $[\Omega_\alpha\,;\,\Omega_\omega]$. In practice, the centrifugal stiffening effects have to be taken into account when building the reduction basis and when computing the stiffness (stiffness matrix and nonlinear internal forces) of the structure.

5.6.2.1 Construction of the reduction basis

In order to build a reduction basis encompassing the main features of the dynamics of the structure at different rotation speeds, the reduction basis is enriched with modes at various operating points [239]. In practice, a good compromise is obtained by computing the reduction basis with the chosen reduction technique at three distinct rotation speeds Ω_0, Ω_1 and Ω_2 in the interval $[\Omega_\alpha\,;\,\Omega_\omega]$. The modes are combined in a matrix $\mathbf{\Phi}^\Omega$ by

$$\mathbf{\Phi}^\Omega = \begin{bmatrix} \mathbf{I} & \mathbf{0} & \mathbf{I} & \mathbf{0} & \mathbf{I} & \mathbf{0} \\ \mathbf{\Psi}_i^{(0)} & \mathbf{X}^{(0)} & \mathbf{\Psi}_i^{(1)} & \mathbf{X}^{(1)} & \mathbf{\Psi}_i^{(2)} & \mathbf{X}^{(2)} \end{bmatrix}, \tag{5.11}$$

where $\mathbf{\Psi}_i^{(j)}$ are the Guyan static modes at rotation speed Ω_j and $\mathbf{X}^{(j)}$ are the fixed interface linear normal modes, POD modes or modal derivatives (depending on the choice of the reduction method) at rotation speed Ω_j. Since the interface motion is already fully represented by the Guyan static modes at Ω_0, the other two sets of constraint modes are modified to fixed interface modes by subtracting the components already present in the first set of constraint modes. The modified matrix $\bar{\mathbf{\Phi}}^\Omega$ is defined as

$$\bar{\mathbf{\Phi}}^\Omega = \begin{bmatrix} \bar{\mathbf{\Phi}}_i^\Omega & \bar{\mathbf{\Phi}}_m^\Omega \end{bmatrix}, \tag{5.12}$$

where

$$\bar{\mathbf{\Phi}}_i^\Omega = \begin{bmatrix} \mathbf{I} \\ \mathbf{\Psi}_i^{(0)} \end{bmatrix} \qquad \text{and} \qquad \bar{\mathbf{\Phi}}_m^\Omega = \begin{bmatrix} \mathbf{0} & \mathbf{0} & \mathbf{0} & \mathbf{0} & \mathbf{0} \\ \mathbf{X}^{(0)} & \mathbf{\Psi}_i^{(1)} - \mathbf{\Psi}_i^{(0)} & \mathbf{X}^{(1)} & \mathbf{\Psi}_i^{(2)} - \mathbf{\Psi}_i^{(0)} & \mathbf{X}^{(2)} \end{bmatrix}. \tag{5.13}$$

The obtained reduction basis $\bar{\mathbf{\Phi}}_m^\Omega$ is then orthonormalized by a SVD and reduced by retaining only the s modes corresponding to the highest singular values, forming the basis $\bar{\mathbf{\Phi}}_{m,s}^\Omega$. The reduction basis of the parametric model is defined as

$$\mathbf{\Phi} = \begin{bmatrix} \bar{\mathbf{\Phi}}_i^\Omega & \bar{\mathbf{\Phi}}_{m,s}^\Omega \end{bmatrix}. \tag{5.14}$$

5.6.2.2 Construction of the reduced-order model at a specific rotation speed

The equation of motion of a rotating structure (2.3) highlights that the rotation speed has an influence on the gyroscopic matrix, the stiffness matrix and the nonlinear internal forces. Whereas the gyroscopic matrix $\mathbf{G}(\Omega)$ can be directly computed from the knowledge of the rotation speed and the mass matrix by (A.32), this is not the case for the stiffness terms.

Some authors have suggested that the stiffness matrix $\mathbf{K}(\Omega, \mathbf{u}_s)$ can be estimated by a polynomial approximation. When the prestressed state $\mathbf{u}_s$ is computed through a linear static analysis, *i.e.* by neglecting the term $\mathbf{g}(\mathbf{u}_s)$ in (A.38), Sternchüss and Balmes [211] suggest that the dependency of the stiffness matrix on the rotation speed can be accurately described by a quadratic polynomial of the square rotation speed

$$\mathbf{K}(\Omega, \mathbf{u}_s) = \mathbf{K}^{(0)} + \Omega^2 \mathbf{K}^{(1)} + \Omega^4 \mathbf{K}^{(2)}, \tag{5.15}$$

where the coefficients $\mathbf{K}^{(0)}$, $\mathbf{K}^{(1)}$ and $\mathbf{K}^{(2)}$ are computed from the knowledge of the stiffness matrix at the three rotation speeds Ω_0, Ω_1 and Ω_2. In the specific case where $\Omega_0 = \Omega_\alpha = 0$, $\Omega_1 = \Omega_\omega/2$ and $\Omega_2 = \Omega_\omega$, the coefficients are given by

$$\begin{cases} \mathbf{K}^{(0)} = \mathbf{K}(0) \\ \mathbf{K}^{(1)} = \dfrac{1}{3\Omega_\omega^2}\left[16\mathbf{K}\left(\dfrac{\Omega_\omega}{2}\right) - \mathbf{K}\left(\Omega_\omega\right) - 15\mathbf{K}(0)\right] \\ \mathbf{K}^{(2)} = \dfrac{4}{3\Omega_\omega^4}\left[\mathbf{K}\left(\Omega_\omega\right) - 4\mathbf{K}\left(\dfrac{\Omega_\omega}{2}\right) + 3\mathbf{K}(0)\right] \end{cases} \tag{5.16}$$

When the prestressed state $\mathbf{u}_s$ is computed through a nonlinear static analysis, *i.e.* by solving (A.38), Khalifeh *et al.* [117] suggest that a better estimation of the stiffness matrix can be obtained by interpolating it with a higher order polynomial by

$$\mathbf{K}(\Omega, \mathbf{u}_s) = \sum_{p=0}^{N_p} \Omega^{2p} \mathbf{K}^{(p)}. \tag{5.17}$$

These relations remain valid for the reduced stiffness matrix $\tilde{\mathbf{K}}(\Omega, \mathbf{u}_s)$, which can be computed at an arbitrary rotation speed in the same way.

The nonlinear internal forces in the reduced space are given by (4.13), where the coefficients $\tilde{\mathbf{A}}$ and $\tilde{\mathbf{B}}$ depend on the prestressed state. Parametric reduced-order models have been most of the time studied for linear systems [117, 126, 131, 211, 239]. In a nonlinear context, Balmaseda *et al.* built a parametric reduced-order model of a geometrically nonlinear system

by computing the coefficients $\tilde{\mathbf{A}}$ and $\tilde{\mathbf{B}}$ at a single rotation speed and using these values whatever the rotation speed [13]. In practice, if $\tilde{\mathbf{A}}$ and $\tilde{\mathbf{B}}$ are evaluated at zero rotation speed, the nonlinear term is computed by

$$\tilde{g}_{\mathrm{nl}}^{m}(\mathbf{q},\mathbf{u}_s) = \sum_{i=1}^{r}\sum_{j=i}^{r} \tilde{A}_{ij}^{m}\left(\mathbf{u}_s=\mathbf{0}\right) q_i q_j + \sum_{i=1}^{r}\sum_{j=i}^{r}\sum_{k=j}^{r} \tilde{B}_{ijk}^{m}\left(\mathbf{u}_s=\mathbf{0}\right) q_i q_j q_k, \tag{5.18}$$

whatever the rotation speed. Even if this way of proceeding provides interesting results, it is proposed here to apply the same interpolation as the stiffness matrix for the nonlinear term, *i.e.* to interpolate the tensors $\tilde{\mathbf{A}}$ and $\tilde{\mathbf{B}}$ from their values at given rotation speeds. In practice, for $N_p = 2$, the coefficients $\tilde{\mathbf{A}}$ and $\tilde{\mathbf{B}}$ at a given rotation speed are computed by

$$\tilde{\mathbf{X}}\left(\mathbf{u}_s\left[\Omega\right]\right) = \tilde{\mathbf{X}}^{(0)} + \Omega^2\tilde{\mathbf{X}}^{(1)} + \Omega^4\tilde{\mathbf{X}}^{(2)}, \tag{5.19}$$

where $\tilde{\mathbf{X}}$ stands for $\tilde{\mathbf{A}}$ or $\tilde{\mathbf{B}}$ and

$$\begin{cases} \tilde{\mathbf{X}}^{(0)} = \tilde{\mathbf{X}}(\mathbf{u}_s\left[\Omega=0\right]) \\ \tilde{\mathbf{X}}^{(1)} = \dfrac{1}{3\Omega_\omega^2}\left[16\tilde{\mathbf{X}}\left(\mathbf{u}_s\left[\Omega=\dfrac{\Omega_\omega}{2}\right]\right) - \tilde{\mathbf{X}}\left(\mathbf{u}_s\left[\Omega=\Omega_\omega\right]\right) - 15\tilde{\mathbf{X}}(\mathbf{u}_s\left[\Omega=0\right])\right] \\ \tilde{\mathbf{X}}^{(2)} = \dfrac{4}{3\Omega_\omega^4}\left[\tilde{\mathbf{X}}\left(\mathbf{u}_s\left[\Omega=\Omega_\omega\right]\right) - 4\tilde{\mathbf{X}}\left(\mathbf{u}_s\left[\Omega=\dfrac{\Omega_\omega}{2}\right]\right) + 3\tilde{\mathbf{X}}(\mathbf{u}_s\left[\Omega=0\right])\right] \end{cases} \tag{5.20}$$

For more clarity, Fig. 4.1 is adapted for parametric reduced-order models in Fig. 5.24.

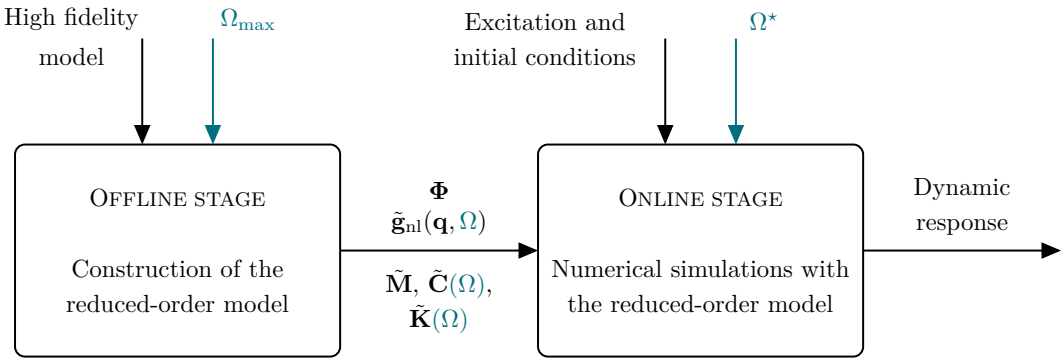

Figure 5.24 – Offline and online stages in parametric model order reduction.

5.6.2.3 Application to the rotating blade

The reduction basis is built by SVD of the reduction bases computed with the modal derivatives approach at the three rotation speeds 0, $\Omega_{\max}/2$ and $\Omega_{\max}$. Because the difference

between the eigenfrequency of the first bending mode computed with a linear or a nonlinear prestress of the structure is very small (see Fig. 5.22), the stiffness matrix is interpolated with (5.15).

As a first step, the upper limit of the rotation speed interval is set to $\Omega_{\max} = 5,000$ RPM. The size of the reduced basis is fixed to $r = 45$. The parametric reduced-order model is used to compute the response of the blade to the excitation E_1 at different rotation speeds $\Omega \in [0\,;\,5,000]$ RPM. Figure 5.25a compares the values of the performance indicator for different speeds of rotation when the nonlinear term $\tilde{\mathbf{g}}_{\text{nl}}$ is evaluated by its expression at zero rotation speed, *i.e.* by (5.18), and when the nonlinear term $\tilde{\mathbf{g}}_{\text{nl}}$ is evaluated by (4.10) where $\tilde{\mathbf{A}}(\mathbf{u}_s)$ and $\tilde{\mathbf{B}}(\mathbf{u}_s)$ are interpolated by (5.19) from the values at 0, 2,500 and 5,000 RPM. The parametric reduced-order model where the nonlinear term is not interpolated provides satisfying results in the rotation speed range of interest. However, Fig. 5.25a shows that interpolating the nonlinear terms enhances the performance indicator in the whole rotation speed range. As expected the performance of the parametric reduced-order model slightly decreases when the rotation speed departs from the values 0, 2,500 and 5,000 RPM used to build the model.

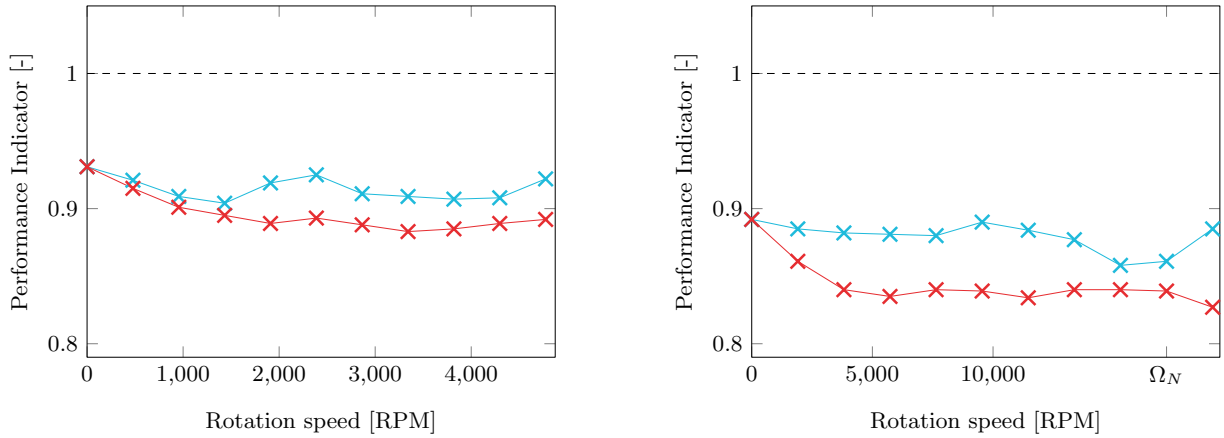

(a) $\Omega_{\max} = 5,000$ RPM.

(b) $\Omega_{\max} = 20,000$ RPM.

FIGURE 5.25 – Performance indicator as a function of the angular speed: without interpolation of $\tilde{\mathbf{g}}_{\text{nl}}$ (×) and with interpolation of $\tilde{\mathbf{g}}_{\text{nl}}$ (×).

A second parametric reduced-order model is built with the same approach on a wider rotation speed range, for $\Omega_{\max} = 20,000$ RPM. The results are represented in Fig. 5.25b. Although the performance is slightly decreased, the results show that interpolating the nonlinear term still allows to get better results than without interpolation.

5.7 Partial conclusions

The study of the NASA rotor 37 blade subjected to a harmonic loading and accounting for geometric nonlinearities illustrates the strengths and weaknesses of the different reduction methods investigated. The model reduction by POD gives excellent results, provided that the shape of the excitation is known *a priori*. The Craig-Bampton method with POD filtering of the nonlinear forces provides good results locally at the blade-tip, but fails to provide accurate stress fields which indicates an inaccurate representation of the displacement fields far from the boundary. The modal derivative approach provides good results, both locally and globally, and is robust with respect to changes of the external excitation. Larger sizes of reduction bases are however required to capture the nonlinear dynamics of the structure compared to the other reduction methods.

In the following, only the POD and the modal derivative approaches are considered to study the blade subjected to contact interactions. The Craig-Bampton method with POD filtering of the nonlinear forces is not considered in the subsequent studies as it does not allow to capture the global dynamics of the blade.

CHAPTER 6 SINGLE BLADE WITH GEOMETRIC AND CONTACT NONLINEARITIES

As shown in the previous chapter, simulating the dynamics of not too complex geometrically nonlinear structures subjected to known harmonic excitations with full-order models is computationally expensive, but feasible. In this context, reduced-order models provide an efficient alternative to full-order models. By contrast, simulating the nonsmooth dynamics of industrial structures subjected to contact interactions with full-order models would be computationally too demanding and is not feasible for practical applications. To give an idea, one cycle of revolution of an industrial blade subjected to contact interactions with a surrounding casing can be simulated in 24 hours [3]. The use of reduced-order models is therefore essential in this context to predict the steady-state contact dynamics.

The objective of this chapter is to study how the reduction methods studied in the previous chapter can be used to study the contact interactions of rotating blades with surrounding casings. In particular, we focus in this work on rubbing interactions. As mentioned in section 2.4.3, such interactions typically involve a single blade. In this chapter, a single rotating blade clamped at its root is therefore considered, as it is usually done in the literature [16].

The reduction methods are first applied to the academic clamped-clamped beam already used in previous chapters for which a reference solution can be obtained, and then to an industrial blade. The contact scenario used to initiate contact interactions between the blade and the surrounding casing is first described, together with the parameters of the numerical simulations. Some preliminary analyses then allow to select the reduction method that will be used in the remaining of this work. The final methodology is used to conduct a more extensive study on the industrial structure impacting a rigid casing. The methodology is then adapted to account for the wear of an abradable coating deposited on the casing.

The results with direct contact between the blade and the casing have been partially published in the Journal of Sound and Vibration [63]. The results related to the wear of the abradable coating have been presented at the conference ASME Turbo Expo 2021 [61] and published in the Journal of Engineering for Gas Turbine and Power [62].

6.1 Academic model

Before analyzing industrial structures, the reduction methods by POD and with modal derivatives are applied to an academic test case based on the clamped-clamped beam introduced in section 2.4.2.

6.1.1 Contact scenario

The clamped-clamped beam is positioned at a distance $c_0 = 7$ mm from a rigid obstacle (see Fig. 6.1). A harmonic excitation $\mathbf{F}(t) = A_e \cos(2\pi f_e t)\mathbf{e}_y$ with $A_e = 4,000$ N and $f_e = 165$ Hz is applied at node P_1. The amplitude and pulsation of the external excitation allow to initiate contact between the blade and the obstacle.

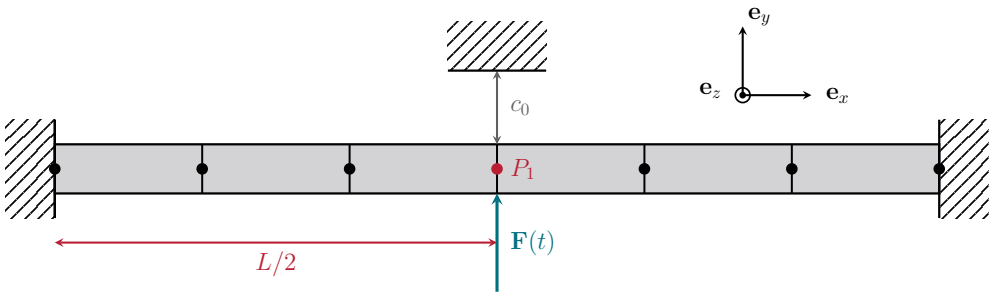

FIGURE 6.1 – Clamped-clamped beam impacting a rigid obstacle.

The time integration algorithm presented in section 3.1.1 is used to integrate the equation of motion forward in time, accounting for possible contact between the beam and the obstacle. The time step of integration is set to $h = 10^{-7}$ s. Friction is not considered in this first application.

6.1.2 Results

The response of the structure is first computed with the full-order model. The results accounting for geometric nonlinearities are shown in Fig. 6.2 both at the beginning of the simulation and when the steady-state regime is reached. The blade first oscillates smoothly until impacting the rigid obstacle when the amplitude of vibration is sufficiently high.

Two reduced-order models are then built. The first ROM is built by POD, as described in section 4.3.2. The reduction basis is composed of $r_b = 1$ static mode (corresponding to the transverse displacement at node P_1) and $r_{\text{POD}} = 10$ POD modes. The POD modes are computed from the snapshots of the response to the actual harmonic excitation, without

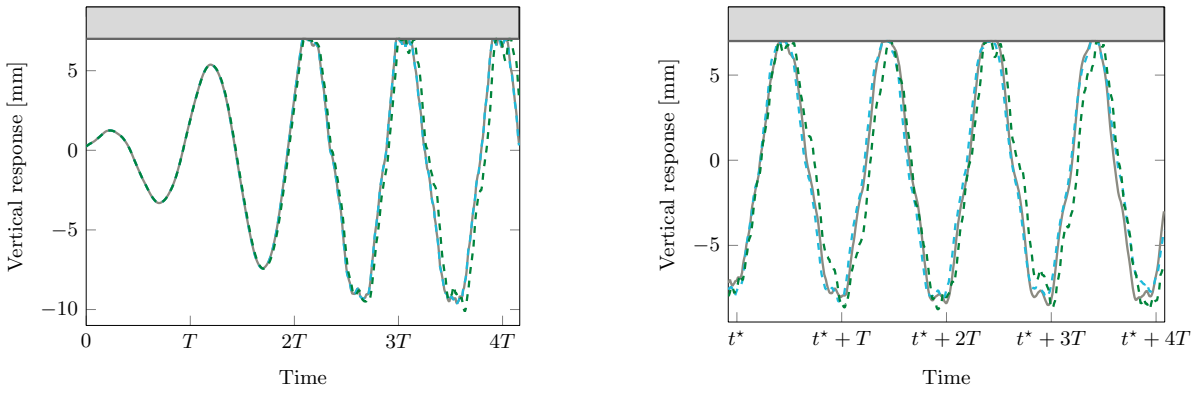

(a) Transient response.

(b) Steady-state response.

FIGURE 6.2 – Transverse displacement at node P_1 for a harmonic excitation of amplitude $A_e = 4,000$ N and frequency $f_e = 165$ Hz computed with the full-order model (——), the POD reduced-order model (- - - -) and the modal derivative reduced-order model (- - - -).

contact nonlinearities. The second ROM is based on the modal derivative approach, as described in section 4.3.4. The reduction basis is composed of $r_b = 1$ static mode, $r_c = 5$ fixed interface linear modes and $r_{\text{MD}} = 10$ modal derivatives.

These two reduced-order models are used to compute the response of the blade to the contact excitation. The corresponding results are shown in Fig. 6.2 and compared with the full-order results.

Both reduced-order models are very accurate to predict the response of the structure on the first two periods, when the beam is not in contact with the obstacle. This is consistent with the results presented in chapter 4. The methods are also accurate to predict the dynamics of the beam following contact events, even if the agreement is not perfect. It should also be noted that the POD reduced-order model is slightly less accurate than the modal derivative reduced-order model.

These contact analyses of the clamped-clamped beam suggest that the reduction methods by POD and with modal derivatives are good candidates to investigate in the context of this work. However, these results do not ensure that the numerical strategy is accurate to study real 3D industrial structures as they may exhibit much more complex behavior compared to the academic test case. In the following, these reduction methods are assessed for an industrial compressor blade.

6.2 Industrial test case and contact scenario

The rest of this chapter is dedicated to the contact analysis of the NASA rotor 37 blade described in section 5.1. As previously, the blade is clamped on the disk. The blade is assumed to rotate at a constant angular speed Ω about the $\mathbf{e}_z$ axis (period of revolution $T = 2\pi/\Omega$). The structure is surrounded by a casing assumed to be infinitely rigid, *i.e.* insensitive to blade contact events. This assumption is justified given the very low levels of vibration of the casing measured experimentally when studying blade-tip/casing contact interactions. The casing follows the shape of the blade-tip in the $\mathbf{e}_z$ direction, so that the clearance c_0 between the blade (at rest) and the casing is uniform from the leading edge (node LE) to the trailing edge (node TE), see Fig. 6.3.

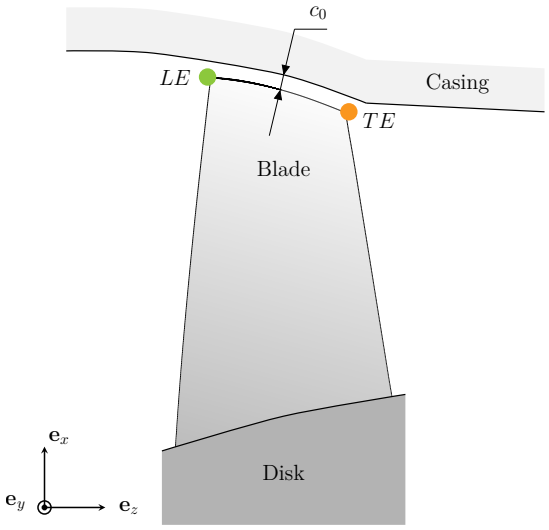

FIGURE 6.3 – Cut view of the NASA rotor 37 blade clamped on the disk and surrounded by the casing.

At the beginning of the simulation, the casing is perfectly circular to avoid any initial penetration, with an operating clearance between the blade-tip nodes and the circular casing c_0. In order to initiate contact, the casing is then progressively deformed in the radial direction until reaching its final distortion

$$f(\theta) = (c_0 + p_0) \exp\left[- \left(\frac{\theta - \lfloor \theta/\pi \rfloor \pi - \pi/2}{0.15} \right)^2 \right], \tag{6.1}$$

where θ is the angular coordinate varying between 0 and 2π and p_0 defines the penetration of the casing profile (----) with respect to the circular trajectory (----) of a blade-tip node (●)

of the sector at rest as shown in Fig. 6.4. This distortion corresponds to an ovalization of the casing with the creation of two diametrically opposed bumps of height $h_b = c_0 + p_0$ corresponding to privileged contact areas (see Fig. 6.4). This two-lobe deformation aims to model the casing ovalization resulting from a thermal imbalance within the engine at rest due to the up motion of the hot gas [168]. The gap between a given blade-tip node and the casing is computed through

$$g(\theta_b, t) = c_0 - (1 - e^{-\alpha t}) f(\theta_b) - u_r(t), \tag{6.2}$$

where θ_b is the current angular position of the blade-tip node, u_r is the radial displacement of the considered node and α is defined such that the ovalization reaches 99% of the maximal distortion at 20% of the total simulation time.

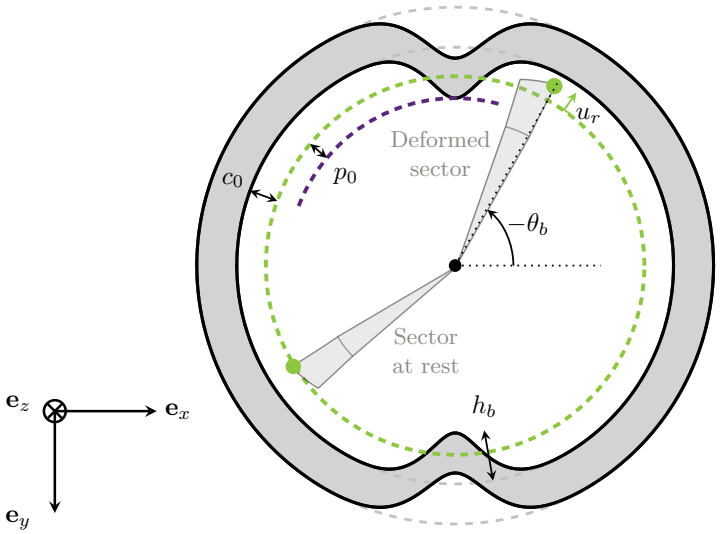

FIGURE 6.4 – Ovalization of the casing from (⬚) to (□), penetration of the casing profile (----) with respect to the circular trajectory (----) of a blade-tip node (●) of the sector at rest and definition of the parameters in Eq. (6.2) for the gap computation (not to scale).

The degrees-of-freedom of the 8 boundary nodes colored in Fig. 5.2 distributed between the nodes LE and TE are kept in the reduced space and define the contact interface. Possible penetrations and contact forces are computed at these nodes only.

As it is often the case for the simulation of blade-tip/casing structural contact simulations, aerodynamic forcing is neglected, *i.e.* $\mathbf{f}_e(t) = \mathbf{0}$ in (2.3). This assumption is consistent with the fact that rubbing interactions have been observed experimentally in vacuum chambers [152].

In the following, the clearance c_0 is set to 0.5 mm, and the height of bumps is defined as $h_b = 0.625$ mm. As detailed in section 3.1.1, contact is numerically handled with Lagrange multipliers and the equation of motion is integrated forward in time using an explicit central difference time integration scheme. Friction is modeled using a Coulomb law, with a friction coefficient $\mu = 0.15$. For the NASA rotor 37 studied, the relative speed between the blade-tip and the casing equals 454 m/s at its nominal speed. It is therefore justified to assume a permanent sliding, without sticking phase. Unless otherwise specified, the time step of integration is set to $h = 10^{-7}$ s.

As contact events may excite high-frequency modes, it is expected that reduction bases significantly larger than the ones used in chapter 5 should be considered to correctly capture the behavior of geometrically nonlinear blades subjected to contact interactions. As the parametric reduced-order models valid on a given angular speed interval introduced in section 5.6 require to multiply by a factor 3 the size of the reduction basis, this may become computationally expensive in the context of the study. In the following, it is therefore chosen to build reduced-order models at zero angular speed and to use them on the whole angular speed interval, neglecting the centrifugal and gyroscopic effects, but keeping in mind that parametric reduced-order models could allow to account for the angular speed effects.

6.3 Preliminary studies

In the context of geometrically linear structures, previous studies showed that the handling of contact with Lagrange multipliers (as described in section 3.1.1) in a Craig-Bampton reduced space allows to correctly capture the contact dynamics of industrial structures.This numerical strategy has been validated numerically against the more elaborated bi-potential formulation and the commercial software Ansys [132]. It has also been validated by comparison with experimental data [8, 16, 20].

When considering geometric nonlinearities, the comparison with full-order model results is feasible for simple academic structures, as in section 6.1, but not for industrial structures. Performance indicators, such as the one defined by (5.2) in section 5.3, can therefore not be directly used to assess the accuracy of the reduced model in the specific case of contact simulations. Different preliminary studies, including time and space convergence analyses, are therefore required in order to give confidence in the numerical models.

Preliminary computations are carried out for a single angular speed $\Omega = 1,400$ rad/s for which the influence of geometric nonlinearities is observed. The transient radial responses of the structure at node LE without and with geometric nonlinearities are compared in Fig. 6.5.

The steady-state responses are compared in Fig. 6.6. The responses have been obtained with a reduced model built with the modal derivative approach, considering $r_b = 24$ constraint modes (corresponding to the 8 boundary nodes kept in the reduced space), $r_c = 15$ fixed interface linear modes and $r_{\text{MD}} = 150$ modal derivatives selected with the selection criterion 2(b), as justified in section 5.4.3. This reduction basis is significantly larger than the reduction bases used in chapter 5 because more boundary nodes are kept in the reduced space to have an accurate description of the contact interface, and because contact events may excite higher frequency modes. The choice of the reduction method and of the corresponding reduction parameters is justified in the next section.

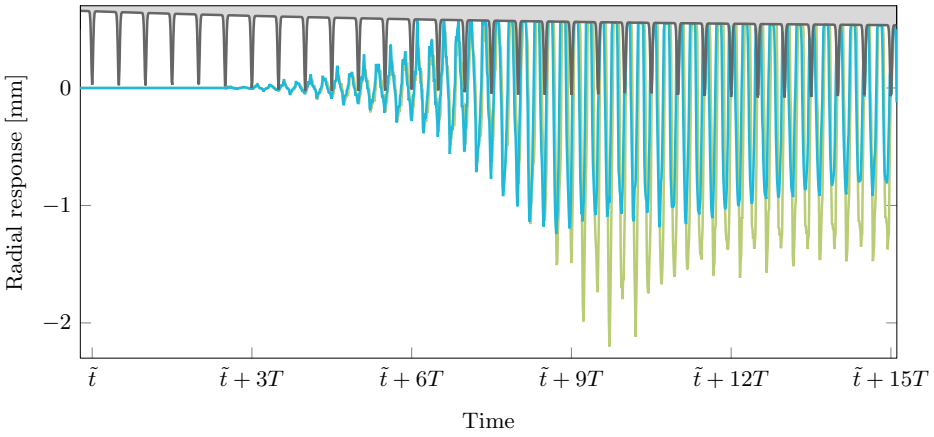

FIGURE 6.5 – Comparison of the transient responses of the blade at node LE in the radial direction at $\Omega = 1,400$ rad/s with geometric nonlinearities (——) and without geometric nonlinearities (——) with rigid casing (□).

During the simulation, the blade is first guided by the first bump on the casing, then oscillates freely until getting in contact with the second bump, and so on (see Fig. 6.5). When the amplitude of vibration increases, the blade can also impact the casing between the lobes, as it is the case at this angular speed. The comparison of the steady-state radial responses in Fig. 6.6a highlights significant differences in amplitude and in frequency content between both cases, even for radial displacement amplitude of the order of 1 mm. This motivates the extension of existing reduction methods to account for geometric nonlinearities in contact simulations. To give an idea of the order of magnitude of the 3D displacement field, the evolution of the tangential displacement is represented in Fig. 6.6b. At this angular speed, displacement amplitudes larger than 1 cm are computed without geometric nonlinearities, corresponding to nearly 20% of the height of the blade. This is therefore not surprising that geometric nonlinear effects are pronounced here.

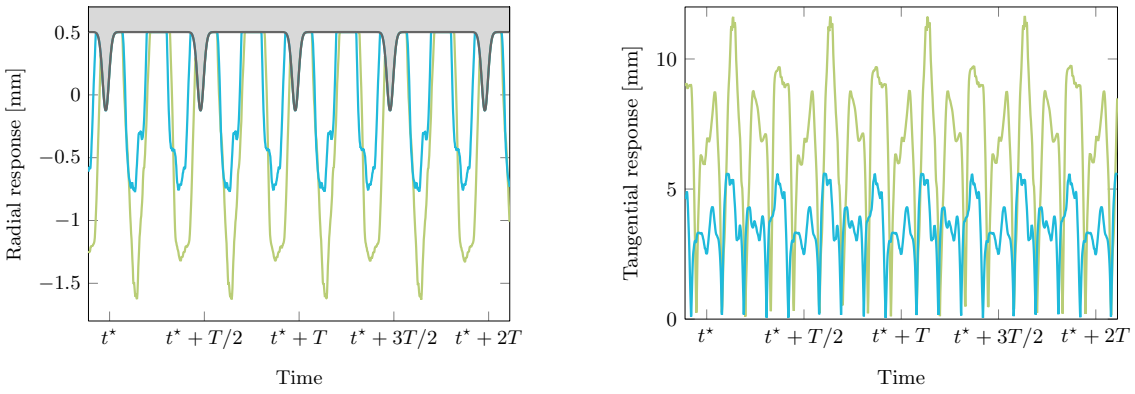

(a) Radial displacement.

(b) Tangential displacement.

FIGURE 6.6 – Comparison of the steady-state responses of the blade at node LE at $\Omega = 1,400$ rad/s with geometric nonlinearities (——) and without geometric nonlinearities (——) with rigid casing (□).

6.3.1 Time and space convergence

Convergence of the numerical procedure is first assessed with respect to the time step h of the time integration procedure described in section 3.1.1. While the use of an explicit time integration scheme implies small time steps, no iterative procedure is required for contact treatment at each time step. In the present case, time steps smaller than 10^{-6} s are required to ensure stable computations due to the high eigenfrequencies of the blade. Figure 6.7 shows the time responses obtained with the modal derivative reduction approach when considering the values $h = 10^{-7}$ s and $h = 10^{-8}$ s for the time step of integration. It confirms that the value $h = 10^{-7}$ s is sufficiently small to accurately predict the displacement of the blade. Similar conclusions hold when considering reduced-order models built by POD.

The asymptotic convergence of the numerical procedure is then assessed with respect to the reduction parameters, in particular with respect to the number of modes in the reduction basis. Because contact events may yield the participation of potentially high-frequency vibration modes, a larger number of modes have to be included in the reduction basis compared to the previous study case with a harmonic excitation. Three reduced-order models are built with the modal derivative approach. They are characterized by $r_b = 24$ constraint modes, $r_c = 15$ fixed interface linear normal modes and respectively $r_{\mathrm{MD}} = 100$, $r_{\mathrm{MD}} = 150$ and $r_{\mathrm{MD}} = 175$ modal derivatives. The responses obtained with these reduced-order models are compared in Fig. 6.8. The results demonstrate the need to include a sufficiently high number of modal derivatives in the reduction basis. Here, $r_{\mathrm{MD}} = 150$ modal derivatives are required

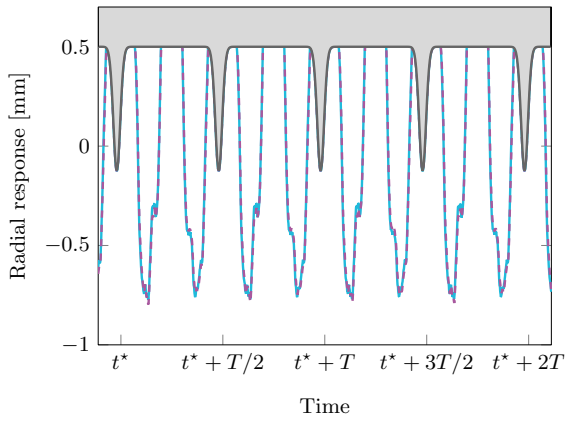

FIGURE 6.7 – Influence of the time step h of the time integration procedure on the response of the blade at node LE at $\Omega = 1,400$ rad/s: $h = 10^{-7}$ s (——), $h = 10^{-8}$ s (- - - -).

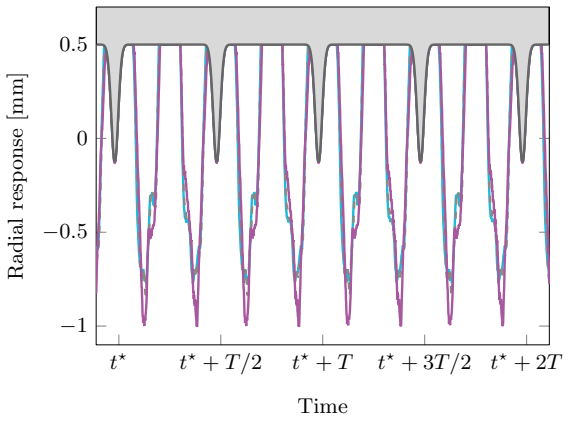

FIGURE 6.8 – Influence of the number of modal derivatives r_{MD} on the response of the blade at node LE at $\Omega = 1,400$ rad/s: $r_{\text{MD}} = 100$ (——), $r_{\text{MD}} = 150$ (——), $r_{\text{MD}} = 175$ (- - - -).

to converge. The weights associated to each modal derivative and the specific modal derivatives selected are represented in Fig. 6.9. The selected modal derivatives ($\star$) correspond to the modal derivatives of the static modes with respect to the generalized coordinates of the static modes and of the first internal modes with respect to the generalized coordinates of the static modes corresponding to the middle of the blade-tip. When building reduced-order models by POD, 30 POD modes are required to reach the asymptotic convergence of the results.

Lastly, the influence of the number of blade-tip nodes retained in the reduced space where possible penetrations are detected is analyzed. The responses computed with 1, 6 and 8 blade-tip nodes (*i.e.* 3, 18 and 24 boundary degrees-of-freedom) are shown in Fig. 6.10. As expected, very different results are obtained when checking for contact only at node LE or at several nodes distributed on the blade-tip surface. The results show that considering 6 blade-tip nodes or more distributed between the leading edge and the trailing edge provides a good description of the contact surface for the contact simulations.

6.3.2 Comparison of the reduction methods

In this section, the time responses predicted with the POD and modal derivatives reduction methods are compared for the time and reduction parameters identified in the previous section. The analyses conducted in section 5.5.3 showed that the training excitation used to

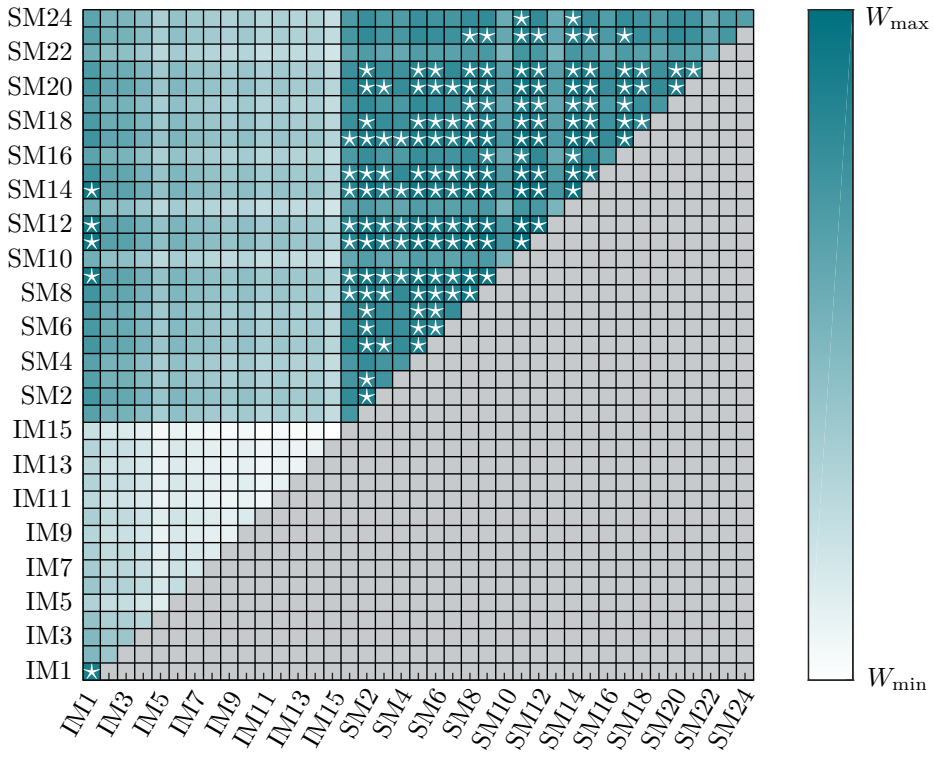

FIGURE 6.9 – Weights $W_{jk}^{(2b)}$ associated to each modal derivative and selected modal derivatives ($\star$) for the contact simulations (logarithmic scale).

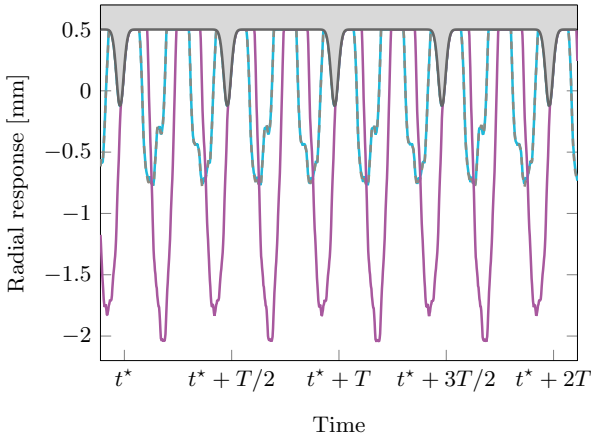

FIGURE 6.10 – Influence of the number of blade-tip nodes used to define the contact interface on the response of the blade at node LE at $\Omega = 1,400$ rad/s: $r_b = 3$ (——), $r_b = 18$ (- - - -), $r_b = 24$ (——).

build the POD reduction basis has to be defined as close as possible to the actual excitation. In the case of contact studies, the excitation is however not known *a priori*.

As a first step, the training excitation of the POD method is defined as a harmonic excitation in the radial direction. The response obtained with this reduced model is compared with the response obtained with the reduced model built with the modal derivative approach in Fig. 6.11. The responses are in good agreement during the first time steps of the simulation, but the accumulation of errors leads to very different time signals in the steady-state regime.

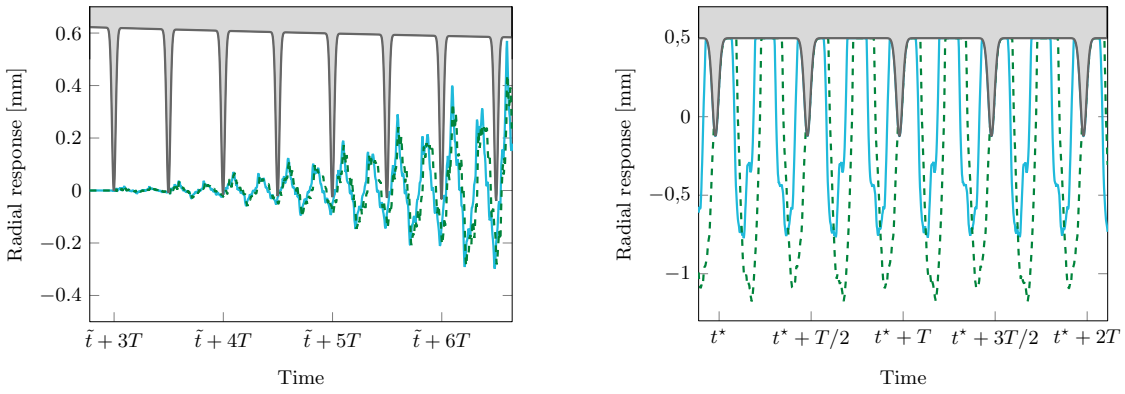

(a) Transient regime.

(b) Steady-state regime.

FIGURE 6.11 – Comparison of the responses of the blade at node LE at $\Omega = 1,400$ rad/s computed with the modal derivative approach (——) and with the POD approach with a harmonic training excitation (- - - -).

As a second step, the training excitation of the POD method is defined as the contact excitation predicted with the modal derivative reduced-order model during the first two cycles of revolution. The radial efforts at the leading edge, at mid-chord and at the trailing edge of the blade-tip are represented in Fig. 6.12.

The response obtained with this reduced model is compared with the response obtained with the reduced model built with the modal derivative approach in Fig. 6.13. An almost perfect agreement between the responses in steady-state regime is observed. Several conclusions can be drawn. First, the difference between the responses predicted with the POD method in Fig. 6.11 and in Fig. 6.13 confirms the extreme numerical sensitivity of the POD reduction method to the training excitation. In practice, it is necessary to know *a priori* the excitation to obtain good results with the POD reduction method, which is not possible in the case of contact simulations. The reduction method by POD is therefore considered not suitable for the present application. Second, this comparison gives confidence in the modal deriva-

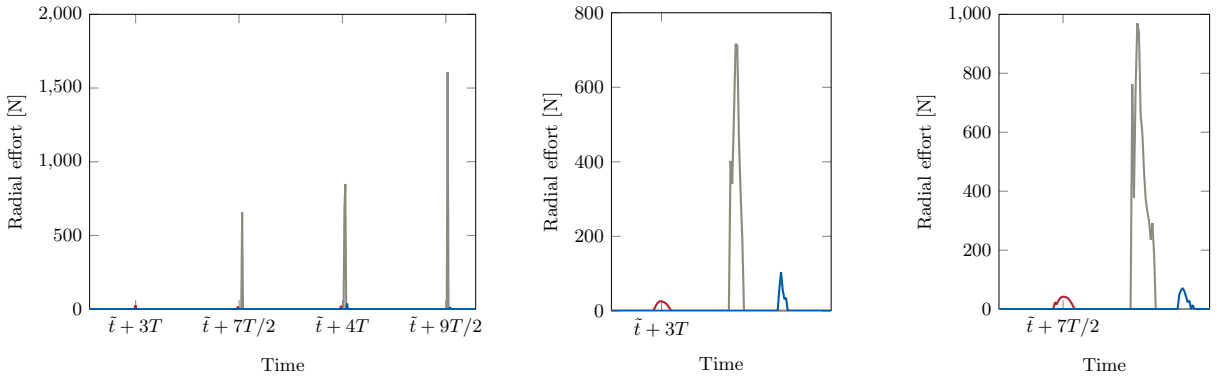

(a) First 2 cycles of revolution. (b) Zoom on the first bump. (c) Zoom on the second bump.

FIGURE 6.12 – Radial effort computed with the modal derivative approach at the leading edge (——), at mid-chord (——) and at the trailing edge (——) of the blade-tip at $\Omega = 1,400$ rad/s.

tive approach to predict contact responses of geometrically nonlinear structures as very close results have been obtained by considering two different reduction bases built with two different approaches. The reduced model built with the modal derivative approach is therefore selected to perform more detailed studies.

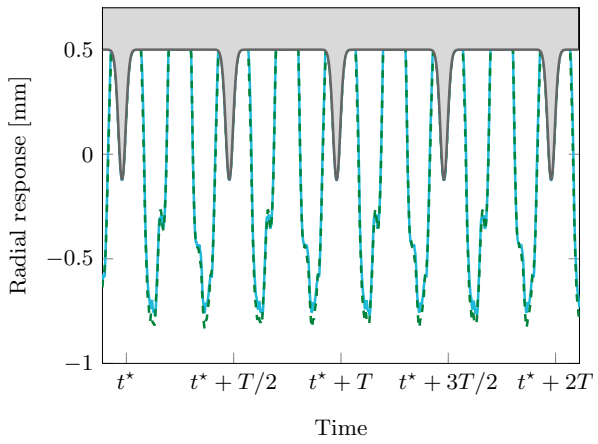

FIGURE 6.13 – Comparison of the responses of the blade at node LE at $\Omega = 1,400$ rad/s computed with the modal derivative approach (——) and with the POD approach with the contact excitation computed with the modal derivative approach (- - - -).

6.4 Clearance consumption

Before embarking in the full analysis of the blade contact dynamics, this section is dedicated to a very important concept in contact dynamics: the clearance consumption, which describes the evolution of the gap between the blade and the casing when the blade vibrates along one of its vibration modes. This concept is important for (at least) two reasons. First, it is directly related to the sensitivity of the blade to rotor/stator interactions. Then, the accuracy of a model to compute the clearance consumption is directly linked to its accuracy to describe the blade-tip radial displacement, which is a key parameter in contact dynamics. As the clearance consumption can be computed directly with the full-order model and compared to reduced-order model results, it is a good indicator of the accuracy of a reduced-order model.

6.4.1 Definition

Clearance consumption is a quantity describing the evolution of the clearance between the blade and the casing as the blade vibrates along one of its free vibration modes [22]. The clearance consumption Δ is computed at a given blade-tip node for a given amplitude of deformation δ as

$$\Delta(\delta) = c_0 - c(\delta), \tag{6.3}$$

where c_0 stands for the clearance at rest and $c(\delta)$ stands for the clearance computed at the level of deformation δ. In the following, $\Delta_\delta^{\mathrm{X}}$ and c_δ^{X} respectively denote the clearance consumption and the clearance in deformation mode X at the level of deformation δ. Figure 6.14 schematically represents the clearance consumption computed for two levels of deformation $\delta = +1$ and $\delta = -1$ for the first bending mode (1B). When $\Delta < 0$, the clearance between the blade and the casing is increased (as for the deformed blade (——) in Fig. 6.14). When $\Delta > 0$, the clearance between the blade and the casing is decreased (as for the deformed blade (——) in Fig. 6.14). It should be noted that the clearance is defined as the distance between the blade-tip node considered and its closer counterpart on the casing. Because of the casing conicity (see Fig. 6.3), the clearance consumption is usually different from the node radial displacement computed in the $\mathrm{O}\mathbf{e}_x\mathbf{e}_y$ plane. These quantities are only equal if the contact surface is perfectly cylindrical.

Clearance consumption has been identified as a key parameter for the design of blades subjected to contact interactions [19, 22]. Blades with lower clearance consumption, *i.e.* for which the blade/casing clearance remains almost constant as the blade vibrates along its first vibration modes, feature lower vibration response to contact. Criteria based on the notion of clearance consumption are therefore developed to estimate blade sensitivity to contact interactions and optimize blade profiles [127].

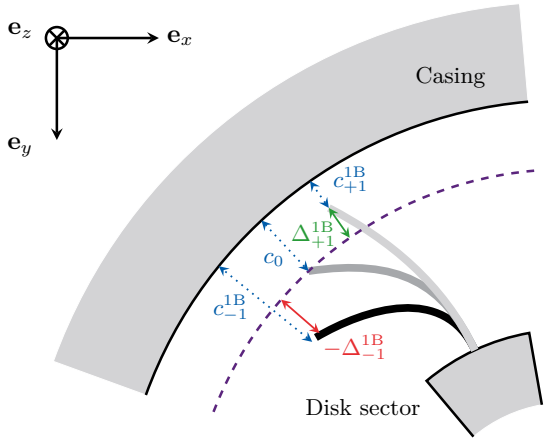

FIGURE 6.14 – Schematic representation of the clearance consumption with blade at rest (——), bended blade for $\delta = +1$ (——) and bended blade for $\delta = -1$ (——).

6.4.2 Geometric nonlinearities influence

The value of the clearance consumption Δ is looked at over a certain amplitude of deformation such that the radial displacement of the blade-tip node at the leading edge $u_{LE,r}$ satisfies

$$|u_{LE,r}| \leqslant \zeta, \tag{6.4}$$

where ζ is a threshold defined further. In practice, a linear modal analysis of the blade finite element model is first performed. This yields the studied mode $\boldsymbol{\phi}^{\mathrm{X}}$, which is normalized so that the radial displacement $u_{LE,r}$ reaches the limit value ζ. A linear static analysis is then performed to recover the external forces $\mathbf{f}_e^{\mathrm{X}}$ that cause the deformation field $\boldsymbol{\phi}^{\mathrm{X}}$. Static analyses with imposed forces $\delta\mathbf{f}_e^{\mathrm{X}}$ are then performed for different values of δ between -1 and $+1$ and the displacement fields (and the corresponding values of the clearance consumption $\Delta_\delta^{\mathrm{X}}$) are computed. These static analyses can be either linear (*i.e.* neglecting the geometric nonlinearities) or nonlinear and therefore allow to assess the influence of geometric nonlinearities. As the procedure is only based on cheap static computations, it can be applied to the full-order finite element model and reference results can be obtained.

The clearance consumption is computed at the leading edge (node LE) for the first bending mode and the first torsion mode of the blade. The parameter ζ is fixed to 1 mm for the first bending mode and 0.5 mm for the first torsion mode. The results obtained with the full-order finite element model with linear and nonlinear solvers are given in Fig. 6.15. These results show that the clearance consumption is reduced in both cases when geometric nonlinearities are taken into account. It is therefore expected that the blade with geometric nonlinearities features lower vibration response to contact.

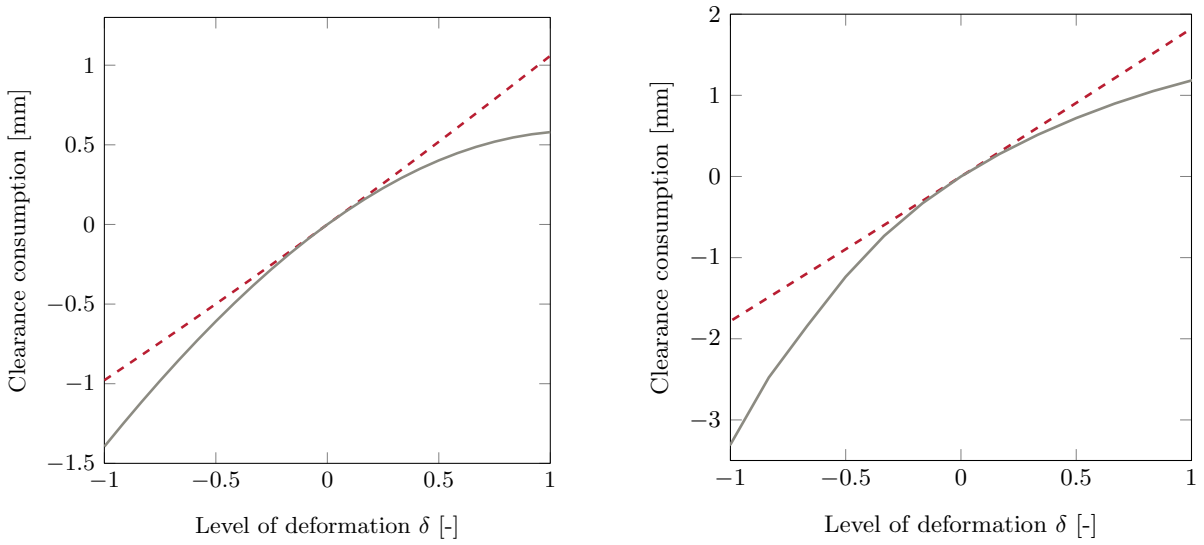

(a) First bending mode.

(b) First torsion mode.

FIGURE 6.15 – Clearance consumption at the leading edge computed with the full-order finite element model with linear (- - - -) and nonlinear (——) solvers.

The results also highlight that the use of the linear model has to be restricted to small deformations. The relative error made on the clearance consumption with the linear model exceeds 10% when the level of deformation δ is outside the interval $[-0.25\,,\,0.2]$ for the first bending mode and outside the interval $[-0.1\,,\,0.1]$ for the first torsion mode.

6.4.3 Reduced-order model accuracy

When studying rubbing phenomena, a very accurate description of the contact interface and of the clearance evolution is required. Reduced-order models should therefore be able to evaluate accurately the clearance consumption. As exact results can be computed with the full-order finite element model, the accuracy of the ROM can be easily assessed by computing the clearance consumption with the ROM itself. The clearance consumption is computed in the same conditions as previously with the reduced-order model used in section 6.3 characterized by $r_b = 24$, $r_c = 15$ and $r_{\text{MD}} = 150$. The clearance consumption is also computed with two other ROMs: one based on a smaller reduction basis characterized by $r_{\text{MD}} = 100$ and one with a larger reduction basis with $r_{\text{MD}} = 175$. The results accounting for geometric nonlinearities are given in Fig. 6.16 where they are also compared with the full-order model results.

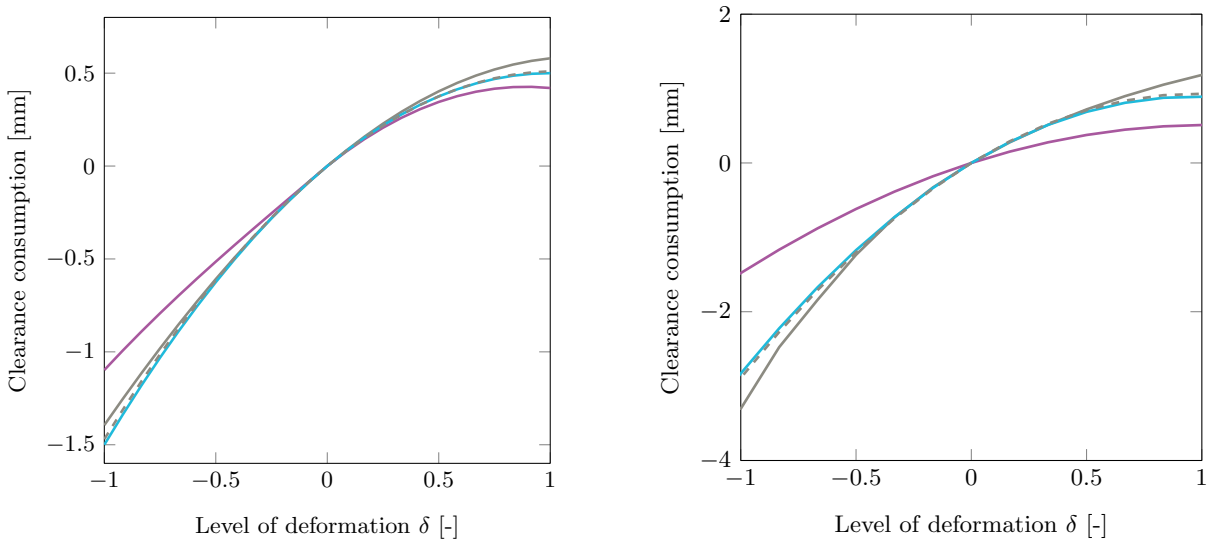

(a) First bending mode.

(b) First torsion mode.

FIGURE 6.16 – Clearance consumption at LE computed with a nonlinear solver with the full-order finite element model (——) and the reduced-order models with $r_{\mathrm{MD}} = 100$ (——), $r_{\mathrm{MD}} = 150$ (——) and $r_{\mathrm{MD}} = 175$ (- - - -) modal derivatives.

These results confirm that the ROM with 100 modal derivatives does not allow to accurately evaluate the clearance between the blade and the casing and is therefore not suitable for contact simulations. The results however give confidence in the reduced-order model used previously for the contact simulations as it allows to compute accurately the clearance consumption (with relative errors less than 10%). Increasing the number of modal derivatives in the reduction basis does not have a significant influence on the results. The results also suggest that clearance consumption could be a good criterion to assess the accuracy of the reduced-order model without having to perform costly contact simulations.

6.5 Direct blade/casing contact

The numerical strategy based on the modal derivative approach is used to study the contact dynamics of the blade on a wider angular speed interval. In this first contact scenario, the rotating blade directly impacts the rigid surrounding casing.

6.5.1 Interaction map

Simulations at constant angular speed are performed over the angular speed range from 750 rad/s to 1,600 rad/s (with a step of 2 rad/s). Given the Campbell diagram of the NASA rotor 37 blade (see Fig. 5.22), this angular speed interval includes the main critical speeds corresponding to intersections between the first bending mode and the engine order lines 4 and 6 that are below the nominal speed Ω_N. For each angular speed, the evolution of the blade-tip nodes radial displacement is computed over 200 cycles of revolution, starting from zero initial conditions. The frequency content of the radial displacement is then computed at each angular speed, on the second half of the time signal to get rid of transient effects. The corresponding interaction maps are plotted in Fig. 6.17a in the case where geometric nonlinearities are not considered and in Fig. 6.17b in the case where geometric nonlinearities are taken into account. Both maps have the same color scale from blue (lowest amplitudes) to red (highest amplitudes). The first eigenfrequencies and the engine order lines (where the frequency is an integer multiple of the angular speed) are also shown in these maps.

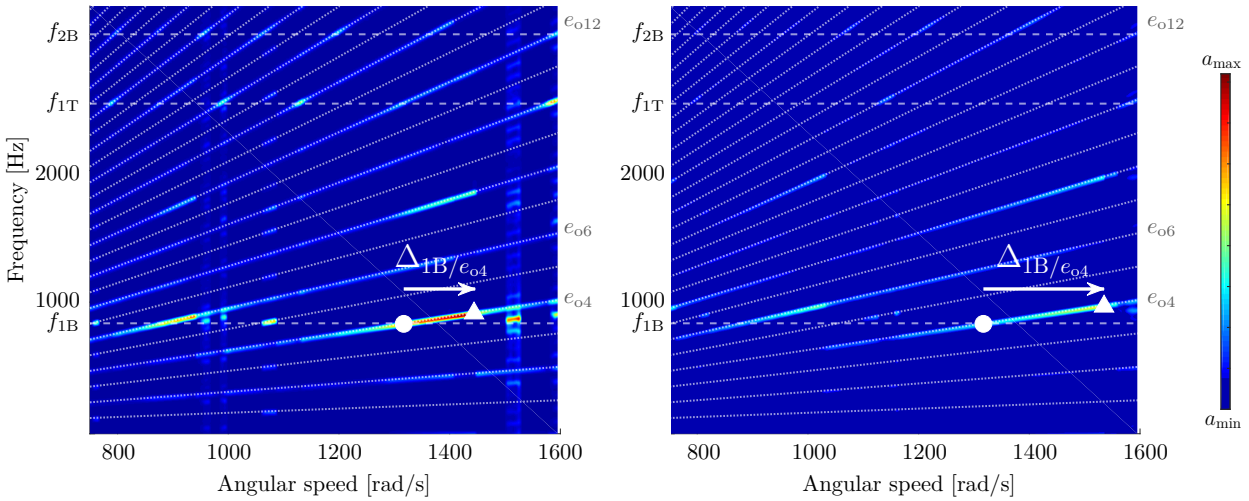

(a) Without geometric nonlinearities.

(b) With geometric nonlinearities.

FIGURE 6.17 – Interaction maps of the radial displacement at node *LE* for the case with direct contact with eigenfrequencies (- - - -), engine order lines (·····), predicted linear resonance (●) and predicted nonlinear resonance (▲).

Both interaction maps show lines of higher amplitudes on even engine order lines, which is consistent with the fact that the casing ovalization leads to an excitation occurring twice per revolution. Non-integer harmonics of the angular speed are also visible around 1,525 rad/s in Fig. 6.17a and around 1,600 rad/s in Fig. 6.17b, which can be related to the nonlinear

nature of the dynamics. It can also be noted that geometric nonlinearities reduce globally the amplitude of vibrations in the whole angular speed range.

The interaction maps highlight the existence of strong contact interactions between the first vibration modes of the blade and the even engine orders. These interactions are characterized by high amplitudes of vibration followed by jumps where the amplitude of the displacement suddenly drops for a small change of the angular speed. Both maps highlight the existence of contact interactions between the first bending mode and the sixth engine order, between the first bending mode and fourth engine order, but also between the first torsion mode and the fourteenth engine order for instance.

In the following, we focus on the interaction between the first bending mode and the fourth engine order denoted by $1B/e_{o4}$, which is the closest from the nominal speed of the structure. Because of contact stiffening, the maximal amplitudes are not reached at the exact intersection between the first bending mode line and the fourth engine order line (●) but are shifted toward higher angular speeds (▲). In a linear context, the studied resonance occurs at $\Omega = 1,317$ rad/s. In the case where geometric nonlinearities are neglected, contact stiffening shifts this resonance to $\Omega = 1,446$ rad/s, which corresponds to a contact stiffening of 9.8%. In the case where geometric nonlinearities are considered, the contact stiffening seems more pronounced as the maximal amplitudes of vibration occur at $\Omega = 1,535$ rad/s, which corresponds to a contact stiffening of 16.6%.

In order to better visualize the jump in the amplitude response of the blade in the vicinity of the interaction speed, the infinity norm of the blade's leading edge radial displacement is depicted in Fig. 6.18 on a limited angular speed range around the intersection $1B/e_{o4}$ in the cases where geometric nonlinearities are neglected and where they are considered. This figure confirms the previous observations. Geometric nonlinearities seem to be responsible for an additional contact stiffening but give rise to interactions of lower amplitudes.

The analysis of the clearance consumption in section 6.4 has shown that the blade with geometric nonlinearities has a smaller clearance consumption compared to the linear blade. These results justify that the blade with geometric nonlinearities features lower vibration response to contact, as observed here when comparing the interactions maps without and with geometric nonlinearities (Fig. 6.17) and the associated nonlinear frequency response curves (Fig. 6.18).

Regarding the additional contact stiffening that seems to be caused by the geometric nonlinearities, more in-depth investigations are performed in the next section where a continuation procedure is used in the contact simulations to build the nonlinear frequency response curves.

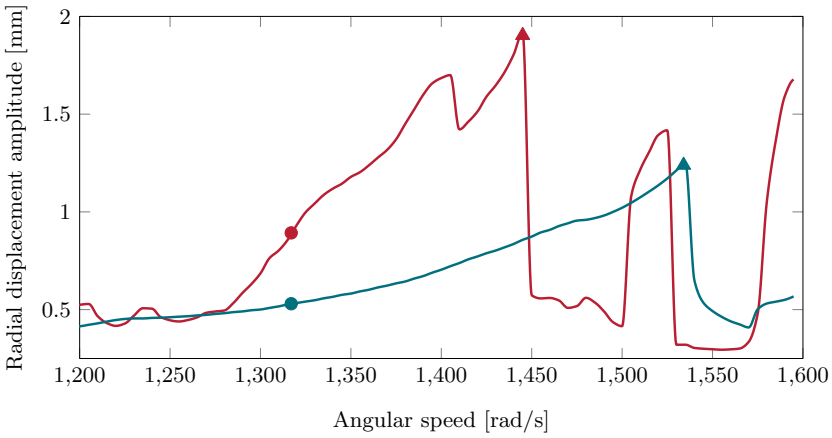

FIGURE 6.18 – Nonlinear frequency response curves of the radial displacement at node LE in the cases where geometric nonlinearities are not considered (——) and where geometric nonlinearities are considered (——) with predicted linear resonance (●) and predicted nonlinear resonance (▲).

6.5.2 Sequential continuation

The amplitude jumps in Fig. 6.18 reveal that the numerical procedure does not capture all solutions and that there certainly exist several branches of solutions near these jumps. Such solutions could be obtained by time integration, starting from well chosen initial conditions, or using frequency methods, such as methods derived from the harmonic balance method [52]. With the results in section 6.5.1, there is no way to ensure that the predicted nonlinear resonances are accurate as higher amplitude solutions that are not captured with the zero initial conditions used to build the curve could exist.

In order to better quantify the contact stiffening, the nonlinear frequency response curve (NFRC) of the blade is built using a sequential continuation procedure. In practice, contact simulations are performed at each angular speed of the studied interval successively, taking as initial conditions of simulation i the final conditions of simulation $i-1$. The first contact simulation is conducted over 200 cycles, in order to reach the steady-state regime, while the following ones are limited to 30 cycles. A step of 2 rad/s is considered. If the steady-state regime is not reached, the step is divided by 2 (with a maximum of 3 divisions). It should be noted that the objective here is not to build the complete nonlinear frequency response curve (with all bifurcations, internal loops, ...), which would require more sophisticated tools, but mainly to correctly assess the contact stiffening. The sequential continuation procedure used here has been validated in the case without geometric nonlinearities by comparison

with the results obtained with a frequency method (RL-HBM) [52]. Note that the optimized implementation described in section 3.1.2 cannot be used in this case as it is necessary to wait for the end of simulation i before starting simulation $i+1$.

The nonlinear frequency response curves computed with the continuation procedure (with upward and downward angular speed sweeps) are given in Fig. 6.19a in the case where geometric nonlinearities are neglected and in Fig. 6.19b in the case they are considered. These curves are also compared to the curves of Fig. 6.18 (obtained from zero initial conditions).

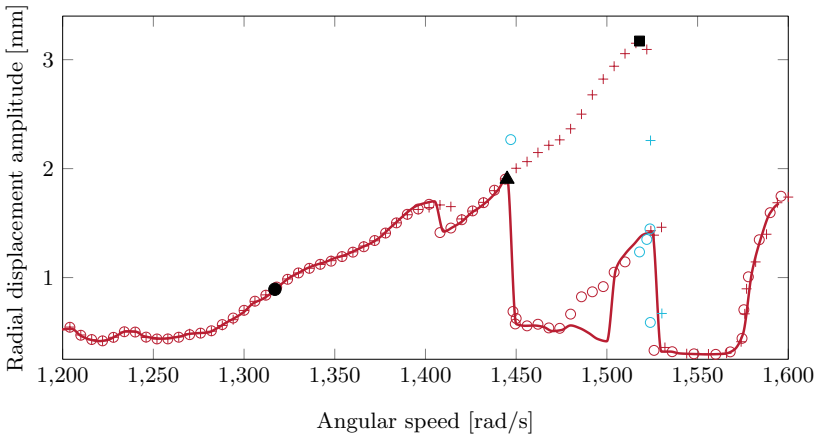

(a) Without geometric nonlinearities.

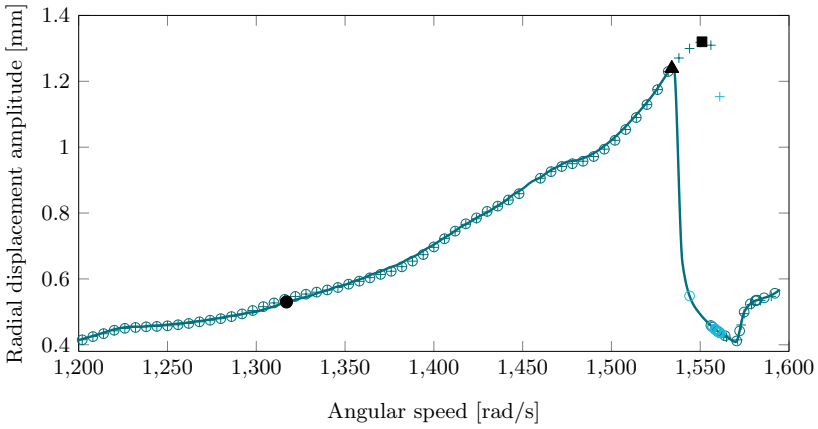

(b) With geometric nonlinearities.

FIGURE 6.19 – Nonlinear frequency response curves without continuation (——) and with continuation (upward (+) and downward (○) angular speed sweeps, simulations where steady-state regime is not reached (+/○)) with predicted linear resonance (●), predicted nonlinear resonance without continuation (▲) and predicted nonlinear resonance with continuation (■).

These figures confirm that the nonlinear resonances were not correctly captured in Fig. 6.18 with simulations starting from zero initial conditions as the continuation procedure highlights the existence of higher amplitude solutions. In the case where geometric nonlinearities are neglected, the nonlinear resonance predicted at $\Omega = 1,446$ rad/s (▲) appears to occur at $\Omega = 1,520$ rad/s (■), which corresponds to a contact stiffening of 15.4%, and leads to amplitudes of vibration more than 50% greater. In the case where geometric nonlinearities are considered, the nonlinear resonance predicted at $\Omega = 1,535$ rad/s (▲) is only slightly shifted to $\Omega = 1,551$ rad/s (■), which corresponds to a contact stiffening of 17.7%, and was therefore well approximated in Fig. 6.18. Neglecting the geometric nonlinearities leads to amplitudes of vibration at the resonance more than two times larger compared to the case with geometric nonlinearities, which is consistent with the clearance consumption analysis in section 6.4.

Even if this was not the objective here, the results also show the existence of other branches of solutions that were not captured in Fig. 6.18 when starting from zero initial conditions. For instance, in the case where geometric nonlinearities are neglected, Fig. 6.18 predicts a low-amplitude branch between 1,475 rad/s and 1,500 rad/s with periodic solutions of period $T/2$. Using the continuation procedure with downward angular speed sweep (see Fig. 6.19a), a higher amplitude branch is obtained on the same angular speed interval, with periodic solutions of period $11T/2$.

These results show that the contact stiffening has to be carefully quantified with appropriate tools to follow the high-amplitude branch of the response and locate correctly the resonance. Also, the observation (in section 6.5.1) that geometric nonlinearities are responsible for a significant additional contact stiffening should be put in perspective. Indeed, results obtained with the continuation procedure show that the contact stiffening with geometric nonlinearities is only slightly greater than the actual stiffening without geometric nonlinearities.

6.5.3 Stress analysis

From an industrial point of view, the stress field in the blade is an important global quantity of interest as it is directly related to the structure integrity. If the maximal stress level exceeds the material yield stress, irreversible deformations may occur, leading eventually to the failure of the structure. Stress fields are here analyzed for the interaction $1B/e_{o4}$, at the nonlinear resonances predicted without continuation, which are indicated by (▲) in the interaction maps in Fig. 6.17. The von Mises stress fields computed at time $t_{\max}$, different for both cases, where the node LE reaches its maximal radial displacement are represented in Fig. 6.20.

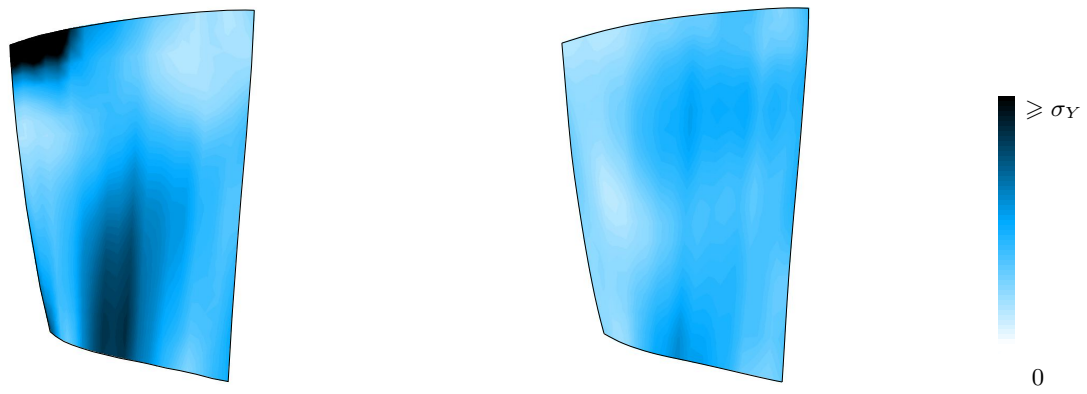

(a) Without geometric nonlinearities. (b) With geometric nonlinearities.

FIGURE 6.20 – Comparison of the von Mises stress fields at $t_{\max}$.

At these interactions, the response of the structure is dominated by the first bending mode of the blade, which shows slightly different shapes when geometric nonlinearities are considered or not. The zones of maximal von Mises stresses are not located at the same place in both cases. When geometric nonlinearities are neglected, the maximal stresses are found near the root of the blade and near the trailing edge at the blade-tip. When considering the geometric nonlinearities, the zone of maximal stresses appears toward the center of the blade. These results suggest that accounting for geometric nonlinearities in bladed disk models could have a significant influence in terms of blade design [121].

Quantitatively, the ratio of the maximal von Mises stresses in both cases is in line with the corresponding ratio of maximal displacements at the blade-tip leading edge (about 2). This confirms that, in the studied case, geometric nonlinearities weaken the interactions, not only locally at the blade-tip, but also globally in the whole blade. The analysis of the stress field at the other interaction angular speeds confirms that the severity of the interaction in terms of displacement amplitudes is reflected in the maximal values of the von Mises stress. Neglecting geometric nonlinearities leads to an overestimation of the stress level in the blade. It is also important to note that in the case where geometric nonlinearities are neglected, stresses higher than the material yield stress are obtained in the blade while the blade remains in the elastic domain when geometric nonlinearities are taken into account.

6.5.4 Computational cost

When performing the simulations at the different angular speeds independently, *i.e.* without memory sharing for the evaluation of the nonlinear internal forces as described in section 3.1.2, each single simulation over 200 cycles takes approximately 10 hours (single CPU sequential

time on an Intel Xeon E5-2698 v4 processor – 2.2 GHz). Building the full interaction map with geometric nonlinearities in Fig. 6.17b, therefore takes approximately 400 hours on 10 cores.

The numerical strategy with memory sharing described in section 3.1.2 allows to considerably reduce computation times. With the considered reduced-order model, building the full interaction map with geometric nonlinearities takes approximately 50 hours on 10 cores on the same computer.

6.6 Blade/casing contact with abradable coating

As explained in section 2.4.3, an abradable coating is usually added along the casing contact surface to mitigate vibratory phenomena. This coating acts as a sacrificial material that is worn out in the case of blade/casing contact. In this section, the methodology is adapted to model the wear of this abradable coating and is then used to perform contact simulations.

6.6.1 Wear modeling

The wear of the abradable coating is modeled by one-dimensional plastic compression [133]. The abradable coating is discretized with one-dimensional two-node rod elements independent from their adjacent neighbors and a linear isotropic hardening law is considered.

The algorithm described in section 3.1.1 is used to integrate the equation of motion forward in time. At each time step, the displacement is predicted using (3.5). The predicted displacement field is then used to evaluate the gap between the impacting nodes on the blade and the abradable coating and between the blade and the casing. If penetrations are detected between the impacting nodes and the abradable coating, the contact forces $\tilde{\mathbf{f}}_{c,n+1}$ are computed through the use of massless compression elements with a piecewise linear plastic law [133]. The abradable coating thickness is then locally reduced to account for abradable removal. If penetrations are detected between the blade and the rigid casing, the contact forces are computed as described in section 3.1.1. In both cases, the contact forces are then used to correct the non-admissible displacements.

Note that the frequency methods introduced in section 3.2 can currently not account for the possible wear of an abradable coating, as this is linked to a time dependence of the surface contact.

In the following, the abradable material is characterized by a Young's modulus $E = 4$ GPa, a plastic modulus $K = 1$ GPa, and a yield stress $\sigma_Y = 1.5$ MPa, which is consistent with values encountered in the literature [140]. An abradable coating thickness of 5 mm is consid-

ered. The coating is modeled with 20,000 abradable elements distributed along the casing circumference.

6.6.2 Results

The blade-tip radial displacement at LE is analyzed for the second contact scenario, with an abradable coating deposited on the casing. The interaction maps without and with geometric nonlinearities are shown in Fig. 6.21 with the same color scale as in Fig. 6.17. These interaction maps are computed as in Fig. 6.17, by performing simulations at constant angular speed Ω between 750 rad/s and 1,600 rad/s, starting from zero initial conditions. The nonlinear frequency response curves around the intersection $1B/e_{o4}$ are shown in Fig. 6.22 and compared with the NFRC obtained for the first contact scenario with direct contact between the blade and the casing.

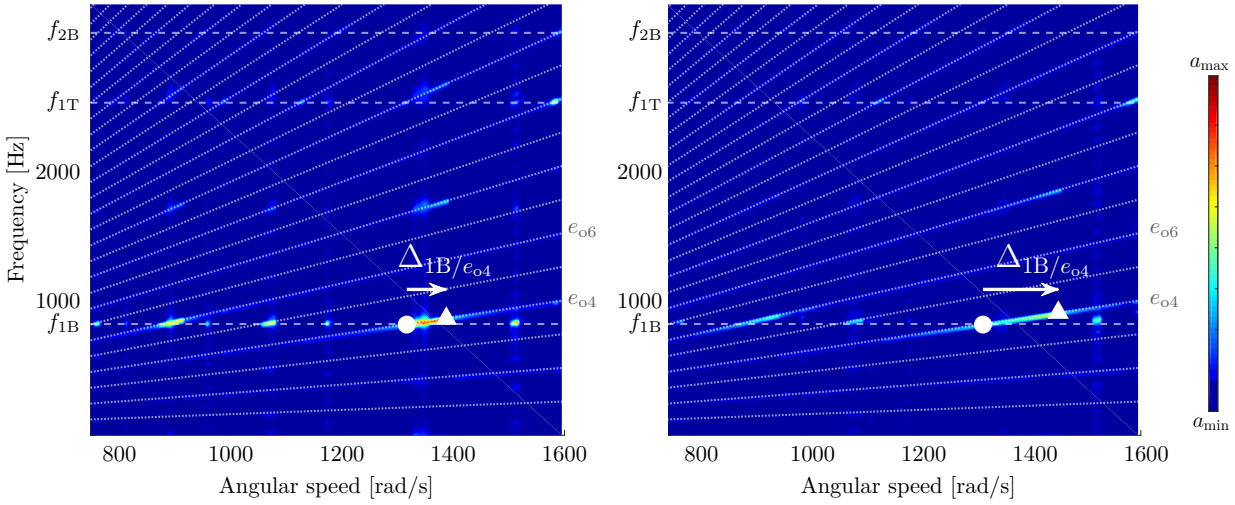

(a) Without geometric nonlinearities. (b) With geometric nonlinearities.

FIGURE 6.21 – Interaction maps of the radial displacement at node LE for the case with an abradable coating with eigenfrequencies (- - - -), engine order lines (·····), predicted linear resonance (●) and predicted nonlinear resonance (▲).

These results show that the spans of the interactions are reduced compared to the first contact scenario with direct contact: high displacement amplitudes are reached on narrower angular speed intervals. The maximal amplitude is also slightly reduced in the presence of the abradable coating. Note that the interactions are still smoother, *i.e.* characterized by smaller maximal amplitudes, when geometric nonlinearities are considered.

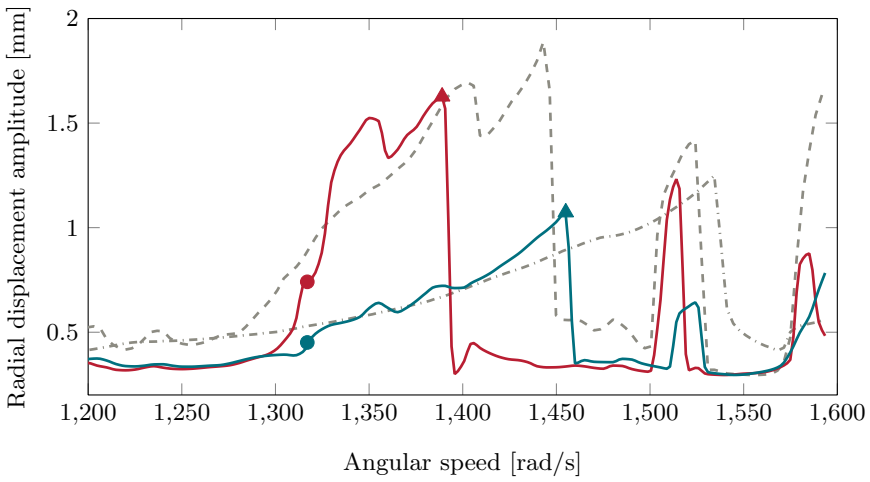

FIGURE 6.22 – Nonlinear frequency response curves of the radial displacement at node LE with an abradable coating in the cases where geometric nonlinearities are not considered (——) and where geometric nonlinearities are considered (——) with predicted linear resonance (●) and predicted nonlinear resonance (▲). In order to ease the comparison with Fig. 6.18, the RMS levels are also represented for the case with direct contact (without geometric nonlinearities (- - - -) and with geometric nonlinearities (-·-·-)).

It is also remarkable that the contact stiffening is reduced compared to the case with direct contact between the blade and the casing. For the case without geometric nonlinearities, the interaction $1\mathrm{B}/e_{\mathrm{o}4}$, now occurs at the angular speed $\Omega = 1,388$ rad/s. Geometric nonlinearities still seem to be responsible for an additional stiffening. The interaction $1\mathrm{B}/e_{\mathrm{o}4}$ occurs at the angular speed $\Omega = 1,452$ rad/s. However, in order to correctly quantify the contact stiffening of the structure, a continuation procedure should be used to build the nonlinear frequency response curve (as detailed in section 6.5.2).

The wear level of the abradable coating along the circumference is also computed at the end of the simulations at each angular speed. The corresponding wear maps are given in Fig. 6.23. The two horizontal lines that appear around $\theta = \pi/2$ rad and $\theta = 3\pi/2$ rad correspond to the wear of the two bumps that occurs rapidly at the beginning of the simulation. The final level of wear of the abradable coating between the lobes provides information on the type of interaction that occurred as deeper lobes are created at positions where the blade has impacted the casing repeatedly.

These interaction maps show that, in both cases, the abradable coating acts as a sacrificial material. This allows to mitigate contact severity, as highlighted in the interaction maps

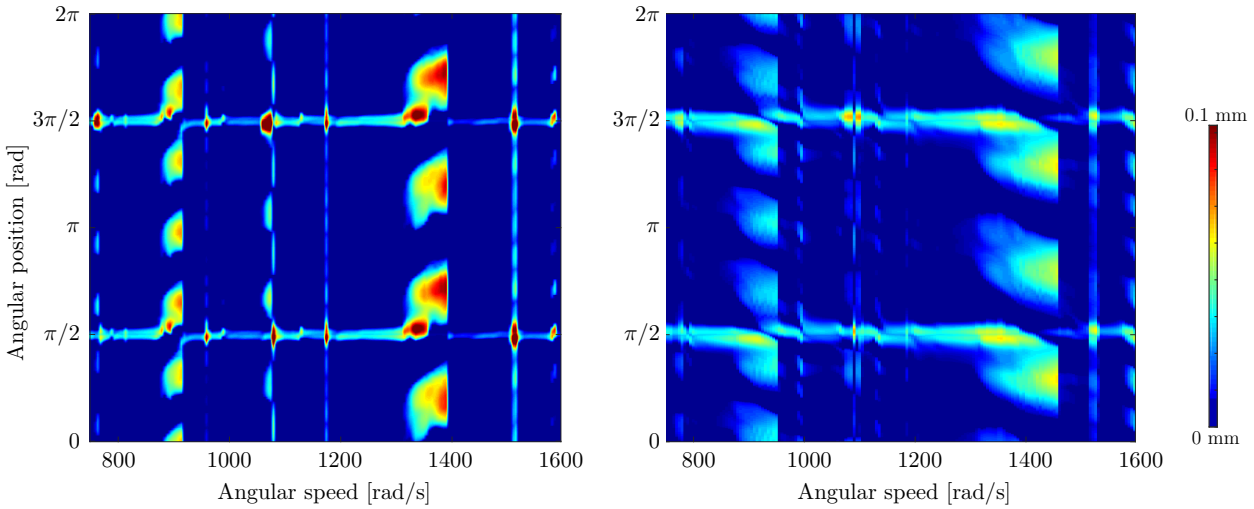

(a) Without geometric nonlinearities.

(b) With geometric nonlinearities.

FIGURE 6.23 – Abradable coating wear maps at node LE.

and the nonlinear frequency response curves. The interactions between the first bending mode and even engine orders are clearly visible in the wear maps in Fig. 6.23 that show the wear of 8, 6 or 4 lobes in the abradable coating at the angular speeds corresponding to the interactions.

6.7 Partial conclusions

The study of the NASA rotor 37 blade subjected to contact events allowed to define a reduction procedure suitable to study structures with both geometric and contact nonlinearities. On the one hand, reduction methods by proper orthogonal decomposition are difficult to use in the context of contact dynamics as the contact excitation is not known *a priori*, making it arduous to define an accurate POD basis. On the other hand, modal derivatives provide an efficient framework for the reduction.

The final methodology is therefore based on the projection of the high fidelity model onto a basis composed of Craig-Bampton modes and a selection of their modal derivatives. Nonlinear internal forces due to large displacements are evaluated with the STEP and contact is numerically handled with Lagrange multipliers. The methodology can also account for an abradable coating deposited along the surrounding casing.

Even if the verification of this methodology by comparison with full-order model data is too costly for industrial structures, different analyses such as the application to an academic test case, the comparison with the POD method and the computation of the clearance consumption in the reduced space, give confidence in the methodology.

The numerical studies have shown that the reduction procedure developed allows to extract quantities of interest that are relevant for both researchers and industrial designers. In particular, it can be used to efficiently identify the critical angular speeds at which high-amplitude interactions occur and to assess the consequences of the interactions on the structure integrity, for instance in terms of stress fields inside the blade. Also, the methodology allows to bring a physical understanding of the nonlinear dynamics of blades and on the influence of geometric nonlinearities. The comparison of the results obtained without and with geometric nonlinearities shows that neglecting the geometric nonlinearities in such studies can lead to wrong estimation of the critical angular speeds of the structure and to poor evaluation of the severity of the interactions in terms of displacement amplitudes and von Mises stress fields.

CHAPTER 7 FULL BLADED DISK

The methodology developed and used in chapters 5 and 6 is limited to a single rotating blade. Real bladed disks are however composed of several blades assembled on a disk. The objective of this chapter is to generalize the single-blade methodology to full bladed disks.

This chapter begins with a short summary of the existing reduced-order modeling techniques relevant for cyclically symmetric structures, both in linear and nonlinear contexts. Based on this literature review, the methodology developed in the previous sections is then generalized to full bladed disks. The methodology is first validated on a geometrically nonlinear bladed disk model without contact events, and then used in contact simulations. It is finally used in combination with mistuning.

The results presented in this chapter are summarized in a manuscript currently under review [64].

7.1 Literature review

The different reduction methods presented in chapter 4 are general methods. In particular, they can be applied to cyclically symmetric structures, as tuned bladed disks. However, under this symmetry assumption, working directly with the structural matrices to build reduced-order models is not computationally efficient. This is particularly true when building ROMs of industrial nonlinear structures. Specific reduced-order techniques have therefore been developed to efficiently build reduced-order models of cyclically symmetric structures.

7.1.1 Linear reduced-order modeling

As detailed in section 2.2.2, the linear dynamics of cyclically symmetric structures is generally studied in the harmonic space where the dynamic problem can be written as a set of sub-problems for each harmonic using Fourier formalism [30, 166, 222]. This cyclic symmetry formulation can be used in classical linear reduced-order modeling techniques (such as Craig-Bampton or Craig-Martinez reduction methods presented in section 4.3.1) to efficiently compute the reduction basis [15].

7.1.2 Nonlinear reduced-order modeling

When geometric nonlinearities are considered or in the case of severe contact nonlinearities, the nonlinearities induce a coupling between the harmonic components and the cyclic symmetry formulation can therefore no longer be used. In this context, different projective reduction methods have been developed. They can be grouped in two categories: reduction methods where the structure is reduced as a whole and reduction methods where the structure is divided into individual sectors.

On the one hand, for simple structures, the equations of motion of the full finite element model of the cyclically symmetric structure can be directly projected onto a reduced space with a reduction basis intrinsically accounting for the nonlinear behavior of the structure based on modal derivatives [78, 80] or on POD [176] for instance. For more complex industrial structures, this reduction can be preceded by a first projection such as a modal reduction [178].

On the other hand, various reduction methods are based on Component Mode Synthesis [54, 96]: the structure dynamics is described by a set of modes of the individual sectors and interface (or constraint) modes that allow to account for the coupling between the sectors. Different definitions of the sector modes have been investigated in a nonlinear context such as linear modes augmented with modal derivatives [142,143] or nonlinear normal modes [103, 104].

7.2 Generalization of the methodology

In this work, the reduction methodology for single-blades is based on the concept of modal derivatives. This reduction method is combined here to a Component Mode Synthesis (CMS) technique and extended to full bladed disk structures. The bladed structure is divided into N_s sectors composed of one blade and the corresponding disk sector (see Fig. 7.1). In the case of a perfectly tuned bladed disk, the N_s sectors are identical. The degrees-of-freedom of sector n, $\mathbf{u}^n$, are partitioned according to

$$\mathbf{u}^n = \begin{bmatrix} \mathbf{u}^n_{\text{left}} \\ \mathbf{u}^n_i \\ \mathbf{u}^n_b \\ \mathbf{u}^n_{\text{right}} \end{bmatrix}, \tag{7.1}$$

where $\mathbf{u}^n_{\text{left}}$ and $\mathbf{u}^n_{\text{right}}$ respectively stand for the n_{left} and n_{right} degrees-of-freedom of the left and right cyclic boundaries (with $n_{\text{left}} = n_{\text{right}}$ because of mesh compatibility), $\mathbf{u}^n_b$ stands for

the r_b boundary degrees-of-freedom that are kept in the reduced space (*i.e.* the blade-tip degrees-of-freedom) and $\mathbf{u}_i^n$ stands for the n_i internal degrees-of-freedom that do not belong to any boundaries.

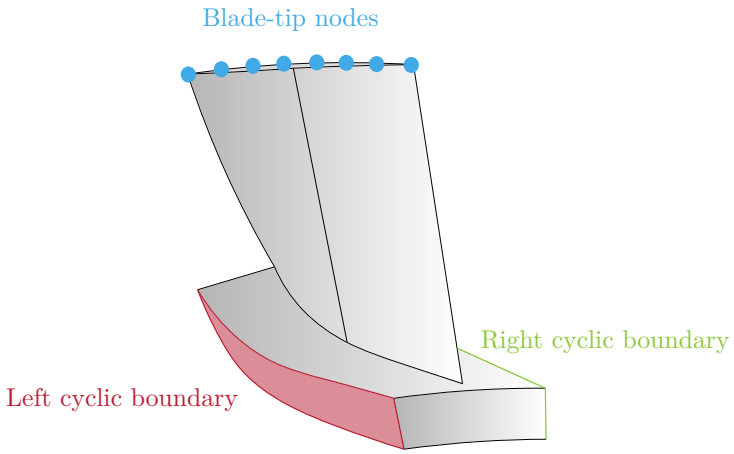

FIGURE 7.1 – Bladed disk sector with definition of the boundaries.

7.2.1 Reduction basis

In the proposed methodology, each sector is reduced in the same way as for the single-sector methodology, *i.e.* projected onto a basis composed of Craig-Bampton modes and a selection of their modal derivatives. The boundary degrees-of-freedom of the single-sector methodology are here defined as the blade-tip degrees-of-freedom and the cyclic boundaries. The reduction of the degrees-of-freedom of sector n therefore writes

$$\mathbf{u}^n = \begin{bmatrix} \mathbf{u}^n_{\text{left}} \\ \mathbf{u}^n_i \\ \mathbf{u}^n_b \\ \mathbf{u}^n_{\text{right}} \end{bmatrix} = \begin{bmatrix} \mathbf{I} & \mathbf{0} & \mathbf{0} & \mathbf{0} \\ \mathbf{\Psi}^n_{i,\text{left}} & \mathbf{\Phi}^n_i & \mathbf{\Psi}^n_{i,b} & \mathbf{\Psi}^n_{i,\text{right}} \\ \mathbf{0} & \mathbf{0} & \mathbf{I} & \mathbf{0} \\ \mathbf{0} & \mathbf{0} & \mathbf{0} & \mathbf{I} \end{bmatrix} \begin{bmatrix} \mathbf{u}^n_{\text{left}} \\ \boldsymbol{\eta}^n \\ \mathbf{u}^n_b \\ \mathbf{u}^n_{\text{right}} \end{bmatrix}; \tag{7.2}$$

where $\mathbf{\Psi}^n_{i,\text{left}}$, $\mathbf{\Psi}^n_{i,\text{right}}$ and $\mathbf{\Psi}^n_{i,b}$ are the constraint modes corresponding to the static deformations of the sector to unit displacements imposed respectively at the degrees-of-freedom $\mathbf{u}^n_{\text{left}}$, $\mathbf{u}^n_{\text{right}}$ and $\mathbf{u}^n_b$ (computed as in (4.28)) and

$$\mathbf{\Phi}^n_i = \begin{bmatrix} \mathbf{\Theta}^n_{i,r_c} & \mathbf{Z}^n \end{bmatrix}, \tag{7.3}$$

where $\mathbf{\Theta}^n_{i,r_c}$ are the first r_c linear normal modes of the sector clamped at the boundary degrees-of-freedom (computed as in (4.30)) and $\mathbf{Z}^n$ are r_{MD} modal derivatives of the sector (computed

as in (4.69)). Based on the analyses performed in section 5.4.3 on a single blade, the modal derivatives are selected according to the selection criterion 2b described in section 4.3.4. In the case of a tuned structure, the matrices $\mathbf{\Psi}^n_{i,\text{left}}$, $\mathbf{\Phi}^n_i$, $\mathbf{\Psi}^n_{i,b}$ and $\mathbf{\Psi}^n_{i,\text{right}}$ are identical for all $n \in \{1, \ldots, N_s\}$. The methodology is however not restricted to tuned structures. Considering the cyclic conditions

$$\mathbf{u}^n_{\text{left}} = \mathbf{u}^{n-1}_{\text{right}} \quad (n = 2, \ldots, N_s) \quad \text{and} \quad \mathbf{u}^1_{\text{left}} = \mathbf{u}^{N_s}_{\text{right}} \tag{7.4}$$

and regrouping the cyclic boundary degrees-of-freedom in

$$\mathbf{u}_{\text{cyclic}} = \begin{bmatrix} \mathbf{u}^1_{\text{left}} \\ \vdots \\ \mathbf{u}^{N_s}_{\text{left}} \end{bmatrix}, \tag{7.5}$$

the reduction of the multi-sector structure writes

$$\mathbf{u} = \begin{bmatrix} \mathbf{u}^1_i \\ \mathbf{u}^1_b \\ \vdots \\ \mathbf{u}^{N_s}_i \\ \mathbf{u}^{N_s}_b \\ \mathbf{u}_{\text{cyclic}} \end{bmatrix} = \begin{bmatrix} \mathbf{\Phi}^1_i & \mathbf{\Psi}^1_{i,b} & \cdots & \mathbf{0} & \mathbf{0} & \mathbf{\Psi}^1_{i,\text{cyclic}} \\ \mathbf{0} & \mathbf{I} & \cdots & \mathbf{0} & \mathbf{0} & \mathbf{0} \\ \vdots & \vdots & \ddots & \vdots & \vdots & \vdots \\ \mathbf{0} & \mathbf{0} & \cdots & \mathbf{\Phi}^{N_s}_i & \mathbf{\Psi}^{N_s}_{i,b} & \mathbf{\Psi}^{N_s}_{i,\text{cyclic}} \\ \mathbf{0} & \mathbf{0} & \cdots & \mathbf{0} & \mathbf{I} & \mathbf{0} \\ \mathbf{0} & \mathbf{0} & \cdots & \mathbf{0} & \mathbf{0} & \mathbf{I} \end{bmatrix} \begin{bmatrix} \boldsymbol{\eta}^1 \\ \mathbf{u}^1_b \\ \vdots \\ \boldsymbol{\eta}^{N_s} \\ \mathbf{u}^{N_s}_b \\ \mathbf{u}_{\text{cyclic}} \end{bmatrix}, \tag{7.6}$$

where

$$\begin{aligned} \mathbf{\Psi}^n_{i,\text{cyclic}} &= \begin{bmatrix} \mathbf{0}_{n_i \times (n-1)n_{\text{left}}} & \mathbf{\Psi}^n_{i,\text{left}} & \mathbf{\Psi}^n_{i,\text{right}} & \mathbf{0}_{n_i \times (N_s - n - 1)n_{\text{left}}} \end{bmatrix} \quad (n = 1, \ldots, N_s - 1) \\ \text{and} \quad \mathbf{\Psi}^{N_s}_{i,\text{cyclic}} &= \begin{bmatrix} \mathbf{\Psi}^{N_s}_{i,\text{right}} & \mathbf{0}_{n_i \times (N_s - 2)n_{\text{left}}} & \mathbf{\Psi}^{N_s}_{i,\text{left}} \end{bmatrix}. \end{aligned} \tag{7.7}$$

In a more compact form, defining

$$\bar{\mathbf{u}}^n = \begin{bmatrix} \mathbf{u}^n_i \\ \mathbf{u}^n_b \end{bmatrix} \quad \text{and} \quad \mathbf{q}^n = \begin{bmatrix} \boldsymbol{\eta}^n \\ \mathbf{u}^n_b \end{bmatrix}, \tag{7.8}$$

the reduction writes

$$\mathbf{u} = \begin{bmatrix} \bar{\mathbf{u}}^1 \\ \vdots \\ \bar{\mathbf{u}}^{N_s} \\ \mathbf{u}_{\text{cyclic}} \end{bmatrix} = \begin{bmatrix} \bar{\mathbf{\Phi}}^1 & \cdots & \mathbf{0} & \mathbf{\Psi}^1_{\text{cyclic}} \\ \vdots & \vdots & \ddots & \vdots \\ \mathbf{0} & \cdots & \bar{\mathbf{\Phi}}^{N_s} & \mathbf{\Psi}^{N_s}_{\text{cyclic}} \\ \mathbf{0} & \cdots & \mathbf{0} & \mathbf{I} \end{bmatrix} \begin{bmatrix} \mathbf{q}^1 \\ \vdots \\ \mathbf{q}^{N_s} \\ \mathbf{u}_{\text{cyclic}} \end{bmatrix} = \mathbf{\Phi}_{\text{I}} \hat{\mathbf{q}}, \tag{7.9}$$

where

$$\bar{\mathbf{\Phi}}^n = \begin{bmatrix} \mathbf{\Phi}_i^n & \mathbf{\Psi}_{i,b}^n \\ \mathbf{0} & \mathbf{I} \end{bmatrix} \qquad \text{and} \qquad \mathbf{\Psi}_{\text{cyclic}}^n = \begin{bmatrix} \mathbf{\Psi}_{i,\text{cyclic}}^n \\ \mathbf{0} \end{bmatrix}. \tag{7.10}$$

This first projection onto the reduced basis $\mathbf{\Phi}_{\text{I}}$ leads to a reduced-order model of size $N_s(r_c + r_{\text{MD}} + r_b + n_{\text{left}})$. For industrial finite element models, n_{left} can be very large and a second reduction of the system is required. Many works regarding interface reduction in substructuring methods can be found in the literature [124]. Here, a modal reduction of the cyclic boundary degrees-of-freedom is performed. Denoting by $\hat{\mathbf{K}}$ and $\hat{\mathbf{M}}$ the projections of the stiffness and mass matrices onto $\mathbf{\Phi}_{\text{I}}$, the modes $\mathbf{\Pi}$ related to the sub-matrices corresponding to the cyclic boundary degrees-of-freedom, $\hat{\mathbf{K}}_{\text{cyclic}}$ and $\hat{\mathbf{M}}_{\text{cyclic}}$, are computed as

$$\hat{\mathbf{K}}_{\text{cyclic}}\mathbf{\Pi} = \hat{\mathbf{M}}_{\text{cyclic}}\mathbf{\Pi}\boldsymbol{\omega}^2. \tag{7.11}$$

The second reduction writes

$$\hat{\mathbf{q}} = \begin{bmatrix} \mathbf{q}^1 \\ \vdots \\ \mathbf{q}^{N_s} \\ \mathbf{u}_{\text{cyclic}} \end{bmatrix} = \begin{bmatrix} \mathbf{I} & \cdots & \mathbf{0} & \mathbf{0} \\ \vdots & \ddots & \mathbf{0} & \mathbf{0} \\ \mathbf{0} & \cdots & \mathbf{I} & \mathbf{0} \\ \mathbf{0} & \cdots & \mathbf{0} & \mathbf{\Pi}_{r_{\text{cyclic}}} \end{bmatrix} \begin{bmatrix} \mathbf{q}^1 \\ \vdots \\ \mathbf{q}^{N_s} \\ \boldsymbol{\eta}_{\text{cyclic}} \end{bmatrix} = \mathbf{\Phi}_{\text{II}}\mathbf{q}, \tag{7.12}$$

where $\mathbf{\Pi}_{r_{\text{cyclic}}}$ is formed by extracting from $\mathbf{\Pi}$ the r_{cyclic} modes whose frequencies are the closest from the frequencies of modes $\mathbf{\Theta}_{i,r_c}^n$ $(n = 1, \ldots, N_s)$. Combining Eq. (7.9) and Eq. (7.12), the complete reduction writes

$$\mathbf{u} = \mathbf{\Phi}_{\text{I}}\mathbf{\Phi}_{\text{II}}\mathbf{q} = \mathbf{\Phi}\mathbf{q}. \tag{7.13}$$

The size of the reduced-order model is therefore given by

$$r = N_s(r_c + r_{\text{MD}} + r_b) + r_{\text{cyclic}}. \tag{7.14}$$

7.2.2 Reduced nonlinear internal forces

The nonlinear internal forces write

$$\mathbf{g}_{\text{nl}}(\mathbf{u}) = \begin{bmatrix} \mathbf{g}_{\text{nl}}^1(\mathbf{u}) \\ \vdots \\ \mathbf{g}_{\text{nl}}^{N_s}(\mathbf{u}) \\ \mathbf{g}_{\text{nl}}^{\text{cyclic}}(\mathbf{u}) \end{bmatrix}, \tag{7.15}$$

where $\mathbf{g}_{\text{nl}}^{n}(\mathbf{u})$ stands for the forces on degrees-of-freedom $\bar{\mathbf{u}}^{n}$ and $\mathbf{g}_{\text{nl}}^{\text{cyclic}}(\mathbf{u})$ for the forces on degrees-of-freedom $\mathbf{u}_{\text{cyclic}}$. Their projection on the reduced basis $\boldsymbol{\Phi}$ are computed as in Eq. (4.6) and writes

$$\tilde{\mathbf{g}}_{\text{nl}}(\mathbf{q}) = \begin{bmatrix} \tilde{\mathbf{g}}_{\text{nl}}^{1}(\mathbf{q}) \\ \vdots \\ \tilde{\mathbf{g}}_{\text{nl}}^{N_s}(\mathbf{q}) \\ \tilde{\mathbf{g}}_{\text{nl}}^{\text{cyclic}}(\mathbf{q}) \end{bmatrix} = \begin{bmatrix} \bar{\boldsymbol{\Phi}}^{1\text{T}} \mathbf{g}_{\text{nl}}^{1}(\boldsymbol{\Phi}\mathbf{q}) \\ \vdots \\ \bar{\boldsymbol{\Phi}}^{N_s\text{T}} \mathbf{g}_{\text{nl}}^{N_s}(\boldsymbol{\Phi}\mathbf{q}) \\ \boldsymbol{\Pi}_{r_{\text{cyclic}}}^{\text{T}} \left[\sum_{k=1}^{N_s} \boldsymbol{\Psi}_{\text{cyclic}}^{k\text{T}} \mathbf{g}_{\text{nl}}^{k}(\boldsymbol{\Phi}\mathbf{q}) + \mathbf{g}_{\text{nl}}^{\text{cyclic}}(\boldsymbol{\Phi}\mathbf{q}) \right] \end{bmatrix} \tag{7.16}$$

In order to extend the CMS procedure to the computation of these nonlinear forces, it is assumed that the constraint modes related to the cyclic boundaries remain linear. This assumption implies the linearity of the couplings between the substructure [11, 143]. In the case of bladed structures, the sectors are connected by a relatively thick and stiff disk. Geometric nonlinear effects can occur in the blade, but it seems justified to assume that the displacement of the disk remains small and, therefore, that the degrees-of-freedom of the disk boundaries are linear. In this context, the internal forces in each sector are also simplified. It is assumed that the reduced nonlinear internal forces in sector n ($n = 1, \ldots, N_s$), $\tilde{\mathbf{g}}_{\text{nl}}^{n}$, only depend on the internal and blade-tip generalized coordinates of the sector, $\mathbf{q}^{n}$. The projected nonlinear internal forces therefore write

$$\tilde{\mathbf{g}}_{\text{nl}}(\mathbf{q}) = \begin{bmatrix} \tilde{\mathbf{g}}_{\text{nl}}^{1}(\mathbf{q}^{1}) \\ \vdots \\ \tilde{\mathbf{g}}_{\text{nl}}^{N_s}(\mathbf{q}^{N_s}) \\ \mathbf{0} \end{bmatrix} = \begin{bmatrix} \bar{\boldsymbol{\Phi}}^{1\text{T}} \mathbf{g}_{\text{nl}}^{1}(\bar{\boldsymbol{\Phi}}^{1}\mathbf{q}^{1}) \\ \vdots \\ \bar{\boldsymbol{\Phi}}^{N_s\text{T}} \mathbf{g}_{\text{nl}}^{N_s}(\bar{\boldsymbol{\Phi}}^{N_s}\mathbf{q}^{N_s}) \\ \mathbf{0} \end{bmatrix}. \tag{7.17}$$

Under these assumptions, the STEP presented in section 4.2 can be applied to compute the reduced nonlinear internal forces of each sector. The nonlinear internal forces of sector n are expressed as the polynomial

$$\tilde{\mathbf{g}}_{\text{nl}}^{n}(\mathbf{q}^{n}) = \tilde{\boldsymbol{\mathcal{A}}}^{n}(\mathbf{q}^{n}, \mathbf{q}^{n}) + \tilde{\boldsymbol{\mathcal{B}}}^{n}(\mathbf{q}^{n}, \mathbf{q}^{n}, \mathbf{q}^{n}) \tag{7.18}$$

using a functional notation for the quadratic and cubic terms with coefficients gathered in the third-order tensor $\tilde{\mathbf{A}}^{n}$ and the fourth-order tensor $\tilde{\mathbf{B}}^{n}$. The components of these tensors are determined as described in section 4.2. The nonlinear forces static evaluations are performed on the sector finite element model clamped at the cyclic boundaries degrees-of-freedom and with imposed displacements defined as linear combinations of the modes $\bar{\boldsymbol{\Phi}}^{n}$. In the case of

tuned structures, the tensors $\tilde{\mathbf{A}}^n$ (and respectively $\tilde{\mathbf{B}}^n$) are identical for each sector n and have to be computed only once. In the case of detuned structures, one STEP analysis has to be performed for each kind of sector. These analyses are independent and can be performed in parallel.

7.2.3 Contact treatment

The time integration algorithm described in section 3.1.1 for a single blade with contact is also valid for the full bladed disk and does not need to be adapted. At each time step, possible penetrations are computed at the boundary degrees-of-freedom $\mathbf{u}_b^n$ $(n = 1, \ldots, N_s)$ corresponding to the blade-tip nodes of the N_s sectors, which are kept in the reduced space, and the associated contact forces are computed at these nodes.

7.2.4 Efficient implementation of nonlinear forces computation

The numerical strategy described in section 3.1.2 consisting in evaluating several vectors of nonlinear internal forces at the same time can still be used to build contact interaction maps for full bladed disks on wide angular speed ranges in an efficient way.

Moreover, in the case of tuned bladed disks, the tensors $\tilde{\mathbf{A}}^n$ (and respectively $\tilde{\mathbf{B}}^n$) in (7.18) are identical for each sector n. Under the assumption of linear coupling between the sectors that is made here, the strategy can therefore also be used to compute the nonlinear internal forces in each sector at the same time, which is more efficient than computing them independently.

7.2.5 Extension to frequency domain

The extension of the methodology to frequency domain with the HBM does not give rise to specific issues. As described in section 3.2.2, contact can be treated with the RL-HBM and the nonlinear internal forces due to large displacements can be determined analytically or evaluated with the AFT scheme.

7.3 Bladed disk model

The methodology is applied on an industrial bladed-disk model based on the NASA rotor 37. A disk sector is added to the blade model presented in section 5.1, as shown in Fig. 7.2. Note that the height of the blade is decreased by 4 mm compared to section 5.1 in order to ensure a good merge between the blade and the disk. The 36 sectors of the bladed disk are supposed identical. The discretized mesh counts $44,535$ nodes, *i.e.* $133,605$ degrees-of-freedom. The sectors are clamped at the disk lower surfaces. The material properties are identical to the ones given in section 5.1.

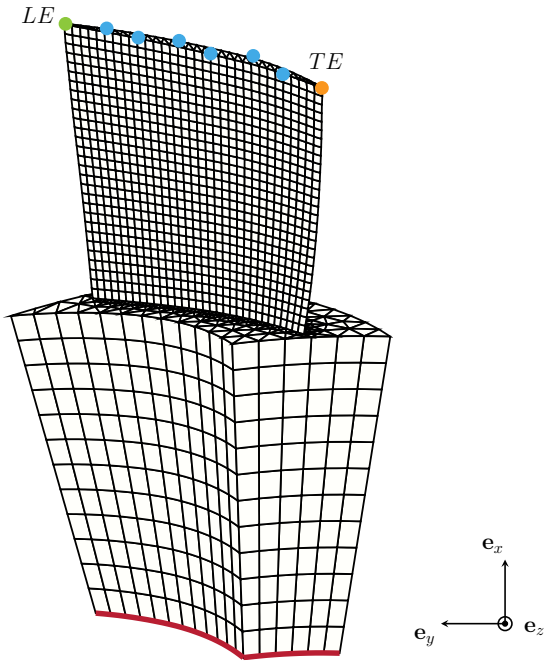

FIGURE 7.2 – Single sector of NASA rotor 37 with mesh used for the finite element simulations and clamped surface (■). The eight colored nodes are the blade-tip nodes retained for contact simulations. Among those nodes, the node TE is located at the trailing edge (●) and the node LE is located at the leading edge (●).

Based on the finite element model, the SAFE diagram (Singh's Advanced Frequency Evaluation diagram, *i.e.* the eigenfrequencies as a function of the number of nodal diameters [198]), is built and represented in Fig. 7.3. The figure highlights the existence of different mode families: modes dominated by blade deformation (corresponding to the successive bending and torsion modes of the blade) and modes with high participation of the disk.

7.4 Verification of the methodology without contact

In order to validate the proposed methodology, the reduction procedure is first applied on the bladed disk of interest subjected to an equivalent aerodynamic loading of sufficiently high amplitude to activate geometric nonlinear effects. Contact interactions are not considered in this section. The performance indicator I introduced in section 5.3 is used to assess the accuracy of the reduction method both locally (at the blade-tips) and globally. This performance indicator ranges from 0 to 1, the closer to one, the better the reduced-order model.

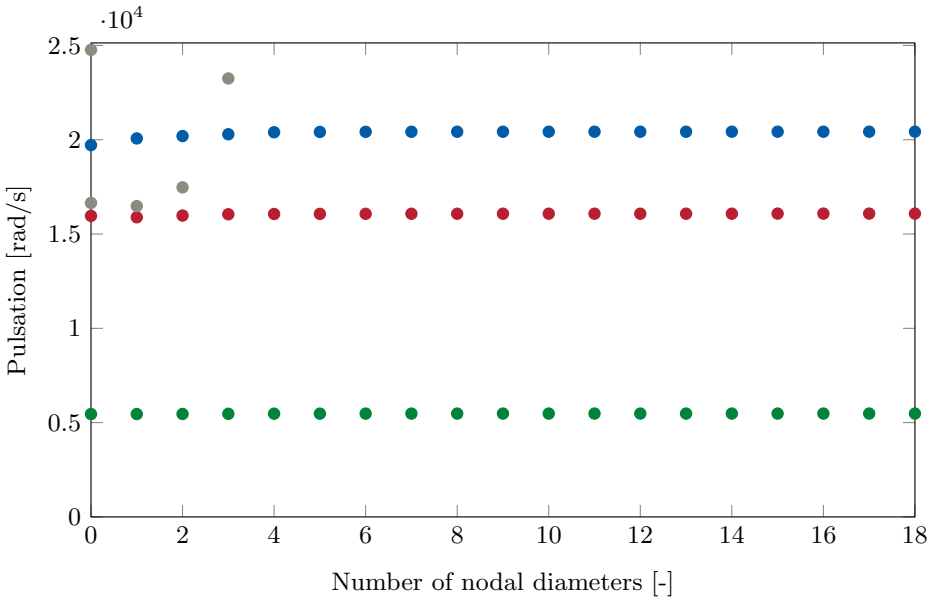

FIGURE 7.3 – SAFE diagram of the studied bladed disk for mode families 1B (●), 1T (●) and 2B (●) and disk-dominated modes (●).

7.4.1 Accuracy of the reduction method

A reduced-order model characterized by $r_b = 3$, $r_c = 10$, $r_{\text{MD}} = 10$ and $r_{\text{cyclic}} = 144$ is built. The training excitation for the selection of the modal derivatives is defined as a harmonic excitation in the $\mathbf{e}_z$ direction with an amplitude $A_t = 400$ N, a pulsation $\omega_t = 4,500$ rad/s applied on $N_t = 1$ blade-tip node.

This reduced-order model with $r_{\text{MD}} = 10$ modal derivatives per sector is first used to compute the response of the structure to the same harmonic excitation as for the training. A zero-diameter excitation is considered ($N_d = 0$). The time response obtained is shown in Fig. 7.4, both in the transient and steady-state regimes. The response is compared with the reference nonlinear solution computed with the full-order model. The linear reference solution is also shown to confirm that the amplitude of the excitation is sufficient to activate the geometric nonlinearities. The good match between the full-order model and reduced-order model solutions gives confidence in the methodology, at least to study external excitations close to the training excitation used for the selection of the modal derivatives. The initial errors at the beginning of the simulation do not build up during the simulation.

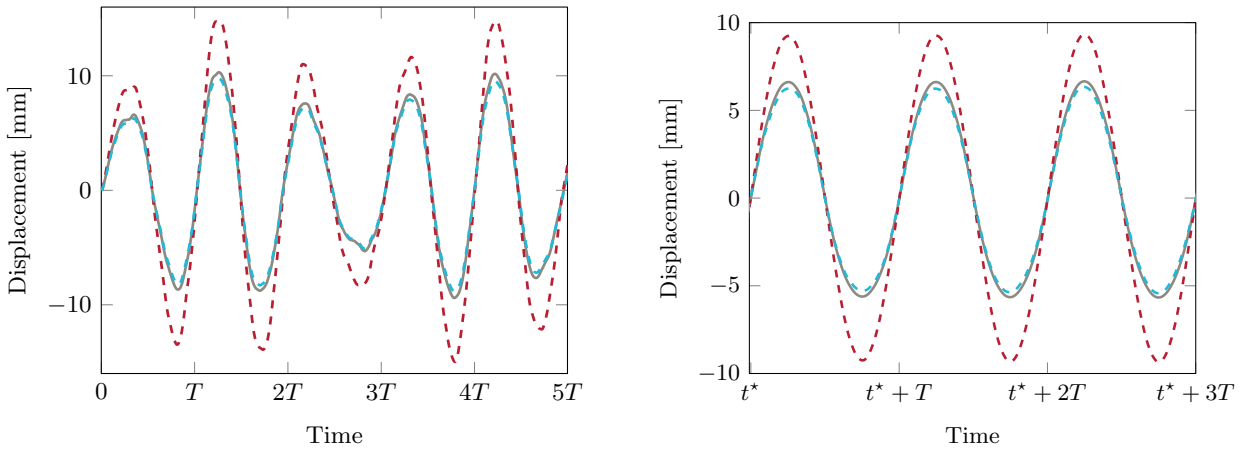

(a) Transient response.

(b) Steady-state response.

FIGURE 7.4 – Responses of the bladed disk at node LE in the $\mathbf{e}_z$ direction: linear reference solution (- - - -), nonlinear reference solution (——) and nonlinear solution obtained with the reduced-order model (- - - -).

7.4.2 Versatility of the reduction method

The performance indicator introduced in section 5.3 is then used to study the influence of the number of modal derivatives included in the reduction basis and assess the versatility of the reduction method for different external excitations. Reduction bases characterized by $r_b = 3$, $r_c = 10$, $r_{\text{cyclic}} = 144$ and r_{MD} between 2 and 30 are built. The value of r_c has been fixed based on convergence analyses on linear and nonlinear simulations. Increasing r_c beyond this value does not increase the accuracy of the results on the studied frequency range.

The modal derivatives are selected according to the selection criterion 2b (see section 4.3.4), with the same training excitation as in the previous section: a harmonic excitation in the $\mathbf{e}_z$ direction with an amplitude $A_t = 400$ N, a pulsation $\omega_t = 4,500$ rad/s applied on $N_t = 1$ blade-tip node. Figure 7.5 shows the weights $W_{ij}^{(2b)}$ associated to each modal derivative and the ranking of the first 30 modal derivatives. The modal derivative with the highest weight is the derivative of the third static mode with respect to itself, the modal derivative with the second highest weight is the derivative of the second static mode with respect to the third static mode, and so on. More generally, the modal derivatives included in the reduction basis mainly correspond to the derivatives of the static modes with respect to themselves and of the static modes with respect to the first internal modes.

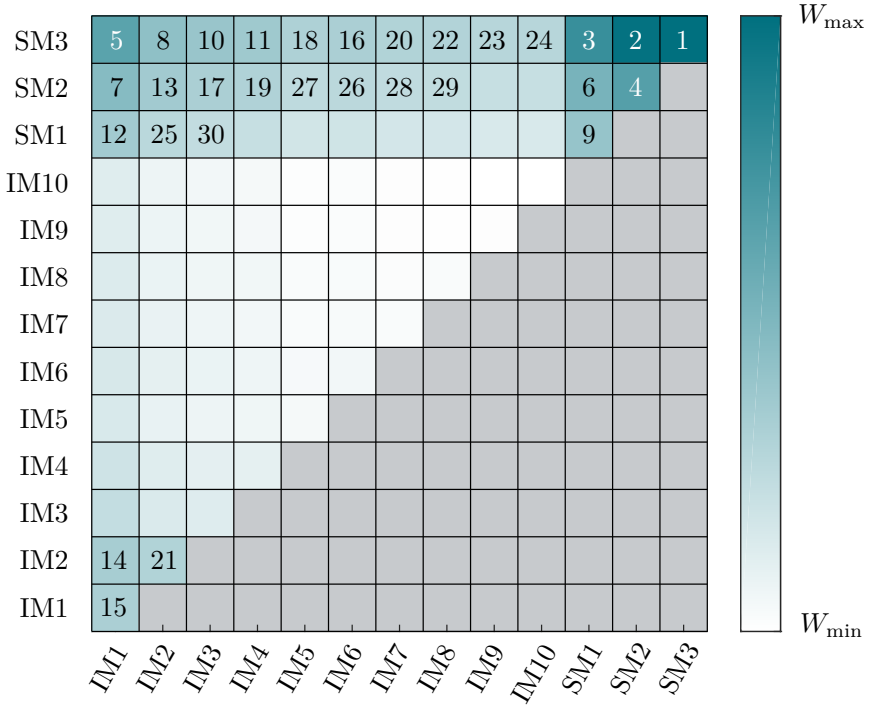

FIGURE 7.5 – Weights $W_{jk}^{(2b)}$ associated to each modal derivative and their ranking (logarithmic scale).

The different reduced-order models are first used to compute the response of the bladed disk to harmonic excitations characterized by $A_e = 400$ N, $\omega_e = 4,500$ rad/s, $N_d = 0$ and distributed on respectively $N_e = 1$, 4 and 8 blade-tip nodes. Although the training excitation is limited to a single period, the external excitation is here extended to ten periods in order to assess the capability of the reduced-order models to accurately predict nonlinear transient phenomena. Results are provided in Fig. 7.6. The results highlight that the reduced-order modeling technique allows to predict the dynamic behavior of the bladed disk for the three values of N_e as the performance indicator eventually reaches values above 0.95 in the three cases. However, the accuracy of the reduced-order model decreases as N_e increases and increasing the number of modal derivatives beyond 30 does not seem to improve the performance. The results could be improved by increasing the number of boundary nodes retained in the reduced space, *i.e.* by increasing the value of r_b. However, as shown in chapter 6, increasing the number of static modes also leads to a significant increase of the size of the reduction basis as more modal derivatives have to be included in the reduction basis.

The reduced-order models are then used to compute the response of the bladed disk to harmonic excitations characterized by $A_e = 400$ N, $N_e = 1$, $N_d = 0$ at different pulsations ω_e.

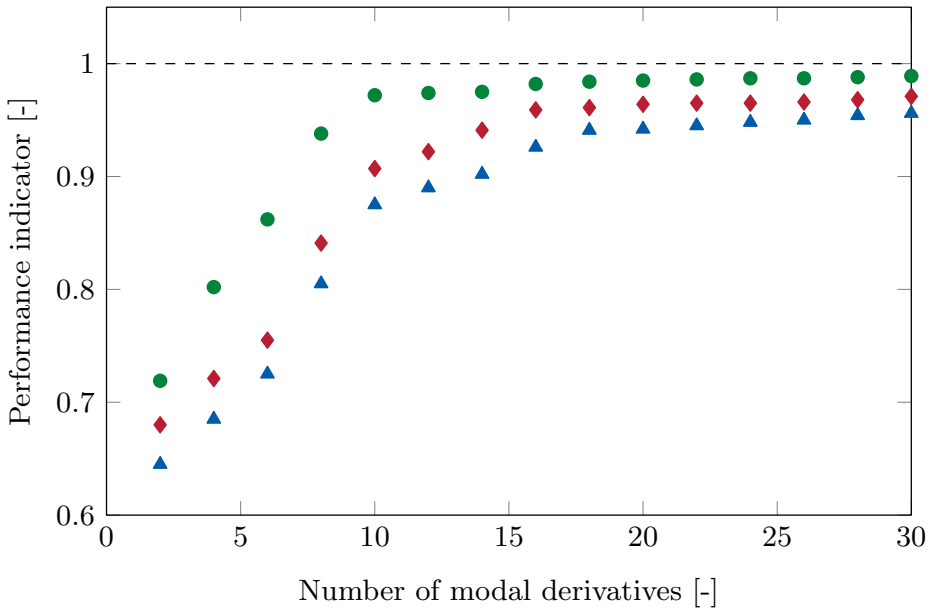

FIGURE 7.6 – Evolution of the performance indicator as a function of the number of modal derivatives r_{MD} for external excitations characterized by $A_e = 400$ N, $\omega_e = 4,500$ rad/s, $N_d = 0$ and $N_e = 1$ (●), $N_e = 4$ (♦) and $N_e = 8$ (▲).

Results are provided in Fig. 7.7. Results at $\omega_e = 4,000$ rad/s have already been presented in Fig. 7.6. At this pulsation, the structure mainly responds in the blade first mode and the reduced-order models with at least $r_{\mathrm{MD}} = 10$ modal derivatives predict with accuracy the dynamic response.

When the pulsation of the excitation is increased to $\omega_e = 13,000$ rad/s, nearly the same level of accuracy is achieved when a high number of modal derivatives is considered but the convergence is slower: 22 modal derivatives are required to reach a performance indicator I greater than 0.95. In fact, at this pulsation, the second blade mode is also excited (see Fig. 7.3) and it is necessary to include the modal derivatives related to this torsion mode in the reduction basis. Figure 7.5 shows that the modal derivative of the second internal mode with respect to itself is included in position 21 in the reduction basis. Given the results in Fig. 7.7, this modal derivative seems particularly important to represent the dynamics of the structure at this pulsation.

The same conclusions hold at the pulsation $\omega_e = 17,000$ rad/s where the third blade mode is slightly excited. At this pulsation, a disk-dominated mode is also excited. Provided the appropriate modal derivatives are included in the reduction basis, the methodology is still accurate to describe the structure dynamics.

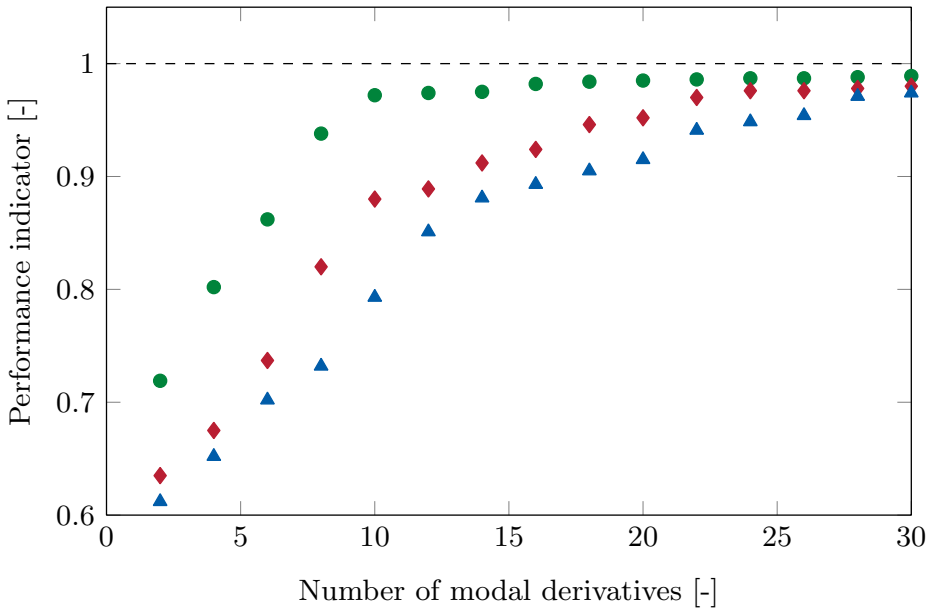

FIGURE 7.7 – Evolution of the performance indicator as a function of the number of modal derivatives r_{MD} for external excitations characterized by $A_e = 400$ N, $N_e = 1$, $N_d = 0$ and $\omega_e = 4,500$ rad/s (●), $\omega_e = 13,000$ rad/s (♦) and $\omega_e = 17,000$ rad/s (▲).

It is worth reminding that the modal derivatives selection criterion is based on a training excitation, here defined at a pulsation $\omega_e = 4,500$ rad/s that mainly excites the first mode of the structure. Faster convergence of the results (in terms of number of modal derivatives) could be reached by modifying the pulsation of this training excitation. Depending on the application and if the frequency range of application of the reduced-order model is *a priori* known, it could be relevant to adjust the training excitation characteristics.

Lastly, the reduced-order models are used to compute the response of the structure at the three pulsations studied before but with harmonic excitations characterized by $N_d = 9$ nodal diameters. The results are illustrated in Fig. 7.8. The tendency of the three curves is very similar to what has been observed in Fig. 7.7. The reduced-order models are also accurate to study excitations with a number of nodal diameters different from 0.

Also, the level of accuracy at pulsation $\omega_e = 17,000$ rad/s is close to the one obtained for $N_d = 0$ where a disk-dominated mode was also excited. This confirms that such modes do not give rise to any particular issue in the methodology.

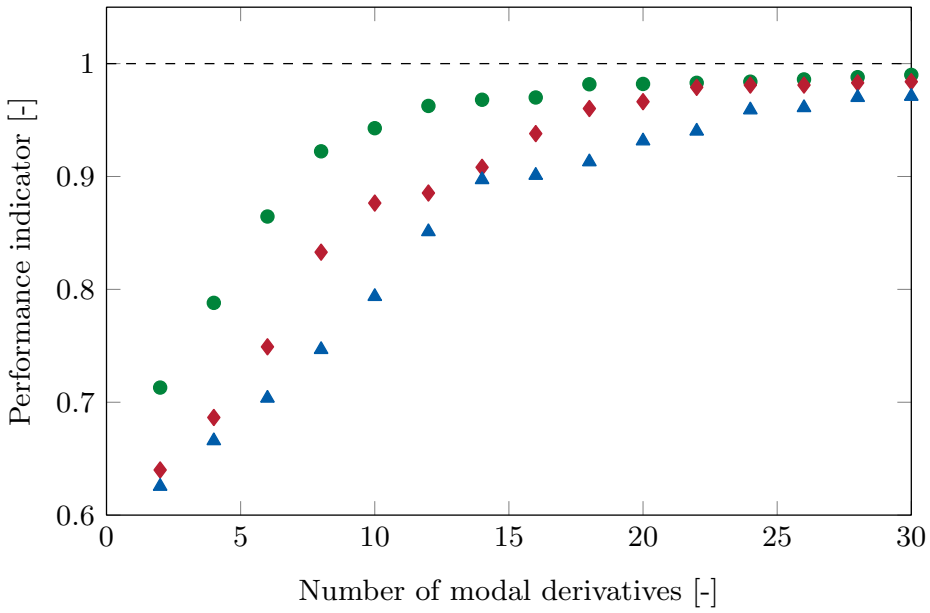

FIGURE 7.8 – Evolution of the performance indicator as a function of the number of modal derivatives r_{MD} for external excitations characterized by $A_e = 400$ N, $N_e = 1$, $N_d = 9$ and $\omega_e = 4,500$ rad/s (●), $\omega_e = 13,000$ rad/s (♦) and $\omega_e = 17,000$ rad/s (▲).

7.4.3 Computational cost

As a reminder, the reduction procedure decomposes into an expensive offline stage where the reduced-order model is built and an efficient online stage where the reduced-order model is used in simulations. As previously, the different computation times presented here are obtained on an Intel Xeon E5-2698 v4 processor (2.2 GHz).

Considering a reduction basis of size $r = 972$ ($r_b = 3$, $r_c = 10$, $r_{\text{MD}} = 10$, $r_{\text{cyclic}} = 144$), the single CPU sequential time required to build the reduced-order model, *i.e.* the offline time, is approximately 20 hours. Note that parallel computing can be used to reduce computation times as the nonlinear force static evaluations of the STEP can be done in parallel to build the tensors $\tilde{\mathbf{A}}^n$ and $\tilde{\mathbf{B}}^n$.

The online time, *i.e.* the time required to integrate forward in time the equation of motion, is directly related to the size of the reduction basis, r. With the reduced-order model built above ($r = 972$), a dynamic simulation of length 56 ms (approximately 40 periods at 4,500 rad/s) with a time step of integration $h = 10^{-5}$ s takes about 1 minute. By comparison, the same simulation with the full-order finite element modes would take about 18 hours. The use of the reduced-order model therefore allows a significant reduction of CPU time by a factor 1,000.

Given the computational cost for building the reduced-order model, the reduced-order model is profitable as soon as two such simulations have to be carried out.

7.5 Contact simulations

The methodology is then applied to the bladed structure with geometric and contact nonlinearities. As previously, we focus on the rubbing interactions due to contact events between the blades and the surrounding casing. Even if rubbing interactions typically involve a single blade, previous studies have shown that it is possible, at least from a numerical standpoint, to generate a rubbing interaction with a full bladed disk [164]. The contact scenario described in section 6.2, with two bumps on the casing, is considered through this section. No abradable coating is considered in this section, but the methodology is compatible with the wear modeling described in section 6.6.1.

7.5.1 Reduced-order model

Based on the analyses performed on a single rotating blade, a reduced-order model with $r_b = 24$ boundary degrees-of-freedom per sector, $r_c = 15$ internal modes per sector, $r_{\mathrm{MD}} = 150$ modal derivatives per sector and $r_{\mathrm{cyclic}} = 144$ is built. This leads to a reduction basis of size $r = 6,948$. This reduced-order model is used to perform the contact simulations. Convergence studies as in section 6.3 confirm that the size of the reduced-order model is appropriate.

7.5.2 Interaction map

Simulations at constant angular speed Ω between 1,200 rad/s and 1,650 rad/s are performed (with a step of 5 rad/s). The interaction maps are built as described in section 6.5.1. The interaction maps corresponding to the radial displacement at the node LE of one sector (sector 1) are shown in Fig. 7.9 in the cases where geometric nonlinearities are neglected and where they are taken into account.

The interaction maps highlight the existence of a strong contact interaction between the first mode family of the bladed disk (corresponding to the first bending mode of the blade) and the fourth engine order. At the resonance, the bladed disk responds in its first bending mode with four nodal diameters. The contact stiffening is indicated by an arrow in both maps. Again, geometric nonlinearities seem to give rise to smoother interactions and be responsible for an additional contact stiffening.

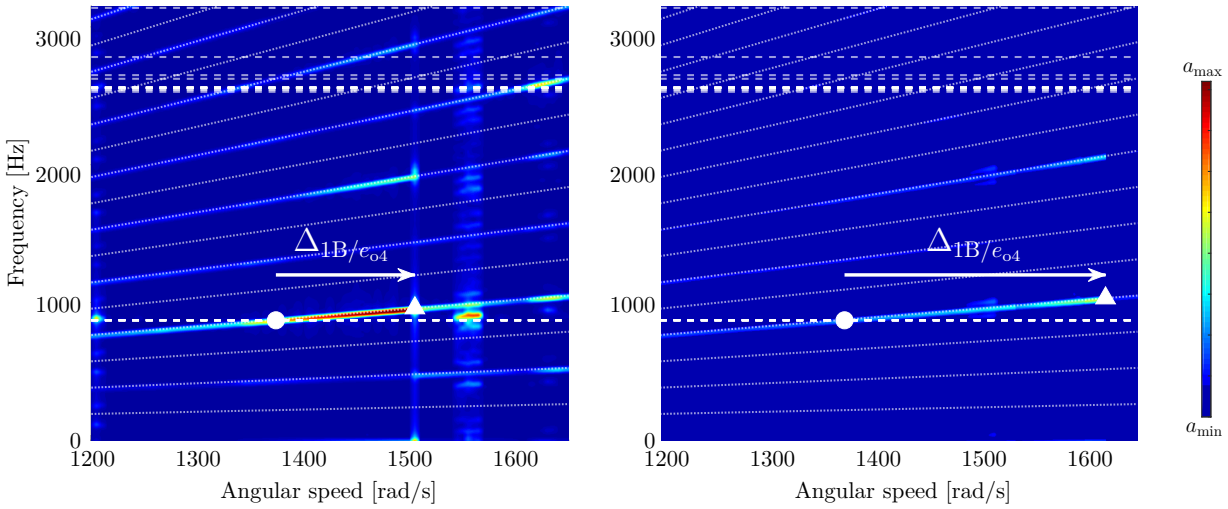

(a) Without geometric nonlinearities.

(b) With geometric nonlinearities.

FIGURE 7.9 – Interaction maps of the radial displacement at node LE for the case with direct contact with eigenfrequencies (- - - -), engine order lines (·····), predicted linear resonance (●) and predicted nonlinear resonance (▲).

The radial displacement amplitude at node LE is shown in Fig. 7.10. This figure confirms the observations made with the interaction maps. In order to correctly quantify the contact stiffening of the structure, a continuation procedure should be used to build the nonlinear frequency response curve (as detailed in section 6.5.2). Given the computer resources available and the cost of such simulations, this has not been done here. Indeed, when building a NFRC with a continuation procedure, simulations at each angular speed have to be done one after the other with a relatively small angular speed step. The strategy detailed in section 3.1.2 can therefore not be used. It can however be expected that the contact stiffening is strongly underestimated in the case where geometric nonlinearities are neglected.

The comparison between the results in Figs. 7.9 and 7.10 with the corresponding results in Figs. 6.17 and 6.18 for the single rotating blade structure suggests that a similar type of vibration response occurs for the single blade and the full bladed disk models. Vibration amplitudes and contact stiffening are of comparable magnitudes and the frequency content is very similar. It suggests that the predicted interaction on the full bladed disk may be seen as a sum of rubbing interactions occurring at each blade. The disk dynamics does therefore not play any significant role for this interaction, which is consistent with the fact that the 1B modal family is very clustered in the SAFE diagram (see Fig. 7.3).

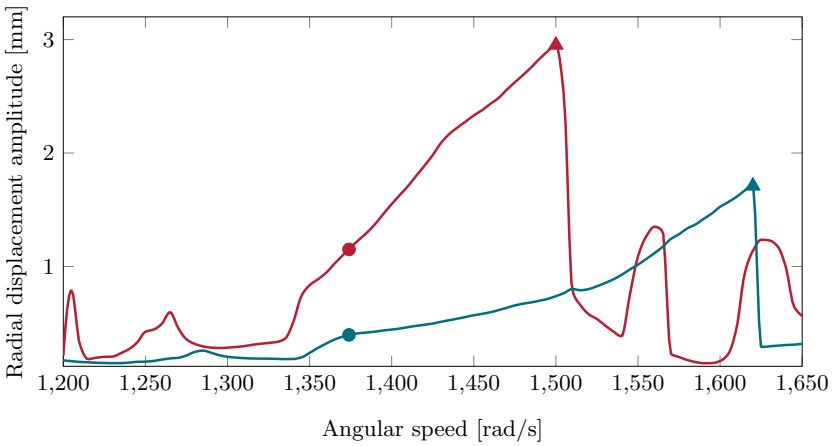

FIGURE 7.10 – Nonlinear frequency response curves of the radial displacement at node LE in the cases where geometric nonlinearities are not considered (——) and where geometric nonlinearities are considered (——) for the full bladed disk.

7.5.3 Stress analysis

Stress fields are here studied at the angular speeds of the nonlinear resonances corresponding to the interaction $1\mathrm{B}/e_{\mathrm{o}4}$ indicated by the symbol (▲) in Fig. 7.9 and Fig. 7.10. The von Mises stress fields are computed at time $t_{\max}$ where the node LE of sector 1 reaches its maximal radial displacement. These stress fields are represented in Fig. 6.20 for the cases where geometric nonlinearities are neglected and where they are taken into account.

At these interactions, the response of the structure is dominated by the first bending mode of the blade, which shows slightly different shapes when geometric nonlinearities are considered or not. The zones of maximal von Mises stresses are not located exactly at the same place in both cases. When geometric nonlinearities are neglected, the maximal stresses are found near the root of the blade. When considering the geometric nonlinearities, the zone of maximal stresses appears toward the center of the blade. Also, the results without geometric nonlinearities highlight non-negligible stresses in the disk. These results suggest again that accounting for geometric nonlinearities in bladed disk models could have a significant influence in terms of bladed disks design.

Quantitatively, the ratio of the maximal von Mises stresses in both cases is in line with the corresponding ratio of maximal displacements at the blade-tip leading edge. It is important to note that in the case where geometric nonlinearities are neglected, stresses higher than the material yield stress are obtained in the blade while the blade remains in the elastic domain when geometric nonlinearities are taken into account. This confirms that, in the studied case,

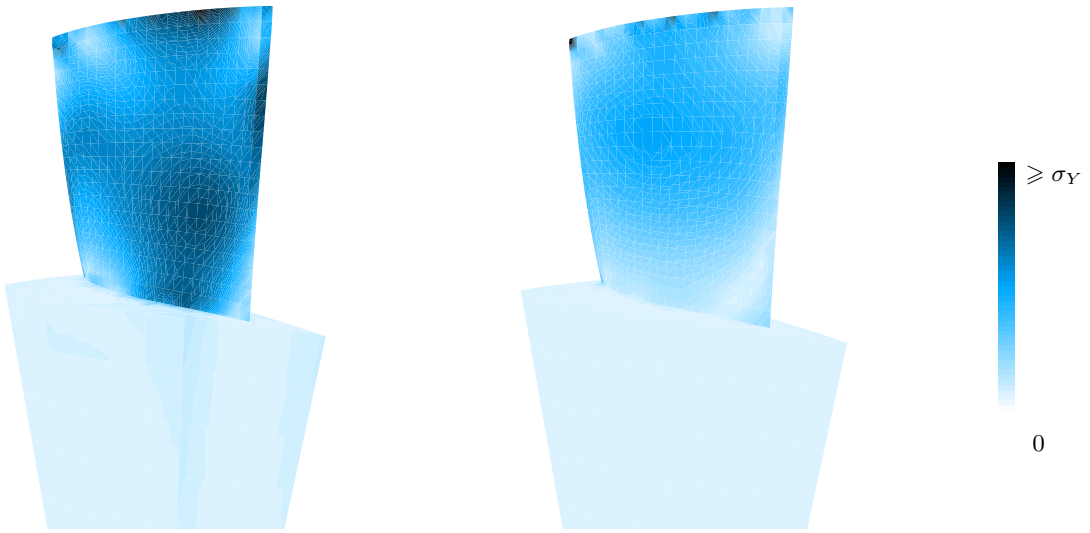

(a) Without geometric nonlinearities. (b) With geometric nonlinearities.

FIGURE 7.11 – Comparison of the Von Mises stress fields at $t_{\max}$.

geometric nonlinearities weaken the interactions, not only locally at the blade-tip, but also globally in the whole blade. The analysis of the stress field at the other interaction angular speeds confirms that the severity of the interaction in terms of displacement amplitudes is reflected in the maximal values of the von Mises stress.

7.6 Introduction of mistuning

7.6.1 Methodology

As explained in section 7.2, the methodology developed for full bladed disks can be used to study mistuned bladed disks. In practice, the reduced-order models related to the different sectors, characterized by different geometries or material properties for instance, are built in the offline stage. The corresponding reduced mass matrix, reduced linear stiffness matrix, projection basis and reduced nonlinear stiffness tensors are saved. In the online stage, the mistuning pattern is defined and the reduced-order models of the corresponding sectors are loaded and assembled. The second projection, corresponding to the reduction of the cyclic boundary degrees-of-freedom, is then performed.

7.6.2 Mistuning patterns

Mistuning is introduced in the full bladed disk model presented in section 7.3 in terms of variation of the Young's modulus of the sectors. In this preliminary study, three values of the Young's modulus are considered: $0.97E_n$, E_n and $1.03E_n$, where $E_n = 180$ GPa is the nominal value of the Young's modulus. This variation of the Young's modulus of $\pm 3\%$ corresponds to the values typically encountered in the literature when dealing with small mistuning [23, 164]. The three reduced-order models of the corresponding sectors are built in the offline stage of the procedure.

These sectors reduced-order models are then used to build reduced-order models of full bladed disks with different mistuning patterns for which the Young's moduli of each of the 36 sectors of the bladed disk are picked randomly among the three values $0.97E_n$, E_n and $1.03E_n$, with a uniform probability distribution.

7.6.3 Contact simulations

The reduced-order models of the mistuned bladed disks are then used to perform contact simulations.

7.6.3.1 Quantities of interest

As described in section 2.3, mistuning can be responsible for an increase of the maximum forced response amplitude and a localization of the energy on a subset of blades rather than being uniformly distributed throughout the system. In order to quantify the influence of mistuning, two quantities of interest are generally investigated [69, 238]. First, the amplification factor is defined as the ratio between the maximum radial amplitude of all sectors in the mistuned case and in the tuned case. Then, the localization factor is defined as

$$LF = \frac{x-1}{\sqrt{N_s}-1} \quad \text{with} \quad x = \frac{\max\left(\mathbf{u}_r\right)}{\text{rms}\left(\mathbf{u}_r\right)}, \tag{7.19}$$

where $\mathbf{u}_r$ stands for the radial displacement amplitudes at node LE for each blade for the last engine revolution [119]. The localization factor ranges from 0, corresponding to a uniform distribution of the energy in all blades, to 1, for the case where only one blade vibrates. The localization factor, contrary to the amplification factor, allows to distinguish cases where several blades reach high magnification factors and cases where only one single blade reaches a higher displacement level, which is important in terms of an optimum blade selection for strain gages.

These two quantities of interest can be computed for each mistuning pattern at each angular speed studied. Statistical analyses can then be performed on these data. It should however be noted that, because of the cost of the numerical simulations with both geometric and contact nonlinearities, only 30 mistuning patterns are here considered. It is obvious that these 30 samples are not sufficient to reach the statistical convergence. The following results therefore have to be analyzed carefully. They correspond to preliminary results that may show some trends but cannot be used to draw general conclusions. The main objective is here to show that the methodology is suitable to study nonlinear mistuned bladed disks.

7.6.3.2 Results

Contact simulations are performed starting from zero initial conditions, as described in section 7.5. The contact interaction between the first bending mode of the blade and the fourth engine order is studied.

First, the 90$^{\text{th}}$ percentile of the radial displacement amplitude is shown in Fig. 7.12, without and with geometric nonlinearities. The results are also compared with the NFRC obtained for the tuned bladed disk already presented in Fig. 7.10.

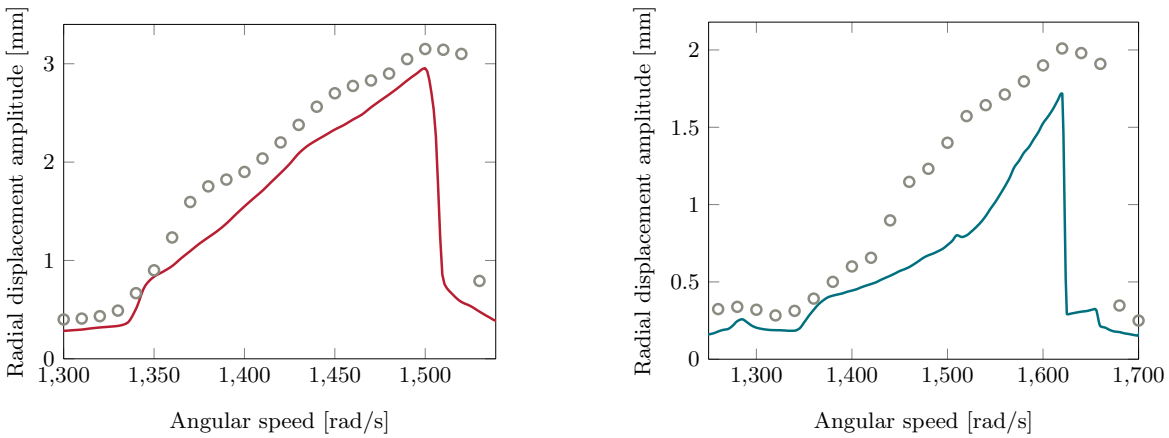

(a) Without geometric nonlinearities.

(b) With geometric nonlinearities.

FIGURE 7.12 – Radial displacement amplitude: tuned case (——/——) and 90$^{\text{th}}$ percentile for mistuned case (○).

In the case where geometric nonlinearities are neglected (Fig. 7.12a), the response is slightly amplified in the whole angular speed range compared to the tuned case. These predicted amplification factors are small compared to values encountered in the literature for linear

systems. In fact, as highlighted in the contact studies performed in section 6.5.2, the time integration procedure starting from zero initial conditions may fail to capture the nonlinear resonances. The true value of the amplification factor may therefore not be correctly quantified with this methodology. Continuation algorithms should be used to correctly capture the nonlinear resonance and the associated amplification factor.

In the case where geometric nonlinearities are taken into account (Fig. 7.12b), a higher amplification of the response is observed. Two possible explanations may be suggested. First, it is possible that geometric nonlinearities are responsible for an additional amplification of the response. Second, it is also likely that, in this case, the nonlinear resonance is well estimated (as observed in section 6.5.2 for the single blade). The computed amplification factor may therefore correspond to the actual amplification factor, that should be compared with the value at the true nonlinear resonance in the case without geometric nonlinearities. In any case, using a continuation algorithm to build the NFRC could allow to better understand the contact dynamics.

The localization factor is then studied in the same angular speed interval. In order to visualize the meaning of the localization factor values, the envelope of the radial displacement at node LE for each blade is shown in Fig. 7.13 for two contact simulations characterized by different values of the localization factor. Figure 7.13a corresponds to $LF = 0.63$. The energy is essentially located on two blades. In Fig. 7.13b, $LF = 0.91$. Only one blade features significant amplitude of vibration.

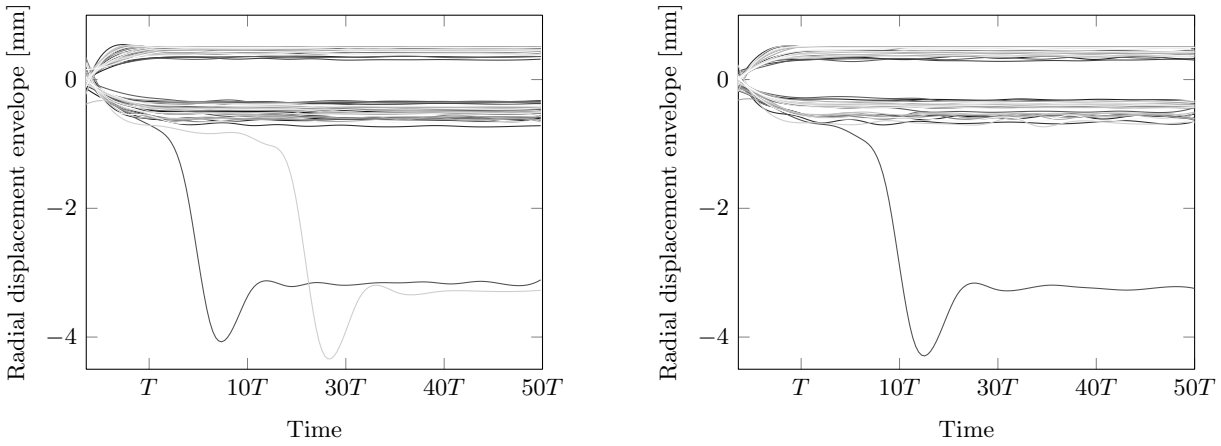

(a) $LF = 0.63$.

(b) $LF = 0.91$.

FIGURE 7.13 – Envelopes of the radial displacement at LE for blade 1 (——) to blade 36 (——).

The 90^{th} percentile of the localization factor is shown in Fig. 7.14 for the cases without and with geometric nonlinearities. The maximum values of the localization factor are reached at the nonlinear resonances. Higher values of the localization factor are obtained for the case with geometric nonlinearities.

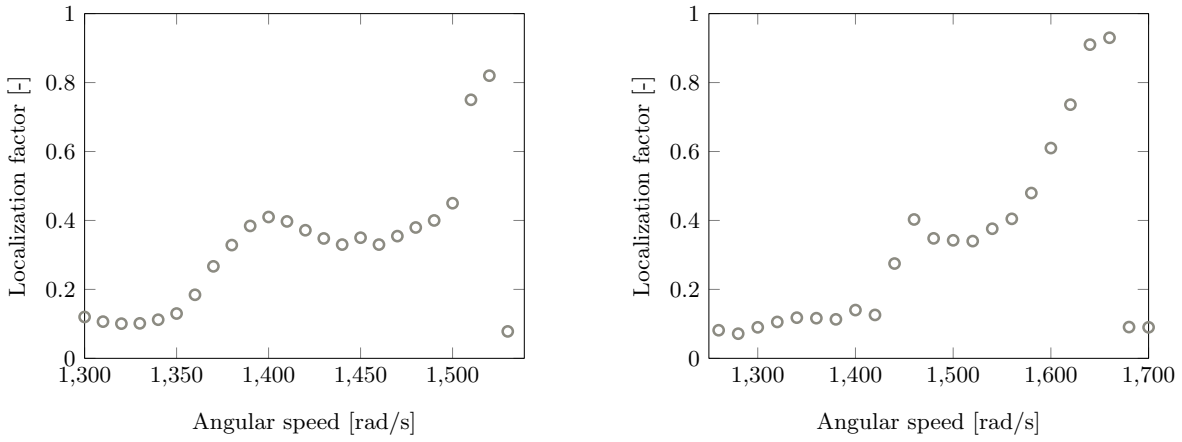

(a) Without geometric nonlinearities.

(b) With geometric nonlinearities.

FIGURE 7.14 – Localization factor (percentile 90).

7.7 Partial conclusions

In this chapter, the methodology developed for single blades has been generalized to full bladed disks based on CMS techniques. The methodology has been validated on an industrial bladed disk model subjected to an equivalent aerodynamic loading and then used in contact simulations.

Some preliminary studies have also shown that the methodology is compatible with the introduction of mistuning in the reduced-order model. These studies have also begun to show the limitations of the methodology in terms of numerical resources needs. In the offline stage of the procedure, the computation time is directly related to the time required to perform the static simulations with the full-order finite element model. Here, these simulations are performed with SAMCEF and are limited by the number of software licenses. That's why only a limited number of values were considered for the Young's modulus. In this context, it could be very interesting to use the developed methodology in combination with an open finite element software, as code_aster, which could allow to build a large number of ROMs at the same time. In the online stage, the simulations are also costly, especially for structures with many sectors and when an accurate description of the contact interface is required. With the present methodology, it seems difficult to reduce this cost but other avenues could be explored to build ROMs of reduced size, as invariant manifold methods.

CHAPTER 8 CONCLUSIONS AND PERSPECTIVES

Contributions

This thesis presents the set up of a new methodology to predict the dynamics of geometrically nonlinear mistuned bladed disks subjected to contact interactions in a numerically efficient way through the use of reduced-order models. Most specifically, this work focuses on rubbing events between the blade-tip and the surrounding casing.

In order to develop this methodology, the use of different reduction bases has been investigated following respectively the proper orthogonal decomposition approach, the Craig-Bampton approach and the modal derivative approach. The different reduction methods have been adapted, when needed, and used to study the dynamics of a compressor blade from the NASA rotor 37 in the case of a harmonic excitation, representative of an aerodynamic loading, and in the case of contact excitation. These studies allow to highlight the strengths and weaknesses of the different methods. The reduction method by POD proves to be very sensitive to the spatial shape of the excitation. In contact simulations where the exact excitation is not known *a priori*, POD does not provide accurate results. The Craig-Bampton reduction method does not allow to capture globally the dynamics of the blade, even in the simple case of a harmonic excitation. In contrast, the modal derivative approach allows to build robust reduced-order models. In order to limit the size of the reduced system, a modal derivative selection criterion has been proposed.

The final methodology proposed here to predict the nonlinear and nonsmooth dynamics of the blade in a computationally efficient way is based on the projection of the high fidelity model onto a reduction basis composed of Craig-Bampton modes and a selection of their modal derivatives. This reduction basis is computed directly from the mechanical properties of the structure and does not require training data from previous simulations or experiments. The nonlinear internal forces due to large displacements are evaluated with the stiffness evaluation procedure. Contact is numerically handled with Lagrange multipliers and the equation of motion is integrated forward in time using an explicit central difference time integration scheme. Parametric reduced-order models, valid on a given angular speed interval, can also be built by interpolating the linear and nonlinear stiffness terms between three angular speeds.

In order to ease the subsequent possible technology transfer to the industry, the core numerical tool is, in this work, written in Python, which is an efficient, open-source and portable scientific programming language. The finite element software SAMCEF is used to perform

the analyses with the full-order finite element model required for building the reduced-order model. The numerical strategy could however be easily included in any commercial finite element software as it is non-intrusive. Once built, the reduced-order model is completely independent from the full-order finite element model, which avoids costly simulations with the full-order model and data exchange between the finite element software and the specific software used for the treatment of nonlinearities.

This methodology has been applied to study in more details the contact interactions of the NASA rotor 37 blade with a surrounding rigid casing. The modeling of the wear of an abradable coating deposited along the casing has also been addressed. On the one hand, the numerical studies have shown that the reduction procedure developed allows to extract quantities of interest that are relevant for both researchers and industrial designers. In particular, it can be used to efficiently identify the critical angular speeds at which high-amplitude interactions occur and to assess the consequences of the interactions on the structure integrity, for instance in terms of stress fields inside the blade. On the other hand, the comparison of the results obtained without and with geometric nonlinearities shows that neglecting the geometric nonlinearities in such studies can lead to wrong estimation of the critical angular speeds of the structure and to bad evaluation of the severity of the interactions in terms of displacement amplitudes and von Mises stress fields.

The methodology has then been generalized to full bladed disks using component mode synthesis techniques with fixed interfaces based on the assumption that the constraint modes related to the cyclic boundaries remain linear. The methodology has first been applied to the NASA rotor 37 full bladed disk subjected to known harmonic excitations, and then used to study the contact interactions of the structure with the casing. In this context, the repeated evaluation of the nonlinear internal forces due to large displacements in the contact algorithm can become numerically costly because of the size of the reduced-order model. A dedicated numerical strategy, with memory sharing, has therefore been developed to reduce the computation time. It has finally been shown that mistuning can be taken into account in the reduced-order model, for instance, but not only, with a Young's modulus variability between the sectors.

Perspectives

Some perspectives are suggested for future works.

First, it would be very interesting to validate the methodology by comparing the results obtained with results from experimental tests.

As a direct extension of this work, the mistuning analyses presented in the last chapter could be further developed with deeper stochastic analyses with Monte Carlo simulations, polynomial chaos expansion or perturbation techniques. Using an open finite element software could allow to build ROMs for a large number of values of the Young's modulus in the studied range of variation, that could be used to generate mistuned bladed disks ROMs.

As detailed through this thesis, the proposed methodology is compatible with the harmonic balance method and could be used to study the contact dynamics of bladed structures in the frequency domain. From a numerical point of view, it could be interesting to use these frequency methods to build the complete nonlinear frequency response curve of the structure, identify the bifurcations and study the solutions stability. This numerical strategy could also be applied to more slender structures, such as fan stages, which are likely to experience more pronounced geometrically nonlinear effects.

The numerical strategy could also be combined with existing methodologies to introduce more physics in the model. For instance, observations made on several experimental set-ups underlined the very high temperature increases measured in the vicinity of contact areas and within abradable coatings following contact events [152]. Thermal effects could be accounted for by coupling the reduced-order model to a thermal model. Also, the modeling of a flexible casing could allow to study the modal interactions between a full bladed disk and the surrounding casing. For more realism, the imposed external loading could be obtained from aeroelastic studies and the reduced-order model could be coupled with a CFD solver.

As shown in the chapter dedicated to full bladed disks, computations with the ROMs built in this work still can be particularly costly for structures with a large number of sectors. The current work could therefore be extended to achieve further reduction of the computational costs in this context. Preliminary studies showed that it is not necessary to consider all the components of the reduced nonlinear stiffness tensors $\tilde{\mathbf{A}}$ and $\tilde{\mathbf{B}}$ to obtain an accurate description of the reduced nonlinear internal forces. *A priori* identification of the dominant coefficients could allow to reduce the computational burden of the STEP in the offline stage, but also the cost of the online stage provided the presence of zero nonlinear stiffness terms is properly taken into account in the implementation of the calculation of the tensor products involved in the nonlinear forces. Alternative numerical strategies could also be explored, as invariant manifold approaches recently developed for systems with geometric nonlinearities. The results obtained with the theory of spectral submanifolds and the direct normal form theory are both very encouraging in terms of accuracy and size of the resulting ROM. The extension of these methods to problems with contact is however very challenging and requires further investigations.

APPENDIX A EQUATION OF MOTION OF A ROTATING STRUCTURE

In this appendix, the differential equation governing the motion of a rotating structure is mathematically established based on the Hamilton principle and the space discretization of the problem based on the finite element formalism. Starting from the general equation of motion expressed in an inertial frame, the equation of motion is rewritten in the rotating frame of an equilibrium configuration considered as a natural configuration.

The equation of motion is established using the assumptions usually made in the field of turbomachinery. First, the material is homogeneous, isotropic, non-dissipative and elastic. Then, the angular speed is assumed to be constant, both in direction and in module.The only nonlinear behavior considered here are geometric nonlinearities (due to large displacements) and contact nonlinearities.

Inertial and rotating frames

Let's consider a deformable solid of volume V and boundary Γ at rest whose geometry is well known and can be meshed. Because of external excitations, this solid will be subjected to displacements and deformations over time. Let's define R_g a fixed reference frame of origin O and R_m the moving reference frame of origin O' following the motion of the structure (see Fig. A.1). The displacement of R_m with respect to R_g can be decomposed into the translation of O' with respect to O, represented by the vector with components $\mathbf{b}(t)$ defined in R_g, and the rotation of R_m with respect to R_g described by the angular speed vector $\boldsymbol{\omega}(t) = \boldsymbol{\omega}$, with components ω_x, ω_y and ω_z in R_m.

Let's introduce $\mathbf{x}$, the components in R_m of the position vector of a point M of the solid at rest, $\mathbf{s}(\mathbf{x}, t)$ the components of the displacement vector of M in R_m at time t and $\mathbf{y}(\mathbf{x}, t)$ the components of the position vector of M in R_g in the deformed configuration. The quantities in the different frames are related through

$$\mathbf{y}(\mathbf{x}, t) = \mathbf{b}(t) + \mathbf{R}\left[\mathbf{x} + \mathbf{s}(\mathbf{x}, t)\right], \tag{A.1}$$

where $\mathbf{R}$ is the rotation matrix from R_g to R_m. This rotation matrix is orthogonal, *i.e.*

$$\mathbf{R}^{\mathrm{T}}\mathbf{R} = \mathbf{I}, \tag{A.2}$$

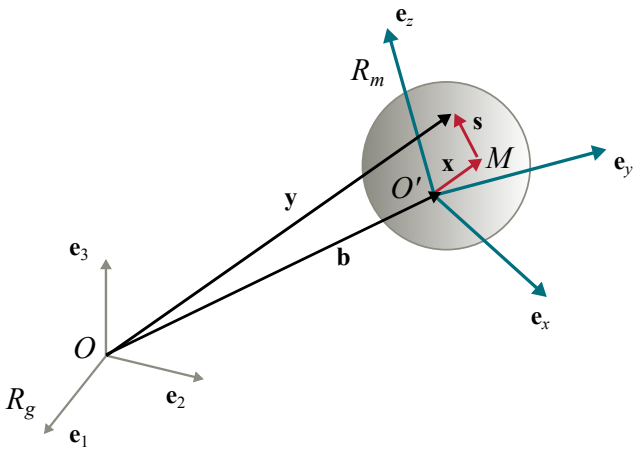

FIGURE A.1 – Rotating structure with fixed reference frame R_g and rotating frame R_m.

and

$$\dot{\mathbf{R}} = \mathbf{R}\boldsymbol{\Omega}, \tag{A.3}$$

where $\boldsymbol{\Omega}$ is the skew symmetric angular velocity matrix

$$\boldsymbol{\Omega} = \begin{pmatrix} 0 & -\omega_z & \omega_y \\ \omega_z & 0 & -\omega_x \\ -\omega_y & \omega_x & 0 \end{pmatrix}. \tag{A.4}$$

In the following, the time and space dependency of the different quantities in (A.1) will be omitted for brevity.

In the present application, the frame R_m is linked to the rotating bladed disk and it is assumed that it only has a rotating motion with respect to R_g, *i.e.* $\mathbf{b} = 0$. The time derivative of $\mathbf{y}$ in R_g is given by

$$\begin{aligned} \dot{\mathbf{y}} &= \dot{\mathbf{R}}(\mathbf{x} + \mathbf{s}) + \mathbf{R}(\dot{\mathbf{x}} + \dot{\mathbf{s}}) \\ &= \mathbf{R}\boldsymbol{\Omega}(\mathbf{x} + \mathbf{s}) + \mathbf{R}\dot{\mathbf{s}}. \end{aligned} \tag{A.5}$$

Hamilton principle

The equation of motion are derived from Hamilton principle [73]. Hamilton's principle states that the solution $\mathbf{s}(t)$ between t_1 and t_2 is a stationary point of the mechanical action in Hamilton's sense, *i.e.*

$$\delta \int_{t_1}^{t_2} (\mathcal{T} - \mathcal{V})\, dt + \int_{t_1}^{t_2} \delta\mathcal{W} dt = 0 \quad \text{with} \quad \delta\mathbf{s}(\mathbf{x}, t_1) = \delta\mathbf{s}(\mathbf{x}, t_2) = 0, \tag{A.6}$$

where $\mathcal{T}$ is the kinetic energy of the system, $\mathcal{V}$ is the strain energy of the system and $\mathcal{W}$ is the work done by the external forces.

Strain energy The strain energy writes

$$\mathcal{V} = \frac{1}{2}\int_V \boldsymbol{\sigma} : \boldsymbol{\epsilon}\ dV \tag{A.7}$$

where $\boldsymbol{\sigma}$ and $\boldsymbol{\epsilon}$ respectively stand for the stress and strain tensors. In index notation and using Einstein summation convention, the double dot product between these tensors writes

$$\boldsymbol{\sigma} : \boldsymbol{\epsilon} = \sigma_{ij}\epsilon_{ij}. \tag{A.8}$$

Different measures of stress and strain, which are equivalent in a linear context, can be defined. In a nonlinear context, the second Piola-Kirchhoff stress tensor is largely used [113]. This tensor is defined as

$$\mathbf{S} = J\mathbf{F}^{-1}\bar{\boldsymbol{\sigma}}\mathbf{F}^{-\mathrm{T}}, \tag{A.9}$$

where $\bar{\boldsymbol{\sigma}}$ is the Cauchy stress tensor, the deformation gradient

$$\mathbf{F} = \frac{\partial\left(\mathbf{x}+\mathbf{s}\right)}{\partial\mathbf{x}} = \mathbf{I} + \frac{\partial\mathbf{s}}{\partial\mathbf{x}}, \tag{A.10}$$

and $J = \det\mathbf{F}$. Regarding the strain definition, the Green-Lagrange tensor

$$\mathbf{E} = \frac{1}{2}\left(\mathbf{F}^{\mathrm{T}}\mathbf{F} - \mathbf{I}\right) = \frac{1}{2}\left(\frac{\partial\mathbf{s}}{\partial\mathbf{x}} + \left[\frac{\partial\mathbf{s}}{\partial\mathbf{x}}\right]^{\mathrm{T}} + \frac{\partial\mathbf{s}}{\partial\mathbf{x}}\left[\frac{\partial\mathbf{s}}{\partial\mathbf{x}}\right]^{\mathrm{T}}\right) \tag{A.11}$$

is used in a nonlinear context. This tensor is the sum of a linear term and a quadratic term. When studying small deformations, the nonlinear part of the strain tensor can be neglected. Under the assumption of linear elasticity, the Saint Venant-Kirchhoff model is used, which assumes a linear relationship exists between the second Piola-Kirchhoff stress tensor and the Green-Lagrange tensor. Defining $\mathbf{H}$ as the fourth-order elasticity tensor, the tensors are related through

$$\mathbf{S} = \mathbf{H} : \mathbf{E}, \tag{A.12}$$

or in index notation,

$$S_{ij} = H_{ijkl}E_{kl}. \tag{A.13}$$

The stress and strain tensors are symmetric, so that the elasticity tensor satisfies the relations

$$H_{ijkl} = H_{jikl} = H_{ijlk}. \tag{A.14}$$

Moreover, by assuming that the stress tensor derived from a potential, one can show that

$$H_{ijkl} = H_{klij}. \tag{A.15}$$

Injecting (A.11) and (A.12) in (A.7), the strain energy writes, in index notations,

$$\begin{aligned}\mathcal{V} &= \frac{1}{2}\int_V H_{ijkl}E_{ij}E_{kl}dV \\ &= \frac{1}{8}\int_V H_{ijkl}\left(\frac{\partial s_i}{\partial x_j}+\frac{\partial s_j}{\partial x_i}+\frac{\partial s_i}{\partial x_m}\frac{\partial s_j}{\partial x_m}\right)\left(\frac{\partial s_k}{\partial x_l}+\frac{\partial s_l}{\partial x_k}+\frac{\partial s_k}{\partial x_n}\frac{\partial s_l}{\partial x_n}\right)dV.\end{aligned} \tag{A.16}$$

Using the relations (A.14) and (A.15), the strain energy simply writes

$$\mathcal{V} = \frac{1}{2}\int_V H_{ijkl}\left(\frac{\partial s_i}{\partial x_j}\frac{\partial s_k}{\partial x_l}+\frac{\partial s_i}{\partial x_m}\frac{\partial s_j}{\partial x_m}\frac{\partial s_k}{\partial x_l}+\frac{\partial s_i}{\partial x_m}\frac{\partial s_j}{\partial x_m}\frac{\partial s_k}{\partial x_n}\frac{\partial s_l}{\partial x_n}\right)dV. \tag{A.17}$$

Kinetic energy The kinetic energy writes

$$\begin{aligned}\mathcal{T} &= \frac{1}{2}\int_V \rho\dot{\mathbf{y}}^{\mathrm{T}}\dot{\mathbf{y}}dV \\ &= \frac{1}{2}\int_V \rho\left[(\mathbf{x}^{\mathrm{T}}+\mathbf{s}^{\mathrm{T}})\boldsymbol{\Omega}^{\mathrm{T}}\mathbf{R}^{\mathrm{T}}+\dot{\mathbf{s}}^{\mathrm{T}}\mathbf{R}^{\mathrm{T}}\right]\left[\mathbf{R}\boldsymbol{\Omega}(\mathbf{x}+\mathbf{s})+\mathbf{R}\dot{\mathbf{s}}\right]dV \\ &= \frac{1}{2}\int_V \rho\left[\mathbf{x}^{\mathrm{T}}\boldsymbol{\Omega}^{\mathrm{T}}\boldsymbol{\Omega}\mathbf{x}+2\mathbf{x}^{\mathrm{T}}\boldsymbol{\Omega}^{\mathrm{T}}\boldsymbol{\Omega}\mathbf{s}+\mathbf{s}^{\mathrm{T}}\boldsymbol{\Omega}^{\mathrm{T}}\boldsymbol{\Omega}\mathbf{s}+2\mathbf{x}^{\mathrm{T}}\boldsymbol{\Omega}^{\mathrm{T}}\dot{\mathbf{s}}+2\mathbf{s}^{\mathrm{T}}\boldsymbol{\Omega}^{\mathrm{T}}\dot{\mathbf{s}}+\dot{\mathbf{s}}^{\mathrm{T}}\dot{\mathbf{s}}\right]dV.\end{aligned} \tag{A.18}$$

Lagrange equations

Using the finite element formulation, the continuous displacement $\mathbf{s}$ is written as

$$\mathbf{s}(\mathbf{x},t) = \mathbf{N}(\mathbf{x})\mathbf{u}_p(t), \tag{A.19}$$

where $\mathbf{u}_p$ is the discretized displacement field in the rotating frame and $\mathbf{N}$ stands for the matrix of shape functions of the finite element formalism. Injecting (A.19) in (A.17), the

strain energy writes

$$\mathcal{V} = \frac{1}{2}\int_V H_{ijkl}\left(\frac{\partial N_{i\alpha}}{\partial x_j}u_{p,\alpha}\frac{\partial N_{k\beta}}{\partial x_l}u_{p,\beta} + \frac{\partial N_{i\alpha}}{\partial x_m}u_{p,\alpha}\frac{\partial N_{j\beta}}{\partial x_m}u_{p,\beta}\frac{\partial N_{k\gamma}}{\partial x_l}u_{p,\gamma} + \frac{\partial N_{i\alpha}}{\partial x_m}u_{p,\alpha}\frac{\partial N_{j\beta}}{\partial x_m}u_{p,\beta}\frac{\partial N_{k\gamma}}{\partial x_n}u_{p,\gamma}\frac{\partial N_{l\delta}}{\partial x_n}u_{p,\delta}\right)dV. \tag{A.20}$$

The strain energy is a fourth-order polynomial in $\mathbf{u}_p$. Injecting (A.19) in (A.18), the kinetic energy writes

$$\mathcal{T} = \frac{1}{2}\int_V \rho\mathbf{x}^{\mathrm{T}}\mathbf{\Omega}^{\mathrm{T}}\mathbf{\Omega}\mathbf{x}dV + \left(\int_V \rho\mathbf{x}^{\mathrm{T}}\mathbf{\Omega}^{\mathrm{T}}\mathbf{\Omega}\mathbf{N}dV\right)\mathbf{u}_p + \frac{1}{2}\mathbf{u}_p^{\mathrm{T}}\left(\int_V \rho\mathbf{N}^{\mathrm{T}}\mathbf{\Omega}^{\mathrm{T}}\mathbf{\Omega}\mathbf{N}dV\right)\mathbf{u}_p + \left(\int_V \rho\mathbf{x}^{\mathrm{T}}\mathbf{\Omega}^{\mathrm{T}}\mathbf{N}dV\right)\dot{\mathbf{u}}_p + \mathbf{u}_p^{\mathrm{T}}\left(\int_V \rho\mathbf{N}^{\mathrm{T}}\mathbf{\Omega}^{\mathrm{T}}\mathbf{N}dV\right)\dot{\mathbf{u}}_p + \frac{1}{2}\dot{\mathbf{u}}_p^{\mathrm{T}}\left(\int_V \rho\mathbf{N}^{\mathrm{T}}\mathbf{N}dV\right)\dot{\mathbf{u}}_p. \tag{A.21}$$

With the discretization (A.19), the Hamilton principle (A.6) is equivalent to solving the Lagrange equations

$$\frac{d}{dt}\left(\frac{\partial\mathcal{L}}{\partial\dot{\mathbf{u}}_p}\right) - \frac{\partial\mathcal{L}}{\partial\mathbf{u}_p} = \mathbf{Q}, \tag{A.22}$$

where the Lagrangian of the system is defined as

$$\mathcal{L}(\mathbf{u}_p, \dot{\mathbf{u}}_p) = \mathcal{T} - \mathcal{V}, \tag{A.23}$$

and where $\mathbf{Q}$ stands for the generalized force term.

Injecting (A.21) and (A.23) in (A.22), the equation of motion can be written as

$$\left(\int_V \rho\mathbf{N}^{\mathrm{T}}\dot{\mathbf{\Omega}}^{\mathrm{T}}\mathbf{x}dV\right) + \dot{\mathbf{u}}_p^{\mathrm{T}}\left(\int_V \rho\mathbf{N}^{\mathrm{T}}\mathbf{\Omega}^{\mathrm{T}}\mathbf{N}dV\right) + {\mathbf{u}_p}^{\mathrm{T}}\left(\int_V \rho\mathbf{N}^{\mathrm{T}}\dot{\mathbf{\Omega}}^{\mathrm{T}}\mathbf{N}dV\right) + \left(\int_V \rho\mathbf{N}^{\mathrm{T}}\mathbf{N}dV\right)\ddot{\mathbf{u}}_p - \left(\int_V \rho\mathbf{N}^{\mathrm{T}}\mathbf{\Omega}^{\mathrm{T}}\mathbf{\Omega}\mathbf{x}dV\right) - \left(\int_V \rho\mathbf{N}^{\mathrm{T}}\mathbf{\Omega}^{\mathrm{T}}\mathbf{\Omega}\mathbf{N}dV\right)\mathbf{u}_p - \left(\int_V \rho\mathbf{N}^{\mathrm{T}}\mathbf{\Omega}^{\mathrm{T}}\mathbf{N}dV\right)\dot{\mathbf{u}}_p + \frac{\partial\mathcal{V}}{\partial\mathbf{u}_p} = \mathbf{Q}, \tag{A.24}$$

where

$$\mathbf{Q} = \mathbf{f}_e(t) + \mathbf{f}_c(\mathbf{u}_p, \dot{\mathbf{u}}_p) = \int_V \mathbf{N}^{\mathrm{T}}\mathbf{f}(t)dV + \int_\Gamma \mathbf{N}^{\mathrm{T}}\mathbf{t}(t)dS + \int_\Gamma \mathbf{N}^{\mathrm{T}}\mathbf{t}_c(\mathbf{s}, \dot{\mathbf{s}})dS, \tag{A.25}$$

where $\mathbf{f}$ is the vector of external body forces expressed in the rotating frame, $\mathbf{t}$ is the vector of surface tractions and $\mathbf{t}_c$ stands for the contact forces expressed in the rotating frame acting on Γ. The normal and tangential components of the contact forces have to meet some conditions, as detailed in section 2.4.3.

The derivative of the strain energy can be written as

$$\frac{\partial \mathcal{V}}{\partial \mathbf{u}_p} = \mathbf{K}^{(e)}\mathbf{u}_p + \mathbf{g}(\mathbf{u}_p), \tag{A.26}$$

where $\mathbf{K}^{(e)}$ is the elastic stiffness matrix and $\mathbf{g}(\mathbf{u}_p)$ accounts for the nonlinear internal forces. Under the assumptions of linear elasticity and when using the Green-Lagrange tensor for the definition of the strain, the derivative of the strain energy is a third order polynomial in $\mathbf{u}_p$. The elastic stiffness matrix takes the expression

$$K^{(e)}_{\alpha\beta} = \int_V H_{ijkl} \frac{\partial N_{i\alpha}}{\partial x_j} \frac{\partial N_{k\beta}}{\partial x_l} dV. \tag{A.27}$$

Assuming a constant rotation speed, the equation of motion can be rewritten as

$$\begin{aligned} &\left(\int_V \rho \mathbf{N}^{\mathrm{T}}\mathbf{N} dV\right)\ddot{\mathbf{u}}_p + 2\left(\int_V \rho \mathbf{N}^{\mathrm{T}}\boldsymbol{\Omega}\mathbf{N} dV\right)\dot{\mathbf{u}}_p \\ -\left(\int_V \rho \mathbf{N}^{\mathrm{T}}\boldsymbol{\Omega}^{\mathrm{T}}\boldsymbol{\Omega}\mathbf{N} dV\right)\mathbf{u}_p &+ \mathbf{K}^{(e)}\mathbf{u}_p + \mathbf{g}(\mathbf{u}_p) = \mathbf{Q} + \int_V \rho \mathbf{N}^{\mathrm{T}}\boldsymbol{\Omega}^{\mathrm{T}}\boldsymbol{\Omega}\mathbf{x} dV. \end{aligned} \tag{A.28}$$

The mass matrix $\mathbf{M}$ is defined as

$$\mathbf{M} = \int_V \rho \mathbf{N}^{\mathrm{T}}\mathbf{N} dV. \tag{A.29}$$

The gyroscopic matrix $\mathbf{G}(\boldsymbol{\Omega})$ is defined as

$$\mathbf{G}(\boldsymbol{\Omega}) = 2\int_V \rho \mathbf{N}^{\mathrm{T}}\boldsymbol{\Omega}\mathbf{N} dV. \tag{A.30}$$

The term

$$\mathbf{G}(\boldsymbol{\Omega})\dot{\mathbf{u}}_p \tag{A.31}$$

is defined as the Coriolis force. This force is proportional to the rotation speed and acts perpendicularly to the axis of rotation and to the velocity vector. The gyroscopic coupling matrix can be directly deduced from the knowledge of the mass matrix. When the structure rotates at a constant rotation speed Ω about the $\mathbf{e}_3$-axis, the gyroscopic matrix writes

$$\mathbf{G}(\Omega) = 2\Omega\mathbf{M}\ \mathrm{diag}\left(\begin{bmatrix} 0 & -1 & 0 \\ 1 & 0 & 0 \\ 0 & 0 & 0 \end{bmatrix}\right). \tag{A.32}$$

The centrifugal stiffness matrix $\mathbf{K}^{(c)}(\boldsymbol{\Omega})$ is defined as

$$\mathbf{K}^{(c)}(\boldsymbol{\Omega}) = -\left(\int_V \rho \mathbf{N}^{\mathrm{T}} \boldsymbol{\Omega}^{\mathrm{T}} \boldsymbol{\Omega} \mathbf{N} dV\right). \tag{A.33}$$

The term

$$\mathbf{K}^{(c)}\left(\boldsymbol{\Omega}\right)\mathbf{u}_p \tag{A.34}$$

is defined as the centrifugal force. This force is proportional to the square of the speed of rotation of the structure. The changing direction of the centrifugal force induces a softening effect. The centrifugal stiffness matrix can be directly deduced from the knowledge of the mass matrix. When the structure rotates at a constant rotation speed Ω about the $\mathbf{e}_3$-axis, the centrifugal stiffness matrix writes

$$\mathbf{K}^{(c)}(\Omega) = -\Omega^2 \mathbf{M}\ \mathrm{diag}\left(\begin{bmatrix} 1 & 0 & 0 \\ 0 & 1 & 0 \\ 0 & 0 & 0 \end{bmatrix}\right). \tag{A.35}$$

The term

$$\int_V \rho \mathbf{N}^{\mathrm{T}} \boldsymbol{\Omega}^{\mathrm{T}} \boldsymbol{\Omega} \mathbf{x} dV \tag{A.36}$$

is defined as the centrifugal force vector $\mathbf{f}_{ei}(\boldsymbol{\Omega})$. Adding a viscous damping term $\mathbf{D}\dot{\mathbf{u}}_p$, the equation of motion writes

$$\mathbf{M}\ddot{\mathbf{u}}_p + \left[\mathbf{D} + \mathbf{G}\left(\boldsymbol{\Omega}\right)\right]\dot{\mathbf{u}}_p + \left[\mathbf{K}^{(e)} + \mathbf{K}^{(c)}\left(\boldsymbol{\Omega}\right)\right]\mathbf{u}_p + \mathbf{g}(\mathbf{u}_p) = \mathbf{f}_e(t) + \mathbf{f}_c(\mathbf{u}_p, \dot{\mathbf{u}}_p) + \mathbf{f}_{ei}(\boldsymbol{\Omega}). \tag{A.37}$$

Note that the same expression is obtained by introducing the finite element approximation (A.19) in the weak form of the problem based on the principle of virtual work, obtained by multiplying the strong form of the problem by a virtual displacement kinematically admissible and integrating it on the volume [13, 210].

Prestressed static equilibrium state as a natural configuration

The dynamics of the structure is generally studied with respect to the prestressed static equilibrium state $\mathbf{u}_s$ due to the structure rotation. According to (A.37), the static equilibrium position $\mathbf{u}_s$ satisfies

$$\left[\mathbf{K}^{(e)} + \mathbf{K}^{(c)}\left(\boldsymbol{\Omega}\right)\right]\mathbf{u}_s + \mathbf{g}(\mathbf{u}_s) = \mathbf{f}_{ei}(\boldsymbol{\Omega}). \tag{A.38}$$

The relative displacement $\mathbf{u}$ is related to $\mathbf{u}_s$ and $\mathbf{u}_p$ through

$$\mathbf{u} = \mathbf{u}_p - \mathbf{u}_s, \tag{A.39}$$

so that the equation of motion (A.37) can be rewritten

$$\mathbf{M}\ddot{\mathbf{u}} + [\mathbf{D} + \mathbf{G}(\boldsymbol{\Omega})]\,\dot{\mathbf{u}} + \left[\mathbf{K}^{(e)} + \mathbf{K}^{(c)}(\boldsymbol{\Omega})\right](\mathbf{u}_s + \mathbf{u}) + \mathbf{g}(\mathbf{u}_s + \mathbf{u}) = \mathbf{f}_e(t) + \mathbf{f}_c(\mathbf{u} + \mathbf{u}_s, \dot{\mathbf{u}}) + \mathbf{f}_{ei}(\boldsymbol{\Omega}). \tag{A.40}$$

Injecting (A.38) in (A.40),

$$\mathbf{M}\ddot{\mathbf{u}} + [\mathbf{D} + \mathbf{G}(\boldsymbol{\Omega})]\,\dot{\mathbf{u}} + \left[\mathbf{K}^{(e)} + \mathbf{K}^{(c)}(\boldsymbol{\Omega})\right]\mathbf{u} + \mathbf{g}(\mathbf{u}_s + \mathbf{u}) - \mathbf{g}(\mathbf{u}_s) = \mathbf{f}_e(t) + \mathbf{f}_c(\mathbf{u} + \mathbf{u}_s, \dot{\mathbf{u}}). \tag{A.41}$$

The development of the nonlinear forces $\mathbf{g}(\mathbf{u} + \mathbf{u}_s)$ in the neighborhood of the static displacement $\mathbf{u}_s$ is given by

$$\mathbf{g}(\mathbf{u}_s + \mathbf{u}) = \mathbf{g}(\mathbf{u}_s) + \left.\frac{\partial \mathbf{g}(\mathbf{u}_p)}{\partial \mathbf{u}_p}\right|_{\mathbf{u}_p = \mathbf{u}_s} \mathbf{u} + \mathbf{g}_{\mathrm{nl}}(\mathbf{u}, \mathbf{u}_s) \tag{A.42}$$

$$= \mathbf{g}(\mathbf{u}_s) + \mathbf{K}^{(g)}(\mathbf{u}_s)\mathbf{u} + \mathbf{g}_{\mathrm{nl}}(\mathbf{u}, \mathbf{u}_s), \tag{A.43}$$

where $\mathbf{K}^{(g)}(\mathbf{u}_s)$ is the geometric prestressed stiffness matrix and $\mathbf{g}_{\mathrm{nl}}(\mathbf{u}, \mathbf{u}_s)$ accounts for the nonlinear terms. Under the assumptions of linear elasticity and when using the Green-Lagrange tensor for the definition of the strain, $\mathbf{g}_{\mathrm{nl}}(\mathbf{u}, \mathbf{u}_s)$ is a third order polynomial in $\mathbf{u}$ whose coefficients depend on the prestressed state $\mathbf{u}_s$.

The discretized equation of motion governing the relative displacement $\mathbf{u}$ around an initial prestressed static equilibrium state $\mathbf{u}_s$ induced by the rotation of the structure therefore writes

$$\mathbf{M}\ddot{\mathbf{u}} + [\mathbf{D} + \mathbf{G}(\boldsymbol{\Omega})]\,\dot{\mathbf{u}} + \left[\mathbf{K}^{(e)} + \mathbf{K}^{(c)}(\Omega) + \mathbf{K}^{(g)}(\mathbf{u}_s)\right]\mathbf{u} + \mathbf{g}_{\mathrm{nl}}(\mathbf{u}, \mathbf{u}_s) = \mathbf{f}_e(t) + \mathbf{f}_c(\mathbf{u} + \mathbf{u}_s, \dot{\mathbf{u}}). \tag{A.44}$$

REFERENCES

[1] D. E. Adams and R. J. Allemang, *Frequency domain method for estimating the parameters of a non-linear structural dynamic model through feedback*, Mechanical Systems and Signal Processing, 14 (2000), pp. 637–656. doi:10.1006/mssp.2000.1292.

[2] S. Adhikari and A. S. Phani, *Rayleigh's Classical Damping Revisited*, 2007.

[3] Q. Agrapart, *Bilan d'énergie au contact et contribution de la thermomécanique sur la dynamique d'interaction aube - revêtement abradable de turboréacteur aéronautique*, PhD thesis, Université de Lille (France), 2018.

[4] Airbus, *Annual Report 2018*, tech. rep., Airbus, 2018.

[5] P. Aivaliotis, K. Georgoulias and G. Chryssolouris, *The use of Digital Twin for predictive maintenance in manufacturing*, International Journal of Computer Integrated Manufacturing, 32 (2019), pp. 1067–1080. doi:10.1080/0951192X.2019.1686173.

[6] B. Al Sayed, *Comportement dynamique des ensembles tournants de turbomachines. Maîtrise des effets des dispositifs de liaisonnement amortisseurs*, PhD thesis, Institut National des Sciences Appliquées de Lyon (France), 2011.

[7] P. Almeida, C. Gibert, F. Thouverez, X. Leblanc and J.-P. Ousty, *Experimental Analysis of Dynamic Interaction Between a Centrifugal Compressor and Its Casing*, Journal of Turbomachinery, 137 (2014). doi:10.1115/1.4028328.

[8] ——, *Numerical Analysis of Bladed Disk-Casing Contact with Friction and Wear*, Journal of Engineering for Gas Turbines and Power, 138 (2016). doi:10.1115/1.4033065.

[9] D. Amsallem and C. Farhat, *An online method for interpolating linear parametric reduced-order models*, SIAM Journal on Scientific Computing, 33 (2011), pp. 2169–2198. doi:10.1137/100813051.

[10] P. W. Anderson, *Absence of Diffusion in Certain Random Lattices*, Physical Review, 109 (1958), pp. 1492–1505. doi:10.1103/PhysRev.109.1492.

[11] P. Apiwattanalunggarn, *Modal reduction of nonlinear structural systems using nonlinear normal modes and component mode synthesis*, PhD thesis, Michigan State University (USA), 2003.

[12] Z. Bai and R. C. Li, *Structure-Preserving Model Reduction Using a Krylov Subspace Projection Formulation*, Communications in Mathematical Sciences, 3 (2005), pp. 179–199. doi:10.4310/CMS.2005.v3.n2.a6.

[13] M. Balmaseda, G. Jacquet-Richardet, A. Placzek and D.-M. Tran, *Reduced order models for nonlinear dynamic analysis with application to a fan blade*, in Proceedings of ASME Turbo Expo 2019, Phoenix (USA), 2019. doi:10.1115/GT2019-90813.

[14] M. Barrault, Y. Maday, N. C. Nguyen and A. T. Patera, *An "empirical interpolation" method: application to efficient reduced-basis discretization of partial differential equations*, Comptes Rendus Mathematique, 339 (2004), pp. 667–672. doi:10.1016/j.crma.2004.08.006.

[15] A. Batailly, *Simulation de l'interaction rotor/stator pour des turbo-machines aéronautiques en configuration non-accidentelle*, PhD thesis, École Centrale de Nantes (France), 2008.

[16] A. Batailly, Q. Agrapart, A. Millecamps and J.-F. Brunel, *Experimental and numerical simulation of a rotor/stator interaction event localized on a single blade within an industrial high-pressure compressor*, Journal of Sound and Vibration, 375 (2016), pp. 308–331. doi:10.1016/j.jsv.2016.03.016.

[17] A. Batailly and M. Legrand, *Unilateral contact induced blade/casing vibratory interactions in impellers: Analysis for flexible casings with friction and abradable coating*, Journal of Sound and Vibration, 348 (2015), pp. 344–364. doi:10.1016/j.jsv.2015.03.027.

[18] A. Batailly, M. Legrand, P. Cartraud and C. Pierre, *Assessment of reduced models for the detection of modal interaction through rotor stator contacts*, Journal of Sound and Vibration, 329 (2010), pp. 5546–5562. doi:10.1016/j.jsv.2010.07.018.

[19] A. Batailly, M. Legrand, A. Millecamps, S. Cochon and F. Garcin, *Redesign of a High-Pressure Compressor Blade Accounting for Nonlinear Structural Interactions*, Journal of Engineering for Gas Turbines and Power, 137 (2014). doi:10.1115/1.4028263.

[20] A. Batailly, M. Legrand, A. Millecamps and F. Garcin, *Numerical-experimental comparison in the simulation of rotor/stator interaction through blade-tip/abradable coating contact*, Journal of Engineering for Gas Turbines and Power, 134 (2012). doi:10.1115/1.4006446.

[21] A. Batailly, M. Meingast and M. Legrand, *Unilateral contact induced blade/casing vibratory interactions in impellers: Analysis for rigid casings*, Journal of Sound and Vibration, 337 (2015), pp. 244–262. doi:10.1016/j.jsv.2014.10.010.

[22] A. Batailly and A. Millecamps, *Minimising clearance consumption: A key factor for the design of blades robust to rotor/stator interactions?*, Proceedings of the ASME Turbo Expo, (2016). doi:10.1115/GT2016-56721.

[23] B. Beirow, F. Figaschewsky, A. Kühhorn and A. Bornhorn, *Vibration analysis of an axial turbine blisk with optimized intentional mistuning pattern*, Journal of Sound and Vibration, 442 (2019), pp. 11–27. doi:10.1016/j.jsv.2018.10.064.

[24] B. Beirow, A. Kühhorn, F. Figaschewsky and J. Nipkau, *Effect of Mistuning and Damping on the Forced Response of a Compressor Blisk Rotor*, in Proceedings of ASME Turbo Expo 2015, Montréal (Canada), 2015. doi:10.1115/GT2015-42036.

[25] B. Beirow, A. Kühhorn and J. Nipkau, *On the Influence of Strain Gauge Instrumentation on Blade Vibrations of Integral Blisk Compressor Rotors Applying a Discrete Model*, in Proceedings of ASME Turbo Expo 2009, Orlando (USA), 2009, pp. 245–253. doi:10.1115/GT2009-59207.

[26] ——, *An equivalent blisk model considering the influence of the air flow on blade vibrations of a mistuned compressor blisk*, in Springer Proceedings in Physics, vol. 139, Springer, Dordrecht, 2011, pp. 549–555. doi:10.1007/978-94-007-2069-5_74.

[27] B. Beirow, A. Kühhorn and S. Schrape, *A Discrete Model to Consider the Influence of the Air Flow on Blade Vibrations of an Integral Blisk Compressor Rotor*, in Proceedings of ASME Turbo Expo 2008, Berlin (Germany), 2008, pp. 381–392. doi:10.1115/GT2008-50613.

[28] R. Benamar, M. Bennouna and R. White, *The Effects of Large Vibration Amplitudes on the Mode Shapes and Natural Frequencies of Thin Elastic Structures, Part II: Fully Clamped Rectangular Isotropic Plates*, Journal of Sound and Vibration, 164 (1993), pp. 295–316. doi:10.1006/JSVI.1993.1215.

[29] O. O. Bendiksen, *Flutter of Mistuned Turbomachinery Rotors*, Journal of Engineering for Gas Turbines and Power, 106 (1984), pp. 25–33. doi:10.1115/1.3239546.

[30] R. Bladh, *Efficient predictions of the vibratory response of mistuned bladed disks by reduced order modeling*, PhD thesis, University of Michigan (USA), 2001.

[31] R. Bladh, M. P. Castanier and C. Pierre, *Component-Mode-Based Reduced Order Modeling Techniques for Mistuned Bladed Disks. Part I: Theoretical Models*, Journal of Engineering for Gas Turbines and Power, 123 (2001), pp. 89–99. doi:10.1115/1.1338947.

[32] ——, *Component-Mode-Based Reduced Order Modeling Techniques for Mistuned Bladed Disks. Part II: Application*, Journal of Engineering for Gas Turbines and Power, 123 (2001), pp. 100–108. doi:10.1115/1.1338948.

[33] N. N. Bogoliubov and Y. Mitropolsky, *Asymptotic Methods in the Theory of Non-linear Oscillations*, Gordon et Breach Science Publishers, 1961. doi:10.1007/BF01056172.

[34] A. Bossavit, *Symmetry, groups, and boundary value problems. A progressive introduction to noncommutative harmonic analysis of partial differential equations in domains with geometrical symmetry*, Computer Methods in Applied Mechanics and Engineering, 56 (1986), pp. 167–215. doi:10.1016/0045-7825(86)90119-2.

[35] ——, *Boundary Value Problems with Symmetry and Their Approximation by Finite Elements*, SIAM Journal on Applied Mathematics, 53 (1993), pp. 1352–1380. doi:10.1137/0153064.

[36] J. Bretheim and E. Bardy, *A Review of Power-Generating Turbomachines*, tech. rep., Grove City College, 2012.

[37] T. Bui-Thanh, K. Willcox, O. Ghattas and B. van Bloemen Waanders, *Goal-oriented, model-constrained optimization for reduction of large-scale systems*, Journal of Computational Physics, 224 (2007), pp. 880–896. doi:10.1016/J.JCP.2006.10.026.

[38] T. M. Cameron and J. H. Griffin, *An Alternating Frequency/Time Domain Method for Calculating the Steady-State Response of Nonlinear Dynamic Systems*, Journal of Applied Mechanics, 56 (1989), pp. 149–154. doi:10.1115/1.3176036.

[39] E. Capiez-Lernout, C. Soize, J. P. Lombard, C. Dupont and E. Seinturier, *Blade Manufacturing Tolerances Definition for a Mistuned Industrial Bladed Disk*, Journal of Engineering for Gas Turbines and Power, 127 (2005), pp. 621–628. doi:10.1115/1.1850497.

[40] E. Capiez-Lernout, C. Soize and M. P. Mignolet, *Computational stochastic statics of an uncertain curved structure with geometrical nonlinearity in three-dimensional elasticity*, Computational Mechanics, 49 (2012), pp. 87–97. doi:10.1007/s00466-011-0629-y.

[41] L. Carassale, V. Denoël, C. Martel and L. Panning-von Scheidt, *Key Features of the Transient Amplification of Mistuned Systems*, Journal of Engineering for Gas Turbines and Power, 143 (2021). doi:10.1115/1.4049501.

[42] N. J. Carpenter, R. L. Taylor and M. G. Katona, *Lagrange constraints for transient finite element surface contact*, International Journal for Numerical Methods in Engineering, 32 (1991), pp. 103–128. doi:10.1002/nme.1620320107.

[43] T. J. Carter, *Common failures in gas turbine blades*, Engineering Failure Analysis, 12 (2005), pp. 237–247. doi:10.1016/j.engfailanal.2004.07.004.

[44] M. P. Castanier and C. Pierre, *Using Intentional Mistuning in the Design of Turbomachinery Rotors*, AIAA Journal, 40 (2002), pp. 2077–2086. doi:10.2514/2.1542.

[45] ——, *Modeling and Analysis of Mistuned Bladed Disk Vibration: Current Status and Emerging Directions*, Journal of Propulsion and Power, 22 (2006), pp. 384–396. doi:10.2514/1.16345.

[46] S. Chaturantabut and D. C. Sorensen, *Discrete Empirical Interpolation for Nonlinear Model Reduction*, in Proceedings of the 48th IEEE Conference, Shanghai (China), 2009, pp. 4316–4321. doi:10.1109/CDC.2009.5400045.

[47] D. Chelidze and W. Zhou, *Smooth orthogonal decomposition-based vibration mode identification*, Journal of Sound and Vibration, 292 (2006), pp. 461–473. doi:10.1016/j.jsv.2005.08.006.

[48] D. W. Childs, *A Modal Transient Rotordynamic Model for Dual-Rotor Jet Engine Systems*, Journal of Engineering for Industry, 98 (1976), pp. 876–882. doi:10.1115/1.3439046.

[49] Y. Chong and M. Imregun, *Development and Application of a Nonlinear Modal Analysis Technique for MDOF Systems*, Journal of Vibration and Control, 7 (2001), pp. 167–179. doi:10.1177/107754630100700202.

[50] J. Chung and G. M. Hulbert, *A time integration algorithm for structural dynamics with improved numerical dissipation: The generalized-α method*, Journal of Applied Mechanics, 60 (1993), pp. 371–375. doi:10.1115/1.2900803.

[51] C. Cohen-Tannoudji, B. Diu and F. Laloe, *Mécanique quantique*, Hermann Paris, 1973.

[52] Y. Colaïtis and A. Batailly, *The harmonic balance method with arc-length continuation in blade-tip/casing contact problems*, Journal of Sound and Vibration, 502 (2021). doi:10.1016/j.jsv.2021.116070.

[53] R. R. Craig, *Coupling of substructures for dynamic analyses: An overview*, in Collection of Technical Papers - AIAA/ASME/ASCE/AHS/ASC Structures, Structural Dynamics and Materials Conference, vol. 5, AIAA, 2000, pp. 3–14. doi:10.2514/6.2000-1573.

[54] R. R. Craig and M. Bampton, *Coupling of substructures for dynamic analyses*, AIAA Journal, 6 (1968), pp. 1313–1319. doi:10.2514/3.4741.

[55] R. R. Craig and C.-J. Chang, *Free-interface methods of substructure coupling for dynamic analysis*, AIAA Journal, 14 (1976), pp. 1633–1635. doi:10.2514/3.7264.

[56] ——, *On the use of attachment modes in substructure coupling for dynamic analysis*, in AIAA/ASME 18th Structures, Structural Dynamics and Materials Conference, San Diego (USA), 1977. doi:10.2514/6.1977-405.

[57] M. Cruz Varona, R. Gebhart, P. Bilfinger, B. Lohmann and D. J. Rixen, *A Novel Derivation for Modal Derivatives Based on Volterra Series Representation and Its Use in Nonlinear Model Order Reduction*, in Proceedings of the 7th ECCOMAS Thematic Conference on Computational Methods in Structural Dynamics and Earthquake Engineering, Crete (Greece), 2019, pp. 2376–2394. doi:10.7712/120119.7081.19178.

[58] M. Cuny, S. Philippon, P. Chevrier and F. Garcin, *Experimental Measurement of Dynamic Forces Generated during Short-Duration Contacts: Application to Blade-Casing Interactions in Aircraft Engines*, Experimental Mechanics, 54 (2014), pp. 101–114. doi:10.1007/s11340-013-9780-z.

[59] T. Daniel, F. Casenave, N. Akkari and D. Ryckelynck, *Model order reduction assisted by deep neural networks (ROM-net)*, Advanced Modeling and Simulation in Engineering Sciences, 7 (2020). doi:10.1186/s40323-020-00153-6.

[60] E. Delhez, F. Nyssen, J.-C. Golinval and A. Batailly, *Comparative study of blades reduced order models with geometrical nonlinearities and contact interfaces*, in Proceedings of ASME Turbo Expo 2020, Virtual (Online), 2020. doi:10.1115/GT2020-14882.

[61] ——, *Assessment of geometric nonlinearities influence on NASA rotor 37 response to blade tip/casing rubbing events*, in Proceedings of ASME Turbo Expo 2021, Virtual (Online), 2021. doi:10.1115/gt2021-58931.

[62] ——, *Assessment of Geometric Nonlinearities Influence on NASA Rotor 37 Response to Blade Tip/Casing Rubbing Events*, Journal of Engineering for Gas Turbines and Power, 143 (2021). doi:10.1115/1.4051968.

[63] ——, *Reduced order modeling of blades with geometric nonlinearities and contact interactions*, Journal of Sound and Vibration, 500 (2021). doi:10.1016/j.jsv.2021.116037.

[64] ——, *Numerical study of bladed structures with geometric and contact nonlinearities*, Journal of Sound and Vibration (revised version submitted), (2022).

[65] J. D. Denton, *Lessons from Rotor 37*, Journal of Thermal Science, 6 (1997). doi:10.1007/s11630-997-0010-9.

[66] N. Di Palma, A. Martin, F. Thouverez and V. Courtier, *Nonlinear Harmonic Analysis of a Blade Model Subjected To Large Geometrical Deflection and Internal Resonance*, in Proceedings of ASME Turbo Expo 2019, Phoenix (USA), 2019. doi:10.1115/GT2019-91213.

[67] J. Dréau, B. Magnain, F. Nyssen and A. Batailly, *Polynomial chaos expansion for permutation and cyclic permutation invariant systems: Application to mistuned bladed disks*, Journal of Sound and Vibration, 503 (2021). doi:10.1016/j.jsv.2021.116103.

[68] R. C. F. Dye and T. A. Henry, *Vibration Amplitudes of Compressor Blades Resulting From Scatter in Blade Natural Frequencies*, Journal of Engineering for Gas Turbines and Power, 91 (1969), pp. 182–187. doi:10.1115/1.3574726.

[69] D. J. Ewins, *The effects of detuning upon the forced vibrations of bladed disks*, Journal of Sound and Vibration, 9 (1969), pp. 65–79. doi:10.1016/0022-460X(69)90264-8.

[70] ——, *Vibration Characteristics of Bladed Disc Assemblies*, Journal of Mechanical Engineering Science, 15 (1973), pp. 165–186. doi:10.1243/JMES_JOUR_1973_015_032_02.

[71] S. Fresca and A. Manzoni, *POD-DL-ROM: Enhancing deep learning-based reduced order models for nonlinear parametrized PDEs by proper orthogonal decomposition*, Computer Methods in Applied Mechanics and Engineering, 388 (2022). doi:10.1016/j.cma.2021.114181.

[72] G. Genta and M. Silvagni, *On Centrifugal Softening in Finite Element Method Rotordynamics*, Journal of Applied Mechanics, 81 (2014). doi:10.1115/1.4024073.

[73] M. Géradin and D. J. Rixen, *Mechanical Vibrations: Theory and Application to Structural Dynamics*, Wiley, 2015.

[74] F. Ghavamian, P. Tiso and A. Simone, *POD–DEIM model order reduction for strain softening viscoplasticity*, Computer Methods in Applied Mechanics and Engineering, 317 (2017), pp. 458–479. doi:10.1016/j.cma.2016.11.025.

[75] C. Gibert, *Fitting measured frequency response using non-linear modes*, Mechanical Systems and Signal Processing, 17 (2003), pp. 211–218. doi:10.1006/MSSP.2002.1562.

[76] A. Givois, A. Grolet, O. Thomas and J. F. Deü, *On the frequency response computation of geometrically nonlinear flat structures using reduced-order finite element models*, Nonlinear Dynamics, 97 (2019), pp. 1747–1781. doi:10.1007/s11071-019-05021-6.

[77] R. L. Goldman, *Vibration analysis by dynamic partitioning*, AIAA Journal, 7 (1969), pp. 1152–1154. doi:10.2514/3.5290.

[78] A. Grolet, *Dynamique non-linéaire des structures mécaniques : application aux systèmes à symétrie cyclique*, PhD thesis, École Centrale de Lyon (France), 2013.

[79] A. Grolet and F. Thouverez, *Vibration Analysis of a Nonlinear System With Cyclic Symmetry*, Journal of Engineering for Gas Turbines and Power, 133 (2011). doi:10.1115/1.4001989.

[80] ——, *Free and forced vibration analysis of a nonlinear system with cyclic symmetry: Application to a simplified model*, Journal of Sound and Vibration, 331 (2012), pp. 2911–2928. doi:10.1016/j.jsv.2012.02.008.

[81] B. Haasdonk, M. Dihlmann and M. Ohlberger, *A training set and multiple bases generation approach for parameterized model reduction based on adaptive grids in parameter space*, Mathematical and Computer Modelling of Dynamical Systems, 17 (2011), pp. 423–442. doi:10.1080/13873954.2011.547674.

[82] G. Haller and S. Ponsioen, *Nonlinear normal modes and spectral submanifolds: existence, uniqueness and use in model reduction*, Nonlinear Dynamics, 86 (2016), pp. 1493–1534. doi:10.1007/s11071-016-2974-z.

[83] D. Hartmann, M. Herz, M. Paffrath, J. Rommes, T. Tamarozzi, H. V. der Auweraer and U. Wever, *Model order reduction and digital twins*, De Gruyter, 2020, pp. 379–430.

[84] A. Hay, J. T. Borggaard and D. Pelletier, *Local improvements to reduced-order models using sensitivity analysis of the proper orthogonal decomposition*, Journal of Fluid Mechanics, 629 (2009), pp. 41–72. doi:10.1017/S0022112009006363.

[85] Z. He, B. I. Epureanu and C. Pierre, *Effects of unsteady aerodynamics on the dynamic response of mistuned bladed disks*, in Proceedings of the 3rd M.I.T. Conference on Computational Fluid and Solid Mechanics, Boston (USA), 2005, pp. 250–255.

[86] F. M. Hemez and S. W. Doebling, *Review and assessment of model updating for non-linear, transient dynamics*, Mechanical Systems and Signal Processing, 15 (2001), pp. 45–74. doi:10.1006/MSSP.2000.1351.

[87] R. Henry, *Contribution à l'étude dynamique des machines tournantes*, PhD thesis, INSA Lyon (France), 1981.

[88] High Level Group on Aviation Research, *Flightpath 2050 Europe's Vision for Aviation*, tech. rep., European Commission, 2011.

[89] H. M. Hilber, T. J. R. Hughes and R. L. Taylor, *Improved numerical dissipation for time integration algorithms in structural dynamics*, Earthquake Engineering & Structural Dynamics, 5 (1977), pp. 283–292. doi:10.1002/eqe.4290050306.

[90] C. Hoareau, L. Shang and A. Zilian, *ANN-reconstruction of nonlinear operator in projection-based ROM for elastic structures*, in Proceedings of the 8th European Congress on Computational Methods in Applied Sciences and Engineering, Oslo (Norway), 2022.

[91] C. Hodges, *Confinement of vibration by structural irregularity*, Journal of Sound and Vibration, 82 (1982), pp. 411–424. doi:10.1016/S0022-460X(82)80022-9.

[92] C. Hodges and J. Woodhouse, *Confinement of vibration by one-dimensional disorder, I: Theory of ensemble averaging*, Journal of Sound and Vibration, 130 (1989), pp. 237–251. doi:10.1016/0022-460X(89)90552-X.

[93] ——, *Confinement of vibration by one-dimensional disorder, II: A numerical experiment on different ensemble averages*, Journal of Sound and Vibration, 130 (1989), pp. 253–268. doi:10.1016/0022-460X(89)90553-1.

[94] J. Hou, B. J. Wicks and R. A. Antoniou, *An investigation of fatigue failures of turbine blades in a gas turbine engine by mechanical analysis*, Engineering Failure Analysis, 9 (2002), pp. 201–211. doi:10.1016/S1350-6307(01)00005-X.

[95] D. Hubler, *Rotor 37 and stator 37 assembly*, Series: Photographs Relating to Agency Activities, Facilities and Personnel, 1973 - 2013, (1977).

[96] W. C. Hurty, *Dynamic Analysis of Structural Systems Using Component Modes*, AIAA Journal, 3 (1965). doi:10.2514/3.2947.

[97] S. R. Idelsohn and A. Cardona, *A reduction method for nonlinear structural dynamic analysis*, Computer Methods in Applied Mechanics and Engineering, 49 (1985), pp. 253–279. doi:10.1016/0045-7825(85)90125-2.

[98] G. Jacquet-Richardet, G. Ferraris and P. Rieutord, *Fequencies and modes of rotating flexible bladed disc-shaft assemblies: A global cyclic symmetry approach*, Journal of Sound and Vibration, 191 (1996), pp. 901–915. doi:10.1006/jsvi.1996.0162.

[99] S. Jain, P. Tiso, J. B. Rutzmoser and D. J. Rixen, *A quadratic manifold for model order reduction of nonlinear structural dynamics*, Computers & Structures, 188 (2017), pp. 80–94. doi:10.1016/j.compstruc.2017.04.005.

[100] A. J. Jerri, *The Gibbs Phenomenon in Fourier Analysis, Splines and Wavelet Approximations*, Springer, Boston (USA), 1998. doi:10.1007/978-1-4757-2847-7.

[101] L. Jezequel and C. H. Lamarque, *Analysis of non-linear dynamical systems by the normal form theory*, Journal of Sound and Vibration, 149 (1991), pp. 429–459. doi:10.1016/0022-460X(91)90446-Q.

[102] C. Joannin, B. Chouvion and F. Thouverez, *A new dynamic substructuring method for nonlinear and dissipative systems*, in Proceedings of the VII European Congress on Computational Methods in Applied Sciences and Engineering, Hersonissos (Greece), 2016. doi:10.7712/100016.2135.4830.

[103] C. Joannin, B. Chouvion, F. Thouverez, J.-P. Ousty and M. Mbaye, *A nonlinear component mode synthesis method for the computation of steady-state vibrations in non-conservative systems*, Mechanical Systems and Signal Processing, 83 (2017), pp. 75–92. doi:10.1016/j.ymssp.2016.05.044.

[104] C. Joannin, F. Thouverez and B. Chouvion, *Reduced-order modelling using nonlinear modes and triple nonlinear modal synthesis*, Computers & Structures, 203 (2018), pp. 18–33. doi:10.1016/j.compstruc.2018.05.005.

[105] A. Joseph, *Cyclic Symmetry in MSC/NASTRAN*, in MSC/NASTRAN Application Manual, The MacNeal-Schwendler Corporation, Los Angeles (USA), 1981.

[106] J. A. Judge, C. Pierre and O. Mehmed, *Experimental Investigation of Mode Localization and Forced Response Amplitude Magnification for a Mistuned Bladed Disk*, Journal of Engineering for Gas Turbines and Power, 123 (2001), pp. 940–950. doi:10.1115/1.1377872.

[107] G. Kahl, *Aeroelastic Effects of Mistuning and Coupling in Turbomachinery Bladings*, PhD thesis, École Polytechnique Fédérale de Lausanne (Switzerland), 2002.

[108] R. K. Kapania and C. Byun, *Reduction methods based on eigenvectors and Ritz vectors for nonlinear transient analysis*, Computational Mechanics, 11 (1993), pp. 65–82. doi:10.1007/BF00370072.

[109] M. Karamooz Mahdiabadi, P. Tiso, A. Brandt and D. J. Rixen, *A non-intrusive model-order reduction of geometrically nonlinear structural dynamics using modal derivatives*, Mechanical Systems and Signal Processing, 147 (2021). doi:10.1016/j.ymssp.2020.107126.

[110] K. Karhunen, *Uber Lineare Methoden in der Wahrscheinlichkeitsrechnung [About linear methods in probability]*, Annals of Academic Science Fennicae, Series A1 Mathematics and Physics, 37 (1946), pp. 3–79.

[111] H. Kayadelen and Y. Üst, *Marine Gas Turbines*, in Proceedings of the 7th Advanced Technologies Symposium, Istanbul (Turkey), 2013.

[112] K. R. Kaza and R. E. Kielb, *Flutter and Response of a Mistuned Cascade in Incompressible Flow*, AIAA Journal, 20 (1982), pp. 1120–1127. doi:10.2514/3.51172.

[113] P. Kelly, *Stress Measures for Large Deformations*, in Mechanics Lecture Notes: Foundations of Continuum Mechanics, University of Auckland (New Zealand), 2015, pp. 341–350.

[114] J. A. Kenyon, J. H. Griffin and D. M. Feiner, *Maximum Bladed Disk Forced Response From Distortion of a Structural Mode*, Journal of Turbomachinery, 125 (2003), pp. 352–363. doi:10.1115/1.1540118.

[115] G. Kerschen, J.-C. Golinval, A. F. Vakakis and L. A. Bergman, *The method of proper orthogonal decomposition for dynamical characterization and order reduction of mechanical systems: An overview*, Nonlinear Dynamics, 41 (2005), pp. 147–169. doi:10.1007/s11071-005-2803-2.

[116] G. Kerschen, M. Peeters, J.-C. Golinval and A. F. Vakakis, *Nonlinear normal modes, Part I: A useful framework for the structural dynamicist*, Mechanical Systems and Signal Processing, 23 (2009), pp. 170–194. doi:10.1016/j.ymssp.2008.04.002.

[117] E. Khalifeh, E. Piollet, A. Millecamps and A. Batailly, *Non-linear modeling of centrifugal stiffening effects for accurate bladed component reduced-order models*, in Proceedings of ASME Turbo Expo 2017, Charlotte (USA), 2017. doi:10.1115/GT2017-63629.

[118] R. E. Kielb and M. Imregun, *Aeroelasticity in Axial Flow Turbomachines - Damping Characteristics*, in VKI Lecture Series 1999-05, von Karman Institute for Fluid Dynamics (Belgium), 1999.

[119] T. Klauke, A. Kühhorn, B. Beirow and M. Golze, *Numerical Investigations of Localized Vibrations of Mistuned Blade Integrated Disks (Blisks)*, Journal of Turbomachinery, 131 (2009). doi:10.1115/1.2985074.

[120] D. A. Knoll and D. E. Keyes, *Jacobian-free Newton–Krylov methods: a survey of approaches and applications*, Journal of Computational Physics, 193 (2004), pp. 357–397. doi:https://doi.org/10.1016/j.jcp.2003.08.010.

[121] S. Kojtych, *Contributions à l'optimisation de systèmes mécaniques non réguliers : reconception d'aubes de compresseur*, PhD thesis, Polytechnique Montréal (Canada), 2022.

[122] D. Kosambi, *Statistics in Function Space*, Journal of Indian Mathematical Society, 7 (1943), pp. 76–88. doi:10.1007/978-81-322-3676-4_15.

[123] M. Krack, L. Panning-von Scheidt, J. Wallaschek, C. Siewert and A. Hartung, *Reduced Order Modeling Based on Complex Nonlinear Modal Analysis and Its Application to Bladed Disks With Shroud Contact*, Journal of Engineering for Gas Turbines and Power, 135 (2013). doi:10.1115/1.4025002.

[124] D. Krattiger, L. Wu, M. Zacharczuk, M. Buck, R. J. Kuether, M. S. Allen, P. Tiso and M. R. Brake, *Interface reduction for Hurty/Craig-Bampton substructured models: Review and improvements*, Mechanical Systems and Signal Processing, 114 (2019), pp. 579–603. doi:10.1016/j.ymssp.2018.05.031.

[125] N. M. Krylov and N. N. Bogoliubov, *Introduction to non-linear mechanics*, Princeton University Press, 1943.

[126] E. Kurstak, R. Wilber and K. D'Souza, *Parametric reduced order models for bladed disks with mistuning and varying operational speed*, in Proceedings of ASME Turbo Expo 2018, Oslo (Norway), 2018. doi:10.1115/GT201875563.

[127] J. Lainé, E. Piollet, F. Nyssen and A. Batailly, *Blackbox optimization for aircraft engine blades with contact interfaces*, Journal of Engineering for Gas Turbines and Power, 141 (2019). doi:10.1115/1.4042808.

[128] S. B. Lattime and B. M. Steinetz, *Turbine engine clearance control systems: Current practices and future directions*, 38th AIAA/ASME/SAE/ASEE Joint Propulsion Conference and Exhibit, (2002). doi:10.2514/6.2002-3790.

[129] D. Laxalde and F. Thouverez, *Complex non-linear modal analysis for mechanical systems: Application to turbomachinery bladings with friction interfaces*, Journal of Sound and Vibration, 322 (2009), pp. 1009–1025. doi:10.1016/j.jsv.2008.11.044.

[130] A. Lazarus, O. Thomas and J. F. Deü, *Finite element reduced order models for nonlinear vibrations of piezoelectric layered beams with applications to NEMS*, Finite Elements in Analysis and Design, 49 (2012), pp. 35–51. doi:10.1016/j.finel.2011.08.019.

[131] J. Lee and M. Cho, *An interpolation-based parametric reduced order model combined with component mode synthesis*, Computer Methods in Applied Mechanics and Engineering, 319 (2017), pp. 258–286. doi:10.1016/j.cma.2017.02.010.

[132] M. Legrand, A. Batailly, B. Magnain, P. Cartraud and C. Pierre, *Full three-dimensional investigation of structural contact interactions in turbomachines*, Journal of Sound and Vibration, 331 (2012), pp. 2578–2601. doi:10.1016/j.jsv.2012.01.017.

[133] M. Legrand, A. Batailly and C. Pierre, *Numerical investigation of abradable coating removal in aircraft engines through plastic constitutive law*, Journal of Computational and Nonlinear Dynamics, 7 (2012), pp. 1–11. doi:10.1115/1.4004951.

[134] M. Legrand, C. Pierre, P. Cartraud and J. P. Lombard, *Two-dimensional modeling of an aircraft engine structural bladed disk-casing modal interaction*, Journal of Sound and Vibration, 319 (2009), pp. 366–391. doi:10.1016/j.jsv.2008.06.019.

[135] R. Lewandowski, *Computational formulation for periodic vibration of geometrically nonlinear structures - Part 1: Theoretical background*, International Journal of Solids and Structures, 34 (1997), pp. 1925–1947. doi:10.1016/S0020-7683(96)00127-8.

[136] S.-H. Lim, M. P. Castanier and C. Pierre, *Vibration Modeling of Bladed Disks Subject to Geometric Mistuning and Design Changes*, in Proceedings of the 45th AIAA/ASME/ASCE/AHS/ASC Structures, Structural Dynamics & Materials Conference, Palm Springs (USA), 2004, American Institute of Aeronautics and Astronautics. doi:10.2514/6.2004-1686.

[137] M. Loeve and P. Levy, *Fonctions aléatoires du second ordre*, in Processus stochastiques et mouvement Brownien, Gauthier-Villars, Paris, 1948.

[138] F. A. Lülf, D.-M. Tran and R. Ohayon, *Reduced bases for nonlinear structural dynamic systems: A comparative study*, Journal of Sound and Vibration, 332 (2013), pp. 3897–3921. doi:10.1016/J.JSV.2013.02.014.

[139] H. Ma, D. Wang, X. Tai and B. Wen, *Vibration response analysis of blade-disk dovetail structure under blade tip rubbing condition*, Journal of Vibration and Control, 23 (2017), pp. 252–271. doi:10.1177/1077546315575835.

[140] X. Ma and A. Matthews, *Investigation of abradable seal coating performance using scratch testing*, Surface and Coatings Technology, 202 (2007), pp. 1214–1220. doi:10.1016/j.surfcoat.2007.07.076.

[141] R. MacNeal, *A hybrid method of component mode synthesis*, Computers & Structures, 1 (1971), pp. 581–601. doi:10.1016/0045-7949(71)90031-9.

[142] A. Martin, *Réduction en dynamique non-linéaire géométrique : Application au cas des structures à symétrie cyclique*, PhD thesis, Ecole Centrale de Lyon (France), 2019.

[143] A. Martin and F. Thouverez, *Dynamic Analysis and Reduction of a Cyclic Symmetric System Subjected to Geometric Nonlinearities*, in Proceedings of ASME Turbo Expo 2018, Oslo (Norway), 2018, ASME. doi:10.1115/GT2018-75709.

[144] B. Martinet, A. Cappella, S. Philippon and C. Montebello, *Effect of temperature on wear mechanisms of an aluminium - based abradable coating for aircraft engines after a dynamic interaction with a Ti6Al4V blade*, Wear, 446-447 (2020). doi:https://doi.org/10.1016/j.wear.2020.203202.

[145] D. R. Martinez, T. Carne, D. L. Gregory and A. K. Miller, *Combined experimental/analytical modeling using component mode synthesis*, Computers & Structures, 78 (1984). doi:10.2514/6.1984-941.

[146] M. I. McEwan, J. R. Wright, J. E. Cooper and A. Y. Leung, *A combined modal/finite element analysis technique for the dynamic response of a non-linear beam to harmonic excitation*, Journal of Sound and Vibration, 243 (2001), pp. 601–624. doi:10.1006/jsvi.2000.3434.

[147] M. B. Meingast, M. Legrand and C. Pierre, *A linear complementarity problem formulation for periodic solutions to unilateral contact problems*, International Journal of Non-Linear Mechanics, 66 (2014), pp. 18–27. doi:10.1016/j.ijnonlinmec.2014.01.007.

[148] M. P. Mignolet and C.-C. Lin, *The Combined Closed Form-Perturbation Approach to the Analysis of Mistuned Bladed Disks*, Journal of Turbomachinery, 115 (1993), pp. 771–780. doi:10.1115/1.2929315.

[149] M. P. Mignolet, A. Przekop, S. Rizzi and S. M. Spottswood, *A review of indirect/non-intrusive reduced order modeling of nonlinear geometric structures*, Journal of Sound and Vibration, 332 (2013), pp. 2437–2460. doi:10.1016/j.jsv.2012.10.017.

[150] M. P. Mignolet, A. J. Rivas-Guerra and J. P. Delor, *Identification of Mistuning Characteristics of Bladed Disks From Free Response Data—Part I*, Journal of Engineering for Gas Turbines and Power, 123 (2001), pp. 395–403. doi:10.1115/1.1338949.

[151] A. Millecamps, A. Batailly, M. Legrand and F. Garcin, *Snecma's Viewpoint on the Numerical and Experimental Simulation of Blade-Tip/Casing Unilateral Contacts*, in Proceedings of ASME Turbo Expo 2015, Montréal (Canada), 2015. doi:10.1115/GT2015-42682.

[152] A. Millecamps, J.-F. Brunel, P. Dufrenoy, F. Garcin and M. Nucci, *Influence of Thermal Effects During Blade-Casing Contact Experiments*, in Proceedings of ASME 2009 International Design Engineering Technical Conferences & Computers and Information in Engineering Conference (IDETC/CIE 2011), San Diego (USA), 2009. doi:10.1115/DETC2009-86842.

[153] C. D. Monjaraz Tec, J. Gross and M. Krack, *A massless boundary component mode synthesis method for elastodynamic contact problems*, Computers & Structures, 260 (2022), p. 106698. doi:10.1016/j.compstruc.2021.106698.

[154] R. D. Moore and L. Reid, *Performance of Single-Stage Axial-Flow Transonic Compressor With Rotor and Stator Aspect Ratios of 1.19 and 1.26, Respectively, and With Design Pressure Ratio of 2.05*, tech. rep., NASA TP 1659, 1980.

[155] A. Muravyov and S. Rizzi, *Determination of nonlinear stiffness with application to random vibration of geometrically nonlinear structures*, Computers & Structures, 81 (2003), pp. 1513–1523. doi:10.1016/S0045-7949(03)00145-7.

[156] S. Nacivet, C. Pierre, F. Thouverez and L. Jezequel, *A dynamic Lagrangian frequency-time method for the vibration of dry-friction-damped systems*, Journal of Sound and Vibration, 265 (2003), pp. 201–219. doi:10.1016/S0022-460X(02)01447-5.

[157] A. H. Nayfeh and B. Balachandran, *Applied nonlinear dynamics: analytical, computational, and experimental methods*, Wiley, 1995. doi:10.1002/9783527617548.

[158] A. H. Nayfeh and D. T. Mook, *Nonlinear oscillations*, Wiley, 2004. doi:10.1002/9783527617586.

[159] A. H. Nayfeh and P. F. Pai, *Linear and Nonlinear Structural Mechanics*, Wiley, 2004. doi:10.1002/9783527617562.

[160] N. Newmark, *A Method of Computation for Structural Dynamics*, Journal of the Engineering Mechanics Division, 85 (1959), pp. 67–94.

[161] M. Nikolic, *New insights into the blade mistuning problem*, PhD thesis, University of London (UK), 2006.

[162] J. Nipkau, *Analysis of Mistuned Blisk Vibrations Using a Surrogate Lumped Mass Model with Aerodynamic Influences in Herzberg/Elster*, PhD thesis, Brandenburg University of Technology (Germany), 2011.

[163] S. Nitschke, T. Wollmann, C. Ebert, T. Behnisch, A. Langkamp, T. Lang, E. Johann and M. Gude, *An advanced experimental method and test rig concept for investigating the dynamic blade-tip/casing interactions under engine-like mechanical conditions*, Wear, 422-423 (2019), pp. 161–166. doi:https://doi.org/10.1016/j.wear.2018.12.072.

[164] F. Nyssen, Y. Colaïtis and A. Batailly, *Numerical investigation of a mistuned industrial bladed disk dynamics with structural contacts using time and frequency methods*, Journal of Sound and Vibration, 535 (2022). doi:10.1016/j.jsv.2022.117077.

[165] F. Nyssen, N. Tableau, D. Lavazec and A. Batailly, *Experimental and numerical characterization of a ceramic matrix composite shroud segment under impact loading*, Journal of Sound and Vibration, 467 (2020). doi:10.1016/j.jsv.2019.115040.

[166] V. Omprakash and V. Ramamurti, *Cyclic symmetry approach to the structural dynamic analysis of bladed discs*, Communications in Applied Numerical Methods, 8 (1992), pp. 81–91. doi:10.1002/cnm.1630080203.

[167] G. Óttarsson and C. Pierre, *On the effects of interblade coupling on the statistics of maximum forced response amplitudes in mistuned bladed disks*, in Proceedings of the 36th Structures, Structural Dynamics and Materials Conference, Reston (USA), 1995, American Institute of Aeronautics and Astronautics. doi:10.2514/6.1995-1494.

[168] H. Palfrey-Sneddon, A. J. Neely and E. O. Smith, *The influence of descent and taxi profiles on the thermal state of a jet engine at shutdown*, Proceedings of the 27th ISABE Conference, (2017), pp. 1–11.

[169] M.-O. Parent, F. Thouverez and F. Chevillot, *Whole Engine Interaction in a Bladed Rotor-to-Stator Contact*, in Proceedings of ASME Turbo Expo 2014, Düsseldorf (Germany), 2014. doi:10.1115/GT2014-25253.

[170] M. Peeters, R. Viguié, G. Sérandour, G. Kerschen and J.-C. Golinval, *Nonlinear normal modes, Part II: Toward a practical computation using numerical*

continuation techniques, Mechanical Systems and Signal Processing, 23 (2009), pp. 195–216. doi:10.1016/j.ymssp.2008.04.003.

[171] R. A. Perez, X. Q. Wang and M. P. Mignolet, *Nonintrusive Structural Dynamic Reduced Order Modeling for Large Deformations: Enhancements for Complex Structures*, Journal of Computational and Nonlinear Dynamics, 9 (2014). doi:10.1115/1.4026155.

[172] E. P. Petrov, *A Method for Use of Cyclic Symmetry Properties in Analysis of Nonlinear Multiharmonic Vibrations of Bladed Disks*, Journal of Turbomachinery, 126 (2004), pp. 175–183. doi:10.1115/1.1644558.

[173] ——, *A High-Accuracy Model Reduction for Analysis of Nonlinear Vibrations in Structures With Contact Interfaces*, Journal of Engineering for Gas Turbines and Power, 133 (2011). doi:10.1115/1.4002810.

[174] E. P. Petrov and D. J. Ewins, *Generic friction models for time-domain vibration analysis of bladed disks*, Journal of Turbomachinery, 126 (2004), pp. 184–192. doi:10.1115/1.1644557.

[175] ——, *Method for Analysis of Nonlinear Multiharmonic Vibrations of Mistuned Bladed Disks With Scatter of Contact Interface Characteristics*, Journal of Turbomachinery, 127 (2005), p. 128. doi:10.1115/1.1812781.

[176] A. Picou, *Robust analysis under uncertainties of bladed disk vibration with geometrical nonlinearities and detuning*, PhD thesis, Université Paris-Est (France), 2019.

[177] A. Picou, E. Capiez-Lernout, C. Soize and M. Mbaye, *Effects of geometrical nonlinearities for a rotating intentionally mistuned bladed-disk*, in Proceedings of the 28th International Conference on Noise and Vibration Engineering, Leuven (Belgium), 2018.

[178] ——, *Mistuning analysis of a detuned bladed-disk with geometrical nonlinearities*, in Proceedings of the ASME Turbo Expo 2019, Phoenix (USA), 2019. doi:10.1115/GT2019-90820.

[179] C. Pierre and E. Dowell, *Localization of vibrations by structural irregularity*, Journal of Sound and Vibration, 114 (1987), pp. 549–564. doi:10.1016/S0022-460X(87)80023-8.

[180] E. Piollet, F. Nyssen and A. Batailly, *Blade/casing rubbing interactions in aircraft engines: Numerical benchmark and design guidelines based on NASA rotor 37*, Journal of Sound and Vibration, 460 (2019). doi:10.1016/j.jsv.2019.114878.

[181] A. Prasad, *Improvements in Aircraft Gas Turbine Engines for the 90s*, Defence Science Journal, 43 (1993), pp. 449–452. doi:10.14429/dsj.43.4333.

[182] L. Prchlik and S. Sampath, *Effect of the microstructure of thermally sprayed coatings on friction and wear response under lubricated and dry sliding conditions*, Wear, 262 (2007), pp. 11–23. doi:10.1016/j.wear.2006.03.042.

[183] J. S. Rao, *History of Rotating Machinery Dynamics*, vol. 20, Springer Netherlands, 2011. doi:10.1007/978-94-007-1165-5_16.

[184] L. Reid and R. D. Moore, *Design and Overall Performance of Four Highly-Loaded, High Speed Inlet Stages for an Advanced High-Pressure Ratio Core Compressor*, tech. rep., NASA TP 1337, 1978.

[185] R. Rosenberg, *On nonlinear vibrations of systems with many degrees of freedom*, Academic Press, 1966. doi:10.1016/S0065.

[186] S. Rubin, *Improved Component-Mode Representation for Structural Dynamic Analysis*, AIAA Journal, 13 (1975), pp. 995–1006. doi:10.2514/3.60497.

[187] J. B. Rutzmoser, *Model Order Reduction for Nonlinear Structural Dynamics Simulation-free Approaches*, PhD thesis, Technische Universität München (Germany), 2018.

[188] J. B. Rutzmoser, D. J. Rixen, P. Tiso and S. Jain, *Generalization of quadratic manifolds for reduced order modeling of nonlinear structural dynamics*, Computers & Structures, 192 (2017), pp. 196–209. doi:10.1016/J.COMPSTRUC.2017.06.003.

[189] S. Sakulkaew, C. S. Tan, E. Donahoo, C. Cornelius and M. Montgomery, *Compressor efficiency variation with rotor tip gap from vanishing to large clearance*, Journal of Turbomachinery, 135 (2013). doi:10.1115/1.4007547.

[190] N. Salvat, A. Batailly and M. Legrand, *Two-dimensional modeling of unilateral contact-induced shaft precessional motions in bladed-disk/casing systems*, International Journal of Non-Linear Mechanics, 78 (2016), pp. 90–104. doi:10.1016/j.ijnonlinmec.2015.10.001.

[191] C. W. Schwingshackl, E. P. Petrov and D. J. Ewins, *Effects of Contact Interface Parameters on Vibration of Turbine Bladed Disks With Underplatform Dampers*, Journal of Engineering for Gas Turbines and Power, 134 (2012). doi:10.1115/1.4004721.

[192] P. Seshu, *Substructuring and Component Mode Synthesis*, Shock and Vibration, 4 (1997), pp. 199–210. doi:10.3233/SAV-1997-4306.

[193] S. Setio, H. D. Setio and L. Jezequel, *Modal analysis of nonlinear multi-degree-of-freedom structures*, The International Journal of Analytical and Experimental Modal Analysis, 7 (1992), pp. 75–93.

[194] L. F. Shampine, *Numerical Solution of Ordinary Differential Equations*, Routledge, New York (USA), 1994. doi:10.1201/9780203745328.

[195] C. E. Shannon, *Communication in the Presence of Noise*, in Proceedings of the IRE, 1949, pp. 10–21.

[196] B. Shapiro, *Passive control of flutter and forced response in bladed disks via mistuning*, Dissertation, California Institute of Technology (USA), 1999.

[197] Siemens, *Siemens PLM Software – LMS Samtech Samcef Mecano*, tech. rep., 2014.

[198] M. Singh, J. Vargo, D. Schiffer and J. Dello, *Safe diagram - a design and reliability tool for turbine blading*, Proceedings of the 17th Turbomachinery Symposium, (1988).

[199] A. Sinha, *Calculating the statistics of forced response of a mistuned bladed disk assembly*, AIAA Journal, 24 (1986), pp. 1797–1801. doi:10.2514/3.9526.

[200] ——, *Computation of the Statistics of Forced Response of a Mistuned Bladed Disk Assembly via Polynomial Chaos*, Journal of Vibration and Acoustics, 128 (2006), pp. 449–457. doi:10.1115/1.2215620.

[201] S. K. Sinha, *Rotordynamic analysis of asymmetric turbofan rotor due to fan blade-loss event with contact-impact rub loads*, Journal of Sound and Vibration, 332 (2013), pp. 2253–2283. doi:10.1016/j.jsv.2012.11.033.

[202] P. Slaats, J. de Jongh and A. Sauren, *Model reduction tools for nonlinear structural dynamics*, Computers & Structures, 54 (1995), pp. 1155–1171. doi:10.1016/0045-7949(94)00389-K.

[203] J. C. Slater, G. Minkiewicz and A. Blair, *Forced response of bladed disk assemblies - A survey*, The Shock and Vibration Digest, 31 (1999), pp. 17–24. doi:10.2514/6.1998-3743.

[204] T. M. Smith, R. van de Geijn, M. Smelyanskiy, J. R. Hammond and F. G. V. Zee, *Anatomy of High-Performance Many-Threaded Matrix Multiplication*, in 28th International Parallel and Distributed Processing Symposium, 2014, pp. 1049–1059. doi:10.1109/IPDPS.2014.110.

[205] C. S. Sombroek, P. Tiso, L. Renson and G. Kerschen, *Numerical computation of nonlinear normal modes in a modal derivative subspace*, Computers & Structures, 195 (2018), pp. 34–46. doi:10.1016/j.compstruc.2017.08.016.

[206] S. M. Spottswood and R. J. Allemang, *On the Investigation of Some Parameter Identification and Experimental Modal Filtering Issues for Nonlinear Reduced Order Models*, Experimental Mechanics, 47 (2007), pp. 511–521. doi:10.1007/s11340-007-9047-7.

[207] A. V. Srinivasan, *Flutter and Resonant Vibration Characteristics of Engine Blades*, Journal of Engineering for Gas Turbines and Power, 119 (1997), pp. 742–777. doi:10.1115/1.2817053.

[208] K. Steffens, *Next engine generation: Materials, surface technology, manufacturing processes, What comes after 2000?*, in Proceedings of SurTec Conference, Cannes (France), 2000.

[209] ——, *Advanced Compressor Technology - Key Success Factor for Competitiveness in Modern Aero Engines*, in Proceedings of the 15th International Symposium on Air Breathing Engines, Bagalore (India), 2001.

[210] A. Sternchüss, *Multi-level parametric reduced models of rotating bladed disk assemblies*, PhD thesis, École Centrale de Paris (France), 2009.

[211] A. Sternchüss and E. Balmès, *On the reduction of quasi-cyclic disk models with variable rotation speeds*, in Proceedings of the 22nd International Conference on Noise and Vibration Engineering, Leuven (Belgium), 2006.

[212] B. Strachan, S. W. Shaw and O. Kogan, *Subharmonic resonance cascades in a class of coupled resonators*, Journal of Computational and Nonlinear Dynamics, 8 (2013). doi:10.1115/1.4024542.

[213] U. Strehlau and A. Kühhorn, *Experimental and Numerical Investigations of HPC Blisks With a Focus on Travelling Waves*, in Proceedings of ASME Turbo Expo 2010, Glasgow (UK), 2010, pp. 865–877. doi:10.1115/GT2010-22463.

[214] W. Szemplińska-Stupnicka, *The modified single mode method in the investigations of the resonant vibrations of non-linear systems*, Journal of Sound and Vibration, 63 (1979), pp. 475–489. doi:10.1016/0022-460X(79)90823-X.

[215] D. L. Thomas, *Dynamics of rotationally periodic structures*, International Journal for Numerical Methods in Engineering, 14 (1979), pp. 81–102. doi:10.1002/nme.1620140107.

[216] A. Thorin, N. Guérin, M. Legrand, F. Thouverez and P. Almeida, *Non-smooth Thermoelastic Simulations of Blade–Casing Contact Interactions*, Journal of Engineering for Gas Turbines and Power, 141 (2018). doi:10.1115/1.4040857.

[217] P. Tiso, *Effective modal derivatives based reduction method for geometrically nonlinear structures*, in Proceedings of ASME 2011 International Design Engineering Technical Conferences & Computers and Information in Engineering Conference (IDETC/CIE 2011), Washington (USA), 2011, pp. 399–406. doi:10.1115/DETC2011-48315.

[218] C. Touzé, *Normal form theory and nonlinear normal modes: Theoretical settings and applications*, in Modal Analysis of Nonlinear Mechanical Systems, vol. 555, Springer, 2014.

[219] C. Touzé, O. Thomas and A. Chaigne, *Hardening/softening behaviour in non-linear oscillations of structural systems using non-linear normal modes*, Journal of Sound and Vibration, 273 (2004), pp. 77–101. doi:10.1016/J.JSV.2003.04.005.

[220] C. Touzé, M. Vidrascu and D. Chapelle, *Direct finite element computation of non-linear modal coupling coefficients for reduced-order shell models*, Computational Mechanics, 54 (2014), pp. 567–580. doi:10.1007/s00466-014-1006-4.

[221] D.-M. Tran, *Component mode synthesis methods using partial interface modes: Application to tuned and mistuned structures with cyclic symmetry*, Computers & Structures, 87 (2009), pp. 1141–1153. doi:10.1016/J.COMPSTRUC.2009.04.009.

[222] R. Vaidyanathan, S. Santhanam and V. Ramamurti, *Static and dynamic analysis of an aerofoil bladed disc using the concept of cyclic symmetry*, Communications in Numerical Methods in Engineering, 19 (2003), pp. 313–324. doi:10.1002/cnm.571.

[223] A. F. Vakakis, *Dynamics of a nonlinear periodic structure with cyclic symmetry*, Acta Mechanica, 95 (1992), pp. 197–226. doi:10.1007/BF01170813.

[224] ——, *Normal modes and localization in nonlinear systems*, Springer Netherlands, New York (USA), 1996.

[225] ——, *Non-linear normal modes (NNMs) and their applications in vibration theory: An overview*, Mechanical Systems and Signal Processing, 11 (1997), pp. 3–22. doi:10.1006/mssp.1996.9999.

[226] R. Valid and R. Ohayon, *Théorie et calcul statique et dynamique des structures à symétries cycliques*, La Recherche Aérospatiale, 4 (1985), pp. 251–263.

[227] F. G. Van Zee and R. A. van de Geijn, *BLIS: A Framework for Rapidly Instantiating BLAS Functionality*, ACM Transactions on Mathematical Software, 41 (2015). doi:10.1145/2764454.

[228] F. Vetrano, C. Le Garrec, G. Mortchelewicz and R. Ohayon, *Assessment of Strategies for Interpolating POD Based Reduced Order Models and Application to Aeroelasticity*, ASDJournal, 2 (2011), pp. 85–104. doi:10.3293/asdj.2011.13.

[229] A. Vizzaccaro, A. Givois, P. Longobardi, Y. Shen, J. F. Deü, L. Salles, C. Touzé and O. Thomas, *Non-intrusive reduced order modelling for the dynamics of geometrically nonlinear flat structures using three-dimensional finite elements*, Computational Mechanics, 66 (2020), pp. 293–1319. doi:10.1007/s00466-020-01902-5.

[230] A. Vizzaccaro, Y. Shen, L. Salles, J. Blahoš and C. Touzé, *Direct computation of nonlinear mapping via normal form for reduced-order models of finite element nonlinear structures*, Computer Methods in Applied Mechanics and Engineering, 384 (2021). doi:10.1016/j.cma.2021.113957.

[231] N. Wang, C. Liu, D. Jiang and K. Behdinan, *Casing vibration response prediction of dual-rotor-blade-casing system with blade-casing rubbing*, Mechanical Systems and Signal Processing, 118 (2019), pp. 61–77. doi:10.1016/j.ymssp.2018.08.029.

[232] X. Q. Wang, R. A. Perez, M. P. Mignolet, R. Capillon and C. Soize, *Nonlinear reduced order modeling of complex wing models*, in Proceedings of the 54th AIAA/ASME/ASCE/AHS/ASC Structures, Structural Dynamics, and Materials Conference, Boston (USA), 2013.

[233] W. Waschka, K. Rüd, M. Metscher and A. Michel, *ATFI-HDV: Design of a new 7 stage innovative compressor for 10 – 18 klbf thrust*, in Proceedings of the 17th International Symposium on Air Breathing Engines, Munich (Germany), 2005.

[234] O. Weeger, U. Wever and B. Simeon, *Nonlinear frequency response analysis of structural vibrations*, Computational Mechanics, 54 (2014), pp. 1477–1495. doi:10.1007/s00466-014-1070-9.

[235] ——, *On the use of modal derivatives for nonlinear model order reduction*, International Journal for Numerical Methods in Engineering, 108 (2016), pp. 1579–1602. doi:10.1002/nme.5267.

[236] S.-T. Wei and C. Pierre, *Localization Phenomena in Mistuned Assemblies with Cyclic Symmetry Part I: Free Vibrations*, Journal of Vibration Acoustics Stress and Reliability in Design, 110 (1988), pp. 429–438. doi:10.1115/1.3269547.

[237] F. Wenneker and P. Tiso, *A substructuring method for geometrically nonlinear structures*, Conference Proceedings of the Society for Experimental Mechanics Series, 1 (2014), pp. 157–165. doi:10.1007/978-3-319-04501-6_14.

[238] D. S. Whitehead, *Effect of Mistuning on the Vibration of Turbo-Machine Blades Induced by Wakes*, Journal of Mechanical Engineering Science, 8 (1966), pp. 15–21. doi:10.1243/JMES_JOUR_1966_008_004_02.

[239] S. Willeke, L. Panning-Von Scheidt and J. Wallaschek, *Reduced order modeling of mistuned bladed disks under rotation*, Technische Mechanik, 37 (2017), pp. 314–325. doi:10.24352/UB.OVGU-2017-107.

[240] R. J. Williams, *Simulation of blade casing interaction phenomena in gas turbines resulting from heavy tip rubs using an implicit time marching method*, in Proceedings of ASME Turbo Expo 2011, Vancouver (Canada), 2011. doi:10.1115/GT2011-45495.

[241] L. Woiwode, N. N. Balaji, J. Kappauf, F. Tubita, L. Guillot, C. Vergez, B. Cochelin, A. Grolet and M. Krack, *Comparison of two algorithms for Harmonic Balance and path continuation*, Mechanical Systems and Signal Processing, 136 (2020). doi:10.1016/j.ymssp.2019.106503.

[242] L. Wu and P. Tiso, *Nonlinear model order reduction for flexible multibody dynamics: a modal derivatives approach*, Multibody System Dynamics, 36 (2016), pp. 405–425. doi:10.1007/s11044-015-9476-5.

[243] L. Wu, P. Tiso and F. van Keulen, *A modal derivatives enhanced Craig-Bampton method for geometrically nonlinear structural dynamics*, in Proceedings of the 27th International Conference on Noise and Vibration Engineering, Leuven (Belgium), 2016, pp. 3615–3624.

[244] J. Xiao, Y. Chen, D. Chen, J. Tian, H. Ouyang and A. Wang, *Interactions between blades and abradable coatings: a numerical approach considering geometrical nonlinearity*, International Journal of Mechanical Sciences, (2020). doi:10.1016/j.ijmecsci.2020.106052.

[245] L. Xie, S. Baguet, B. Prabel and R. Dufour, *Numerical Tracking of Limit Points for Direct Parametric Analysis in Nonlinear Rotordynamics*, Journal of Vibration and Acoustics, 138 (2016). doi:10.1115/1.4032182.

[246] M.-T. Yang and J. H. Griffin, *A Reduced-Order Model of Mistuning Using a Subset of Nominal System Modes*, Journal of Engineering for Gas Turbines and Power, 123 (2001), pp. 893–900. doi:10.1115/1.1385197.

[247] M. Yi, J. He, B. Huang and H. Zhou, *Friction and wear behaviour and abradability of abradable seal coating*, Wear, 231 (1999), pp. 47–53. doi:10.1016/S0043-1648(99)00093-9.

[248] J. Zenneck, *Ueber die freien Schwingungen nur annähernd vollkommener kreisförmiger Platten*, Annalen der Physik und Chemie, 303 (1899), pp. 165–184. doi:10.1002/andp.18993030110.

[249] B. Zhang and M. Marshall, *Investigating material removal mechanism of Al-Si base abradable coating in labyrinth seal system*, Wear, 426-427 (2019), pp. 239–249. doi:10.1016/j.wear.2019.01.034.